STRUCTURE/FUNCTION ANALYSES OF *SCHIZOSACCHAROMYCES POMBE* PROTEINS PPN1 AND ASP1, TWO AGENTS OF TRANSCRIPTION TERMINATION AND PHOSPHATE HOMEOSTASIS

by

Bradley Benjamin

A Dissertation

Presented to the Faculty of the Louis V. Gerstner, Jr. Graduate School of Biomedical Sciences, Memorial Sloan-Kettering Cancer Center

in Partial Fulfillment of the Requirements for the Degree of Doctor of Philosophy

New York, NY

September, 2022

_____ _____

Stewart H. Shuman Date

PhD Dissertation Mentor

DEDICATION

To my mother, Dr. Barbara Vogt, who taught me that we are not only the people we are today, but also the people we are becoming – our dreams and ambitions. I could never have persevered without your encouragement and example.

ABSTRACT

Transcriptional interference is a phenomenon by which transcription of one gene physically represses expression of another. While it is frequently thought of as an unwelcome byproduct of transcription in small, crowded genomes, transcriptional interference can also be used in a regulated manner to control gene expression. The fission yeast *Schizosaccharomyces pombe* uses a scheme in which transcription of upstream lncRNAs actively represses expression of genes involved in phosphate homeostasis (*PHO*) in phosphate replete conditions. Fission yeast upregulate the *PHO* regulon during acute phosphate starvation by turning off *PHO* lncRNA transcription, allowing RNA Polymerase II (Pol II) to access *PHO* promoters.

Our laboratory has uncovered mutations that perturb *PHO* lncRNA termination, which in turn affects *PHO* gene expression. These mutations provide insight into fundamental control points of transcription termination that are difficult to observe through other systems, either because they are buffered by redundant processes, or because they are so essential that their perturbation is lethal. This research has elucidated termination control exhibited by the conserved Pol II C-terminal domain, members of the cleavage and polyadenylation factor (CPF), and by the signaling molecule 1,5-IP_8, respectively. The interplay between these factors, as well as the biochemical and structural characterization of Asp1 – an enzyme responsible for 1,5-IP_8 synthesis and catabolism – constitute the focus of this dissertation.

The first part of my dissertation is a structure-function analysis of Ppn1, a component of fission yeast CPF. My findings identified the essential and inessential components of Ppn1, mapped Ppn1's interactions with other CPF members Dis2 and Swd22 to specific amino acid regions, found several point mutants that selectively disrupt Ppn1•Dis2 or Ppn1•Swd22 association, and showed that Ppn1's essential role in transcription depends on its ability to bind either Dis2 or its paralog Sds21. This chapter provides a framework for understanding a conserved CPF submodule.

The latter chapters of my dissertation describe my biochemical and structural characterization of Asp1, a bifunctional enzyme consisting of an N-terminal inositol phosphate kinase and a C-terminal inositol phosphate pyrophosphatase. Using recombinant proteins, I demonstrate that Asp1 performs futile cycles of phosphorylation and dephosphorylation of 5-IP_7 at the 1-phosphate position. I provide evidence that physiologically relevant concentrations of inorganic phosphate inhibit pyrophosphatase activity, thus enabling net accumulation of 1,5-IP_8. *In vivo* overexpression of Asp1 proteins that lack pyrophosphatase activity de-represses a *PHO* gene, with magnitude of de-repression correlating to *in vitro* kinase activity. Crystallization of Asp1 kinase domain in the presence of substrates revealed that this enzyme adopts an "ATP-grasp" fold. A second protomer in the asymmetric unit lacked substrates in its active site and adopted an open conformation as compared to the enzyme with bound substrates. I present a model of enzyme ligand recognition in which active site opening and closing facilitates substrate binding, catalysis, and product

release. Together, these chapters increase our understanding of an enzyme involved in phosphate homeostasis and transcription termination.

BIOGRAPHICAL SKETCH

Bradley was born in Stamford Connecticut to Drs. Barbara Vogt, PhD and Sanford Benjamin, MD. He performed undergraduate study at Tufts University, where he majored in biology and minored in computer science. Bradley received mentorship from Dr. Sergei Mirkin, whose seminars on DNA structure and function encouraged Bradley's scientific curiosity. Upon graduation, Bradley joined the lab of Dr. Evgeny Nudler at New York University Langone Medical as a Research Associate. In this role, Bradley investigated transcription-coupled nucleotide excision repair, sparking interest in the field of transcription mechanics.

Bradley earned a master's degree in biomedical sciences from the Icahn School of Medicine at Mount Sinai in 2017. Working in the lab of Dr. Robert Fisher, Bradley performed research on the regulation of transcription termination. His master's thesis, entitled "Regulation of Spt5 phosphorylation and transcription elongation by P-TEFb and PP1," explored a dephosphorylation event on the Spt5 C-terminal domain (CTD) which coincides with the transition from transcription elongation to termination. Bradley credits Dr. Fisher's support as the most important influence on his decision to pursue a PhD.

Between his master's and PhD tenure, Bradley joined the Inez Rogatsky lab at the Hospital for Special Surgery, where he investigated transcriptional responses to inflammation and glucocorticoid treatment in macrophages.

In 2018, Bradley joined the Gerstner Sloan Kettering Graduate School of Biomedical Sciences to pursue a PhD. Bradley rotated in the labs of Dr. Stewart Shuman and Dr. Christopher Lima, choosing the Shuman lab for his thesis

research. Bradley received informal co-mentorship from Dr. Beate Schwer of Weill-Cornell Medical Center, whose guidance was essential for his investigation of Ppn1 structure/function.

In 2019, Bradley married Ariel Janet ‘AJ’ Velarde in a ceremony in New Rochelle, New York. AJ and Bradley began dating in 2008, and their nuptials followed many years of growth, both individually and as a couple. In 2021, they welcomed a baby daughter, Tessa Curie Benjamin. Tessa’s middle name was inspired by Marie Skłodowska Curie, who serves as personal and professional role model to Bradley.

Upon earning his PhD, Bradley will join Regeneron Pharmaceuticals as a postdoctoral fellow.

ACKNOWLEDGEMENTS

First and foremost, I must thank my wife, AJ (Velarde) Benjamin. Like couch cushions, pasta dishes, and our beautiful daughter, this accomplishment is shared between us. I could not have done this without your support.

I would like to thank all my lab-mates. I have always thought of bench science as “us against the PI” – jokes like these made my PhD possible. Thank you for training me, for commiserating with me, and for laughing with me over these last nine years. I owe particular thanks to Drs. Venu Kamarthapu, Pabitra Parua, and Angad Garg – I am extremely lucky to have had you as mentors.

Ana Sanchez also deserves special appreciation. For the last four years, everything I wrote and every presentation I made was thoroughly vetted by your eyes – thank you for your selflessness. I wish I had half of your work ethic and a quarter of your organizational skill. Though I aspire each day to follow your example by talking a little less and listening a little more, I fear I will always trail you. In the meantime, I hope my embarrassing karaoke performances bring you a little bit of happiness! You are a unique talent; I know you will go on to make great discoveries.

My graduate student classmates, particularly Alex Settle, Eleanor Johns, Katelyn Mullen, Ella Melnik, and Yanyang Chen, have made these past four years a wonderful experience. Thank you for countless memories, and for always offering a listening ear when I need to vent about lab.

To my committee, Drs. Christine Mayr and Chris Lima, I owe you tremendous credit. While I am grateful for your sharp constructive criticism, I would

be remiss to not mention how much you transcended your scientific responsibility by caring about my mental health. You were there for me in moments when I really needed it. Any student would be lucky to have you in their corner.

My parents, Sandy Benjamin and Barbara Vogt, instilled within me a sense of purpose and gave me all the means to fulfill that dream. Thank you so much. My inlaws, Stacy and Len Velarde, taught me to break rules, push boundaries, and make the easy choice when possible. As someone who by nature makes his own life as hard as possible, I appreciate your attempts to mold me!

Finally, Stewart and Beate, thank you for taking me on as a student. I knew that I needed mentors who would challenge me, and I found exactly that in you two. I leave MSK with a million stories in which I thought I knew better than you and was later proven wrong. I learned to speak with precision and not assert something as fact without the data to back it up. I learned to not cut corners – that taking the extra day to do it right meant saving a week of failure using the quick and dirty method. I learned that asking small, clear questions can yield exciting, surprising answers. I learned to not make assumptions that what we expect to see is the whole story. I may not be the best grad student to ever sail from your shores (I know you have your list!), but I think I might challenge for ‘most improved.’ That makes a PhD very worth it.

Table of Contents

List of Tables

List of Figures

List of Abbreviations

1-IP_7 – 1-pyrophosphate inositol 2,3,4,5,6-pentakisphosphate
1,5-IP_8 – 1,5-pyrophosphate inositol 2,3,4,6-tetrakisphosphate
5-IP_7 – 5-pyrophosphate inositol 1,2,3,4,6-pentakisphosphate
ADP – adenosine diphosphate
ASU – Asymmetric Unit
ATP – adenosine triphosphate
C- – carboxy, as in the C-terminus of a protein
ChIP-seq – Chromatin immunoprecipitation followed by sequencing
CK2 – Casein Kinase 2
CPF – Cleavage and polyadenylation factor
CTD – C-terminal domain
CTP – cytosine triphosphate
dATP – deoxyadenosine triphosphate
DNA – deoxyribonucleic acid
GTP – guanosine triphosphate
HAP – histidine acid phosphatase
HPLC – High-performance liquid chromatography
IP_3 – Inositotol 1,4,5-triphosphate
IP3K – IP_3 kinase
IP3R – IP_3 receptor
IP_6 – Inositol hexakisphosphate
IPMK – Inotisol phosphate multi-kinase
IPP – Inositol pyrophosphate
lncRNA – Long non-coding RNA
mRNA – messenger RNA
N- – amino, as in the N-terminus of a protein
PAGE – Polyacrylamide gel electrophoresis
PAS – Polyadenylation signal
PHO – Phosphate homeostasis
P_i – Inorganic phosphate
PI – Phosphatidylinositol
PIP_2 – Phosphatidylinositol 4,5-bisphosphate
PNPP – para-nitrophenyl phosphate
Pol2 – RNA Polymerase II
RNA – ribonucleic acid
SDS – Sodium dodecyl sulfate

TLC – thin layer chromatography
UTP – uridine triphosphate

Chapter 1: Introduction and Scope of Dissertation

It is a profound and necessary truth that the deep things in science are not found because they are useful; they are found because it was possible to find them.

-J. Robert Oppenheimer

1.1: The *Schizosaccharomyces pombe PHO* regulon and transcriptional interference

Homeostasis, the maintenance of stability despite changing environmental conditions, is a defining feature of living organisms. The fission yeast *Schizosaccharomyces pombe* possesses a variety of genetic programs to sense environmental conditions and buffer itself against fluctuations in temperature, osmotic pressure, or nutrient availability. Inorganic phosphate (P_i) is a one such essential nutrient. Phosphate homeostasis is maintained by a genetic program called *PHO* defined by three genes: a cell-surface acid phosphatase encoded by *pho1*, a P_i transporter encoded by *pho84*, and a glycerophosphate transporter encoded by *tgp1* (1, 2). In phosphate-replete conditions, these genes exhibit low expression. During phosphate starvation, the *PHO* genes are turned on, enabling accumulation of each of the three protein products which promote phosphate scavenging from the environment.

Significant attention has been paid to identifying the rules that dictate *PHO* gene expression. Screening for *PHO* regulators is made easier by the fact that phosphatase activity of Pho1, the cell-surface acid phosphatase, can be assessed using a simple colorimetric assay (3). This assay allows for both quantitative

assessment of Pho1 activity in liquid cultures or qualitative assessment of Pho1 activity of cells growing on plates. The former leverages Pho1's ability to dephosphorylate para-nitrophenyl phosphate to yield P_i and para-nitrophenol, which can be detected quantitatively by alkaline adjustment and spectroscopic measurement at 410 nm (a wavelength at which de-protonated para-nitrophenoxide, but not protonated para-nitrophenol, exhibits strong light absorbance). The latter utilizes 1-napthylphosphate as a Pho1 target – subjecting colonies treated with 1-napthylphosphate with a diazo-coupling reagent such as Fast Blue Salt B enables the distinction of colonies with high Pho1 activity (which appear red) from those with medium (pink) and low (white) activity. Acid phosphatase activity tracks with Pho1 protein abundance and *pho1* gene expression, which in turn expresses consistently with other *PHO* genes, making acid phosphatase activity an excellent proxy for *PHO* gene expression (4).

Characterization of the fission yeast *PHO* regulon was carried out by the work of several research groups encompassing the Wykoff, O'Shea, Allshire, Grewal, Vasiljeva, and Shuman/Schwer labs. In 2011, Wykoff and colleagues published results of a screen of a library of fission yeast gene knockout strains to identify genes whose mutation dysregulated fission yeast *PHO* expression (3). This study found mutants which either failed to induce *PHO* expression in phosphate-starved conditions and or caused constitutive *PHO* expression even in phosphate-replete conditions. The former class included the *PHO* master transcription factor Pho7. However, this class also included Ctf1, a component of the cleavage and polyadenylation factor (CPF) that executes RNA 3' end

processing and promotes transcription termination. This finding prompted researchers to seek a mechanistic link between transcription termination efficacy and basal *PHO* regulation.

A first clue to the organization of the *PHO* regulon was found in the discovery that Pho7 levels and cellular localization are constant despite phosphate availability (2, 3). This finding raised the possibility that *PHO* genes were actively repressed, and loss of this repressive signal in the presence of Pho7 enabled constitutive expression. In studying a non-coding RNA silencing complex associated with the RNA exosome, the Grewal group noticed complex recruitment to loci upstream of *pho1* (5). Pursuing this lead enabled identification of a long non-coding RNA (lncRNA) termed *prt* that overlaps with *pho1* and its promoter that is rapidly degraded by the RNA exosome (6, 7). Interfering lncRNAs termed *nc-tgp1* and *prt2* were later discovered upstream of *tgp1* and *pho84,* respectively (8, 9). Synthesizing these findings generated a model outlined in Figure 1 in which transcription of upstream lncRNAs occludes the promoters of each of the *PHO* genes, preventing stable Pho7 binding and recruitment of RNA Polymerase II (Pol2) (9). Therefore, basal *PHO* gene expression is low while the lncRNA genes are transcribed.

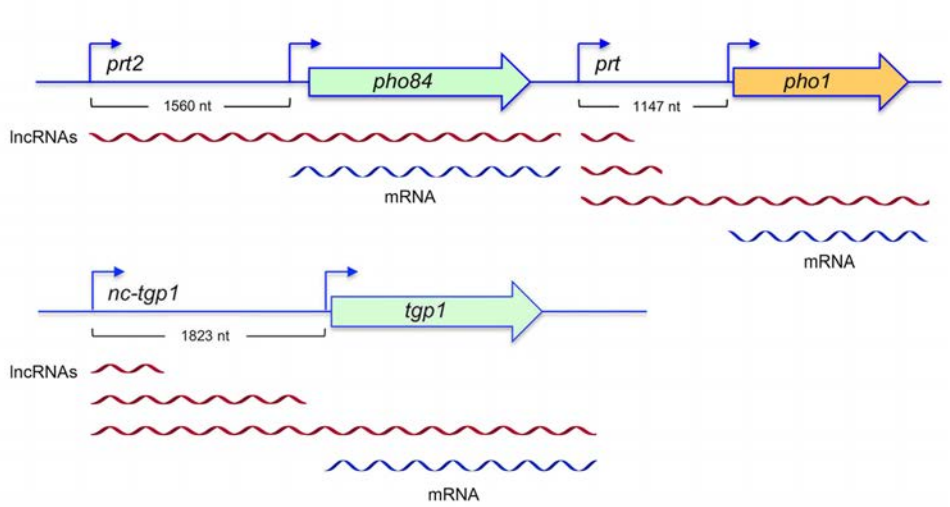

Figure 1. **Genomic architecture of the fission yeast *PHO* regulon.** Genes that are upregulated during phosphate starvation are represented as filled arrows; *pho84* and *tgp1* are green, while *pho1* is yellow. RNA species are shown below each gene, with red wavy lines indicating lncRNA and blue wavy lines indicating mRNA. Transcription of *PHO* lncRNAs which span the mRNA promoters blocks Pho7 access, silencing *PHO* coding genes. Note that the *pho1* gene is colored yellow because its expression can be gauged using a colorimetric assay that detects the yellow product of a Pho1-catalyzed reaction, providing a simple means of assaying *PHO* gene expression. Figure courtesy of Stewart Shuman.

This architecture of upstream lncRNA transcription actively repressing expression of downstream genes is known as transcriptional interference, and has been established as a hallmark of *PHO* gene expression regulation (1); the genomic organization of this type of regulatory system is outlined in Figure 2. Tandem lncRNA•protein coding gene transcriptional interference is also used in the regulation of serine metabolism genes in the budding yeast *Saccharomyces cerevisiae*, and was recently identified in the higher eukaryote *Drosophila melanogaster* in regulating the temporal sequestration of developmental gene expression (10, 11).

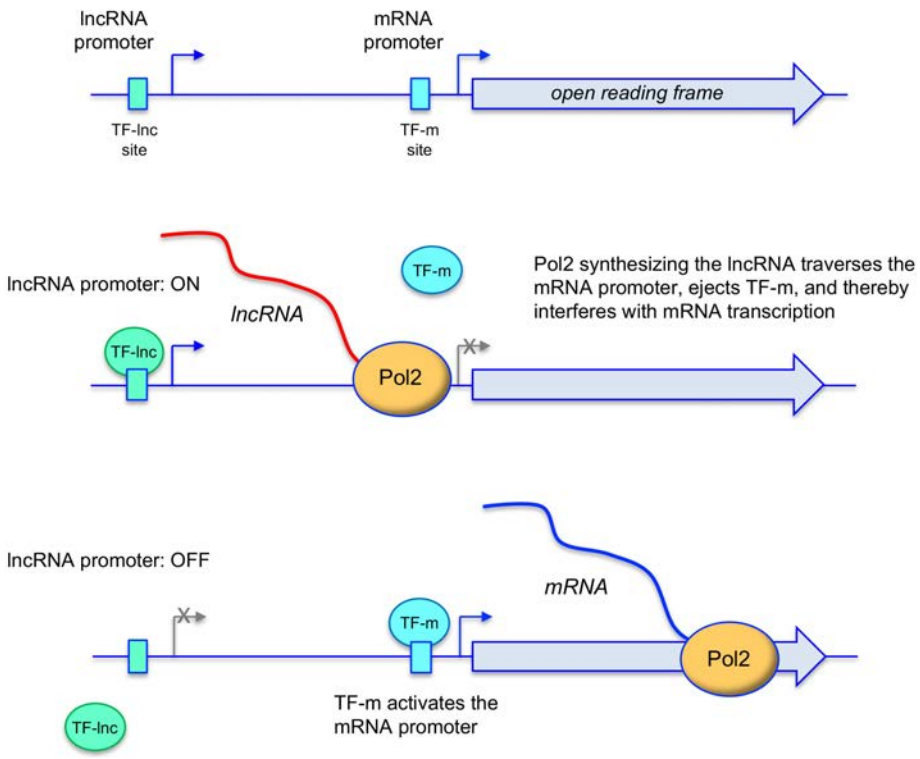

Figure 2. **Transcriptional interference at tandem lncRNA and protein coding genes.** (Top panel) Depiction of a regulatory scheme showing how transcription of an upstream lncRNA can control expression of a downstream coding gene. lncRNA transcription is regulated by a transcription factor (TF-lnc) which responds to cellular signals. During conditions when the coding gene is turned off (middle panel), TF-lnc binds its promoter, driving lncRNA transcription, which prevents the mRNA transcription factor (TF-m) from binding its promoter. To drive mRNA expression (bottom panel), cellular signals to TF-lnc prevent it from binding its lncRNA promoter. Because no lncRNA is transcribed, TF-m can now access the mRNA promoter and drive gene expression. Figure courtesy of Stewart Shuman.

Characterization of the regulatory scheme of the *PHO* system prompted researchers to search for the mechanistic triggers which drive *PHO* gene expression during phosphate starvation. Pho7 abundance and nuclear localization remain unchanged upon phosphate starvation – however, *PHO* interfering lncRNA expression is switched off, turning *PHO* genes on by allowing Pho7 to bind to promoters proximal to each *PHO* gene (2). The mechanism by which phosphate

starvation instructs the cell to shut off *PHO* lncRNA transcription remains unclear – though promoter elements including TATA and HomolD boxes have been identified upstream of each *PHO* lncRNA start site (4, 7, 9), no activating or repressive transcription factors have yet been implicated the regulation of these genes (1).

Although the native regulator of *PHO* lncRNA transcription has not yet been identified, research has uncovered several factors that tune *PHO* gene expression. The low basal expression of *PHO* mRNA can be driven even lower by mutations that reduce termination efficiency of the *PHO* lncRNAs, a state termed *PHO* hyper-repression (12, 13). Alternatively, mutations that promote precocious termination of *PHO* lncRNA upstream of the *PHO* mRNA promoter sites upregulate *PHO* gene expression even in phosphate-rich conditions (4, 12-14). These studies demonstrate that the *PHO* regulon is remarkably sensitive to mutation of core termination machinery. For example, a mutation that prevents phosphorylation of the threonine-4 repeat (*T4A*) of the conserved Pol2 carboxy-terminal domain (CTD) resulted in dysregulation of just four genes. Included among these four genes were two of the three members of the *PHO* regulon: *pho1* and *tgp1 (12)*. Thus, quite serendipitously, *PHO* became a useful tool for the investigation of general mechanisms of transcription termination – the simple acid phosphatase assay could be co-opted to screen for mutants that ablate or increase termination efficiency. Research into this field is briefly discussed below and outlined in Figure 3.

.

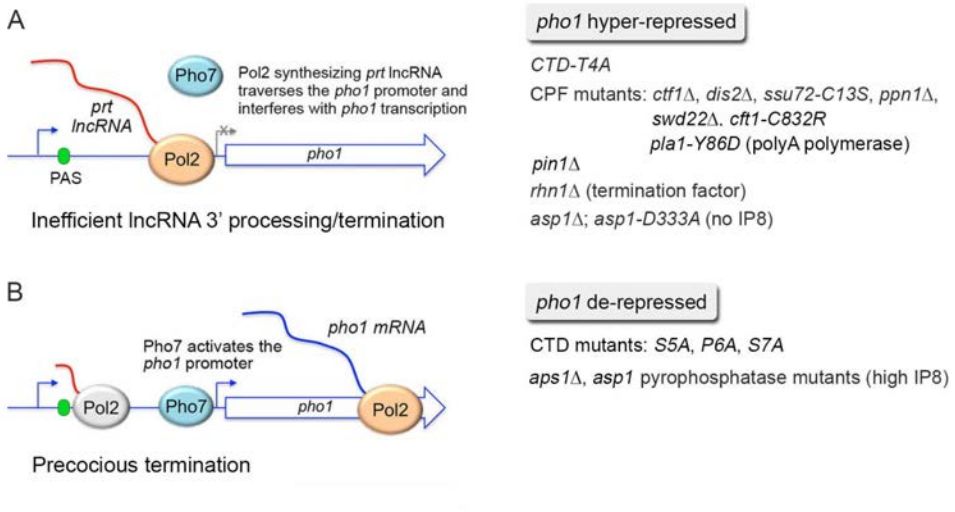

Figure 3. **Factors that influence *prt* lncRNA termination.** (A) Inefficient transcription termination at the *prt•pho1* locus causes transcription read-through, which reads as low acid phosphatase activity. (B) Precocious termination of *prt* allows Pho7 to bind the *pho1* promoter in phosphate-rich conditions, resulting in high acid phosphatase activity. Mutations that cause *pho1* to be hyper-repressed or de-repressed are listed to the right of the associated graphic. Figure courtesy of Stewart Shuman.

1.2: Transcription termination and RNA 3' end processing in *Schizosaccharomyces pombe*

A general mechanism for the transition from mRNA elongation to termination has been proposed that depends on endonucleolytic cleavage and 3'-polyadenylation of the nascent RNA. In *Schizosaccharomyces pombe*, the RNA 3'-end processing complex CPF recognizes a polyadenylation signal (PAS) in the nascent RNA (usually AAUAAA) (2, 6). The CPF complex contains 13 subunits, 8 of which are essential for fission yeast viability (14, 15). These include enzymes that catalyze essential reactions such as RNA cleavage, 3' polyadenylation, and Pol2 post-translational modification. The culmination of CPF activity is the release of mature mRNA and exposure of a new 5'-phosphate end of the cleaved nascent

RNA. The "torpedo" 5'→3' exoribonuclease Dhp1 targets this newly formed 5'-phosphate end, degrading RNA until it collides with and dislodges the now slow-moving Pol2 from template DNA.

The Shuman/Schwer lab works to characterize the players which shape termination efficiency using the *prt•pho1* interface as a convenient gauge. I have grouped these termination site choice influencers into three categories: the CTD Code, CPF (and termination factors), and 1,5-IP_8. A brief history of the research which established the influence of these players on *PHO* regulation and termination efficacy is detailed below.

1.2.1: The Pol II CTD Code

Rpb1, the largest subunit of Pol2, possesses a conserved, intrinsically disordered C-terminal domain (CTD) which in fission yeast consists of 29 heptapeptide repeats of consensus $Y_1S_2P_3T_4S_5P_6S_7$ (16). Each residue possesses two potential states – Y, S, and T residues may be phosphorylated or non-phosphorylated, while P residues may be cis- or trans-isomerized – creating 2^{203} possible CTD combinations. Different phosphorylation patterns convey signals to RNA processing machinery and transcription elongation factors to regulate the repertoire of bound accessory factors. Associated RNA processing machinery, elongation factors, and termination factors in turn help Pol2 accomplish different goals at discrete locations along the gene. For example, during the transition from initiation to elongation, the 5' end of nascent mRNA must be modified with a m^7G(5')ppp cap to prevent exonucleolytic degradation (17, 18). Mcs6, a cyclin-

dependent kinase, phosphorylates the Pol2 CTD at the Ser5 position, creating a binding platform for capping enzymes Pce1 and Pct1 (16, 19, 20). These enzymes are unable to bind non-phosphorylated CTD, establishing CTD Ser5 phosphorylation as an essential step in capping enzyme recruitment and subsequent transcription elongation (20). This scheme is graphically depicted in Figure 4.

Chromatin immunoprecipitation followed by sequencing (ChIP-seq) experiments targeting different CTD phosphorylation marks have revealed how CTD phosphorylation status changes as Pol2 traverses the gene. Ser5 phosphorylation occurs at the 5' ends of genes near transcription start sites, consistent with its role in recruiting the capping enzyme (21). Tyr1, Ser2, and Thr4 phosphorylations peak at the 3' ends of genes, suggesting a role for these 'letters' in recruiting 3' end processing and/or termination factors (21, 22). Recently, two studies reported the relative phosphorylation of each letter along the length of the CTD in budding yeast and human cells, respectively (23, 24). These demonstrated that Ser5 and Ser2 phosphorylation are most abundant, with Tyr1, Thr4, and Ser7 phosphorylation occurring less frequently. They also reported on the context-dependent nature of phosphorylation, indicating that certain phosphorylation events are more likely to appear on a single repeat or adjacent to a neighbor with a given phosphorylation pattern. These data provide support that the CTD Code is governed by rules which determine where phosphorylation events occur.

While we may know where and how much these phosphorylation patterns change, we do not unambiguously understand their function. Seminal work from

the Buratowski and Shuman labs described specific roles of phospho-Ser2 and phospho-Ser5 (20, 25-27), respectively, but genetics-based approaches were needed to ascribe function to the other 'orphan residues' Tyr1, Thr4, and Ser7. To this end, the Schwer group generated mutants in which alanine[1] was substituted into specific consensus positions in each heptad repeat throughout the length of the CTD (13, 14, 19). These mutants have provided insights into the effect of not being able to phosphorylate the CTD at a given position.

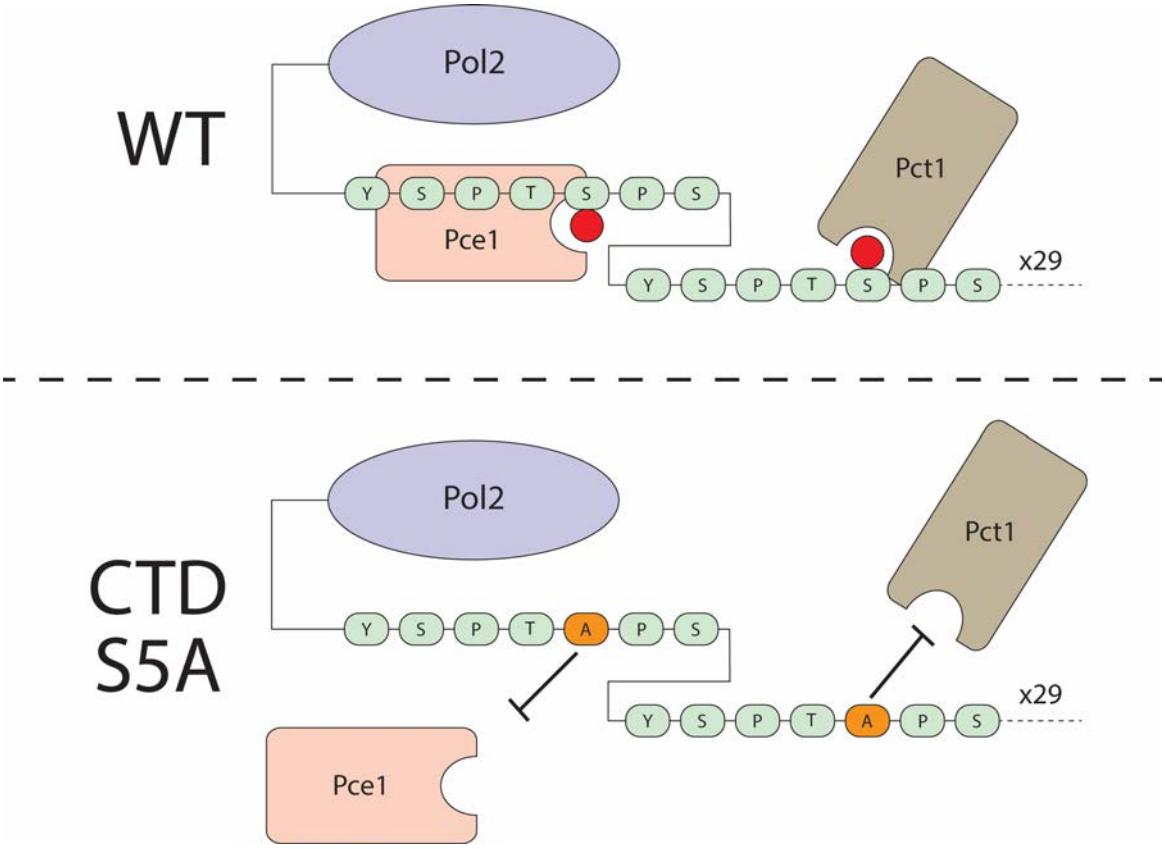

[1] *Tyr1 was replaced with Phe, a non-phosphorylatable residue that is isosteric to Tyr

Figure 4. **CTD phosphorylation recruits co-transcriptional RNA processing factors.** (Top panel) Phosphorylation (red circle) of CTD serine 5 recruits capping enzymes (in fission yeast, Pce1 and Pct1) to elongating Pol2, thereby linking CTD phosphorylation to co-transcriptional RNA modification. (Bottom panel) Replacing serine 5 with alanine at each CTD repeat prevents phosphorylation of this residue. Since capping enzymes only recognize phospho-Ser5 CTD, they are not recruited to Pol2.

The only essential CTD positions are Ser5 and Pro6. Lethal ala mutations to these residues (S5A and P6A) can be rescued by fusing a capping enzyme to Rpb1, demonstrating that Ser5 phosphorylation's essential function is to recruit capping machinery to RNA (19). Among other *CTD-Ala* mutants, synthetic lethal relationships exist with mutants which lack transcription termination machinery or RNA 3' end processing factors, indicating functional redundance (14). Acid phosphatase assay provided an analogous means of evaluating the effect of non-phosphorylatable CTD residues on transcription termination. *S7A* and *Alt-S5A* (a mutant that reduces the number of phosphorylatable Ser5 residues by alternating serine and alanine at consecutive repeats) de-repress *PHO*, suggesting that phospho-Ser5 and phospho-Ser7 might repress termination by promoting elongation factor retention or preventing termination factors from binding the CTD (13). By contrast, *T4A* hyper-represses *PHO* genes, indicating that the phospho-Thr4 mark might recruit termination or RNA 3' end processing machinery (14, 28). Using the T4A *PHO* hyper-repression phenotype as a criterion for suppression, the Schwer lab identified several mutations which promote precocious termination (28). Taken together, these findings demonstrate how the Pol2 CTD acts as a signaling hub to regulate transcription termination and RNA 3' end processing.

1.2.2: Cleavage and Polyadenylation Factor (and other termination factors)

Transcription termination and RNA 3' processing depends on the activity of the CPF. This versatile complex consists of 13 total proteins (Figure 5, top panel), encompassing essential activities which recognize the PAS, cleave the nascent RNA, and polyadenylate the newly released mRNA (or ncRNA). Genetic ablation of the five non-essential CPF components (Ssu72, Ctf1, Dis2, Ppn1, and Swd22) invariably causes *PHO* hyper-repression (14). Genetic evaluation of null mutants enabled their binning into complementation groups. Mutants which are synthetic lethal with each other presumably operate through distinct but redundant pathways – double mutants do not survive because of defective transcription termination that catastrophically disrupts expression of at least one essential gene. Conversely, double mutant survival is indicative of epistasis. An instructive example of this is the case of the two CPF phosphatases, Ssu72 and Dis2.

Ssu72, a cysteinyl phosphatase (29) and Dis2, a binuclear metallophosphoesterase (30), are functionally redundant in that mutational inactivation of one is tolerated but both is not (15). These phosphatases execute two termination-related dephosphorylation events: 1) stripping the CTD of the phospho-marks it has accrued during its passage through the gene to recycle it for fresh rounds of transcription (which require unphosphorylated CTD) (25, 29, 31) and 2) dephosphorylating the transcription elongation factor Spt5 to promote its release from Pol2 and replacement by the termination factor Seb1 (21, 22, 32, 33). Deconvoluting the *in vivo* specificity of these phosphatases for different CTD residues has proven challenging due to their functional redundancy, as well as the

presence of a third CTD phosphatase Fcp1 that is not associated with the CPF (34).

Dis2 requires two additional proteins, Swd22 or Ppn1, to associate with the core CPF – Dis2•Ppn1•Swd22 (DPS) constitutes a "submodule" (shown in Figure 5) which can associate independently of the rest of CPF (15). Ppn1 shares homology to PNUTS, a human regulator of the Dis2 homolog PP1 (35). Ppn1 therefore may be involved in shaping Dis2 target specificity as well as localizing it to the CPF. *ppn1*Δ and *swd22*Δ share identical synthetic relationships with *CTD-Ala* mutants, as well as null mutants of the other inessential CPF components (14), providing further evidence that these proteins function cooperatively (Figure 5, bottom panel). However, *dis2*Δ double-mutants with either *CTD-Ala* or *CPF-null* are frequently tolerated, raising the possibility that the Ppn1•Swd22 dimer may play a role in termination and RNA 3' end processing independent of Dis2's phosphatase activity.

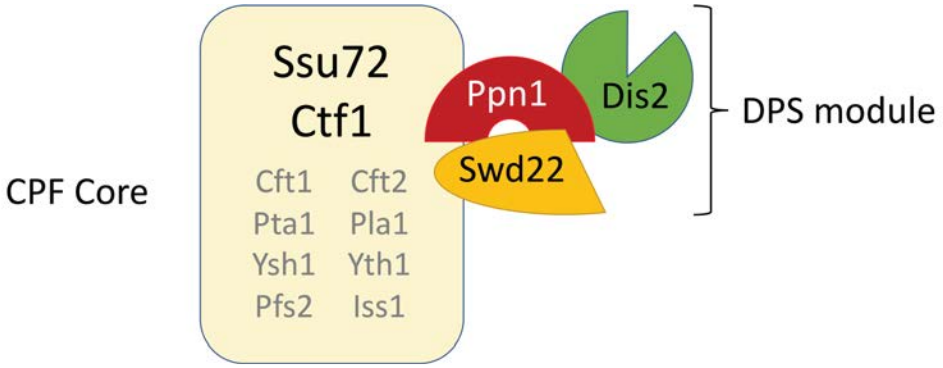

	dis2Δ	*ppn1Δ*	*swd22Δ*	*ssu72-C13S*	*ctf1Δ*	*rhn1Δ*	*pin1Δ*
dis2Δ		healthy	healthy	lethal	healthy	healthy	healthy
ppn1Δ			healthy	lethal	lethal	lethal	lethal
swd22Δ				lethal	lethal	lethal	lethal
ssu72-C13S					sick	sick	healthy
ctf1Δ						healthy	healthy
rhn1Δ							healthy
pin1Δ							

Figure 5. **CPF organization and genetic interactions.** The top panel shows the physical organization of the CPF, highlighting the submodule DPS. Essential CPF components are listed in grey. The bottom panel shows genetic relationships between the inessential members of CPF determined by generating double mutants consisting of the alleles listed in the left column and the top row. DPS members Ppn1 and Swd22 track together, while Dis2 is only synthetic lethal with inactivated Ssu72.

CPF is not the only *trans* influence upon Pol2 termination site usage. Sanchez et al identified two additional factors, the termination factor Rhn1 and the CTD prolyl isomerase Pin1, as having similar impact on termination efficacy. This insight was provided by testing mutant alleles for acid phosphatase activity and by determining their genetic relationships with *CTD* and *CPF* mutants (14, 36). Rhn1 is a putative CTD 'reader' by virtue of its homology to budding yeast Rtt103p, a protein that links CTD phosphorylation status to torpedo exonuclease recruitment (26, 37). Pin1 is an enzyme that interconverts *cis* and *trans* proline. As the CPF-associated CTD phosphatase Ssu72 preferentially recognizes the phospho-Ser–*cis*-Pro motif, Pin1 activity is a prerequisite for Ssu72-catalyzed dephosphorylation of CTD phospho-Ser5 (38). Though I have placed the CTD and CPF into different categories for the purpose of this introduction, the findings above demonstrate that these factors are integrally interwoven.

1.2.3: 1,5-IP_8 (1,5-diphosphoinositol tetrakisphosphate)

1,5-IP_8 is a signaling molecule produced in fission yeast by the enzyme Asp1(39, 40). It belongs to a class of highly phosphorylated inositol metabolites called inositol pyrophosphates (IPPs); the fission yeast IPP metabolic pathway is shown in Figure 6. The 2011 Wykoff lab screen identified two IPP metabolizing

enzymes, the confusingly named Asp1 and Aps1, as regulators of *PHO* gene expression (3). In budding yeast, IPPs influence *PHO* gene expression by physically interacting with the cyclin-dependent kinase complex which regulates the *PHO* transcription factor Pho4 (41, 42). However, this mechanism is not conserved to fission yeast, suggesting that IPP control of *PHO* gene expression evolved via convergent evolution or that IPP-*PHO* coupling mechanisms diverged as fission and budding yeast grew apart.

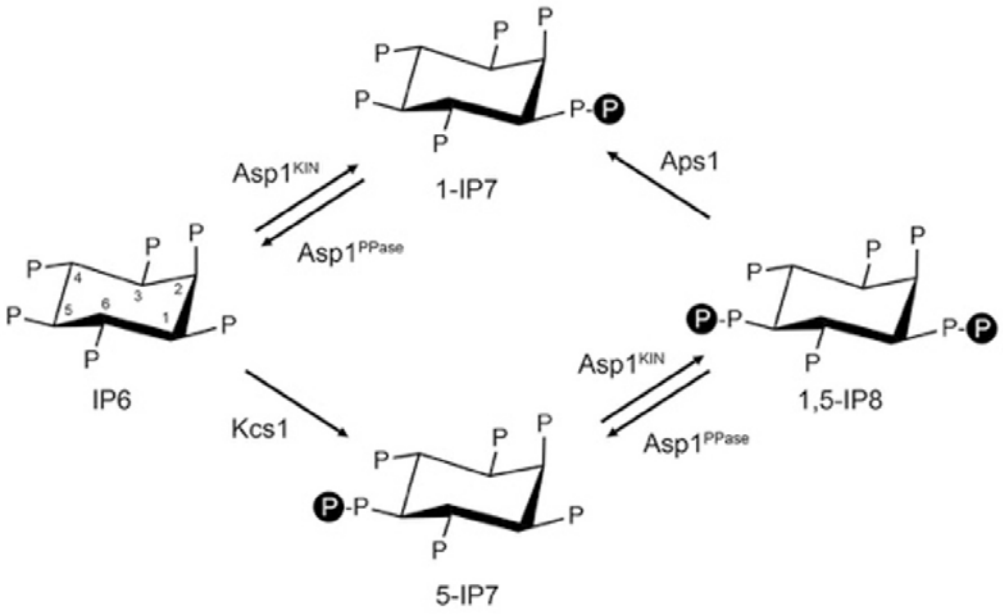

Figure 6. **IPP biosynthetic pathway in *S. pombe*.** IP_6 serves as a common precursor to all IPPs. Kcs1 phosphorylates the 5-P position of IP_6 to generate 5-IP_7. Asp1 kinase phosphorylates 5-IP_7 to 1,5-IP_8, while Asp1 pyrophosphatase dephosphorylates 1,5-IP_8 to regenerate 5-IP_7. Aps1 pyrophosphatase dephosphorylates the 5-pyrophosphate position to generate 1-IP_7.

Interested in the link between IPPs and *PHO*, the Schwer lab investigated the effect of Asp1 mutations on *PHO* expression, demonstrating that Asp1 mutants unable to produce 1,5-IP_8 exhibit *PHO* hyper-repression (43). Alternatively, mutations that cause 1,5-IP_8 accumulation de-repress *PHO*. In an independent

screen, they found that *PHO* hyper-repression observed in the *CTD-T4A* mutant could be reversed by mutants that are unable to catabolize 1,5-IP_8 (28). These mutants exhibit profound morphological and growth defects when taken out of the *PHO* hyper-repressive context of the *CTD-T4A* background, suggesting global influence on transcription termination. They suggest a model in which 1,5-IP_8 concentration tunes transcription termination, with higher 1,5-IP_8 promoting precocious termination and lower 1,5-IP_8 causing defective termination. A mechanistic link between 1,5-IP_8 and termination has yet to be established, sparking a keen interest in understanding the role of this metabolite in signaling.

1.3: Inositol phosphate signaling

1.3.1: Definitions, synthesis, and role of lower-order inositol phosphates

The term inositol phosphate connotes a diverse class of metabolites involved in a wide variety of cellular activities. The backbone of these species is myo-inositol, a cyclic 6-carbon sugar alcohol (chemical name cyclohexane-1,2,3,4,5,6-hexol) with one of the positions axially oriented and the others equatorial (44). It is produced by cyclization of D-glucose 6-phosphate by the action of glucose-6-phosphate-D-myo-inositol-1-phosphate cyclase (45), and has a plane of symmetry across its axial position, making it and many of its symmetrical phosphorylated derivatives optically inactive (44). Though the myo-inositol stereoisomer is the most abundant and biologically relevant inositol species in nature, scillo-, muco-, D-chiro-, and neo-inositol are also present to a lesser degree; they are derived by isomerization of myo-inositol (44). Phosphorylation of

this inositol backbone at different positions gives rise to numerous and multifunctional inositol phosphate species.

An abundant cellular pool of inositol phosphate exists in the form of the membrane lipid phosphatidylinositol (PI). Inositol is incorporated into PI by the action of the enzyme PI synthase, which combines CDP-diacylglycerol and myo-inositol (46). Importantly, inositol is attached to phosphatidic acid at the position to the right of the axial hydroxyl (orienting the 6-carbon ring like a clock with the axial hydroxyl positioned at 12:00 and pointing toward the viewer, the phospholipid ligates to the hydroxyl positioned at 2:00) (46). Naming conventions establish this phosphorylated position along the inositol ring as '1', with counterclockwise positions correspondingly labeled 2-6 (the axial position is thus labeled '2'). PI is then trafficked from the endoplasmic reticulum to the plasma membrane and phosphorylated at the '4' and '5' positions to make PIP_2. In higher eukaryotes, PIP_2 serves as a substrate for two important signaling pathways.

PIP_2 can be phosphorylated at the 3-position by PI3K to make PIP_3, whose dense negative charge attracts pleckstrin-homology (PH) domain-containing proteins, most notably the kinase Akt, to the plasma membrane (47). Clustering of Akt and its targets to a PIP_3 hub generates powerful downstream signals which promote nutrient acquisition and cell cycle progression, establishing the PI3K-Akt pathway as a flash point for mutations which dysregulate growth and lead to cancer in complex organisms. PIP_2 also serves as a substrate for phospholipase C, which cleaves the phosphate-lipid bond, liberating soluble inositol 1,4,5-triphosphate (IP_3) from the plasma membrane (48). IP_3-binding stimulates a dedicated ER-

bound receptor IP3R to open its calcium-permeable pore and release ER-sequestered calcium into the cytoplasm, where it serves as a secondary messenger in widespread cellular functions including muscle contraction and neuronal action potential propagation (48, 49). While no IP3R homolog exists in yeast (50), IP_3 liberation causes calcium release from stores within the vacuole in *Saccharomyces cerevisiae* (51), suggesting convergent evolution for this inositol phosphate signaling molecule.

While IP_3 garners well-deserved attention for its role in calcium signaling, it also serves as a building block for higher-phosphorylated inositol phosphates. Calcium signaling is halted by the phosphorylation of IP_3 to (1,3,4,5)-IP_4 by IP3K (distinct from PI3K!), which is then phosphorylated at the 6 and 2 positions by IPMK to make inositol-(1,2,3,4,5,6)-hexakisphosphate (IP_6) (40, 52-54). IP_6, also known as phytic acid, is the most abundant store of phosphate in plants, and serves as a stable long-term phosphate storage source in nuts and seeds, in which it constitutes ~75% of cellular phosphate (55).

In addition to serving as a phosphate store, IP_6 plays diverse roles in cellular signaling. It can act as a structural cofactor, as in the case of the ADAR and ADAT families of RNA editing enzymes, which contain IP_6 buried deep in their catalytic domains (56). IP_6 serves as a branch point for filaments of HIV Gag protein as it assembles into a 6-helix bundle during virion maturation (57). IP_6 regulates Casein Kinase 2 (CK2) activity by directly competing with a CK2 inhibitor for binding to an allosteric inhibition site on the CK2 surface (58, 59). Finally, IP_6 serves as foundation for higher phosphorylation into inositol pyrophosphates (IPPs).

IPPs contain a phosphoanhydride bond at one of the 6 available phosphate positions of the IP_6 ring. Inositol pyrophosphates act as signaling molecules through a variety of mechanisms. Two that have been implicated in phosphate homeostasis include SPX domain engagement and nonenzymatic protein pyrophosphorylation (Figure 7).

1.3.2: SPX domains are dedicated IPP sensors

IPPs have pleiotropic effects on cellular signaling, regulating cytoskeletal organization, apoptosis, and phosphate homeostasis (40, 52, 60). They modulate protein function by acting as molecular glue between different polypeptides, by altering catalytic activity, or by competitively inhibiting protein-protein interaction. Many of these functions are mediated by a specialized IPP interaction domain termed “SPX” after three founding members Syg1 (S. cerevisiae), Pho81 (S. cerevisiae), and Xpr1 (H. sapiens) (61). Even before the mechanistic connection between SPX domains and IPPs had been established, SPX domains were appreciated for their roles in phosphate homeostasis (61). SPX containing proteins are widely distributed throughout eukarya, but have been best studied in plants, where different organisms use SPX domains to regulate phosphate homeostasis programs through diverse molecular means. They perform this role by sensing cellular IPP concentration and coupling IPP binding to alteration of protein function.

Recent structural advances revealed the molecular mechanism of SPX-IPP interaction. SPX domains are 6-helix bundles which contain localized positive charge. These motifs directly bind IPPs, whose dense negative charge renders them higher affinity ligands than their non-pyrophosphorylated precursors (62).

SPX-IPP interaction may promote dimerization of two transcription factors, disrupt protein-protein interactions, or propagate signal to catalytic domains C-terminal of the SPX domain (which is always positioned at the N-terminus) (61, 63-65). A representative example of SPX-IPP mediated regulation of phosphate homeostasis is that of *Saccharomyces cerevisiae* Pho81.

In budding yeast, *PHO* gene expression is modulated by SPX-containing protein Pho81, which acts as a negative regulator of the cyclin-dependent kinase Pho85 in an IPP-dependent manner (41). In phosphate-rich conditions, Pho85 phosphorylates the master *PHO* transcription factor Pho4, which promotes its export from the nucleus, keeping *PHO* genes turned off. In phosphate-starved conditions, IPP concentration increases, resulting in Pho81 activation, Pho85 inhibition, Pho4 nuclear localization, and *PHO* gene expression (41). Genetic and biochemical analysis implicated a 1-PP species rather than a 5-PP species as the primary Pho81 regulator (42). Thus, SPX domains sensitively and specifically recognize distinct IPP species to regulate phosphate homeostasis in budding yeast. Though fission yeast uses a different mechanism to regulate *PHO* gene expression, dysregulation of 1-PP IPPs (1-IP_7 and 1,5-IP_8) in both organisms has profound influence on *PHO* expression, implicating these metabolites as *PHO* regulators throughout many walks of life.

1.3.3: Non-enzymatic protein pyrophosphorylation

IPPs carry high energy phosphoanhydride bonds. Free energy of hydrolysis of the β-phosphate on IPPs is comparable to that of the ATP γ phosphate, suggesting that IPPs may serve as cellular phosphate donors (66, 67). Non-

enzymatic protein pyrophosphorylation by 5-IP_7 has been demonstrated in budding yeast and human cell extracts (66). After its discovery in cell extracts, protein pyrophosphorylation was demonstrated to be a regulated cell signaling event. In budding yeast, the transcription factor Gcr1p, which regulates expression of glycolytic genes, is differentially pyrophosphorylated by 5-IP_7 in response to nutrient availability and cellular stress (68). Pyrophosphorylation prevents Gcr1p from activating the glycolysis gene expression program, thereby coupling 5-IP_7 concentration to metabolic program choice.

Protein pyrophosphorylation in fission yeast has not yet been demonstrated. Furthermore, though the IPP 5-IP_7 plays regulatory roles through protein pyrophosphorylation, no evidence has yet implicated fission yeast's other IPP species, 1-IP_7 and 1,5-IP_8 in such a role.

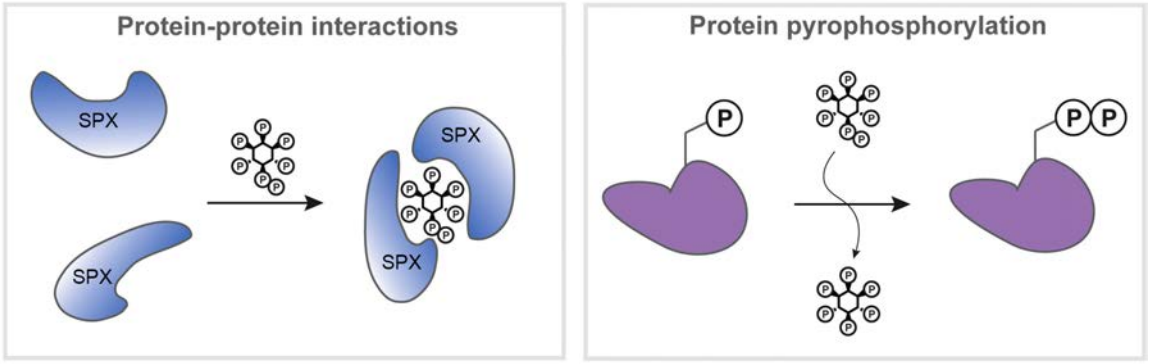

Figure 7. **Two mechanisms of IPP-mediated signaling implicated in phosphate homeostasis.** The left panel demonstrates how 5-IP_7 facilitates interaction between two SPX-containing proteins. Alternatively, IPP binding can disrupt interaction between an SPX-containing protein and a non-SPX protein. The right panel shows non-enzymatic phosphoryl transfer of 5-IP_7's β-phosphate to a pre-phosphorylated protein. Figure adapted from ref 65.

1.4: Asp1 – a bifunctional enzyme that synthesizes and catabolizes 1,5-IP_8

1.4.1: Discovery and naming

The PPIP5K/Vip1/Asp1 family of enzymes is a central cog in IPP metabolism. The fission yeast member of this family, Asp1, was discovered as a high-copy suppressor of the cdc3-124 mutant's cold sensitivity (69). Cdc3+ encodes profilin, a component of the actin patch which establishes fission yeast polarity; the cdc3-124 mutant is unable to produce F-actin and is therefore defective for cytokinesis. Overexpression of the ORF encoding Asp1 rescued cdc3-124 cold sensitivity. Asp1 deletion mutant displays cytoskeletal organization defects and is synthetic lethal with the actin-binding proteins Arp3 and Sop2 (Asp1 was named for its genetic interactions with Arp2/3, Sop2, and Profilin). However, Asp1 does not directly bind to these proteins, suggesting that its effects on cytoskeletal organization are mediated indirectly through a secondary messenger.

Asp1's enzymatic activity was identified by the York lab in 2007 during a hunt for enzymes that generate inositol pyrophosphates. Initial efforts in this direction had led to the discovery of Kcs1p, a budding yeast kinase that phosphorylates IP_6 to 5-IP_7 (70). When researchers measured IPP levels in *kcs1-*Δ cells*,* they detected residual IPP species, suggesting the existence of a second kinase activity (71). This activity emanated from the product of VIP1, the homolog of fission yeast Asp1. As *asp1* had previously been identified as a suppressor of cytoskeletal defect phenotypes, the establishment of Vip1p as an IPP kinase established a connection between inositol pyrophosphates and cytoskeletal organization.

1.4.2: Domain structure

Domain analysis of Asp1 sequence identified two distinct protein folds: an N-terminal kinase and a C-terminal pyrophosphatase (71). This two-domain organization is conserved throughout eukaryotic life with homologs found from yeast through human, suggesting widespread functional relevance (71). Using fission yeast as a model organism, researchers mutated residues predicted to play catalytic roles in the kinase and pyrophosphatase domains. A conserved aspartate (Asp333 in fission yeast) was predicted to coordinate a catalytic metal involved in the phosphoryl transfer reaction of the kinase. Switching this residue to alanine caused a complete loss of *in vitro* kinase activity (72); HPLC analysis of [H^3]-labeled IPPs indicated *asp1-D333A* cells have no 1,5-IP_8 and slightly higher 5-IP_7 levels than WT cells (73). A conserved histidine (His397 in fission yeast) was predicted to serve as the nucleophile that attacks the scissile phosphate and later releases it to water. Mutation of this residue to alanine eliminated *in vitro* pyrophosphatase activity (72); *asp1-H397A* cells contain elevated levels of 1,5-IP_8 (73). While both mutations caused growth phenotypes when introduced into endogenous *asp1*, inactivation of the pyrophosphatase activity was particularly disruptive, causing severe cytoskeletal disorganization and enlarged vacuoles (71, 74, 75).

These findings have threefold relevance. First, they provide substantial support for the model in which Asp1 consists of antagonistic N-terminal IPP kinase and C-terminal IPP pyrophosphatase domains. Second, they suggest that Asp1 is the sole agent of 1,5-IP_8 synthesis in fission yeast. Third, they show that while 1,5-

IP_8 is inessential for normal vegetative growth, the inability to catabolize 1,5-IP_8 is toxic. By manipulating Asp1's two activities, researchers are currently working to understand the mechanism by which 1,5-IP_8 asserts its toxic influence on physiology, as well as its function in phosphate homeostasis.

Asp1's N-terminal kinase domain belongs to the ATP-grasp family of enzymes (71). These enzymes catalyze the transfer of the ATP γ-phosphate to a nucleophilic substrate as the first part of a two-step mechanism, the second of which involves attack of the unstable acylphosphate intermediate and release of P_i (76). However, some enzymes of this family release the products of the first step of the reaction, resulting in a terminally phosphorylated product (thereby establishing these enzymes as kinases). The overall fold consists of three domains, sometimes called A, B, or C, which correspond respectively to the N-lobe, central domain, and C-lobe of protein kinases, to which the ATP-grasp fold is related (77, 78). ATP is bound between two antiparallel β-sheets provided by the A and C domains, which "grasp" the nucleotide. The second substrate also fits between these domains. The smaller B-domain is frequently mobile, becoming more ordered and/or rigid upon substrate binding.

ATP-grasp enzymes are functionally diverse, binding substrates of myriad shape and size. This family includes several inositol phosphate kinases, such as IPTK, PIPK (a phosphoinositide kinase specific for lipid-bound inositol phosphates), and PPIP5K (Asp1's human homolog) (77, 79). IP kinases define their substrate using a variety of positively charged residues which make a grooved active site that positions specific hydroxyls or phosphates close enough to the ATP

γ-phosphate for nucleophilic attack. These shapes may be loose to enable promiscuity (IPTK accommodates several inositol phosphate species and phosphorylates two different positions around the ring), or tight to confer rigid substrate specificity and positioning (PPIP5K phosphorylates the 1-P exclusively). Therefore, active site structure is key for determining function.

Asp1's C-terminal domain is predicted to adopt a canonical histidine acid phosphatase (HAP) fold. Several phytases (phosphatases specific for inositol phosphate substrates) are HAPs (80). Phytases are important for agriculture and industrial farming, as the feed used in livestock contains an abundance of non-bioavailable phytic acid (55). Runoff from livestock waste results in phosphorus deposition and accompanying environmental problems such as algal bloom. Treatment of animal feed with phytase improves the nutritional value by increasing the amount of bioavailable phosphate, while reducing negative environmental impact caused by excreted phytate (80). Improving our understanding of phytases may offer significant economic and environmental benefit.

Asp1 kinase acts specifically on the phosphate attached to the inositol 1-carbon (1-P), while Kcs1 phosphorylates 5-P (72). Asp1's HAP domain is specific for the 1β-P, converting 1,5-IP_8 back to 5-IP_7. Asp1 therefore contains a kinase and pyrophosphatase whose activities counteract each other. Since cellular 1,5-IP_8 levels are dynamic, Asp1's two domains must be subject to regulatory inputs that stimulate its kinase activity to overcome the pyrophosphatase or inhibit the pyrophosphatase to enable accumulation of the product of the kinase. P_i availability and ATP/ADP ratio have been suggested as potential regulatory

agents, but neither has been mechanistically established in the alteration of Asp1 kinase or pyrophosphatase activity (81). Identifying the regulatory inputs that shift Asp1 between 1,5-IP_8 generation and catabolism modes will be key to understanding Asp1's physiological role.

1.4.3: Structural basis of $PPIP5K2^{KD}$ activity and substrate specificity

Asp1 kinase's human homolog is PPIP5K. Structural and biochemical studies by the Shears research group on PPIP5K kinase domain ($PPIP5K2^{KD}$) illuminated the mechanism of phosphoryl transfer (79, 82). This enzyme, which adopts the characteristic ATP-grasp fold, engages ATP within its "grasp," and positions IP_6 or 5-IP_7 in a position to use the 1-P to attack the ATP γ-phosphate in a 1-step phosphoryl transfer mechanism. Two catalytic magnesium ions are coordinated by 3 conserved active site residues (two aspartates and an asparagine). One metal, termed Mg1, stabilizes the phosphorane transition structure. A second metal, Mg2, bridges the α and β phosphates, positioning the γ-phosphate for attack by the 1-P nucleophile while also contributing to charge neutralization of the transition state. Two additional metal ions[2] were observed bound to the inositol phosphates: Mg4 binds the 2-P whereas Mg5 binds 5β-P and 5α-P. Mg5's ability to bind the 5β-P may play a role in $PPIP5K2^{KD}$'s preference for 5-IP_7 over IP_6. This preference is observed *in vitro* by a 22-fold greater first order rate constant for 5-IP_7 over IP_6 by the WT kinase, quantified using HPLC analysis of [H^3]-labeled reactants (82).

[2] A third non-catalytic Mg^{2+} ion denoted Mg3 was observed far from the active site.

PPIP5K2^{KD}'s active site residues are tailored to accommodate its substrates. While its ATP-grasp fold matches closely that of other family members, its inositol phosphate contact points are unique. Unlike other inositol phosphate kinases, PPIP5K^{KD} utilizes positively charged arginines and lysines exclusively for substrate positioning, enabling the enzyme to engage the dense negative charge of IP_6 and 5-IP_7 (79). Comparing nucleotide-bound enzyme to nucleotide + inositol phosphate-bound (ternary substrate complex) illuminates several induced-fit movements in active site residues. Notably, Arg281 and Arg262 make sweeping turns to play important roles in substrate positioning. Snapshots of the reaction in the ground, transition, and product states enable visualization of active site residue dynamics. In the movement from ground to transition state, Lys329, for example, breaks hydrogen bonds with 2-P to make new ones with 5β-P, 5α-P, and 6-P. This movement, along with those made by Arg262 (which makes a new hydrogen bond with 5β-P), Lys54, Arg213, Lys214, may be responsible for pushing the inositol phosphate closer to the ATP γ-phosphate for nucleophilic attack.

Evaluation of physiological concentrations of inositol phosphate species, either by HPLC using [H^3]-labeled inositols, or by PAGE of cellular IPPs concentrated with TiO_2, has shown that IP_6 exists in roughly 20-fold excess of IP_7 (83). Recent improvements in chromatography techniques have enabled the relative quantification of IP_7 species – in two mammalian cells, 98% of observed IP_7 was 5-IP_7, with only 2% being 1-IP_7 (83). Furthermore budding yeast *vip1*-Δ cells retain abundant cellular pools of IP_7, whereas *kcs1*-Δ cells have little or no 1-IP_7 (71, 84) (note, while fission yeast Kcs1 is essential, budding yeast Kcs1p is

inessential). These data suggest that the metabolic pathway of 1,5-IP_8 synthesis is through 5-IP_7 rather than 1-IP_7. Thus, Asp1 kinase is faced with a significant challenge, as it must distinguish its substrate 5-IP_7 from a similar molecule IP_6, which exists in 20-100-fold excess of 5-IP_7.

Structures of PPIP5K2^{KD} show that substrates are bound deep within the core of the enzyme (79). This finding raises the question of how substrates fit through a tiny hole in the active site to nestle into position for phosphoryl transfer (Figure 8). Structures of IPP analogs bound to the exterior of the enzyme raised the possibility that surface-exposed residues “catch” the IPP and “pass” it through the active site aperture to interior residues which position the IPP for reaction chemistry (85). However, no PPIP5K structure has been solved in the absence of substrates, making the “catch and pass” model of substrate positioning one of many possible schemes for substrate engagement.

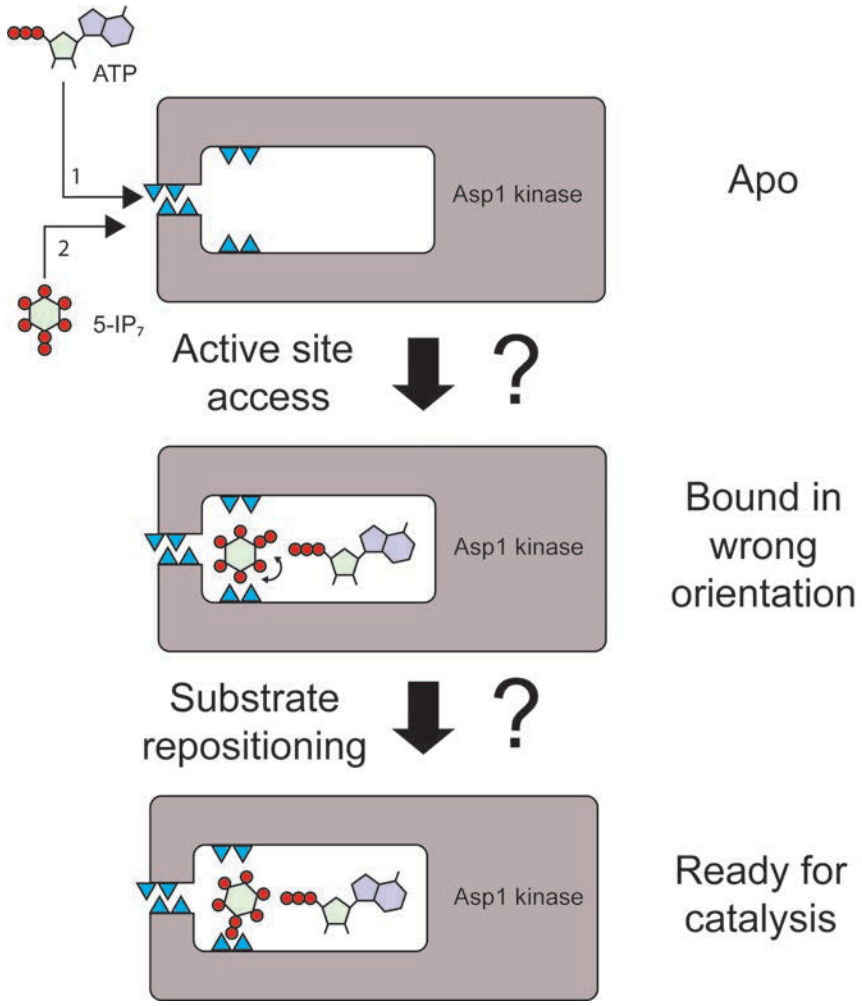

Figure 8. **Questions about Asp1 kinase substrate engagement.** Asp1 must fit ATP and 5-IP_7 into its active site. The human homolog of Asp1 has a small active site opening that is lined with positively charged residues (shown as blue triangles in the above diagram). How does Asp1 fit these residues through this hole? Asp1 specifically phosphorylates the 1-P position. How does Asp1 create proper substrate orientation for phosphoryl transfer to the 1-P position?

1.5: Scope of Dissertation

This study discusses the regulation of *Schizosaccharomyces pombe PHO* gene expression by the CPF submodule DPS and the IPP kinase/pyrophosphatase Asp1. The findings provide key clarifications in the organization of DPS, and characterize Asp1's kinase and pyrophosphatase

domains using biochemical, structural, and molecular biology approaches. Chapter 1 has introduced scientific background pertaining the regulation of fission yeast *PHO* genes and recent developments that have expanded the pool of factors known to influence it. Subsequent chapters concern the following topics.

Chapter 2: This chapter contains a structure/function study of Ppn1, a member of the CPF submodule DPS. Endogenous Ppn1 is replaced by truncated Ppn1 mutants to identify the regions necessary and sufficient for WT behavior using growth and acid phosphatase assay as readouts, as well as the minimum functional domain by assaying for survival in backgrounds in which Ppn1 is essential. Using the yeast two-hybrid method to gauge protein-protein interaction, Ppn1's Dis2- and Swd22-interaction domains are defined, and point mutants that disrupt these interactions are identified. Using these point mutants, I assayed the necessity of DPS interactions for survival in various genetic contexts. Questions raised from previous studies are reconciled by a model in which Ppn1 binds a Dis2 ortholog to compensate for its absence.

Chapter 3: This chapter contains a biochemical characterization of Asp1's kinase domain, Asp1-(1-385). I expressed and purified recombinant Asp1 kinase and full-length proteins. I developed a TLC-based assay using [γ^{32}P]-ATP as a phosphate donor which enabled me to track the kinase's two activities (inositol phosphate 1-P kinase and phosphohydrolase) using IP_6 as a phosphoacceptor. I define biochemical features of the kinase and phosphohydrolase activities including pH profile, metal dependence, and NTP specificity. Using synthetically produced 5-IP_7, I demonstrate the kinetic properties of IPP phosphorylation and

compare these to its activity when IP_6 is used as a phospho-acceptor. Using $PPIP5K2^{KD}$ structure as a template, I perform a mutational analysis of putative active site residues and assay these mutant kinases' ability to de-repress *pho1* in vivo. Finally, I compare the activity of the isolated kinase domain to that of the full-length enzyme and identify conditions that promote accumulation of the kinase product.

Chapter 4: This chapter contains a structural analysis of Asp1 kinase domain 31-364 gained through x-ray diffraction of several Asp1 crystals. Overall fold, metal coordination, and substrate positioning are discussed. Asp1 kinase structure is contrasted to $PPIP5K2^{KD}$. The structure of Asp1 kinase in the absence of substrates provides insight into a conformational switch upon substrate engagement. I show that Asp1 can bind IPP substrates in both on- and off-pathway orientation. I perform a mutational analysis of Asp1 kinase's NTP-binding residues, demonstrating the ability to modulate NTP utilization profiles.

Chapter 5: This chapter discusses Asp1's pyrophosphatase (PPase) domain, Asp1-(383-920). *PHO* genes are de-repressed when Asp1 pyrophosphatase is inactivated, establishing this domain as an important buffer against 1,5-IP_8 overaccumulation. I expressed and purified recombinant Asp1 pyrophosphatase domain. Using PAGE, I determined Asp1 PPase biochemical characteristics, including pH profile, metal independence, and substrate preference.

Chapter 2: Structure-function analysis of fission yeast cleavage and polyadenylation factor (CPF) subunit Ppn1 and its interactions with Dis2 and Swd22

2.1: Abstract

Fission yeast Cleavage and Polyadenylation Factor (CPF), a 13-subunit complex, executes the cotranscriptional 3' processing of RNA polymerase II (Pol2) transcripts that precedes transcription termination. The three-subunit DPS sub-complex of CPF, consisting of a PP1-type phosphoprotein phosphatase Dis2, a WD-repeat protein Swd22, and a putative phosphatase regulatory factor Ppn1, associates with the CPF core to form the holo-CPF assembly. Here we probed the functional, physical, and genetic interactions of DPS by focusing on the Ppn1 subunit, which mediates association of DPS with the core. Transcriptional profiling by RNA-seq defined limited but highly concordant sets of protein-coding genes that were dysregulated in *ppn1*Δ, *swd22*Δ and *dis2*Δ cells, which included the *DPS*Δ down-regulated phosphate homeostasis genes *pho1* and *pho84* that are controlled by lncRNA-mediated transcriptional interference. Essential and inessential modules of the 710-aa Ppn1 protein were defined by testing the effects of Ppn1 truncations in multiple genetic backgrounds in which Ppn1 is required for growth. An N-terminal 172-aa disordered region was dispensable and its deletion alleviated hypomorphic phenotypes caused by deleting C-terminal aa 640–710. A TFIIS-like domain (aa 173–330) was not required for viability but was important for Ppn1 activity in phosphate homeostasis. Distinct sites within Ppn1 for binding to Dis2 (spanning Ppn1 aa 506 to 532) and Swd22 (from Ppn1 aa 533 to 578) were

demarcated by yeast two-hybrid assays. Dis2 interaction-defective missense mutants of full-length Ppn1 (that retained Swd22 interaction) were employed to show that binding to Dis2 (or its paralog Sds21) was necessary for Ppn1 biological activity. Ppn1 function was severely compromised by missense mutations that selectively affected its binding to Swd22.

2.2: Author Summary

Multi-layered regulatory inputs to eukaryal gene expression target the initiation, elongation, and termination steps of RNA polymerase II transcription. Termination is coupled to, and ensues from, the 3' processing of nascent RNA by multi-protein assemblies. The fission yeast Cleavage and Polyadenylation Factor complex, CPF, is an exemplary 3' processing machine composed of 13 protein subunits, three of which (named Dis2, Ppn1, and Swd22) form a DPS sub-complex within CPF. In this study, we interrogated the effects of DPS null mutations on the fission yeast transcriptome. We probed the physical interactions of Ppn1 and its genetic interactions with other components of the transcription and RNA processing machinery. We delineated distinct binding sites within Ppn1 for Dis2 and Swd22 and then showed that perturbation of these sites interdicts Ppn1's essential activities *in vivo*.

2.3: Introduction

Fission yeast *Schizosaccharomyces pombe* Cleavage and Polyadenylation Factor (CPF) is a 13-subunit protein assembly responsible for the cotranscriptional 3' processing of RNA polymerase II (Pol2) transcripts that precedes Pol2

transcription termination [1]. Holo-CPF consists of two component complexes (Figure 1): a 10-subunit CPF core composed of proteins Ysh1 (the cleavage endonuclease), Pla1 (the poly(A) polymerase), Pta1, Yth1 (a zinc finger protein), Pfs2 (a WD repeat protein), Iss1, Cft1 (a WD repeat protein), Cft2 (a metallo-β-lactamase/β-CASP protein), Ctf1, and Ssu72 (a phosphoprotein phosphatase); and a 3-subunit DPS complex comprising Dis2 (a phosphoprotein phosphatase), Ppn1, and Swd22 (a WD repeat protein). Eight of the CPF core subunits, including the cleavage endonuclease and poly(A) polymerase, are essential for fission yeast viability. Two of the core subunits (Ctf1 and Ssu72) and all three DPS complex subunits (Dis2, Ppn1, and Swd22) are dispensable for growth.

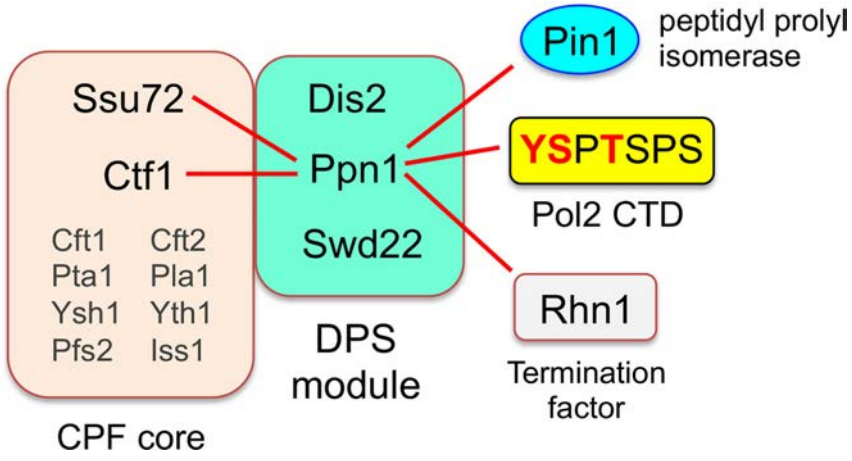

Figure 1. **Organization of fission yeast CPF and genetic interactions of its subunits.** Essential subunits of the CPF core are shown in gray font; inessential subunits of the core and DPS module are in black font. Synthetic lethalities of *ppn1*Δ with mutant alleles of CPF subunits, termination factor Rhn1, Pol2 CTD phospho-site mutants (red font), and prolyl isomerase Pin1 are denoted by red lines.

Whereas there have been great strides made in defining the architecture of the budding yeast and human 3' processing machinery, including structures of

individual subunits and subunit complexes [2–5], structural insights into the fission yeast CPF are relatively sparse. Vanoosthuyse et al. [1] showed by affinity purifications and mass spectrometry that deletion of Ppn1 precluded association of Swd22 and Dis2 with the CPF core, and of Swd22 and Dis2 with each other, but did not affect the integrity of the core itself. A Ppn1-Dis2 binary complex was formed in the absence of Swd22 but did not associate with the CPF core. The association of a Ppn1-Swd22 binary complex with the core was unaffected by deletion of Dis2. Their findings suggest that Ppn1 serves as a scaffold for binding Swd22 and Dis2 (presumably at independent sites on Ppn1) and that both Ppn1 and Swd22 (but not Dis2) are needed for association with the CPF core.

A much richer picture is emerging of the genetic interactions of the inessential fission yeast CPF subunits. There is considerable genetic redundancy within the CPF itself, whereby the effects of ablating one inessential subunit are buffered by other inessential CPF components, such that inactivation of both elicits synthetic lethality. For example: (i) *ppn1Δ* and *swd22Δ* are synthetically lethal with *ctf1Δ*; and (ii) a phosphatase-dead *ssu72-C13S* allele is synthetically lethal with *ppn1Δ*, *swd22Δ*, and *dis2Δ* [6]. Thus, there is functional cross-talk between the core and DPS.

Moreover, Ssu72, Ctf1, Dis2, Swd22, and Ppn1 are constituents of a recently identified genetic interactome connecting 3’ processing/termination, the Pol2 “CTD code,” inositol pyrophosphate (IPP) signaling, and the transcriptional control of fission yeast phosphate homeostasis [6,7]. The carboxyl-terminal domain (CTD) of the Rpb1 subunit of fission yeast Pol2 consists of tandemly

repeated heptapeptides of consensus sequence $Y^1S^2P^3T^4S^5P^6S^7$. The inherently plastic CTD structure is tuned by dynamic phosphorylation and dephosphorylation of the heptad serine, threonine, and tyrosine residues and by isomerization of the prolines between *trans* and *cis* configurations. These variations in the primary structure comprise a CTD code that conveys informational cues about the transcription machinery that are read by CTD-binding proteins [8–10]. Ser5 is the only strictly essential phosphorylation site in fission yeast. *S. pombe* is viable when the other phospho-sites are replaced by a non-phosphorylatable side chain (alanine for Ser2, Thr4, or Ser7; Phe for Tyr1) [6,11,12]. The findings that *ppn1Δ* and *swd22Δ* are synthetically lethal with *rpb1-CTD* mutants *Y1F*, *S2A*, and *T4A* suggested that Tyr1-Ser2-Thr4 form a three-letter CTD code "word" that abets 3' processing/termination [6]. It is proposed that this CTD word is read by termination factor Rhn1, which recognizes the Thr4-PO_4 CTD mark [6]. Consistent with this idea, ChIP-seq analysis has shown that the Thr4-PO_4 CTD mark is inscribed as Pol2 reaches the poly(A) site (PAS) of protein-coding genes and peaks shortly after the PAS [13]. The *rhn1Δ* null allele is synthetically lethal with *ppn1Δ* and *swd22Δ*, as are missense mutations of Rhn1 that perturb its CTD-binding site [6]. *ppn1Δ* and *swd22Δ* are also synthetically lethal with *pin1Δ*, a null mutation of the Pin1 peptidyl-prolyl *cis-trans* isomerase that modifies the CTD [14]. The intersection of this genetic axis with IPP metabolism and phosphate homeostasis is described under Results.

In the present study, we focus on the DPS complex and its Ppn1 subunit. Ppn1 is a 710-amino acid polypeptide that is judged to be a homolog of mammalian

PNUTS (PP1 NUclear Targeting Subunit), a regulator of the mammalian PP1 phosphoprotein phosphatase to which fission yeast Dis2 is homologous [1,15,16]. We take advantage of the several genetic backgrounds in which Ppn1 is essential for fission yeast growth (Figure 1) to conduct a structure-function analysis of Ppn1 aimed at: (i) defining which parts of the Ppn1 protein are dispensable and essential for Ppn1 activity *in vivo*; and (ii) assessing whether different structural features of Ppn1 come into play in different genetic contexts. We employ yeast two-hybrid assays to delineate distinct binding sites within Ppn1 for Dis2 and Swd22 and then gauge the contributions of these sites to Ppn1's essential activities. In addition, we report RNA-seq analyses that identify sets of protein-coding genes that are concordantly up-regulated or down-regulated in *ppn1Δ*, *swd22Δ*, and *dis2Δ* cells.

2.4: Results

2.4.1: Transcription profiling of DPS null mutants

Ppn1, Swd22, and Dis2 comprise a discrete physical entity (the DPS module) within the fission yeast holo-CPF assembly [1]. Although DPS is inessential for vegetative growth, genetic analyses indicate that DPS deficiency is buffered by other factors that promote or affect 3' processing and transcription termination, one of which is the CPF core subunit Ssu72 [6]. Recent RNA-seq studies show that inactivation of the Ssu72 protein phosphatase results in down-regulation or up-regulation of a narrow subset of fission yeast protein-coding genes [7]. By extension, we envision that: (i) the DPS complex also influences the expression of specific genes; and (ii) gauging the extent to which the effects of

ablating individual DPS subunits on the transcriptome overlap and echo those of mutations in other transcription components might afford new insights to gene regulation. To address these issues, we [Angad Garg and Beate Schwer] performed RNA-seq on poly(A)$^+$ RNA isolated from wild-type, *ppn1Δ*, *swd22Δ*, and *dis2Δ* cells. cDNAs obtained from three biological replicates (using RNA from cells grown to mid-log phase in YES medium at 30°C) were sequenced for each strain. In the datasets, 93–95% of the reads were mapped to unique genomic loci (Supplementary Table 1). Read densities (RPKM) for individual genes were highly reproducible between biological replicates (Pearson coefficients of >0.98; Supplementary Table 2). As internal controls, we affirmed that there were no reads for the deleted *ppn1*, *swd22*, or *dis2* coding sequence in the respective null strains. A cutoff of ±2-fold change in normalized transcript read level and a corrected *p*-value of ≤0.05 were the criteria applied to derive an initial list of differentially expressed annotated loci in the DPS mutants versus the wild-type control. We then focused on differentially expressed genes with average normalized read counts ≥100 in either the wild-type or null strains in order to eliminate transcripts that were expressed at very low levels in vegetative cells.

We thereby identified 38, 36, and 60 annotated protein-coding genes that were up-regulated in *ppn1Δ*, *swd22Δ*, and *dis2Δ* cells, respectively. The numbers of overlaps and uniquely affected transcripts are depicted in the Venn diagram in Figure 2A. The set of 27 coding genes that were coordinately up-regulated by ≥2-fold in the *ppn1Δ* and *swd22Δ* mutants is shown in Figure 2B (*p*-value <1.23e-55), of which 19 genes were also up-regulated in the *dis2Δ* strain. There was

extensive overlap with the transcriptome of *ssu72-C13S* cells (7), whereby 20 coding genes up-regulated by *ssu72-C13S* were up-regulated by *ppn1Δ* and *swd22Δ*, 13 of which were also upregulated by *dis2Δ* (Figure 2B). The coordinately up-regulated gene sets included two involved in iron homeostasis, two 5' nucleotidases, two heat-shock chaperones, and several oxidoreductases. Reference to the annotation of these transcription units in Pombase provided no immediate insights to their shared response to CPF mutations.

A

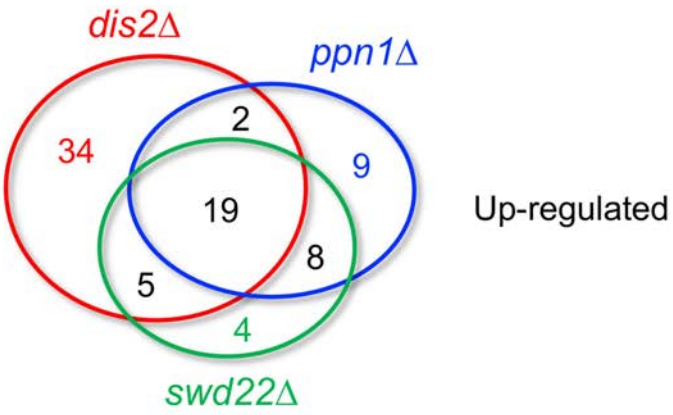

B

gene	log2 change				protein / function
	ppn1Δ	*swd22Δ*	*dis2Δ*	*ssu72-C13S*	
SPBPB2B2.06c	3.32	2.96	4.04	1.92	extracellular 5' nucleotidase
SPAC23H3.15c	3.14	2.29		2.21	
ght5	2.73	2.98	3.65		glucose/fructose:proton symporter
SPCC18B5.02c	2.47	2.19	2.25	3.84	
SPAC27D7.09c	2.44	2.38	1.99	4.03	
hsp16	2.19	2.54	1.83	1.50	heat shock protein
lsd90	2.14	1.50	1.04	2.02	
SPBPB2B2.05	2.09	1.75	1.95	1.18	glutamine amidotransferase
SPAPB18E9.04c	2.07	1.75		2.20	
SPAC11D3.01c	2.02	1.84	1.88	1.36	
gst2	1.77	1.75	1.27	3.21	glutathione S-transferase
SPAC1039.02	1.72	1.48	1.39	2.59	extracellular 5' nucleotidase
pfl9	1.56	1.57	2.20		flocculin
inv1	1.53	1.58	1.68	1.81	invertase
SPBC24C6.09c	1.48	1.06		2.50	phosphoketolase
atd1	1.40	1.49	1.15	1.68	aldehyde dehydrogenase
str1	1.36	1.08		3.46	siderophore-iron transmembrane transporter
ssa1	1.34	1.54			Hsp70
atd2	1.29	1.23	1.46		aldehyde dehydrogenase
ght1	1.28	1.40	1.83		glucose:proton symporter
osr1	1.27	1.11		2.49	oxidoreductase
SPBC1105.13c	1.21	1.33	1.09		
tgd1	1.20	1.01	1.41		nucleotide-sugar 4,6-dehydratase
SPAPB24D3.08c	1.17	1.00		1.54	NADP-dependent oxidoreductase
fio1	1.17	1.36		2.59	membrane iron transport oxidase
bfr1	1.16	1.24	1.33	2.44	brefeldin A efflux transporter
plr1	1.14	1.46	1.35	1.55	pyridoxal reductase

Figure 2. **Coding genes up-regulated in DPS mutants.** (A) Venn diagram depicting numbers of overlapping and non-overlapping up-regulated protein-coding genes. (B) List of 27 protein-coding genes that were coordinately up-regulated at least 2-fold in *ppn1*Δ and *swd22*Δ cells, 19 of which were also up-regulated in *dis2*Δ cells and 20 of which were up-regulated in s*su72-C13S* cells. The log2 fold changes versus wild-type are shown. Angad Garg and Beate Schwer collected RNA and performed data analysis.

Our RNA-seq pinpointed 67, 57, and 26 protein-coding genes that were down-regulated by ≥2-fold in ppn1Δ, swd22Δ, and dis2Δ cells, respectively (Figure 3A). 40 coding transcripts were coordinately down-regulated in the ppn1Δ and swd22Δ mutants ($p < 3.29e-68$), of which 17 were also down-regulated in dis2Δ cells and 14 were down-regulated in ssu72-C13S cells (Figure 3B). Among the most highly down-regulated transcripts in DPSΔ cells were those of two phosphate homeostasis genes–pho1 and pho84 –that are under repressive control imposed by transcription of upstream flanking lncRNAs [17]. Previous studies had established that expression of the cell surface associated Pho1 acid phosphatase enzyme is hyper-repressed in ppn1Δ, swd22Δ, dis2Δ, and ssu72-C13S cells [6], an effect attributed to reduced efficiency of lncRNA 3' processing and transcription termination prior to encounter of Pol2 with the pho1 mRNA promoter, thereby enhancing lncRNA interference with mRNA expression. The Pombase annotation of the SPBC19C7.04c gene, which was downregulated ~8-fold in DPS mutants, suggests that it, too, might be subject to upstream transcription interference. SPBC19C7.04c encodes a 124-amino acid conserved fungal protein. The SPBC19C7.04c mRNA is annotated in PomBase as a 1450-nucleotide transcript that includes a 634-nucleotide 5'-UTR. The 5'-flanking gene, SPNCRNA.1553, specifies a 2044-nucleotide lncRNA that overlaps the putative 5'-UTR of the SPBC19C7.04c mRNA.

A

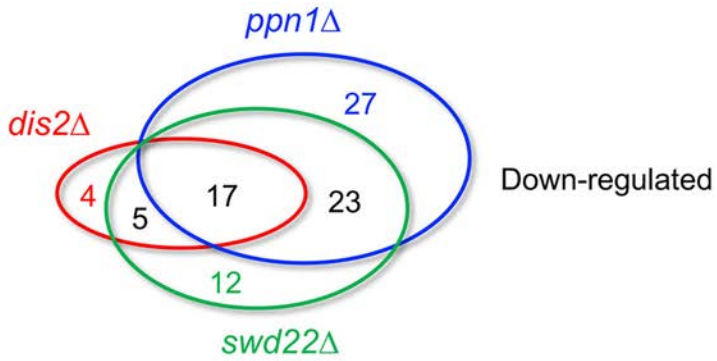

B

gene	log2 change				protein / function
	ppn1Δ	*swd22Δ*	*dis2Δ*	*ssu72-C13S*	
gdt1	−5.01	−6.86			Golgi calcium and manganese antiporter
pho1	−3.83	−3.57	−2.51	−2.47	acid phosphatase
pho84	−3.81	−3.43	−2.05	−2.24	phosphate transporter
SPBC19C7.04c	−2.80	−3.06	−2.79		DUF2406 family conserved fungal protein
dus2	−2.67	−2.13			tRNA dihydrouridine synthase
ste11	−2.60	−2.31	−1.76	−1.29	transcription factor
SPCC330.03c	−2.46	−1.71			NADPH-hemoprotein reductase
mei2	−2.36	−2.07	−1.20	−2.48	RNA binding protein
gep4	−2.15	−1.74		−4.09	phosphatidylglycerol phosphate phosphatase
jmj4	−2.12	−1.71			histone demethylase
SPCC737.04	−2.01	−2.27	−1.91		
SPAPB24D3.07c	−1.89	−1.26	−1.43		
rad31	−1.81	−1.68			SUMO E1
guf1	−1.78	−2.10		−3.13	mitochondrial elongation factor GTPase
abp2	−1.74	−1.51	−1.67	−1.15	
SPAC9.06c	−1.71	−1.29			5'-methylthioribulose-1-phosphate dehydratase
spk1	−1.65	−1.37		−1.19	MAP kinase
SPAC18B11.03c	−1.65	−1.22	−1.15		N-acetyltransferase
rlp1	−1.65	−1.08			RecA family ATPase
ecl3	−1.62	−1.63		−1.61	extender of chronological lifespan
SPAC23C4.04c	−1.58	−1.00			
cnp3	−1.53	−1.56	−1.97		kinetochore protein CENP-C
map1	−1.51	−1.45		−1.25	MADS-box transcription factor
nta1	−1.51	−1.04		−1.71	protein N-terminal amidase
pwi1	−1.49	−1.26			splicing factor Srm160
SPAC13C5.05c	−1.41	−1.09			N-acetylglucosamine-phosphate mutase
prz1	−1.39	−1.45	−1.46		calcineurin responsive transcription factor
hem14	−1.29	−1.04			protoporphyrinogen oxidase
urg2	−1.25	−1.11	−2.15		uracil phosphoribosyltransferase
urg1	−1.23	−1.38	−2.42		GTP cyclohydrolase
SPAC29A4.17c	−1.22	−1.07			mitophagy
ncs1	−1.20	−1.09	−1.06		calcium sensor
mae2	−1.18	−1.18	−1.09		malate dehydrogenase
rsn1	−1.17	−1.16			transmembrane transporter
nde2	−1.09	−1.22	−1.15	−1.97	mitochondrial NADH dehydrogenase
gon7	−1.08	−1.17		−2.00	EKC/KEOPS complex subunit
SPAC16A10.01	−1.06	−1.08			amino acid transmembrane transporter
SPAC664.13	−1.03	−1.02			
SPAC2H10.01	−1.03	−1.18	−1.50	−1.61	Zn2-Cys6 transcription factor
pxl1	−1.00	−1.10			paxillin

Figure 3. **Coding genes down-regulated in DPS mutants.** (A) Venn diagram depicting numbers of overlapping and non-overlapping down-regulated protein-coding genes. (B) List of 40 protein-coding genes that were coordinately down-regulated at least 2-fold in *ppn1*Δ and *swd22*Δ cells, 17 of which were also down-regulated in *dis2*Δ cells and 14 of which were down-regulated in s*su72-C13S* cells. The log2 fold changes versus wild-type are shown. Angad Garg and Beate Schwer collected RNA and performed data analysis.

2.4.2: Ppn1 truncation mutants

We constructed a series of N-terminal and C-terminal deletion variants of S. pombe Ppn1, guided by an alignment of its primary structure to those of Ppn1 homologs from three other *Schizosaccharomyces* species (Figure 4) and a IUPred2A plot [18] of its disorder tendency by position in the primary structure (Figure 6A). The N-terminal 172-aa of S. pombe Ppn1 displays relatively scant conservation with its *S. cryophilus*, *S. octosporus*, and *S. japonicus* counterparts (33 positions of side chain identity/similarity in all four proteins) (Figure 4). This poorly conserved N-terminus is predicted to be disordered in its entirety (Figure 6A). The ensuing region from aa 194–330 (Figure 4, shaded in gold) is highly conserved among the four fission yeast Ppn1 proteins, with 102 positions of identity/similarity, and is predicted to be structurally ordered (Figure 6A). Analysis of this segment of *S. pombe* Ppn1 in Phyre2 [19] engendered a high-confidence (99.4%) structural homology model of Ppn1-(186–325) templated on the solution NMR structure of the N-terminal transcription elongation factor TFIIS-like domain of rat PNUTS [20]. The predicted all-helical fold of Ppn1-(186–325) is shown in stereo in Figure 5. Alignment of the primary structures of the Ppn1 and PNUTS TFIIS-like modules reveals 48 positions of amino acid side chain identity/similarity (Figure 5). The rest of the Ppn1 protein consists of local segments of high

sequence conservation with other fission yeast Ppn1 homologs (aa 388–401, 427–436, 458–467, 502–528, and 533–589), some of which are predicted to have modest structural order (e.g., aa 511–520, 557–582), interspersed with poorly conserved segments that are predicted to be mostly disordered.

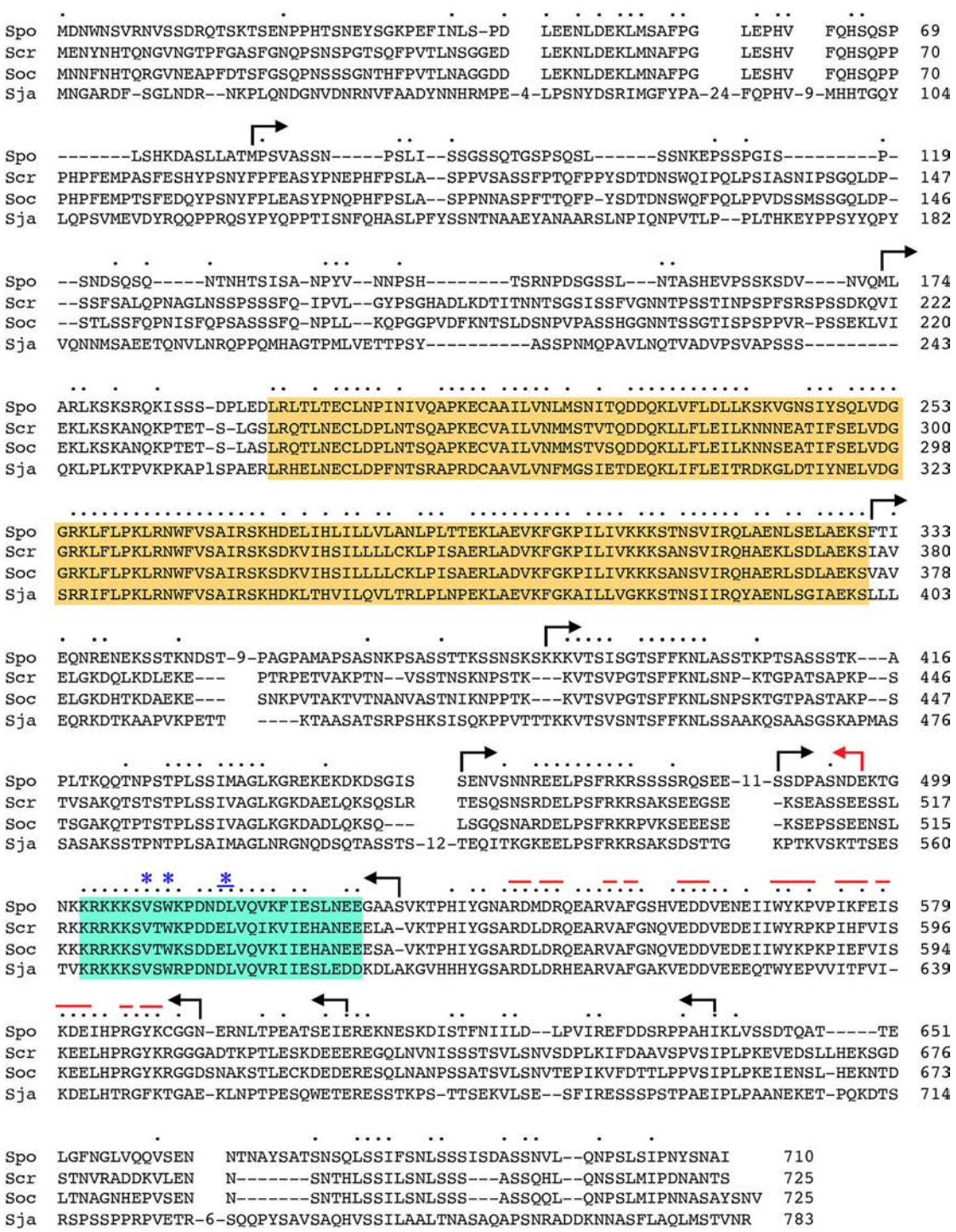
Spo MDNWNSVRNVSSDRQTSKTSENPPHTSNEYSGKPEFINLS-PD LEENLDEKLMSAFPG LEPHV FQHSQSP 69
Scr MENYNHTQNGVNGTPFGASFGNQPSNSPGTSQFPVTLNSGGED LEKNLDEKLMNAFPG LESHV FQHSQPP 70
Soc MNNFNHTQRGVNEAPFDTSFGSQPNSSSGNTHFPVTLNAGGDD LEKNLDEKLMNAFPG LESHV FQHSQPP 70
Sja MNGARDF-SGLNDR--NKPLQNDGNVDNRNVFAADYNNHRMPE-4-LPSNYDSRIMGFYPA-24-FQPHV-9-MHHTGQY 104
Spo -------LSHKDASLLATMPSVASSN-----PSLI--SSGSSQTGSPSQSL------SSNKEPSSPGIS---------P- 119
Scr PHPFEMPASFESHYPSNYFPFEASYPNEPHFPSLA--SPPVSASSFPTQFPPYSDTDNSWQIPQLPSIASNIPSGQLDP- 147
Soc PHPFEMPTSFEDQYPSNYFPLEASYPNQPHFPSLA--SPPNNASPFTTQFP-YSDTDNSWQFPQLPPVDSSMSSGQLDP- 146
Sja LQPSVMEVDYRQQPPRQSYPYQPPTISNFQHASLPFYSSNTNAAEYANAARSLNPIQNPVTLP--PLTHKEYPPSYYQPY 182
Spo --SNDSQSQ-----NTNHTSISA-NPYV--NNPSH--------TSRNPDSGSSL---NTASHEVPSSKSDV----NVQML 174
Scr --SSFSALQPNAGLNSSPSSSFQ-IPVL--GYPSGHADLKDTITNNTSGSISSFVGNNTPSSTINPSPFSRSPSSDKQVI 222
Soc --STLSSFQPNISFQPSASSSFQ-NPLL--KQPGGPVDFKNTSLDSNPVPASSHGGNNTSSGTISPSPPVR-PSSEKLVI 220
Sja VQNNMSAEETQNVLNRQPPQMHAGTPMLVETTPSY----------ASSPNMQPAVLNQTVADVPSVAPSSS--------- 243
Spo ARLKSKSRQKISSS-DPLEDLRLTLTECLNPINIVQAPKECAAILVNLMSNITQDDQKLVFLDLLKSKVGNSIYSQLVDG 253
Scr EKLKSKANQKPTET-S-LGSLRQTLNECLDPLNTSQAPKECVAILVNMMSTVTQDDQKLLFLEILKNNNEATIFSELVDG 300
Soc EKLKSKANQKPTET-S-LASLRQTLNECLDPLNTSQAPKECVAILVNMMSTVSQDDQKLLFLEILKNNSEATIFSELVDG 298
Sja QKLPLKTPVKPKAPlSPAERLRHELNECLDPFNTSRAPRDCAAVLVNFMGSIETDEQKLIFLEITRDKGLDTIYNELVDG 323
Spo GRKLFLPKLRNWFVSAIRSKHDELIHLILLVLANLPLTTEKLAEVKFGKPILIVKKKSTNSVIRQLAENLSELAEKSFTI 333
Scr GRKLFLPKLRNWFVSAIRSKSDKVIHSILLLLCKLPISAERLADVKFGKPILIVKKKSANSVIRQHAEKLSDLAEKSIAV 380
Soc GRKLFLPKLRNWFVSAIRSKSDKVIHSILLLLCKLPISAERLADVKFGKPILIVKKKSANSVIRQHAERLSDLAEKSVAV 378
Sja SRRIFLPKLRNWFVSAIRSKHDKLTHVILQVLTRLPLNPEKLAEVKFGKAILLVGKKSTNSIIRQYAENLSGIAEKSLLL 403
Spo EQNRENEKSSTKNDST-9-PAGPAMAPSASNKPSASSTTKSSNSKSKKKVTSISGTSFFKNLASSTKPTSASSSTK---A 416
Scr ELGKDQLKDLEKE--- PTRPETVAKPTN--VSSTNSKNPSTK---KVTSVPGTSFFKNLSNP-KTGPATSAPKP--S 446
Soc ELGKDHTKDAEKE--- SNKPVTAKTVTNANVASTNIKNPPTK---KVTSVPGTSFFKNLSNPSKTGTPASTAKP--S 447
Sja EQRKDTKAAPVKPETT ----KTAASATSRPSHKSISQKPPVTTTKKVTSVSNTSFFKNLSSAAKQSAASGSKAPMAS 476
Spo PLTKQQTNPSTPLSSIMAGLKGREKEKDKDSGIS SENVSNNREELPSFRKRSSSSRQSEE-11-SSDPASNDEKTG 499
Scr TVSAKQTSTSTPLSSIVAGLKGKDAELQKSQSLR TESQSNSRDELPSFRKRSAKSEEGSE -KSEASSEESSL 517
Soc TSGAKQTPTSTPLSSIVAGLKGKDADLQKSQ--- LSGQSNARDELPSFRKRPVKSEEESE -KSEPSSEENSL 515
Sja SASAKSSTPNTPLSAIMAGLNRGNQDSQTASSTS-12-TEQITKGKEELPSFRKRSAKSDSTTG KPTKVSKTTSES 560
Spo NKKRKKKSVSWKPDNDLVQVKFIESLNEEGAASVKTPHIYGNARDMDRQEARVAFGSHVEDDVENEIIWYKPVPIKFEIS 579
Scr RKKRKKKSVTWKPDDELVQIKVIEHANEEELA-VKTPHIYGSARDLDRQEARVAFGNQVEDDVEDEIIWYRPKPIHFVIS 596
Soc KKKRKKKSVTWKSDDELVQVKIIEHANEEESA-VKTPHIYGSARDLDRQEARVAFGNQVEDDVEDEIIWYKPKPIEFVIS 594
Sja TVKRKKKSVSWRPDNDLVQVRIIESLEDDKDLAKGVHHHYGSARDLDRHEARVAFGAKVEDDVEEEQTWYEPVVITFVI- 639
Spo KDEIHPRGYKCGGN-ERNLTPEATSEIEREKNESKDISTFNIILD--LPVIREFDDSRPPAHIKLVSSDTQAT-----TE 651
Scr KEELHPRGYKRGGGADTKPTLESKDEEEREGQLNVNISSSTSVLSNVSDPLKIFDAAVSPVSIPLPKEVEDSLLHEKSGD 676
Soc KEELHPRGYKRGGDSNAKSTLECKDEDERESQLNANPSSATSVLSNVTEPIKVFDTTLPPVSIPLPKEIENSL-HEKNTD 673
Sja KDELHTRGFKTGAE-KLNPTPESQWETERESSTKPS-TTSEKVLSE--SFIRESSSPSTPAEIPLPAANEKET-PQKDTS 714
Spo LGFNGLVQQVSEN NTNAYSATSNSQLSSIFSNLSSSISDASSNVL--QNPSLSIPNYSNAI 710
Scr STNVRADDKVLEN N-------SNTHLSSILSNLSSS---ASSQHL--QNSSLMIPDNANTS 725
Soc LTNAGNHEPVSEN N-------SNTHLSSILSNLSSS---ASSQQL--QNPSLMIPNNASAYSNV 725
Sja RSPSSPPRPVETR-6-SQQPYSAVSAQHVSSILAALTNASAQAPSNRADDKNNASFLAQLMSTVNR 783

Figure 4. **Primary structure of fission yeast Ppn1.** The amino acid sequence of *S. pombe* (Spo) Ppn1 is aligned to those of the Ppn1 proteins from *S. cryophilus* (Scr), *S. octosporus* (Soc), and *S. japonicus* (Sja). Short gaps in the alignment are indicated by dashes; longer gaps are denoted by numbers of intervening amino acids. Positions of side chain identity/similarity in all four Ppn1 proteins are indicated by dots above the *S. pombe* sequence. Margins of serial N- and C-terminal truncations of *S. pombe* Ppn1 are shown as forward and reverse arrows. A conserved domain with predicted homology to the N-terminal TFIIS-like domain of rat PNUTS is highlighted in gold shading. A conserved segment that embraces the Dis2 binding site is highlighted in cyan shading; amino acids required for Ppn1-Dis2 interaction in a yeast 2-hybrid assay are denoted by asterisks above the alignment. The red lines above the alignment indicate residues within the Swd22 binding module of Ppn1 that were subjected to alanine scanning and testing of mutational effects on 2-hybrid protein-protein interactions.

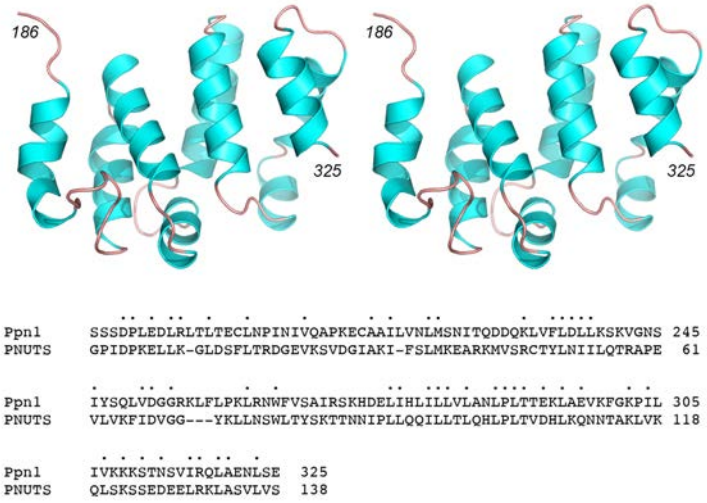

Figure 5. **Predicted structural homology of Ppn1-(186-325) to the TFIIS-like domain of PNUTS.** (Top panel) Stereo view of the Phyre2 homology model of Ppn1 templated on the fold of the transcription elongation factor TFIIS-like N-terminal domain of rat PNUTS (pdb 6VTI). (Bottom panel) Primary structure alignment of the homologous TFIIS-like domains of Ppn1 and PNUTS generated by Phyre2. Positions of amino acids identity and sidechain similarity are denoted by • above the alignment.

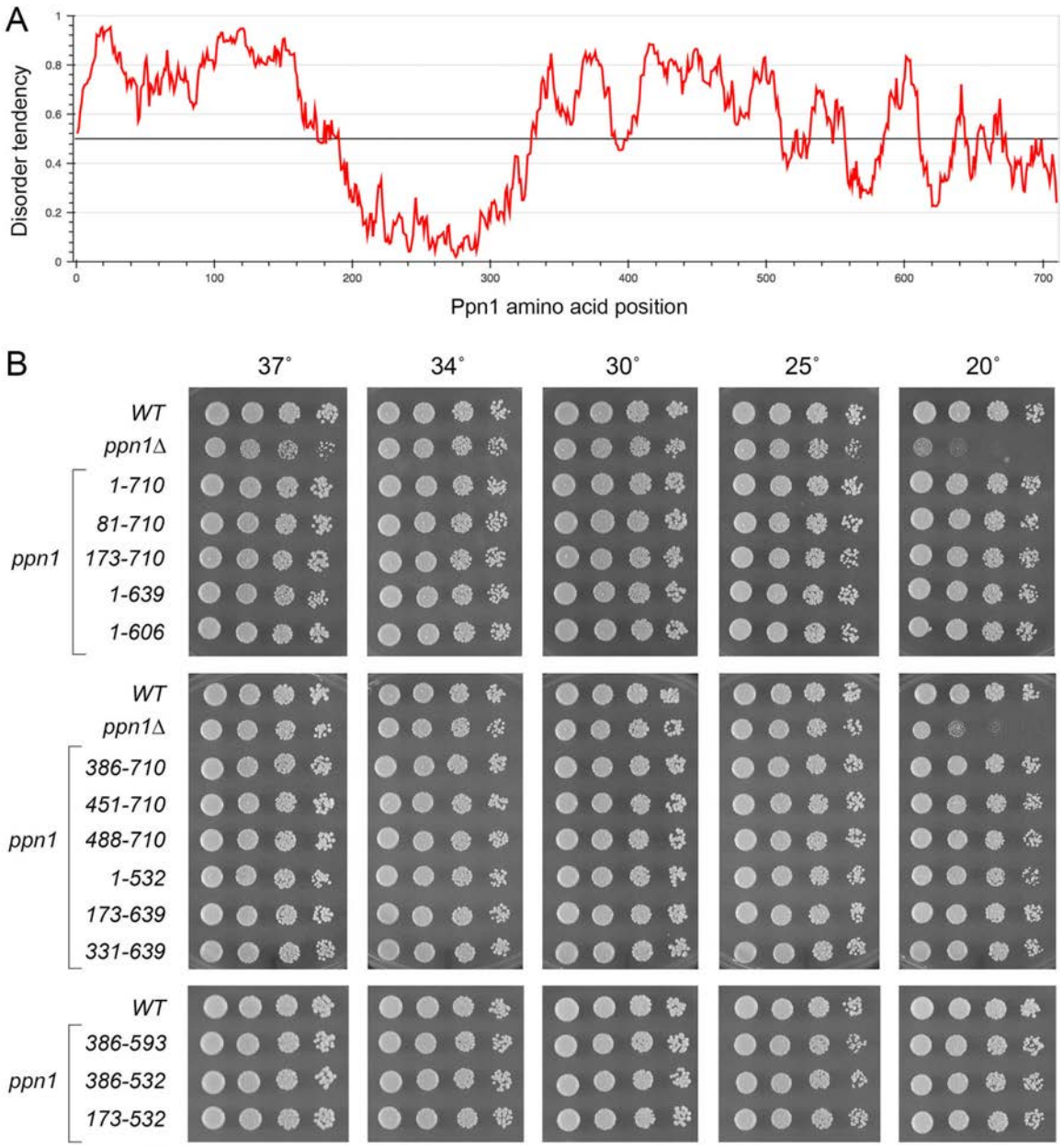

Figure 6. **Fission yeast strains with *ppn1* truncation alleles.** (A) An IUPred2A plot of disorder tendency by position in the *S. pombe* Ppn1 primary structure. (B) Serial dilutions of cultures of wild-type (*WT*), *ppn1*Δ, and the indicated *ppn1* truncation mutants were spot-tested for growth on YES agar at the temperatures specified.

I serially deleted 80, 172, 330, 385, 450, or 487 amino acids from the N-terminus or 71, 104, 117, 178, or 214 amino acids from the C-terminus of S. pombe Ppn1 (the margins of the truncations are indicated by arrows in Figure

4). Full-length and truncated ppn1 alleles, marked by a 3'-flanking drug-resistance cassette, were inserted into the chromosomal *ppn1* locus in lieu of the native *ppn1*$^{+}$ gene and the resulting strains were spot tested for growth on YES agar at 20, 25, 30, 34, and 37°C in parallel with: (i) an unmarked wild-type *ppn1*$^{+}$ strain (WT) that grows well at all temperatures and (ii) a *ppn1Δ* null mutant, which displays a cold-sensitive (cs) growth defect at 20°C (Figure 6B). All of the N-terminal deletion alleles, up to and including *ppn1-(488–710)*, complemented the cs defect, as did the C-terminal deletion alleles, up to and including *ppn1-(1–532)* (Figure 6B). However, a further C-terminal truncation allele *ppn1-(1–496)* was unable to sustain normal growth at 20°C (Figure 7). These results indicate that: (i) the N-terminal 487 amino acids (that includes the disordered N-terminus and the adjacent TFIIS-like domain) and the C-terminal 178 amino acids are individually dispensable for growth at cold temperatures; and (ii) the segment from aa 488–532, which includes a region of strong conservation among Ppn1 homologs (highlighted in cyan in Figure 4) is necessary for growth in the cold. I proceeded to test simultaneous deletions at both ends of Ppn1 and found that alleles *ppn1-(173–639), ppn1-(331–639), ppn1-(386–593), ppn1-(173–532),* and *ppn1-(386–532),* supported growth at 20°C (Figure 6B).

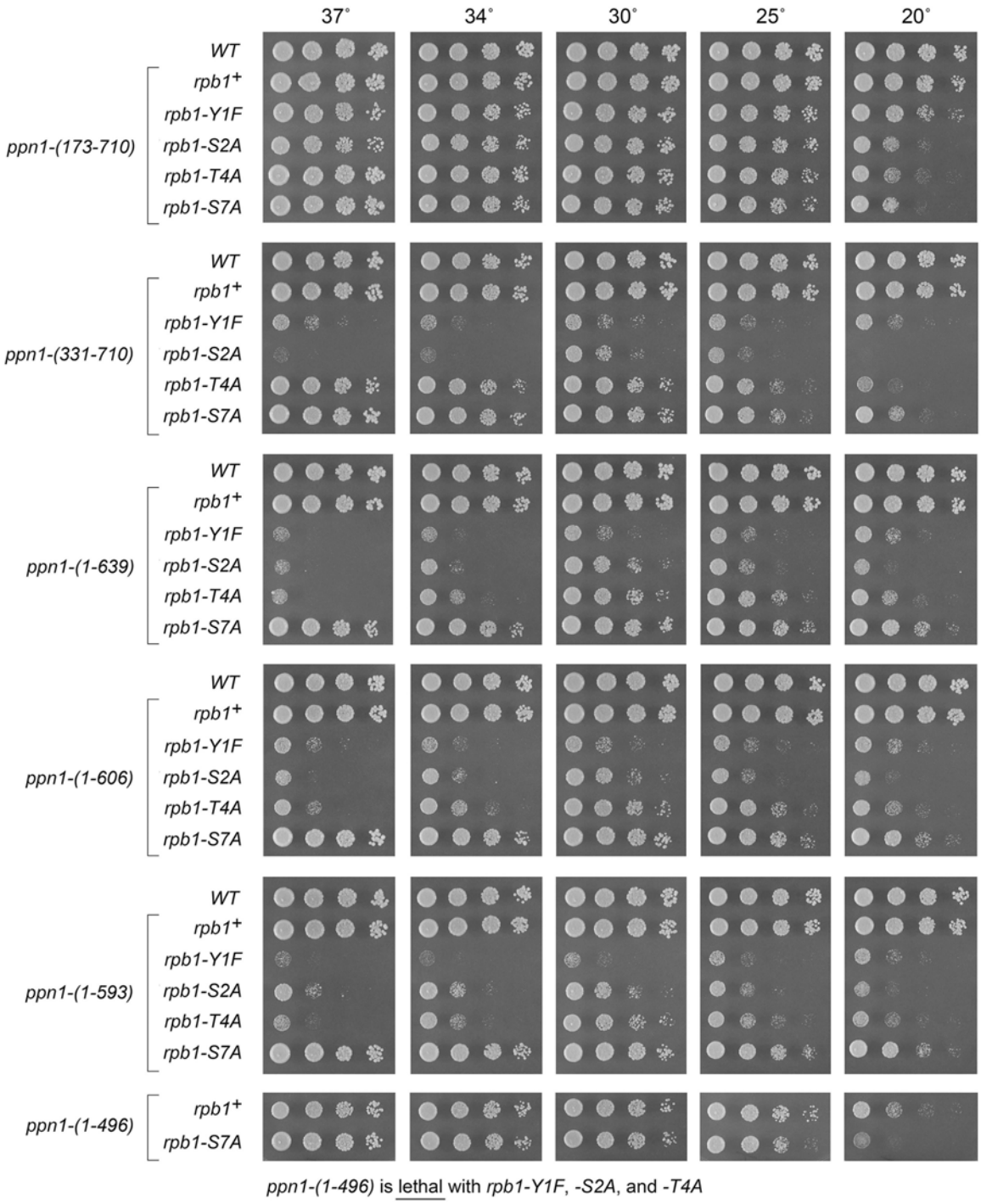

Figure 7. **Activity of Ppn1 truncations in CTD mutant backgrounds in which Ppn1 is essential.** *S. pombe* strains bearing the indicated *ppn1* truncation alleles in combination with *rpb1-CTD* phospho-site mutants were spot-tested for growth on YES agar at the indicated temperatures. The *ppn1-(1–496)* allele, which did not complement the *cs* growth phenotype seen in *ppn1*Δ, was lethal in the *rpb1-Y1F*, *-S2A*, and *-T4A* backgrounds.

To gauge the effects of Ppn1 truncations on the intracellular levels of Ppn1 protein, I raised rabbit polyclonal antibodies against purified recombinant Ppn1-(173–496) produced in *E. coli*. Whole cell extracts of fission yeast strains (normalized for total protein content) were resolved by SDS-PAGE, transferred to membrane, and subjected to Western blotting with affinity-purified anti-Ppn1 antibody. A ~90 kDa immunoreactive polypeptide corresponding to full-length Ppn1 (aa 1–710) was present in the wild-type strain but absent in *ppn1Δ* cells (Figure 8). Incrementally smaller immunoreactive Ppn1 proteins of appropriate size were seen in cells expressing N-terminal truncations Ppn1-(173–710), -(331–710) and -(386–710) and bilateral truncations Ppn1-(173–639) -(331–639), and -(173–532) (Figure 8). A noteworthy finding was that the steady-state level of Ppn1-(173–710) was clearly elevated compared to that of full-length Ppn1, as was the steady state level of the other five aforementioned truncated Ppn1 polypeptides (Figure 8). These findings suggest that the disordered N-terminal 172-aa segment of Ppn1 has a destabilizing influence on Ppn1. Whereas acute decrements in the level of immunoreactive Ppn1 polypeptide were seen when the N-terminal 385-aa deletion was combined with C-terminal truncations at positions 593 and 532, respectively, the steady state levels of the Ppn1-(386–532) and Ppn1-(386–593) proteins were still similar to, for (386–532), or slightly higher than, for (386–593), that of full-length Ppn1 (Figure 8). Immunoreactive C-terminally truncated Ppn1 proteins of incrementally smaller size were detected in *ppn1-(1–639), ppn1-(1–593), ppn1-(1–532),* and *ppn1-(1–496)* cells (Figure 9).

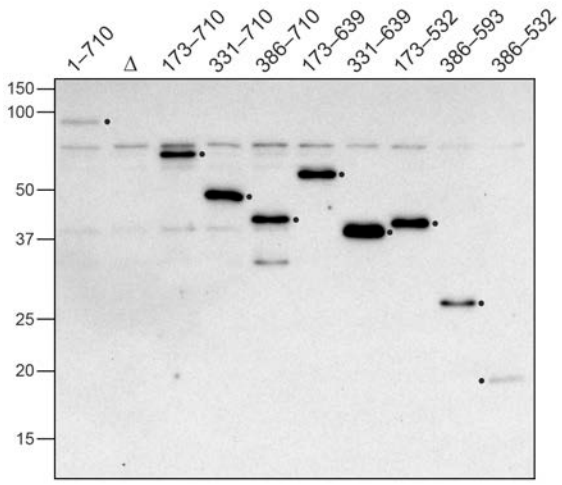

Figure 8. **Western blot of Ppn1 N-terminal truncation mutants.** Whole-cell extracts from wild-type *ppn1-(1-710), ppn1*Δ, and the indicated *ppn1* truncation strains growing logarithmically at 30℃ were resolved by SDS-PAGE and subjected to Western blotting with polyclonal Ppn1 antibodies. The positions and sizes (in kilodaltons) of marker polypeptides are indicated at left.

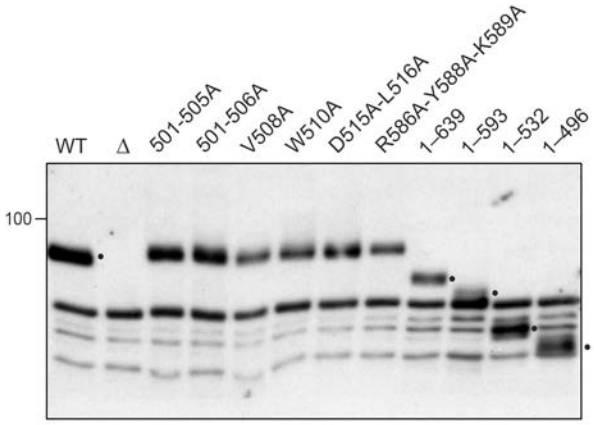

Figure 9. **Western blot of Ppn1 missense and C-terminal truncation mutants.** Whole-cell extracts from wild-type *ppn1-(1-710), ppn1*Δ, and the indicated *ppn1* mutant strains growing logarithmically at 30℃ were resolved by SDS-PAGE and subjected to Western blotting with polyclonal Ppn1 antibodies. The full-length wild-type (WT) and C-terminally truncated Ppn1 polypeptides are denoted by dots. The position of a 100 kDa marker polypeptide is shown on the left.

2.4.3 Activity of Ppn1 truncations in CTD mutant backgrounds in which Ppn1 is essential

S. pombe rpb1-CTD mutant strains, in which the native CTD length was maintained and Tyr1, Ser2, Thr4, or Ser7 in every consensus heptad was replaced by Phe, Ala, Ala, or Ala, respectively, thrive on YES agar medium at 30°C but grow slowly at 20°C [6]. *ppn1Δ* is synthetically lethal in the *CTD-Y1F, -S2A*, and -*T4A* backgrounds, but viable in combination with *CTD-S7A* [6]. Here I tested the capacity of the various *ppn1* truncation mutants to support viability in the three mutant *CTD* genetic backgrounds in which Ppn1 is essential. Haploid strains with *rpb1-CTD* alleles *Y1F, S2A, T4A*, and *S7A* (marked with a 3' flanking *natMX* gene) were mated to haploid strains with *ppn1* truncation mutations. The resulting heterozygous diploids were sporulated and, for each allelic pair, a random collection of 500 to 1000 viable haploid progeny were screened by serial replica-plating for the presence of the flanking markers. A failure to recover any viable haploids with both markers, while recovering the three other haploid progeny (unmarked and the two singly marked haploids) with the expected frequencies, was taken as evidence of synthetic lethality between the CTD allele and the test *ppn1* allele. The double-mutant haploids that passed selection were spotted on YES agar at 20 to 37°C in parallel with two control strains, in which *rpb1* and *ppn1* were both wild-type or *rpb1* was wild-type and *ppn1* was truncated (Figs 6 and 7). As expected, all *ppn1* truncations were viable in combination with *CTD-S7A*.

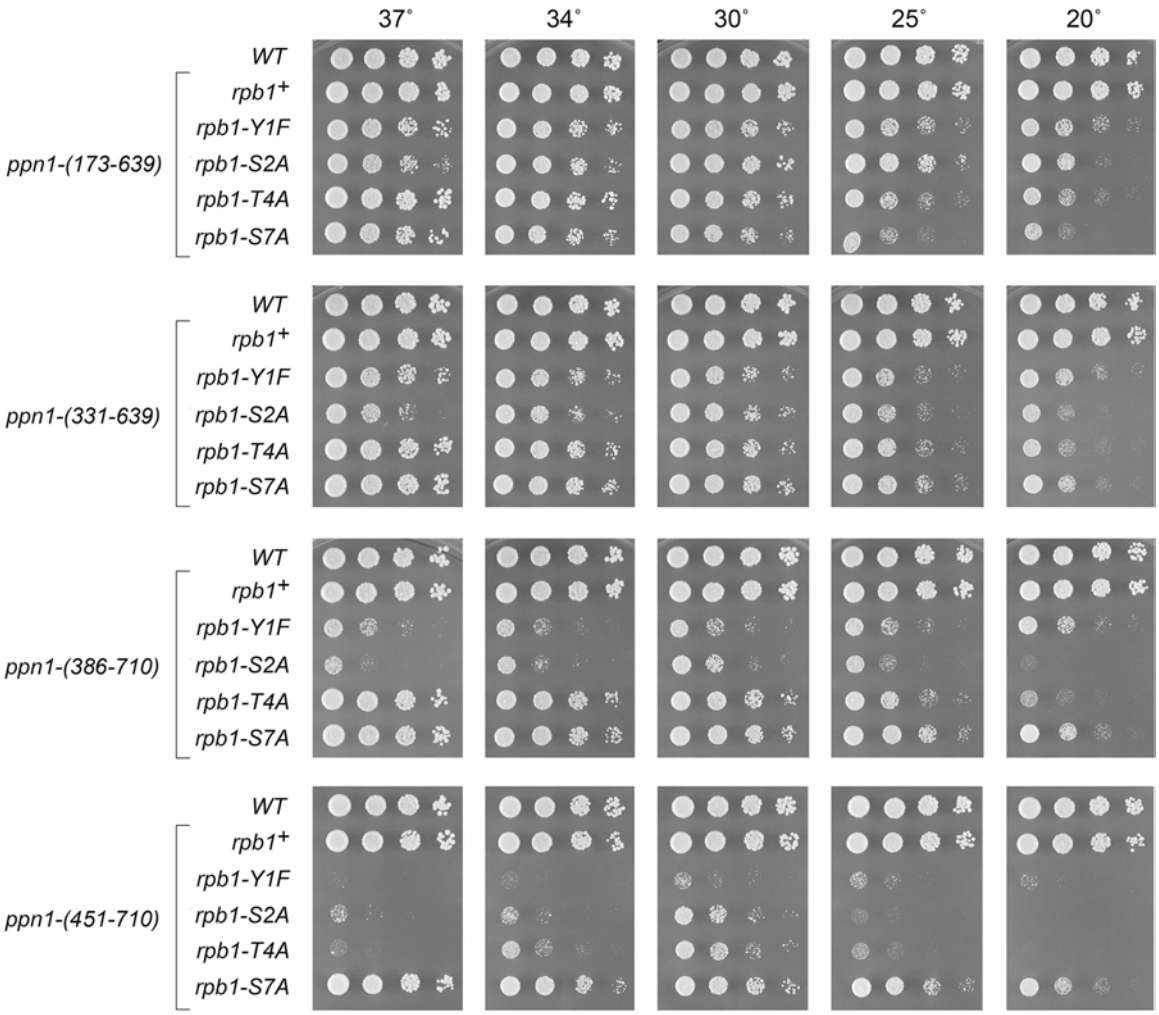

Figure 10. **Activity of Ppn1 truncations in CTD mutant backgrounds.** Strains with the indicated *ppn1* truncation alleles in combination with *rpb1-CTD* phospho-site mutants were spot-tested for growth on YES agar at the indicated temperatures.

We found that whereas N-terminal truncation *ppn1-(173–710)* was fully active in supporting growth of the *Y1F*, *S2A*, and *T4A* strains, *ppn1-(331–710)* caused a severe growth defect in *Y1F* and *S2A* cells (reflected in tiny colony size) but relatively little impact in the *T4A* background (Figure 7). *ppn1-(386–710)* phenocopied *ppn1-(331–710)* (Figure 10). *ppn1-(451–710)* was barely viable in combination with *Y1F* and was severely sick with *S2A* and *T4A* (Figure 10). C-terminal deletion *ppn1-(1–639)* resulted in failure of *Y1F*, *S2A*, and *T4A* cells to

thrive at 37°C as well as synthetic sickness at 30°C in the *Y1F* and *S2A* backgrounds. Serial C-terminal deletions *ppn1-(1–606)* and *ppn1-(1–593)* phenocopied *ppn1-(1–639)* in the *CTD-Ala* strains, but further truncation to *ppn1-(1–496)* was synthetically lethal with *Y1F*, *S2A*, and *T4A* (Figure 7). We surmise from these results that: (i) the N-terminal 172-aa segment of Ppn1 is inessential; (ii) deletion of aa 173–330 or 640–710 elicits hypomorphic phenotypes in CTD mutant backgrounds, to which *Y1F* and *S2A* are more sensitive than *T4A*; and (iii) the segment from aa 452–593 contains elements necessary for Ppn1 function in CTD mutant backgrounds.

Testing combinations of N- and C-terminal truncations generated additional instructive findings. For example, *ppn1-(173–639)* and *ppn1-(331–639)* supported better growth of *Y1F*, *S2A*, and *T4A* cells, especially at 34°C and 37°C, than did *ppn1-(1–639)* (Figure 10, compare to Figure 7), suggesting that the disordered N-terminus exerts an inhibitory effect on Ppn1 function when the C-terminal 71-aa are missing. The growth phenotypes of *ppn1* truncation alleles in combination with CTD mutants are summarized in Figure 11.

N-terminal truncations

	ppn1Δ	*173-710*	*331-710*	*386-710*	*451-710*	*488-710*
ctf1Δ	Lethal		cs	cs	very sick	Lethal
rhn1Δ	Lethal			ts	ts	ts
ssu72-C13S	Lethal		ts	ts	Lethal	Lethal
pin1Δ	Lethal		sick	sick	very sick	Lethal
CTD-Y1F	Lethal		sick	sick	very sick	very sick
CTD-S2A	Lethal		sick	sick	sick	very sick
CTD-T4A	Lethal		cs	cs	sick	very sick

C-terminal truncations

	ppn1Δ	*1-639*	*1-606*	*1-593*	*1-532*	*1-496*
ctf1Δ	Lethal	cs/ts	cs/ts	ts	Lethal	Lethal
rhn1Δ	Lethal	ts	ts	ts	Lethal	Lethal
ssu72-C13S	Lethal	sick	sick	very sick	Lethal	Lethal
pin1Δ	Lethal	ts	ts	ts	Lethal	Lethal
CTD-Y1F	Lethal	very sick	very sick	very sick	Lethal	Lethal
CTD-S2A	Lethal	cs/ts	cs/ts	sick	Lethal	Lethal
CTD-T4A	Lethal	ts	ts	cs/ts	Lethal	Lethal

N/C-terminal truncations

	ppn1Δ	*173-639*	*331-639*	*386-593*	*173-532*	*386-532*
ctf1Δ	Lethal		cs		cs, ts	cs
rhn1Δ	Lethal				ts	ts
ssu72-C13S	Lethal				Lethal	very sick
pin1Δ	Lethal				Lethal	very sick
CTD-Y1F	Lethal		cs	cs	very sick	sick
CTD-S2A	Lethal		cs	cs	sick	cs
CTD-T4A	Lethal		cs	cs	very sick	very sick

Figure 11. **Summary of growth effects of *ppn1* truncations in different genetic backgrounds.** *ppn1* mutants specified in the top rows were crossed to the mutant strains specified in the left-most column. Synthetically lethal pairs of alleles are highlighted in red boxes. The yellow boxes indicate synthetic growth defects (sick or very sick). Viable double mutants without a synthetic defect are indicated by a plain green box. Viable double mutants that displayed temperature-sensitive (*ts*) or cold-sensitive (*cs*) defects are annotated as such in its green box.

2.4.4 Activity of Ppn1 truncations in 3' processing/termination mutant backgrounds

Ppn1 is essential for growth in the absence of CPF core subunit Ctf1, when the cis-proline-requiring Ssu72 CTD phosphatase subunit of CPF core is either deleted or crippled by an active site mutation C13S, and in the absence of the CTD-binding transcription termination factor Rhn1 [6]. Ppn1 is also essential in the absence of Pin1, a peptidyl prolyl isomerase that promotes 3' processing/termination via Ssu72 [14]. Here the *ppn1* truncation alleles were tested for activity in sustaining growth of *ctf1Δ*, *ssu72-C13S*, *rhn1Δ*, and *pin1Δ* cells (via mating and sporulation as described above for the CTD mutants). The results are shown in Figs 8 and 9. (Note that *rhn1Δ* single-mutant cells fail to grow at 37°C.) Key findings are as follows. N-terminal truncation *ppn1-(173–710)* was fully active in supporting growth of the four processing/termination mutants. *ppn1-(331–710)* was cs in the *ctf1Δ* strain and ts in the *ssu72-C13S* strain (Figure 12). *ppn1-(451–710)* exacerbated the growth phenotypes of *rhn1Δ*, *ctf1Δ*, and *pin1Δ* and was lethal in combination with *ssu72-C13S* (Figure 13). *ppn1-(488–710)* was lethal with *ctf1Δ*, *ssu72-C13S*, and *pin1Δ* but thrived in the *rhn1Δ* background at 20–30°C (Figure 13). C-terminal truncations *ppn1-(1–639)* and *ppn1-(1–593)* exacerbated the ts defect of *rhn1Δ* (seen as failure to thrive at 34°C) and elicited ts growth defects in *ssu72-C13S* and *pin1Δ* cells at 34 and 37°C (Figure 12). *ppn1-(1–496)* was uniformly lethal in combination with *ctf1Δ*, *ssu72-C13S*, *rhn1Δ*, or *pin1Δ*. The bilateral deletion alleles *ppn1-(173–639)* and *ppn1-(331–639)* grew better than *ppn1-(1–639)* in all four of the 3'

processing/termination mutant contexts (Figure 13). These results (summarized in Figure 11) echo those obtained for the CTD mutants, insofar as the N-terminal disordered region of Ppn1 is dispensable in all genetic assays of Ppn1 essentiality, deleting the disordered N-terminus alleviates hypomorphic phenotypes caused by deleting the C-terminal segment from aa 640–710, and intermediate truncations have allele-specific severities, with *rhn1Δ* being less sensitive to hypomorphic mutations than *ctf1Δ*, *ssu72-C13S*, and *pin1Δ*.

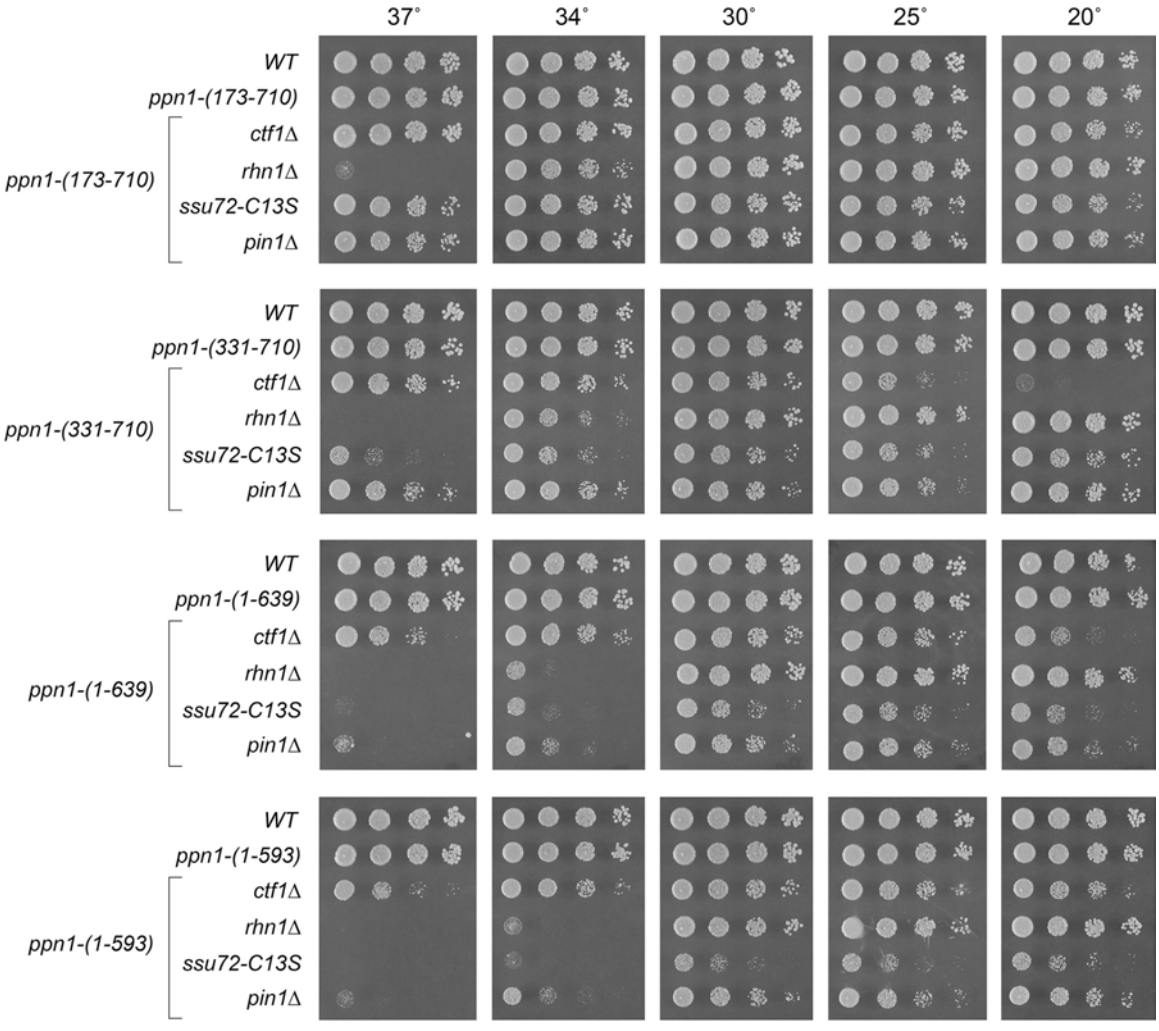

ppn1-(1-496) is lethal with *ctf1Δ*, *rhn1Δ*, *ssu72-C13S*, and *pin1Δ*

Figure 12. **Activity of Ppn1 truncations in 3' processing/termination mutant backgrounds.** *S. pombe* strains bearing the indicated *ppn1* truncation alleles in combination with CPF subunit, Rhn1, or Pin1 mutants as specified were spot-tested for growth on YES agar at the indicated temperatures. The *ppn1-(1–496)* allele was synthetically lethal with *ctf1*Δ, *rhn1*Δ, *ssu72-C13S*, and *pin1*Δ.

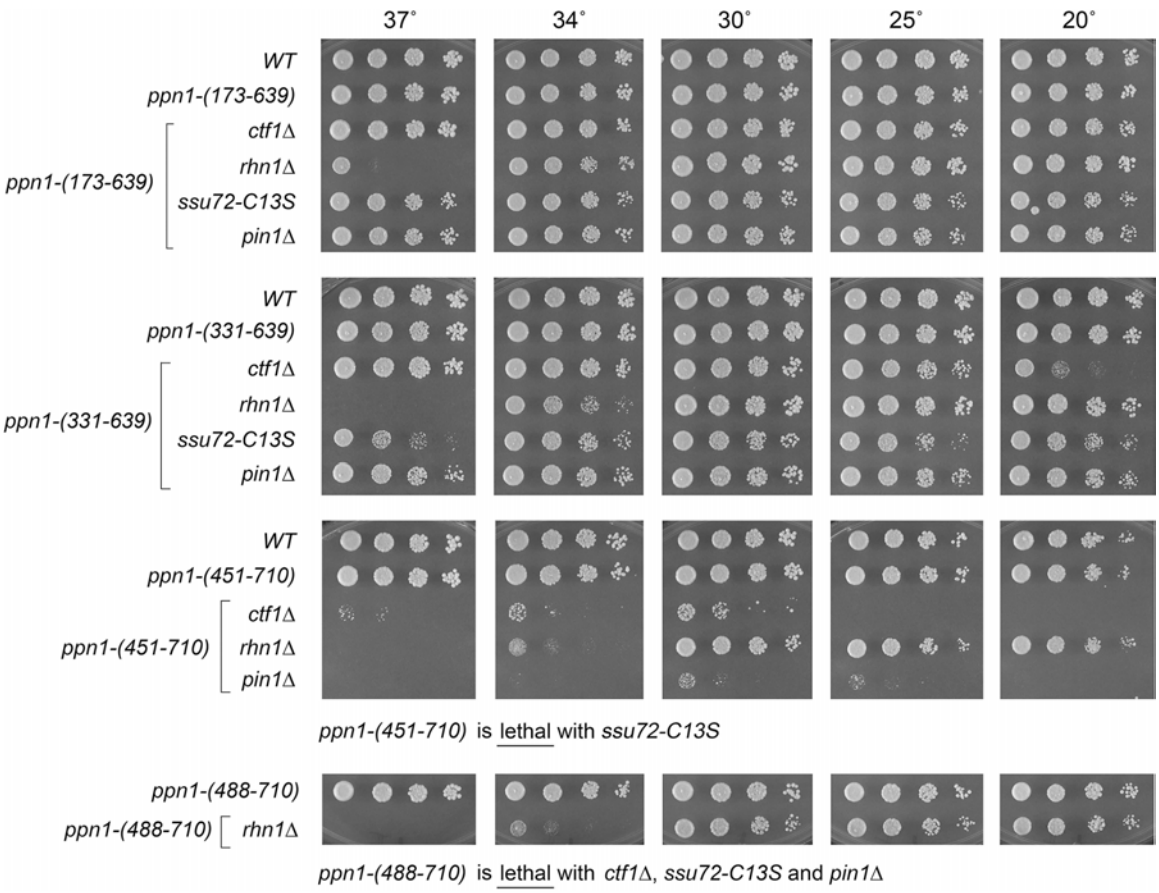

Figure 13. **Activity of Ppn1 truncations in CPF/Rhn1/Pin1 mutant backgrounds.** Strains with the indicated *ppn1* truncation alleles in combination with CPF subunit, Rhn1, or Pin1 mutants as specified were spot-tested for growth on YES agar at the indicated temperatures. Synthetic lethalities of *ppn1-(451–710)* and *ppn1-(488–710)* are specified below the panels.

2.4.5 Effect of Ppn1 truncations on phosphate homeostasis

Fission yeast phosphate homeostasis is a transcriptional program that is governed by the Pol2 CTD code and the 3' processing/termination machinery

[6,21,22]. The *S. pombe* phosphate regulon comprises three genes that specify, respectively, a cell surface acid phosphatase Pho1, an inorganic phosphate transporter Pho84, and a glycerophosphate transporter Tgp1 [23]. Expression of *pho1*, *pho84*, and *tgp1* is actively repressed during growth in phosphate-rich medium by the transcription in *cis* of a long noncoding (lnc) RNA from the respective 5' flanking genes *prt*, *prt2*, and *nc-tgp1* [24–29]. A model for the repressive arm of fission yeast phosphate homeostasis is that transcription of the upstream lncRNA interferes with expression of the downstream mRNA genes by displacing the activating transcription factor Pho7 from its binding site(s) in the mRNA promoters that overlap the lncRNA transcription units [17]. A Pol2 *CTD-S7A* allele that prevents installation of the Ser7-PO_4 mark de-represses *PHO* genes in phosphate-replete cells [6,21,22] by promoting precocious termination of upstream lncRNA transcription prior to encounter of Pol2 with the downstream mRNA promoter (Figure 14A). This model is supported by findings that: (i) mutations of CPF subunits (including *ppn1Δ*), Rhn1, and Pin1 – proteins that normally promote 3' processing/termination–result in hyper-repression of pho1 under phosphate-replete conditions; and (ii) the de-repression of *pho1* elicited by the *CTD-S7A* allele is erased by mutations of CPF subunits (including *ppn1Δ*), Rhn1, and Pin1 [6,14]. Recent studies also implicate the inositol pyrophosphate (IPP) signaling molecule IP_8 as an agent in the nexus of the CTD code with 3' processing/termination, based on biochemical phenotypes and mutational synergies elicited by genetic manipulations of Asp1 [7], a bifunctional enzyme composed of an N-terminal IPP kinase domain and a C-terminal IPP

pyrophosphatase domain [30,31]. The function of the Asp1 kinase is to generate 1,5-IP8 via phosphorylation of its substrate 5-IP_7 and the function of the Asp1 pyrophosphatase is to convert its substrate 1,5-IP_8 back to 5-IP_7. An IPP-pyrophosphatase-dead allele *asp1-H397A* that results in elevated intracellular levels of IP_8 elicits a strong de-repression of the PHO regulon that correlates, in the case of the *prt–pho1* locus, with precocious termination of *prt* lncRNA transcription [7]. The de-repression of *pho1* by *asp1-H397A* is erased by mutations of CPF subunits (including *ppn1Δ*), Rhn1, and Pin1 [7,14].

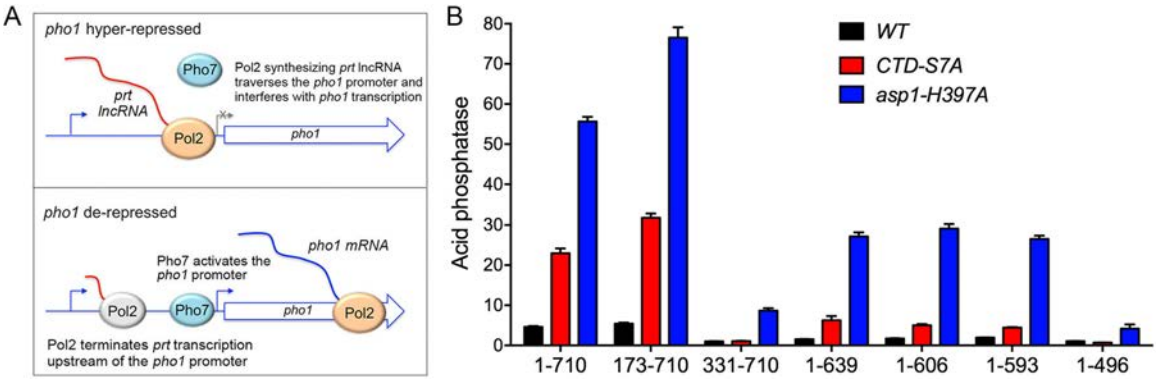

Figure 14. **Effect of Ppn1 truncations on phosphate homeostasis.** (A) Top panel. Decreased termination of *prt* lncRNA synthesis increases interference with the *pho1* mRNA promoter and hyper-represses Pho1 expression in phosphate-replete cells. Bottom panel. Precocious termination of *prt* lncRNA synthesis upstream of the *pho1* mRNA promoter results in de-repression of Pho1. See text for discussion. (B) *S. pombe* strains bearing the *ppn1* alleles shown on the x-axis, in an otherwise wild-type background (WT) or in the context of the *pho1* de-repressive *rpb1-CTD-S7A* or *asp1-H397A* mutations, were grown in liquid culture at 30°C and assayed for acid phosphatase activity.

Here I queried the effect of ppn1 truncations on pho1 expression during exponential growth at 30°C in liquid culture under phosphate-replete conditions, *per se*, and in the *CTD-S7A* and *asp1-H397A* genetic backgrounds in which *pho1* is de-repressed in a manner that relies on Ppn1 function (Figure 14B).

Acid phosphatase activity, a gauge of Pho1 enzyme level, was quantified by incubating suspensions of serial dilutions of the phosphate-replete cells for 5 min with p-nitrophenyl phosphate and assaying colorimetrically the formation of p-nitrophenol. The basal Pho1 activity of wild-type cells was unaffected in *ppn1-(173–710)* cells [*vis-à-vis* the *ppn1-(1–710)* wild-type strain] but was hyper-repressed in *ppn1-(1–496)* cells expressing a non-functional Ppn1 mutant. The de-repression of Pho1 seen in *CTD-S7A* and *asp1-H397A* cells expressing wild-type Ppn1 was erased in the *ppn1-(1–496)* strain (Figure 14B), as shown previously for *ppn1Δ* [7]. A noteworthy finding was that the de-repressed levels of Pho1 activity in *ppn1-(173–710) CTD-S7A* and *ppn1-(173–710) asp1-H397A* cells were 38% higher than in the respective *ppn1-(1–710)* controls (Figure 14B). By contrast, the *ppn1-(331–710)* allele elicited Pho1 hyper-repression *per se* and eliminated (in *CTD-S7A* cells) or severely attenuated (in *asp1-H397A* cells) Pho1 de-repression (Figure 14B). We surmise that the segment from aa 173–330 that includes the predicted TFIIS-like module is important for Ppn1 function in *prt* lncRNA termination. The C-terminal truncation alleles *ppn1-(1–639)*, *-(1–606)*, and *-(1–593)* were hyper-repressive *per se* and partially attenuated the de-repression of Pho1 by *CTD-S7A* and *asp1-H397A* (Figure 14B), consistent with our designation of these mutants as functional hypomorphs.

2.4.6 Yeast 2-hybrid assays identify distinct Dis2 and Swd22 binding sites in Ppn1

Full-length and truncated versions of Ppn1 were tested for interaction with DPS subunits Dis2 and Swd22 in the yeast 2-hybrid assay, with dual reporter

readouts (*His*$^{+}$ and *lacZ*$^{+}$) of a positive interaction between a transcription activation domain (AD) fused to Ppn1 and a DNA binding domain (BD) fused to full-length Dis2 or Swd22 (scored as ++ in Figure 15A). Full-length Ppn1 interacted with both Dis2 and Swd22, signifying that none of the subunits of the *S. pombe* CPF core are needed for binary interactions of Ppn1. Deleting up to 505 amino acids from the N-terminus did not affect Ppn1 interaction with Dis2 and Swd22. Both interactions were preserved when the C-terminus of Ppn1 was truncated at amino acid 593 (Figure 15A). By testing various combinations of N and C terminal truncations, I defined an internal segment from 506–639 as sufficient for Ppn1 interaction with Dis2 and Swd22 (Figure 15A). Neither the N-terminal segment from aa 1–496 nor the C-terminal fragment from 578–710 was able to bind to Dis2 or Swd22 in the 2-hybrid format (Figure 15A).

A

AD-Ppn1	BD-Dis2	BD-Swd22
1-710	++	++
173-710	++	++
331-710	++	++
488-710	++	++
565-710	--	++
578-710	--	--
1-639	++	++
1-593	++	++
1-578	++	++
1-565	++	--
1-548	++	--
1-532	++	--
1-496	--	--
173-639	++	++
331-639	++	++
488-639	++	++
506-639	++	++
386-532	++	--
511-639	--	++
533-639	--	++
533-593	--	++

B

AD-Ppn1	BD-Dis2	BD-Swd22
501-505A	++	++
501-506A	--	++
K506A	++	++
S507A-S509A	++	++
S507D-S509D	--	++
S507D	++	++
S509D	++	++
V508A	--	++
W510A	--	++
K511A-P512A	++	++
D513A-N514A	++	++
D515A-L516A	--	++
V517A-L518A	++	++
V519A-K520A	++	++
F521A	++	++
I522A-E523A	++	++
E527A-E528A	++	++
R543A-D544A	++	++
D546A-R547A	++	++
V552A-F554A	++	++
E559A-D560A-D561A	++	++
W568A-Y569A-K570A	++	++
P571A	++	++
K575A	++	++
I574A-F576A-I578A	++	++
K580A-D581A-E582A	++	++
R586A-Y588A-K589A	++	--
R586A	++	++
Y588A	++	++
K589A	++	++
R586A-Y588A	++	++
Y588A-K589A	++	++
R586A-K589A	++	++

C

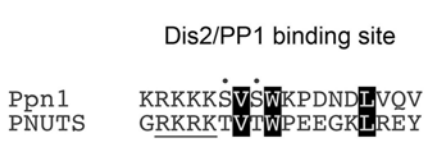

Figure 15. **Yeast 2-hybrid assays identify distinct Dis2 and Swd22 binding sites in Ppn1.** (A) Full-length Ppn1 (aa 1–710) and the indicated Ppn1 fragments fused to the Gal4 AD were tested for 2-hybrid interactions with Gal4 BD fusions to full-length Dis2 and full-length Swd22. AD/BD pairs that scored positive in both reporter assays (LacZ expression and histidine prototrophy) are indicated as ++. Pairs that were negative in both reporter assays are scored as --. (B) Full-length AD-Ppn1 constructs with the indicated amino acid substitutions were tested for 2-hybrid interactions with BD-Dis2 and BD-Swd22. (C) The amino acid sequences of the PP1/Dis2 binding motifs in PNUTS and Ppn1 are aligned. The conserved hydrophobic amino acids important for the Ppn1-Dis2 interaction in the 2-hybrid assay (Val, Trp, Leu) are in white font on black background. Conserved hydroxyamino acids that are potential phosphorylation sites are denoted by dots. The upstream basic patch is underlined.

The findings that: (i) Ppn1-(1–565), -(1–548), -(1–532), and -(386–532) bound to Dis2 but not to Swd22; and (ii) Ppn1-(511–639), -(533–639), and -(533–

593) bound to Swd22 but not Dis2 (Figure 15A) engender the following inferences. First, that Dis2 and Swd22 bind to distinct sites on Ppn1. Second, that the Dis2 binding site is localized within the Ppn1 segment from aa 506–532 and requires the peptide ^{506}KSVSW^{510}. Third, that the Swd22 binding site is located in the segment from aa 533–578 and requires the segment from aa 566–578.

2.4.7 2-hybrid alanine scan of the Dis2 and Swd22 binding regions of Ppn1

The 27-aa segment that encompasses the Dis2 binding site (shaded cyan in Figure 4) is highly conserved among the four *Schizosaccharomyces Ppn1* homologs. In an effort to identify essential constituents of the Dis2 interface, I introduced single-alanine and double-alanine mutations into the full-length AD-Ppn1 2-hybrid bait construct, targeting every amino acid from Lys506 to Glu523, plus Glu527 and Glu528. Controls showed that none of the alanine mutations affected Ppn1 interaction with Swd22 (Figure 15B). Ppn1 binding to Dis2 was abolished by single alanine changes V508A and W510A and by the D515A-L516A double-mutant (Figure 15B). None of the other alanine substitutions of 16 amino acids in the Dis2 box (mostly double-alanine mutants) affected Dis2 binding in the 2-hybrid format. The strictly conserved Val508 and Trp510 residues essential for Dis2 binding are indicated by blue asterisks in Figure 4. The Asp515-Leu516 dipeptide needed for Dis2 interaction is either Asp-Leu or Glu-Leu in the three other *Schizosaccharomyces* Ppn1 homologs (Figure 4). We suggest that the ^{508}VxW^{510} motif in Ppn1 is the putative counterpart of a Vx(F/W) motif that comprises a key part of the PP1 phosphatase-binding site identified in several other PP1 regulatory subunits, including PNUTS, wherein the Vx(F/W) motif binds

to a hydrophobic pocket of the phosphatase remote from the phosphatase active site [32–35] (Figs 11C and 16). A leucine equivalent of Ppn1 Leu516 is a conserved constituent of the hydrophobic PP1-binding interface of other phosphatase regulators, including PNUTS (Figure 15C and 16).

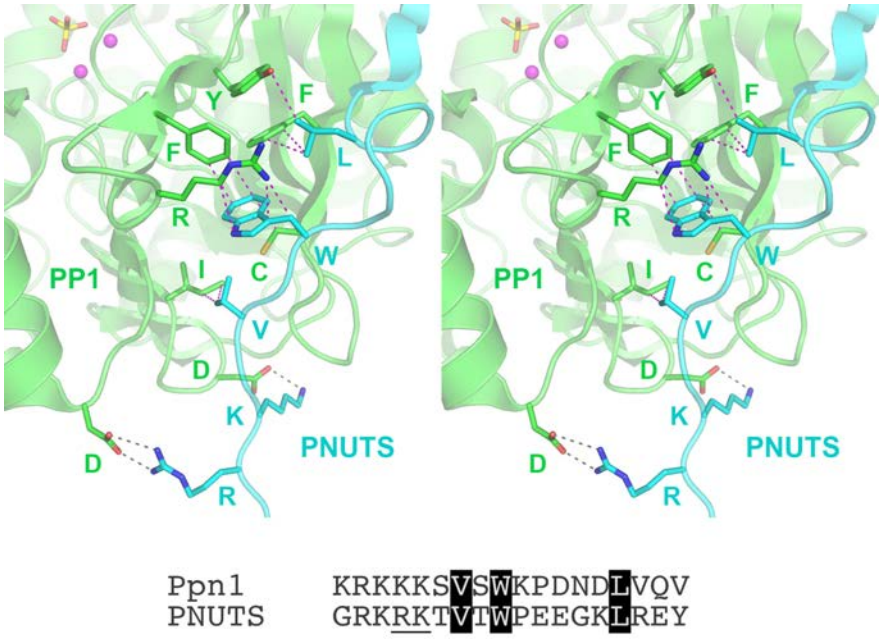

Figure 16. **Conservation of PP1/Dis2 binding motifs in PNUTS and Ppn1.** Stereo view of the interface of PNUTS (colored cyan) with PP1C (colored green) from the 2.2 Å crystal structure (pdb 4MOY). Interfacial amino acid side chains are rendered as stick models. Salt bridges are depicted as black dashed lines. Van der Waals contacts are shown as magenta dashed lines. The two manganese ions in the phosphatase active site are magenta spheres; a phosphate anion in the active site is rendered as a stick model. The amino acid sequences of the PP1/Dis2 binding motifs in PNUTS and Ppn1 are aligned at bottom. The conserved hydrophobic interfacial amino acids – Val, Trp, and Leu – are in white font on black background. The two basic side chains that form salt bridges to the phosphatase are underlined.

The proximal edge of the Dis2-binding "box" in Ppn1 consists of a run of six basic amino acids (^{501}KKRKKK^{506}), five of which are conserved in all three other

fission yeast Ppn1 homologs (Figure 4). Other well-studied PP1 phosphatase-regulatory proteins have at least one, and often several, basic amino acids preceding the Vx(F/W) motif [32–35]. In the case of PNUTS, there is a run of four basic amino acids upstream of VxW (Figure 15C); two of these basic amino acids engage in salt bridges to acidic side chain chains of PP1 (Figure 16). Because mutating Lys506 singly to alanine did not affect Dis2 interaction with full-length Ppn1, I proceeded to change all six basic amino acids to alanine simultaneously. The 501-506A mutation of Ppn1 eliminated Dis2 interaction without affecting Swd22 interaction (Figure 15B). Yet changing only the first five of the basic amino acids to alanine did not affect the 2-hybrid interaction of Ppn1-(501-505A) with Dis2 (Figure 15B). Thus, at least one basic side chain in this basic patch is needed for Dis2 interaction.

The Ppn1 Dis2-binding box contains two serines, Ser507 and Ser509, that are conserved as serine or threonine in the three other fission yeast Ppn1 proteins (Figure 4) and in PNUTS (Figure 15C). Previous studies showed that interaction of PNUTS with PP1 phosphatase can be modulated negatively by threonine phosphorylation at the PP1-binding site (RKRKTVTW) of PNUTS [16]. To query whether serine phosphorylation might affect Ppn1 interaction with Dis2, I introduced phosphomimetic aspartate substitutions at Ser507 and Ser509 of full-length Ppn1, singly and in combination, and tested their effects in the 2-hybrid assay. The single S507D and S509D changes did not compromise Ppn1 interaction with Dis2, but the S507D-S509D double-mutation abolished Dis2 interaction without affecting Ppn1 binding to Swd22 (Figure 15B). Thus, the

simultaneous acquisition of negative charge at these two sites was inimical to the Dis2 binding interface of Ppn1. Mutation of both serines to alanine did not disrupt Ppn1-Dis2 interaction.

To interrogate the Swd22 interface, I constructed 10 single-alanine, double-alanine and triple-alanine mutations in the full-length AD-Ppn1 2-hybrid expression vector, targeting 23 amino acids denoted by the red lines in Figure 4. Nine of the Ppn1-Ala mutants did not affect the 2-hybrid interaction with Swd22 (or with the Dis2 control). Only the R586A-Y588A-K589A triple-mutant failed to score as interacting with Swd22, while maintaining interaction with Dis2 (Figure15B). To deconvolute the Swd22 binding-defective triple-mutant, I changed each amino acid singly to alanine and made all three combinations of double-alanine substitutions, none of which compromised the 2-hybrid interaction with Swd22 (Figure 15B).

2.4.8 Effect of Dis2 binding-defective mutations on Ppn1 activity *in vivo*

The *501-506A*, *V508A*, *W510A*, and *D515A-L516A* mutations that selectively interdicted Ppn1 binding to Dis2 in the 2-hybrid assay were introduced into the fission yeast chromosomal *ppn1* locus. The Dis2 binding-defective mutations resulted in Pho1 hyper-repression in *CTD-WT* cells and eliminated the de-repressive effect of *CTD-S7A* (Figure 18). These mutant *ppn1* alleles were then tested, after mating and sporulation, for activity in several genetic backgrounds in which Ppn1 is essential for growth. Our initial expectations were that Ppn1 mutations that interdict the Dis2 binding site might phenocopy the synthetic lethality of *dis2Δ* with *ssu72-C13S* but not display any of the other synthetic lethal interactions characteristic of *ppn1Δ* (e.g.,

with *ctf1Δ*, *rhn1Δ*, *pin1Δ*, *CTD-Y1F*, *CTD-S2A*, and *CTD-T4A*) [6,14]. Whereas each of the Dis2 binding-defective alleles was indeed lethal with *ssu72-C13S*, the remarkable findings were that these *ppn1* alleles had a wider range of synthetic lethal interactions than did *dis2Δ*, whereby: (i) all of them were lethal with *pin1Δ*, *CTD-Y1F*, and *CTD-T4A*; and (ii) *501-506A* and *W510A* were lethal with *rhn1Δ*, *ctf1Δ*, and *CTD-S2A* (Figure 17). The double mutants that were viable – *ppn1-V508A ctf1Δ*, *ppn1-V508A rhn1Δ*, *ppn1-V508A CTD-S2A*, *ppn1-D515A-L516A ctf1Δ*, *ppn1-D515A-L516A rhn1Δ*, and *ppn1-D515A-L516A CTD-S2A* – were very sick at all temperatures when spot-tested for growth on YES agar (Figure 17).

	501-506A	*V508A*	*W510A*	*D515A-L516A*	*RYK-AAA*
ssu72-C13S	lethal	lethal	lethal	lethal	lethal
pin1Δ	lethal	lethal	lethal	lethal	very sick
rhn1Δ	lethal	very sick	lethal	very sick	
ctf1Δ	lethal	very sick	lethal	very sick	very sick
CTD-T4A	lethal	lethal	lethal	lethal	very sick
CTD-Y1F	lethal	lethal	lethal	lethal	very sick
CTD-S2A	lethal	very sick	lethal	very sick	cs, ts

Figure 17. **Effect of Dis2 and Swd22 binding-defective mutations on Ppn1 activity *in vivo*.** *ppn1* mutants specified in the top row were crossed to the mutant strains specified in the left-most column. Synthetically lethal pairs of alleles are highlighted in red boxes. The yellow boxes indicate severe synthetic growth defects (very sick). A viable double mutant without a synthetic defect is indicated by a plain green box. A viable double mutant that displayed temperature-sensitive (*ts*) or cold-sensitive (*cs*) defects is annotated as such in its green box.

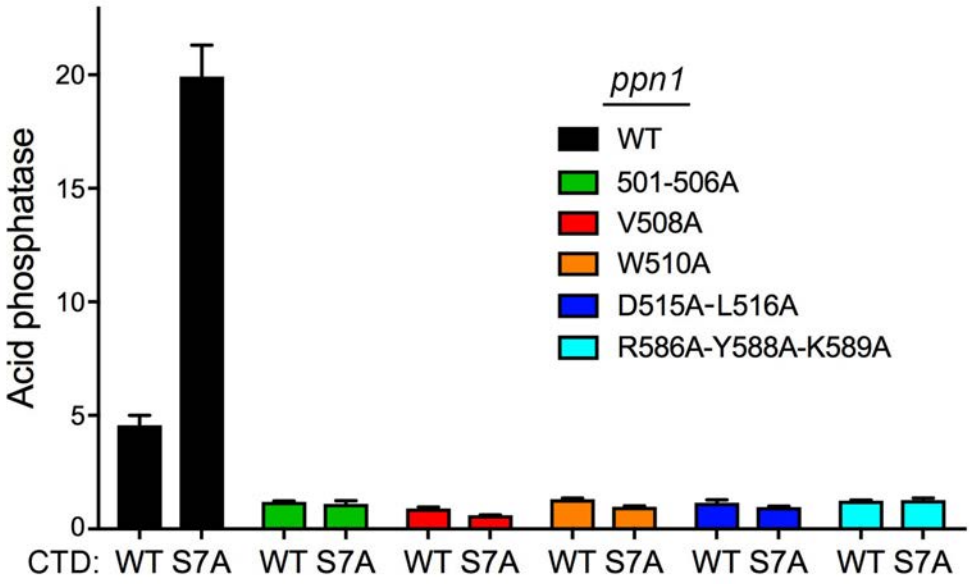

Figure 18. **Ppn1 mutations defective for Dis2 or Swd22 binding hyper-repress Pho1 expression.** *S. pombe CTD-WT* or *CTD-S7A* strains bearing the indicated *ppn1* alleles were grown in liquid culture at 30°C and assayed for acid phosphatase activity.

2.4.9 Dis2 phosphatase paralog Sds21 also interacts with Ppn1

The results in the preceding section engender the conundrum that mutating the Dis2 binding site of Ppn1 is more deleterious than the absence of Dis2. We envisioned two scenarios to account for this: (i) that Dis2 "liberated" from its contacts with Ppn1 might have negative effects on growth in the various genetic backgrounds in which the Ppn1 Dis2-box mutants are lethal; or (ii) in the absence of Dis2, another protein can interact with the Dis2-box of Ppn1 and perform some of the functions normally executed by Dis2, but this compensation is precluded by the Dis2-box mutations. If the "liberated Dis2 is bad" model is operative, then we would expect that synthetic lethality of, for example, *ppn1-W510A rhn1Δ* ought to be rescued by *dis2Δ*. However, we found, after mating and sporulation, that no

viable *ppn1-W510A rhn1Δ dis2Δ* haploids were recovered, which militates against the “liberated Dis2 is bad” model.

A plausible candidate to partly compensate for Dis2 deletion is its PP1 protein phosphatase paralog Sds21 [36]. Sds21, like Dis2, is inessential for fission yeast growth [36] (Figure 19A). Dis2 and Sds21 have non-identical but overlapping functions, whereby a *dis2Δ sds21Δ* double mutant is lethal [36]. That Sds21 does not normally play a role in CPF function when Dis2 is present is in keeping with our finding that an *sds21Δ ssu72-C13S* double-mutant is viable (Figure 19A) whereas *dis2Δ* is synthetically lethal with *ssu72-C13S* [6]. Moreover, deletion of Sds21 does not elicit the hyper-repression of Pho1 seen in *dis2Δ* cells (Figure 19B). Alvarez-Tabarés et al. reported that Dis2 is present in wild-type cells throughout the nucleus, whereas Sds21 is predominantly nucleolar [37]. They found that deleting Dis2 resulted in increased intracellular levels of Sds21 and detection of Sds21 at nuclear locations previously occupied by Dis2 [37]. If our conjecture that Sds21 can abet Ppn1 function in the absence of Dis2 is valid, then it should be the case that Sds21 can bind to Ppn1. A yeast 2-hybrid test affirmed that full-length Sds21 and Ppn1 interact and, moreover, that Sds21 binding was erased by Ppn1 mutations 501-506A, V508A, W510A, and S507D-S509D (Figure 19C). We conclude that Dis2 and Sds21 can interact with Ppn1 via the same Dis2-box element. Yet, the finding that the Ppn1 D515A-L516A mutation did not abolish the 2-hybrid interaction with Sds21 (Figure 19C) hints that there may be subtle differences in the Dis2-Ppn1 and Sds21-Ppn1 interfaces.

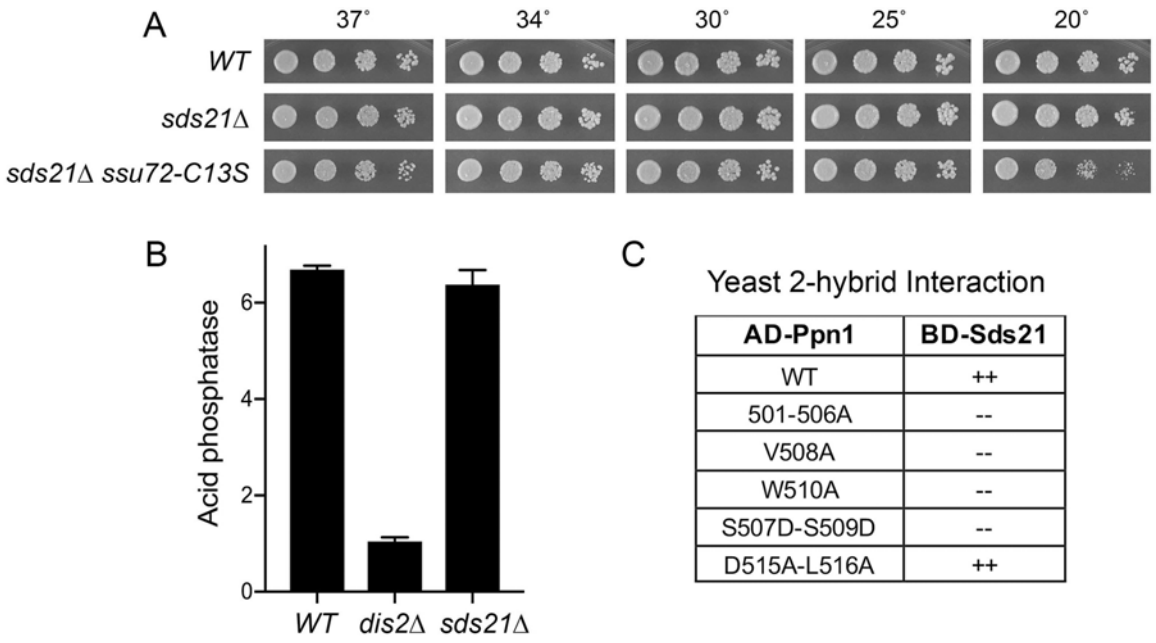

AD-Ppn1	BD-Sds21
WT	++
501-506A	--
V508A	--
W510A	--
S507D-S509D	--
D515A-L516A	++

Figure 19. **Sds21 can interact with Ppn1 via the Dis2 binding site.** (A) *S. pombe* wild-type, *sds21*Δ, and *sds21*Δ *ssu72-C13S* strains were spot-tested for growth on YES agar at the indicated temperatures. (B) *S. pombe* wild-type, *dis2*Δ, and *sds21*Δ cells were grown in liquid culture at 30°C and assayed for acid phosphatase activity. (C) Full-length Ppn1 (WT and the indicated mutants) fused to the Gal4 AD were tested for 2-hybrid interactions with Gal4 BD fusions to full-length Sds21. AD/BD pairs that scored positive in both reporter assays (LacZ expression and histidine prototrophy) are indicated as ++. Pairs that were negative in both reporter assays are scored as --.

2.4.10 The distinctive C-terminal tail of Dis2 is dispensable for Dis2 function

The 327-aa Dis2 and 322-aa Sds21 proteins share 252 positions of amino acid identity and 27 positions of side chain similarity (Figure 20A). Whereas Dis2 and Sds21 are nearly identical with respect to their N-terminal 304-aa and 301-aa polypeptides, the primary structures of their respective 23-aa and 21-aa C-terminal tails diverge almost completely (Figure 20A). Thr316 within the Dis2 C-terminal tail is phosphorylated *in vivo*, whereas the corresponding Thr313 residue in the Sds21 is not, the difference being that Dis2 Thr316 is situated within a Thr-Pro dipeptide

that is targeted by cyclin-dependent protein kinases whereas the Sds21 Thr313 is flanked by an asparagine [38] (Figure 20A). Parua et al. [39] reported that Dis2 Thr316 is phosphorylated by Cdk9 and they propose that this modification diminishes Dis2's activity as a protein phosphatase that dephosphorylates Thr-PO_4 sites in the C-terminal repeat domain of Pol2 transcription elongation factor Spt5 as the Pol2 transcription complex encounters the cleavage/polyadenylation site (CPS) of the transcription unit. This and other studies have coalesced into a model in which Dis2 dephosphorylation of Spt5 slows Pol2 movement after traversal of the CPS and facilitates engagement of the termination machinery [13,39,40]. The impact of Thr316 phosphorylation on this scenario is unclear, insofar as Parua et al. found via PRO-seq that the phospho-ablative T316A and phosphomimetic T316D mutations behaved virtually identically to dis2Δ in eliciting greater read-through elongation by Pol2 to template sites downstream of the CPS [39].

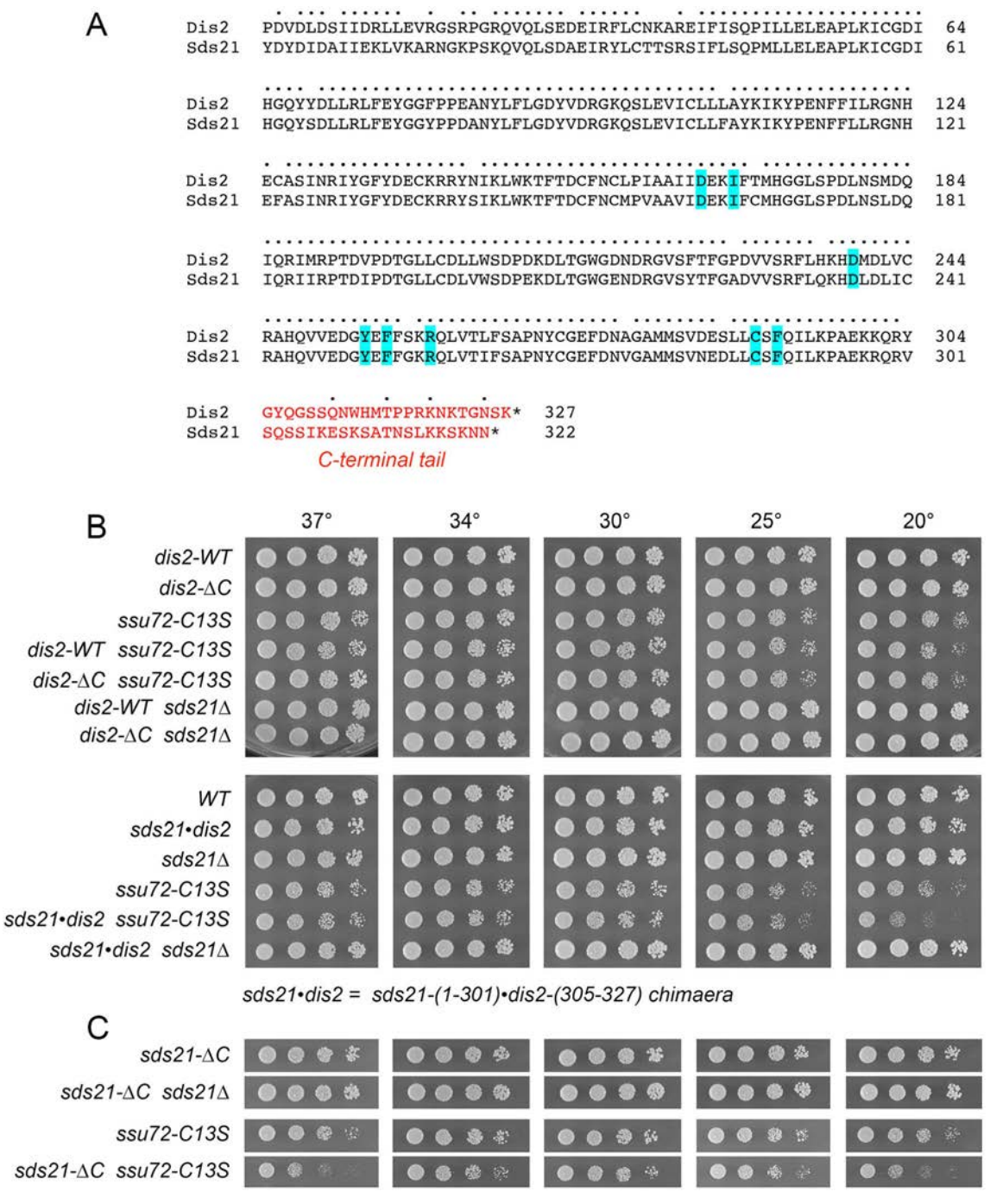

Figure 20. **The distinctive C-terminal tail of Dis2 is dispensable for Dis2 function.** (A) Primary structure alignment of Dis2 and Sds21, with positions of amino acid side chain identity/similarity indicated by dots. The divergent C-terminal tails are shown in red font. The amino acids predicted to comprise the Ppn1 binding pocket are highlighted in blue. (B and C) *S. pombe* strains as specified on the left were spot-tested for growth on YES agar at the indicated temperatures.

To query whether the distinctive C-terminal tail of Dis2, and its phosphorylation site, contribute to Dis2 essential functions *in vivo*, Beate Schwer replaced the endogenous *dis2*$^{+}$ gene with *dis2-ΔC*, which encodes Dis2-(1–304) that lacks the C-terminal tail. The *dis2-ΔC* strain grew as well as *dis2-WT* at all temperatures (Figure 20B). Tests of *dis2-ΔC* function were conducted in two genetic backgrounds–*ssu72-C13S* and *sds21Δ*–in which Dis2 is essential for growth. We obtained *dis2-ΔC ssu72-C13S* and *dis2-ΔC sds21Δ* double-mutants at the expected frequency after mating and sporulation; the double mutants grew as well as the *dis2-WT ssu72-C13S* and *dis2-WT sds21Δ* single-mutants at all temperatures (Figure 20B). We conclude that the C-terminal tail and Thr316 phosphorylation are dispensable for Dis2's essential activities.

In light of these new results, we considered the prospect that the distinctive C-terminal tail of Sds21 might disfavor it acting in lieu of Dis2 in the context of CPF and 3'-processing (which is inessential in an otherwise wild-type background) because it directs Sds21 function elsewhere. Alternatively, the very few amino acid differences within the catalytic domains of Dis2 and Sds21 could be a decisive factor. To address the latter issue, Dr. Schwer created a chimaeric allele, *sds21•dis2*, in which the catalytic domain of Sds21 (aa 1–301) was fused to the C-terminal tail of Dis2 (aa 305–327) and introduced *sds21•dis2* in lieu of the *dis2*$^{+}$ chromosomal gene so that *sds21•dis2* expression is driven by the native *dis2* promoter. The salient findings were that *sds21•dis2* sufficed for growth in an *ssu72-C13S* background and in the *sds21Δ* background (Figure 20B). We surmise that: (i) there is no significant difference between the Dis2 and Sds21

catalytic domains with respect to CPF function; and (ii) swapping the Dis2 C-terminal tail into Sds21 is not deleterious.

Finally, Dr. Schwer introduced an *sds21-ΔC* allele – encoding the Sds21-(1–301) catalytic domain but lacking the Sds21 C-terminal tail – in place of the *dis2*$^{+}$ chromosomal gene so that *sds21-ΔC* expression is driven by the native *dis2* promoter. She found that *sds21-ΔC* sufficed for growth in an *ssu72-C13S* background and in the *sds21Δ* background (Figure 20C). We conclude that the catalytic domain of either Dis2 or Sds21 suffices for vegetative growth and CPF function when expressed from the *dis2* genomic locus.

2.4.11 Dis2 mutations that affect interaction with Ppn1

Inspection of the structure of PNUTS in complex with PP1 (Figure 16) highlighted interfacial PP1 amino acids Ile169, Tyr255, Phe257, Arg261, Cys291, Phe293, Asp166, and Asp240 that are conserved in fission yeast Dis2 as Ile168, Tyr254, Phe256, Arg260, Cys290, Phe292, Asp165, and Asp239. Single alanine mutations at each of these positions were introduced into the full-length BD-Dis2 expression construct and the Dis2 mutants tested for 2-hybrid interaction with full-length AD-Ppn1 (Figure 21). Ppn1 interaction was eliminated by alanine mutations at Dis2 residues Ile168, Phe256, and Phe292 that, in PP1, comprise a hydrophobic interface with the conserved Val, Trp, and Leu moieties of PNUTS/Ppn1 (Figure 16). Mutating interfacial Dis2 residues Tyr254 and Arg260 resulted in weaker 2-hybrid interactions in the lacZ and His reporter readouts. Mutating Dis2 Cys290 did not affect Ppn1 interaction. It was noteworthy that mutating Dis2 Asp165 and Asp239, singly or together, did not affect 2-hybrid interaction with Ppn1 (Figure

21). These amino acids in PP1 make salt bridges to two basic amino acids in PNUTS (Figure 16). Finally, I found that deleting the distinctive C-terminal tail of Dis2 (Figure 20A) had no impact on Ppn1 interaction in the 2-hybrid assay (Figure 21).

BD-Dis2	AD-Ppn1
I168A	--
Y254A	±±
F256A	--
R260A	±±
C290A	++
F292A	--
D165A	++
D239A	++
D165A-D239A	++
ΔC	++

Figure 21. **Dis2 mutations that affect interaction with Ppn1.** Gal4 BD fusions to full-length Dis2 alanine mutants and the C-terminal deletion mutant Dis2-(1-304) were tested for 2-hybrid interactions with full-length Ppn1 fused to the Gal4 AD. BD/AD pairs that scored positive in both reporter assays (LacZ expression and histidine prototrophy) are indicated as ++. Pairs that were negative in both reporter assays are scored as --. Weakly positive pairs are scored as ±±.

2.4.12 Effect of a Swd22 binding-defective mutation on Ppn1 activity *in vivo*

We queried whether the *R586A-Y588A-K589A* mutation (*RYK-AAA*) that selectively impaired Ppn1 binding to Swd22 in the 2-hybrid assay might mimic the synthetic lethal phenotypes of *swd22Δ*, which are identical to those of *ppn1Δ* [6]. I found that *ppn1-(RYK-AAA*) was lethal with *ssu72-C13S* and very sick when paired with *ctf1Δ, pin1Δ, CTD-Y1F, or CTD-T4A* (Figure 17).

2.5 Discussion

Our aim in this study was to dissect the functional, physical, and genetic interactions of the fission yeast DPS (Dis2•Ppn1•Swd22) complex by focusing on its Ppn1 subunit, which mediates association of DPS with the core CPF assembly [1]. Functional output of DPS activity was gauged by transcriptional profiling of *ppn1Δ*, *swd22Δ*, and *dis2Δ* mutants. Drs. Garg and Schwer thereby defined limited but highly concordant sets of protein-coding genes, representing ≤2% of the 5118 annotated fission yeast coding transcripts, that were up-regulated or down-regulated in *ppn1Δ* and *swd22Δ* cells (70–75% overlap). 70% of the *ppn1Δ*/*swd22Δ* up-regulated mRNAs were coordinately up in *dis2Δ* cells; 43% of the *ppn1Δ/swd22Δ* down-regulated mRNAs were down-regulated in *dis2Δ* cells. These transcriptomic data resonate with the DPS genetics, whereby *ppn1Δ* and *swd22Δ* display an identical spectrum of synthetic lethalities, which is broader than that of *dis2Δ* [6,7]. All three DPS null mutants are synthetically lethal with the phosphatase-dead alleles of CPF core subunit Ssu72 [6] and we see here that there was extensive overlap of the *ppn1Δ/swd22Δ* transcriptome with that of *ssu72-C13S* cells. The connection between the RNA-seq data and DPS function in 3' processing and transcription termination was apparent in the case of the mRNAs of phosphate homeostasis genes *pho1* and *pho84*, which were sharply down-regulated in *DPSΔ* cells. The *PHO* genes are under repressive control by transcription of upstream flanking lncRNAs [17] and the steady-state levels of these transcripts (as gauged by Northern blot and primer extension assays), as well as cellular Pho1 activity, are hyper-repressed in *DPSΔ* and other

genetic backgrounds in which 3' processing and transcription termination are negatively affected [6,7]. A previous study that employed tiling array hybridization to analyze the transcriptome of *swd22Δ* cells indicated that 38 protein-coding transcripts were down-regulated by at least 2-fold *vis-à-vis* wild-type cells during growth at 34°C [1], of which 16 overlapped with the down-regulated set of 57 mRNAs determined here by genome-wide RNA-seq. The overlapping *swd22Δ* down-regulated genes in the microarray and RNA-seq data sets include *pho1, pho84, ecl3* (adjacent to *pho84*), and *gep4*.

Essential and inessential modules of the 710-aa Ppn1 protein were defined here by testing the effects of N- and C-terminal Ppn1 truncations in multiple genetic backgrounds in which Ppn1 is required for fission yeast growth. Ppn1 mutants were also tested for their effect on Pho1 expression, which provides a sensitive read-out of mutational effects on 3' processing and transcription termination [6]. The N-terminal 172-aa disordered region of Ppn1 was dispensable in all assays of Ppn1 essentiality and deleting the disordered N-terminus alleviated hypomorphic phenotypes caused by deleting the C-terminal segment from aa 640–710. Assaying steady-state levels of the Ppn1 protein in the mutant strain by Western blotting with anti-Ppn1 antibody implicated the disordered N-terminus as a likely instability determinant.

We were especially interested in the functional contributions of the predicted well-folded TFIIS-like domain of Ppn1. The effects of deleting the N-terminal 330-aa segment that includes the TFIIS-like domain with respect to growth were highly dependent on the genetic background that required Ppn1 for growth. For example,

loss of the TFIIS module was deleterious to *CTD-Y1F* and *CTD-S2A* cells but did not significantly affect growth of *CTD-T4A* and *pin1Δ* cells. These deleterious effects of the NΔ330 truncation were alleviated by deleting the C-terminal segment from aa 640–710 (Figure 11). Thus, whereas the need for the Ppn1 TFIIS domain for healthy growth is contingent on the state of the Pol2 transcription and co-transcriptional RNA processing machinery and the internal domain composition of Ppn1 itself, the TFIIS domain is not strictly required for viability. However, the TFIIS domain is required for de-repression of *pho1* by *CTD-S7A* mutation and perturbation of IPP dynamics that elicit precocious lncRNA termination. Considering the growth properties of the ensemble of truncation mutants (Figure 11), we can surmise that Ppn1-(386–593) represents the minimized state of the protein that can support reasonably healthy growth at 30°C in each of the genetic backgrounds tested here.

Distinct sites within Ppn1 for binding to Dis2 (spanning Ppn1 aa 506 to 532) and Swd22 (from Ppn1 aa 533 to 578) were demarcated here by yeast 2-hybrid assays. Vanoosthuyse et al. [1] had proposed that the Dis2 interaction domain of Ppn1 spans aa 501 to 555 and consists of three motifs (A, B, and C). They reported that an internally deleted version of Ppn1 (ΔABC) that lacks this region failed to interact with Dis2 in a co-IP Western assay [1]. Left untested was whether the deleted segment sufficed for Dis2 interaction; whether the ΔABC internal deletion affected Ppn1 interaction with Swd22; or whether the internal deletion disrupted Ppn1 tertiary structure. Our results define an autonomous Dis2 binding domain of Ppn1 that embraces their motifs A and B but does not include motif C. [Predicted

motif C– ^{550}ARVAFG^{555} –lies within the Swd22-binding domain of Ppn1 defined herein.] Via alanine-scanning of the Dis2 box of Ppn1, we identified Dis2 interaction-defective versions of full-length Ppn1 (that retained Swd22 interaction) and employed them to show that Dis2 binding is necessary for Ppn1 biological activity in multiple genetic backgrounds where Ppn1 is essential.

Intrigued by the findings that mutations in the Dis2-box of Ppn1 elicited more severe growth phenotypes than did deletion of Dis2 itself, I showed that the Dis2-box can also mediate binding to the Dis2 paralog Sds21. This led us to query the basis for the functional redundancy of Dis2 and Sds21 with respect to vegetative growth – whereby neither enzyme is essential but deletion of both is synthetically lethal – and for the seemingly unique function of Dis2 as a component of CPF that is essential for viability when the Ssu72 phosphatase subunit of CPF is inactivated. We focused on the potential role of the divergent Dis2 and Sds21 C-terminal tails as functional discriminators and found that the Dis2 C-terminal tail is dispensable and that a tail-less version of Sds21 can replace Dis2 when expressed from the *dis2* genomic locus. Thus, with respect to the genetic tests of function applied here, there is no essential role for the C-terminal tail, and the catalytic domain of either Dis2 or Sds21 suffices for function. While we do not exclude the possibility that there are other contexts or cellular pathways in which the C-terminal tails do contribute, a parsimonious interpretation and inference from our results is that differences in expression, or regulated expression, from the *dis2* versus *sds21* loci might account for the functional distinctions, e.g., if the *dis2* locus drives a significantly higher level of expression than the *sds21* locus. Indeed, that seems

to be the case insofar as the results of our RNA-seq analyses of wild-type fission yeast, from two independent experiments entailing six biological replicates, show that the normalized read counts for the *dis2* mRNA transcript were 4.1-fold higher than the normalized read counts for the *sds21* transcript.

Whereas alanine scanning across the Swd22-binding domain of Ppn1 was unfruitful with respect to defining single amino acids or pairs of amino acids that were essential for Ppn1•Swd22 interaction in the 2-hybrid assay, I did obtain a triple-mutant of full-length Ppn1 that interdicted Swd22 interaction and preserved Dis2 binding. This *ppn1*-(*RYK-AAA*) allele was lethal with *ssu72-C13S* and very sick with *ctf1*Δ, *pin1*Δ, *CTD-Y1F*, or *CTD-T4A*, i.e., it did not display the full severe spectrum of synthetical lethalities associated with *swd22*Δ. It is conceivable that the Ppn1 triple mutant retained a low level of Swd22 interaction in fission yeast that sufficed for unhealthy viability in tandem with *ctf1*Δ et al.

Having made headway here in clarifying physical and genetic interactions of the DPS complex, the stage is set for a more ambitious quest for: (i) a structure of the DPS complex, potentially with an active version of the Ppn1 subunit that lacks dispensable disordered segments; and (ii) definition of the interface of the DPS complex with the CPF core assembly. There are formidable challenges involved. For example, I find that Dis2 can be abundantly expressed in bacteria but is intractably insoluble and the situation is not improved by co-expressing Dis2 in bacteria with a “biologically active” truncated version of Ppn1. Further progress will hinge on: (i) purifying DPS and CPF core complexes produced in fission yeast in quantities sufficient for biochemical and structural analyses; and (ii) delineating

specific contacts between Ppn1 and CPF core (and potentially other factors involved in 3'-processing/termination), e.g., via 2-hybrid screening of a fission yeast cDNA library (fused to AD) for interactors with BD-Ppn1.

2.6 Materials and Methods

2.6.1 Transcriptome profiling by RNA-seq

All transcriptomic profiling was performed by Angad Garg. RNA was isolated from *S. pombe* wild-type, *ppn1Δ*, *swd22Δ*, and *dis2Δ* cells (6) grown in liquid YES medium at 30°C to an A_{600} of 0.5 to 0.6. Cells were harvested by centrifugation and total RNA was extracted via the hot phenol method. The integrity and quantity of total RNA was gauged with an Agilent Technologies 2100 Bioanalyzer. The Illumina TruSeq stranded mRNA sample preparation kit was used to purify poly(A)$^+$ RNA from 500 ng of total RNA and to carry out the subsequent steps of poly(A)$^+$ RNA fragmentation, strand-specific cDNA synthesis, indexing, and amplification. Indexed libraries were normalized and pooled for paired-end sequencing performed by using an Illumina NovaSeq 6000 system. FASTQ files bearing paired-end reads of length 51 bases were mapped to the S. pombe genome using HISAT2-2.1.0 with default parameters [41]. The resulting SAM files were converted to BAM files using Samtools [42]. Count files for individual replicates were generated with HTSeq-0.10.0 [43] using exon annotations from Pombase (GFF annotations, genome-version ASM294v2; source 'ensembl'). RPKM analysis and pairwise correlations (S1 and S2 Figs) were performed as described previously [21]. Differential gene expression and fold

change analysis was performed in DESeq2 [44]. Cut-off for further evaluation was set for genes that had an adjusted p-value (Benjamini-Hochberg corrected) of ≤0.05 with an average normalized count of ≥100 in either mutants or wild-type datasets, and that were up or down by at least two-fold in comparison to wild-type.

2.6.2 Allelic exchange at the ppn1 locus

Ana Sanchez, Angad Garg, and Beate Schwer assisted in or performed many of the experiments presented in this section. Strains harboring marked wild-type and mutated *ppn1* alleles were constructed as follows. An integration cassette for wild-type *ppn1* consisted of five elements in series from 5' to 3': (i) a 514-bp segment of genomic DNA 5' of the *ppn1*$^+$ start codon; (ii) an open reading frame (ORF) encoding Ppn1; (iii) a 268-bp segment including polyA/termination signals from the *nmt1*$^+$ gene 3' of the *nmt1*$^+$ stop codon, (iv) a *hygMX* gene conferring resistance to hygromycin; and (v) a 486-bp segment of genomic DNA 3' of the *ppn1*$^+$ stop codon. PCR with mutagenic primers was used to introduce truncation and missense mutations into the *ppn1* ORF and mutated DNA restriction fragments were inserted in the integration cassette in lieu of the wild-type *ppn1* ORF. All inserts were sequenced to exclude the presence of unwanted mutations. The integration cassettes were transfected into diploid *S. pombe* cells. Hygromycin-resistant transformants were selected and correct integrations at the target locus were confirmed by Southern blotting. A segment of the *ppn1*::*hygMX* allele was amplified by PCR and sequenced to verify that the desired mutations were present. The heterozygous diploids were then sporulated and hygromycin-resistant haploids were isolated.

2.6.3 Mutational effects on fission yeast growth

Cultures of *S. pombe* strains were grown in YES liquid medium until A_{600} reached 0.6–0.8. The cultures were adjusted to A_{600} of 0.1 and 3 µl aliquots of serial 5-fold dilutions were spotted on YES agar. The plates were photographed after incubation for 2 days at 34°C, 2.5 days at 30°C and 37°C, 4 days at 25°C, and 6 days at 20°C.

2.6.4 Tests of mutational synergies

Standard genetic methods were employed to generate haploid strains harboring mutations/deletions in two differently marked genes (Supplemental Table 3). In brief, pairs of haploids with truncation, missense, or null mutations were mixed on malt agar to allow mating and sporulation and then the mixture was subjected to random spore analysis. Spores (~1,500) were plated on YES agar and on media selective for marked mutant alleles; the plates were incubated at 30°C for up to 5 days to allow slow-growing progeny to germinate and form colonies. At least 500 viable progeny were screened by replica-plating for the presence of the second marker gene, or by sequentially replica-plating from YES to selective media. A finding that no haploids with both marker genes were recovered after 6 to 8 days of incubation at 30°C was taken to indicate synthetic lethality. By sequentially replica-plating and gauging the numbers of colonies at each step, we ensured that wild-type (unmarked) and the differentially marked single mutant alleles were recovered at the expected frequencies. Growth phenotypes of viable double-mutants were assessed in parallel with the individual

mutants and wild-type cells at different temperatures (20°C to 37°C) as described above.

2.6.5 Acid phosphatase activity

Cells were grown at 30°C in YES liquid medium. Aliquots of exponentially growing cultures were harvested, washed with water, and resuspended in water. To quantify acid phosphatase activity, reaction mixtures (200 µl) containing 100 mM sodium acetate (pH 4.2), 10 mM *p*-nitrophenyl phosphate, and cells (ranging from 0.01 to 0.1 A_{600} units) were incubated for 5 min at 30°C. The reactions were quenched by addition of 1 ml of 1 M sodium carbonate, the cells were removed by centrifugation, and the absorbance of the supernatant at 410 nm was measured. Acid phosphatase activity is expressed as the ratio of A_{410} (*p*-nitrophenol production) to A_{600} (cells). The data are averages (± SEM) of at least three assays using cells from three independent cultures.

2.6.6 Yeast 2-hybrid assays of Ppn1 interaction with Dis2, Swd22, and Sds21

Assays were performed using reagents from Clontech as described [45]. The full-length Ppn1, Swd22, and Dis2 ORFs were cloned into pACT2.1 and pAS2-1 to generate Gal4 Activation Domain (AD) and Gal4 DNA-Binding Domain (BD) fusion proteins, respectively. The Sds21 ORF was cloned into pAS2-1. AD and BD plasmids were introduced pairwise into *S. cerevisiae Y190* cells (*MATa, ura3-52, his3-200, ade2-101, lys2-801, trp1-901, leu2-3*

112, gal4Δ, gal80Δ, cyhr^{2}*, LYS2:: GAL1*$_{UAS}$*-HIS3*$_{TATA}$*-HIS3, MEL1*

URA3:: GAL1$_{UAS}$*-GAL1*$_{TATA}$*-lacZ*) and transformants were selected for growth on

SD-Trp⁻Leu⁻agar plates. X-gal assays were performed as follows. Four independent transformants were patched onto -trp-leuD plates and grown overnight at 30°C. Cells were filter-lifted from plates onto Whatman filter paper (No. 50) and immediately flash-frozen in liquid nitrogen. Filters were placed on Whatman paper (No. 3) saturated with X-gal solution (60 μM Na_2HPO_4, 40 μM NaH_2PO_4, 10 μM KCl, 1 μM $MgSO_4$, 40 mM β-mercaptoethanol, 0.24 mg/mL X-gal) and incubated at 30°C for up to 6 h, then dried in a chemical hood. Cell patches that appeared blue after drying were deemed positive; those that remained white were deemed negative. Histidine prototrophy was evaluated by streaking cells to permissive (-trp-leuD), and restrictive (-trp-leu-hisD, -trp-leu-hisD + 25 mM 3AT [3-amino-1,2,4-triazole], and -trp-leu-hisD + 50 mM 3AT) conditions. Streaked cells that grew on -trp-leu-hisD + 50 mM 3AT were scored as positive for 2-hybrid interaction while those that did not grow in restrictive conditions were scored as negative.

2.6.7 Anti-Ppn1 antibody

A cDNA encoding Ppn1-(173–496) was amplified by PCR and cloned into a pET-28(b)-derived vector to generate plasmid pET-His_{10}Smt3-Ppn1-(173–496) for expression of the fusion protein His_{10}Smt3-Ppn1-(173–496). A 1-liter culture of BL21(DE3)Codon$^+$ pET-His_{10}Smt3-Ppn1-(173–496) was grown at 37°C in LB medium containing 50 μg/ml kanamycin and 25 μg/ml chloramphenicol until A_{600} reached 0.5. The culture was then adjusted to 2% (v/v) ethanol and chilled to 4°C for 30 min. Ppn1-(173–496) expression was induced by the addition of IPTG to a final concentration of 0.5 mM and incubating the culture overnight at

17°C. Cells were harvested by centrifugation and resuspended in lysis buffer containing 500 mM NaCl, 50 mM Tris-HCl pH 8.0, 10% glycerol, 10 mM imidazole, 0.5 mM PMSF. All subsequent purification procedures were performed at 4°C. Cell lysis was achieved by adding lysozyme to 0.2 mg/ml and incubation for 1 h, followed by sonication to reduce viscosity. The lysate was centrifuged at 40,000g for 45 min and the supernatant was applied to a 5-ml Ni-NTA-agarose column that had been equilibrated in lysis buffer. The resin was washed twice with 50 ml of lysis buffer containing 20 mM imidazole. His_{10}Smt3-Ppn1-(173–496) was eluted with lysis buffer containing 300 mM imidazole. The His_{10}Smt3 tag was cleaved by treatment with Ulp1 protease during overnight dialysis against lysis buffer. Ppn1-(173–496) was separated from His_{10}Smt3 by a second round of Ni-affinity chromatography, during which Ppn1-(173–496) was recovered in the flow-through fraction. Purified Ppn1-(173–496) was concentrated by centrifugal ultrafiltration to 2 mg/ml.

Rabbit immunization with purified Ppn1-(173–496) and preparation of antiserum were performed by Pocono Hills Rabbit Farm and Laboratory (Canadensis, PA) according to their 70 Day Antibody Production Protocol. Anti-Ppn1 antibody was purified from 5 ml of rabbit serum by affinity chromatography as follows. 2 mg of purified Ppn1-(173–496) was dialyzed against coupling buffer (500 mM NaCl, 50 mM HEPES pH 7.9, 5% glycerol) and then coupled to 3 ml of Affigel-10 resin (BioRad) by incubation overnight at 4°C. The resin was washed serially with 100 mM Tris-HCl (pH 7.4); 200 mM glycine (pH 2.6); 1 M Tris-HCl (pH 7.4); and 150 mM NaCl in 20 mM Tris-HCl (pH 7.4). The antigen-coupled resin

was then mixed with 5 ml of rabbit immune serum overnight at 4°C on a nutator. The resin was poured into a column and washed thoroughly with TBS (150 mM NaCl, 10 mM Tris-HCl pH 7.5) until no further protein was eluted. Bound antibodies were then eluted with 200 mM glycine (pH 2.6). Fractions (0.5 ml) were collected in tubes containing 50 µl of 1 M Tris-HCl (pH 8.3) to adjust to pH 7.5. Protein-containing eluate fractions were pooled and dialyzed against buffer containing 50 mM NaCl, 200 mM Tris-HCl (pH 7.5), 0.1 mM EDTA, 0.1 mM β-mercaptoethanol, 5% glycerol.

2.6.8 Western blotting

Fission yeast cells were grown at 30°C in liquid YES medium until A_{600} reached 0.6 to 0.8. Aliquots (10 ml) of cells were collected by centrifugation and washed with cold 20% trichloroacetic acid (TCA) and washed cell pellets were frozen at –80°C. The cells were resuspended in cold 20% TCA and disrupted by vortexing with glass beads for 3 min at 4°C. Cellular material was separated from beads by low-speed centrifugation, and additional material was recovered by washing beads with one volume 5% TCA. Cellular material was supplemented with one volume of 5% TCA and precipitated by high-speed centrifugation. The precipitate was washed with ice-cold ethanol and resuspended in 1 M Tris-HCl, pH 8.0. Protein concentration was measured according to absorbance at 280 nm using a NanoDrop 2000 spectrophotometer. Samples were heated for 5 min at 95°C in SDS buffer and then resolved by electrophoresis through a 10% polyacrylamide gel containing 0.1% SDS. Polypeptides were transferred to PVDF membranes by using an iBlot2 apparatus (Invitrogen).

Membranes were washed three times with TBST (10 mM Tris-HCl, pH 7.5, 150 mM NaCl, 0.1% Tween 20), then blocked for 16 h with 5% milk in TBST. Primary hybridization was performed with affinity-purified anti-Ppn1 diluted 1:2000 in 5% milk in TBST for 1 h at 22°C. Membranes were again washed three times with TBST. Secondary hybridization was performed with HRP-conjugated anti-Rabbit IgG (produced in donkey, GE Healthcare) diluted 1:10000 in 5% milk in TBST for 1 h at 22°C. Membranes were again washed three times with TBST. Chemiluminescence was induced by incubating membranes with freshly mixed Western Blot detection reagent (GE Healthcare) for 1 min. Membranes were immediately exposed to BioMax x-ray film (Kodak).

2.7 Supporting Information

2.7.1 Supplementary Table 1 – RNA-seq read counts for triplicate biological replicates

Sample	Total Paired Reads	Mapped Reads
WT (1)	26,820,778	25,069,976 (93%)
WT (2)	26,799,612	24,896,074 (93%)
WT (3)	24,623,533	22,981,899 (93%)
*ppn1*Δ (1)	27,074,925	25,654,708 (95%)
*ppn1*Δ (2)	21,792,674	20,210,444 (93%)
*ppn1*Δ (3)	28,302,106	26,637,590 (94%)
*swd22*Δ (1)	24,435,616	23,082,133 (94%)
*swd22*Δ (2)	24,699,951	23,577,405 (95%)
*swd22*Δ (3)	23,445,504	22,211,684 (95%)
*dis2*Δ (1)	26,747,724	25,468,701 (95%)
*dis2*Δ (2)	23,488,584	22,144,361 (94%)
*dis2*Δ (3)	24,673,733	23,340,878 (95%)

2.7.2 Supplementary Table 2 – RNA-seq data reproducibility between biological replicates

Sample pairs	Pearson Coefficient
WT (1) vs (2)	0.987
WT (2) vs (3)	0.987
WT (1) vs (3)	0.987
*ppn1*Δ (1) vs (2)	0.985
*ppn1*Δ (2) vs (3)	0.983
*ppn1*Δ (1) vs (3)	0.988
*swd22*Δ (1) vs (2)	0.984
*swd22*Δ (2) vs (3)	0.983
*swd22*Δ (1) vs (3)	0.987
*dis2*Δ (1) vs (2)	0.987
*dis2*Δ (2) vs (3)	0.987
*dis2*Δ (1) vs (3)	0.986

2.7.3 Supplementary Table 3 – Fission yeast strains used in this study

S1 Table: Fission yeast strains used in this study		
Name	Relevant Genotype	Source
JS77 (parental strain)	*ade6-m216 leu1-32 ura4-D18 his3-D1 (h–)*	[1]
JS78 (parental strain)	*ade6-m210 leu1-32 ura4-D18 his3-D1 (h+)*	[1]
AS 2387	*ppn1Δ::hygMX*	This study
AS 2428	*ppn1-(81-710)::hygMX*	This study
AS 2388	*ppn1-(173-710)::hygMX*	This study
AS 2463	*ppn1-(331-710)::hygMX*	This study
AS 2554	*ppn1-(386-710)::hygMX*	This study
AS 2555	*ppn1-(451-710)::hygMX*	This study
AS 2556	*ppn1-(488-710)::hygMX*	This study
AS 2390	*ppn1-(1-639)::hygMX*	This study
AS 2389	*ppn1-(1-606)::hygMX*	This study
AS 2464	*ppn1-(1-593)::hygMX*	This study
AS 2557	*ppn1-(1-532)::hygMX*	This study
AS 2465	*ppn1-(1-496)::hygMX*	This study
AS 2558	*ppn1-(173-639)::hygMX*	This study
AS 2559	*ppn1-(331-639)::hygMX*	This study
BB0003	*ppn1-(173-532)::hygMX*	This study
BB0001	*ppn1-(386-593)::hygMX*	This study
BB0002	*ppn1-(386-532)::hygMX*	This study
BB0004	*ppn1-(501-506A)::hygMX*	This study
BB0048	*ppn1-V508A::hygMX*	This study
BB0050	*ppn1-W510A::hygMX*	This study
BB0052	*ppn1-(D515A L516A)::hygMX*	This study
BB0054	*ppn1-(R586A Y588A K589A)::hygMX*	This study
BB0109	*rpb1-CTD-Y1F::natMX*	[2]
BB0110	*rpb1-CTD-S2A::natMX*	[3]
BB0111	*rpb1-CTD-T4A::natMX*	[2]
BB0112	*rpb1-CTD-S7A::natMX*	[2]
AS 2218	*dis2Δ::natMX*	[2]
AS 2020	*dis2Δ::ura4+*	[4]
BB0113	*sds21Δ::ura4+*	[4]
BB0114	*ctf1Δ::kanMX*	[2]
BB0115	*rhn1Δ::kanMX*	[2]
BB0116	*ssu72-C13S::kanMX*	[5]
AS612	*ssu72-C13S::natMX*	[2]
BB0117	*pin1Δ::kanMX*	[6]
BS286	*dis2-ΔC::kanMX*	This study
BS350	*dis2-(sds21-dis2)::kanMX*	This study
BS467	*dis2-(sds21-ΔC)::natMX*	This study

2.8 Permission to reprint

This chapter was published in the journal Plos Genetics under the following citation:

Benjamin B, Sanchez AM, Garg A, Schwer B, Shuman S. Structure-function analysis of fission yeast cleavage and polyadenylation factor (CPF) subunit Ppn1 and its interactions with Dis2 and Swd22. PLoS Genet. 2021 Mar 12;17(3):e1009452. doi: 10.1371/journal.pgen.1009452. PMID: 33711009; PMCID: PMC7990198.

Chapter 3: Activities and Structure-Function Analysis of Fission Yeast Inositol Pyrophosphate (IPP) Kinase-Pyrophosphatase Asp1 and Its Impact on Regulation of pho1 Gene Expression

3.1 Abstract

Inositol pyrophosphates (IPPs) are signaling molecules that regulate cellular phosphate homeostasis in diverse eukaryal taxa. In fission yeast, mutations that increase 1,5-IP_8 derepress the *PHO* regulon while mutations that ablate IP_8 synthesis are *PHO* hyper-repressive. Fission yeast Asp1, the principal agent of 1,5-IP_8 dynamics, is a bifunctional enzyme composed of an N-terminal IPP kinase domain and a C-terminal IPP pyrophosphatase domain. Here we conducted a biochemical characterization and mutational analysis of the autonomous Asp1 kinase domain (aa 1–385). Reaction of Asp1 kinase with IP_6 and ATP resulted in both IP_6 phosphorylation to 1-IP_7 and hydrolysis of the ATP γ-phosphate, with near-equal partitioning between productive 1-IP_7 synthesis and unproductive ATP hydrolysis under optimal kinase conditions. By contrast, reaction of Asp1 kinase with 5-IP_7 is 22-fold faster than with IP_6 and is strongly biased in favor of IP_8 synthesis versus ATP hydrolysis. Alanine scanning identified essential constituents of the active site. We deployed the Ala mutants to show that derepression of *pho1* expression correlated with Asp1's kinase activity. In the case of full-length Asp1, the activity of the C-terminal pyrophosphatase domain stifled net phosphorylation of the 1-position during reaction of Asp1 with ATP and either IP_6 or 5-IP_7. We report that inorganic phosphate is a concentration-dependent

enabler of net IP_8 synthesis by full-length Asp1 *in vitro*, by virtue of its antagonism of IP_8 turnover.

3.1.1 Importance

Expression of the fission yeast phosphate regulon is sensitive to the intracellular level of the inositol pyrophosphate (IPP) signaling molecule 1,5-IP_8. IP_8 dynamics are determined by Asp1, a bifunctional enzyme comprising N-terminal IPP 1-kinase and C-terminal IPP 1-pyrophosphatase domains that catalyze IP_8 synthesis and catabolism, respectively. Here, we interrogated the activities and specificities of the Asp1 kinase domain and full length Asp1. We find that reaction of Asp1 kinase with 5-IP_7 is 22-fold faster than with IP_6 and is strongly biased in favor of IP_8 synthesis versus the significant unproductive ATP hydrolysis seen during its reaction with IP_6. We report that full-length Asp1 catalyzes futile cycles of 1-phosphate phosphorylation by its kinase component and 1-pyrophosphate hydrolysis by its pyrophosphatase component that result in unproductive net consumption of the ATP substrate. Net synthesis of 1,5-IP_8 is enabled by physiological concentrations of inorganic phosphate that selectively antagonize IP_8 turnover.

3.2 Introduction

Inositol pyrophosphates (IPPs) IP_7 and IP_8 are signaling molecules that figure prominently in eukaryal phosphate homeostasis, a transcriptional response to phosphate availability in which genes involved in extracellular phosphate acquisition are upregulated (1–6). IP_8 is generated from phytic acid (IP_6) by the

sequential action of IPP kinases Kcs1/IP6K, which converts IP_6 to 5-IP_7, and Asp1/Vip1/PPIP5K, which converts 5-IP_7 to 1,5-IP_8 (7, 8). Asp1, Vip1, and PPIP5K—as they are named in fission yeast, budding yeast, and humans, respectively—are bifunctional enzymes composed of an N-terminal IPP kinase domain that synthesizes IP_8 and a C-terminal IPP pyrophosphatase domain, of the histidine acid phosphatase enzyme family, that converts IP_8 back to 5-IP_7 (9, 10). Asp1/Vip1/PPIP5K can also phosphorylate IP_6 to yield 1-IP_7 and de-phosphorylate 1-IP_7 back to IP_6. The isolated N-terminal IPP kinase domains of Asp1/Vip1/PPIP5K have autonomous IPP kinase activity (9–13). The Shears laboratory has conducted elegant structural and functional studies of the kinase domain of human PPIP5K isoform 2 (14).

The fission yeast phosphate homeostasis (*PHO*) regulon (15) comprises three phosphate acquisition genes—*pho1* (cell surface acid phosphatase), *pho84* (inorganic phosphate transmembrane transporter), and *tgp1* (glycerophosphate transporter)—that are repressed under phosphate-replete conditions by 5′ flanking lncRNAs *prt*, *prt2*, and *nc-tgp1*, respectively (16). lncRNA transcription across the *PHO* mRNA promoters displaces the activating transcription factor Pho7 from its DNA binding sites (16). The *PHO* regulon is derepressed in phosphate-replete cells by genetic manipulations that favor precocious lncRNA 3′-processing/termination in response to poly(A) signals upstream of the mRNA promoters (17, 18).

PHO lncRNA termination is subject to metabolite control by inositol pyrophosphates (19). A pyrophosphatase-defective *asp1-H397A* allele that

increases the level of IP_8 (9,10) derepresses the *PHO* regulon, and prompts precocious termination of *prt* lncRNA synthesis, in a manner dependent on the cleavage and polyadenylation factor complex (CPF) and transcription termination factor Rhn1. An *asp1*Δ null allele that eliminates intracellular IP_8 and 1-IP_7 results in *pho1* hyper-repression. Synthetic lethality of *asp1*Δ (no IP_8) with CPF subunit mutations suggested that IP_8 (or 1-IP_7) plays an important role in essential 3′-processing/termination events, albeit in a manner genetically redundant to CPF (19). These results established a novel action for IPPs in cell physiology as agonists of Pol2 transcription termination.

To better understand the role of 1,5-IP_8 in fission yeast, we set out here to further characterize the fission yeast Asp1 kinase responsible for its synthesis. We report that (i) reaction of purified recombinant Asp1 kinase (aa 1–385) with IP_6 and [γ^{32}P]ATP results in both IP_6 phosphorylation to ^{32}P-IP_7 and ATP hydrolysis to $^{32}P_i$; and (ii) Asp1 kinase hydrolyzes ATP in the absence of IP_6. The partitioning between “productive” IPP synthesis and “unproductive” ATP hydrolysis is sensitive to reaction conditions (e.g., pH and Mg^{2+} concentration). Reaction of Asp1 kinase with 5-IP_7 is 22-fold faster than with IP_6 and is strongly biased in favor of 1,5-IP_8 formation instead of ATP hydrolysis. A mutational analysis of Asp1 kinase, guided by the structure of the human PPIP5K2 transition-state during conversion of 5-IP_7 to 1,5-IP_8 (14), identified essential constituents of the active site. Characterization of purified recombinant full-length Asp1 shows that (i) the activity of the C-terminal pyrophosphatase domain squelches the yield of 1-IPPs during reaction with ATP and IP_6 or 5-IP_7; and (ii) pyrophosphatase inactivating mutation

H397A restores IPP synthesis. We find that inorganic phosphate is a concentration-dependent activator of net IP_8 synthesis by full-length Asp1.

3.3 Results

3.3.1 Purification of recombinant Asp1 kinase

I produced the N-terminal kinase domain of Asp1 (aa 1–385) in *E. coli* as a His_{10}Smt3 fusion and isolated the protein from a soluble bacterial extract by adsorption to a Ni-agarose column and elution with imidazole. The His_{10}Smt3 was removed by treatment with the Smt3 protease Ulp1 and the tag-free native Asp1-(1-385) protein was separated from the tag during a second round of Ni-affinity chromatography. Final purification was achieved by Superdex-200 gel filtration (Fig. 1A). The elution profile of the 44 kDa kinase polypeptide was consistent with it being a monomer in solution. In parallel, I purified a mutated version of Asp1-(1-385) in which the putative catalytic metal-binding residue Asp333 was changed to alanine (Fig. 1C).

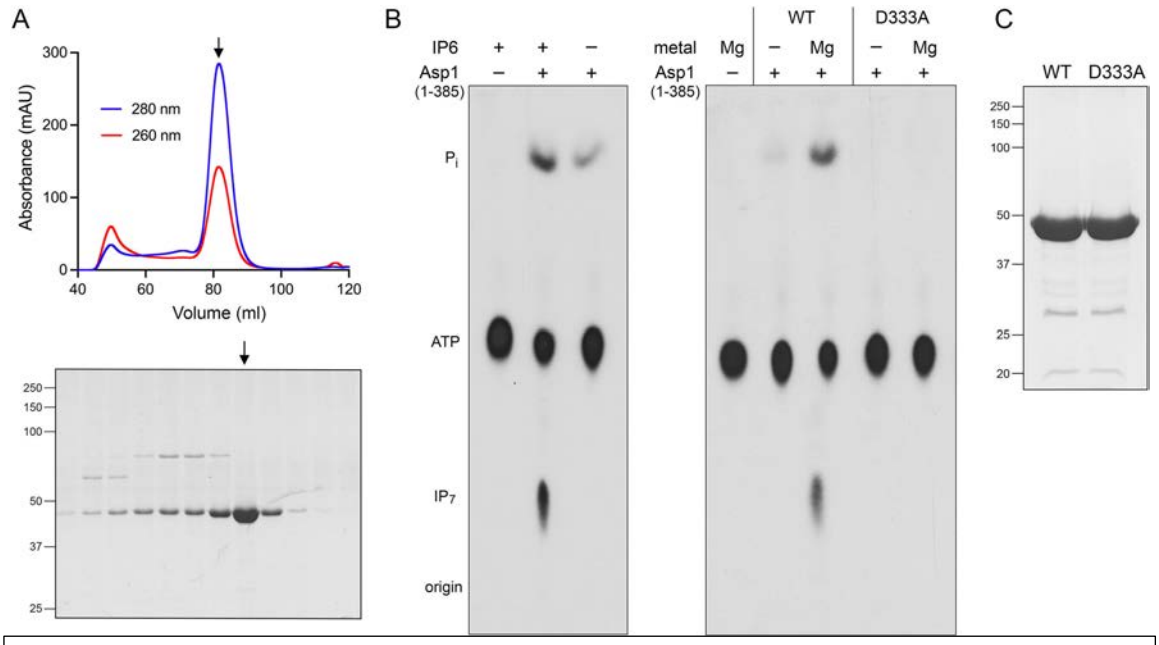

Figure 1. **IP_6 kinase and ATP phosphohydrolase activity of recombinant Asp1-(1-385).** (A) Elution profile of wild-type Asp1-(1-385) during Superdex-200 gel filtration. The top panel shows the absorbance at 280 nm (blue trace) and 260 nm (red trace) as a function of elution volume. The $A_{260} > A_{280}$ peak at 50 mL demarcates the void volume. Aliquots (5 µL) of the fractions spanning and flanking the A_{280} peak were analyzed by SDS-PAGE. The Coomassie blue-stained gel is shown. The positions and sizes (kDa) of marker proteins are indicated on the left. The fraction corresponding to the A_{280} peak containing purified Asp1-(1-385) is indicated by the vertical arrow. (B) Reaction mixtures (20 µL) containing 30 mM HEPES-NaOH (pH 6.8), 50 mM NaCl, 10 mM $MgCl_2$, 0.5 mM [γ^{32}P]ATP, 1 mM IP_6, and 2.5 µM Asp1 kinase were incubated at 37°C for 90 min. Individual reaction components were omitted where indicated by –. The products were resolved by PEI cellulose TLC and visualized by autoradiography. The chromatographic origin and the ^{32}P-labeled species corresponding to ATP, IP_7, and P_i are indicated on the left. (C) Aliquots (10 µg) of the peak Superdex-200 fractions of wild-type and D333A mutant Asp1 kinase preparations were analyzed by SDS-PAGE. The Coomassie blue-stained gel is shown with the positions and sizes (kDa) of marker proteins indicated on the left.

3.3.2 IP6 kinase and ATP phosphohydrolase activity

In previous studies of human PPIP5K2, kinase activity was assayed quantitatively by incubation of enzyme with cold ATP phosphate donor and ^{3}H-labeled IP_6 or IP_7 phosphate acceptor substrates, followed by HPLC anion

exchange column chromatography of the ^{3}H-labeled reaction products and liquid scintillation counting of the fractions (13). A separate assay, employing the malachite green reagent, was implemented to detect PPIP5K2-catalyzed release of inorganic phosphate from cold ATP during the kinase reaction (13). Prior studies of budding yeast Vip1 assayed kinase activity by incubation of enzyme with cold ATP and ^{32}P-labeled IP_6, followed by thin-layer chromatography (TLC) separation of the ^{32}P-labeled IP_6 and IPP reaction products (12). Here I implemented a one-pot assay that simultaneously tracked the IP_6 kinase and potential ATP phosphohydrolase activities of fission yeast Asp1-(1-385). Recombinant protein was incubated for 90 min with 0.5 mM [$\gamma^{32}P$]ATP, 1 mM cold IP_6, and 10 mM Mg^{2+}. The reactions were quenched with EDTA, and the radiolabeled products were resolved by polyethyleneimine (PEI)-cellulose TLC (Fig. 1B). The complete reaction resulted in the transfer of the labeled γ-phosphate from ATP to IP_6 to form a ^{32}P-labeled IP_7 product that migrated more slowly than ATP during TLC, consistent with its greater negative charge. No such product was generated when IP_6 was omitted (Fig. 1B, left panel). Asp1-(1-385) also effected the hydrolysis of the ATP γ-phosphate to liberate $^{32}P_i$, whether or not IP_6 was included in the reaction (Fig. 1B, left panel). The D333A active site mutation eliminated both IP_6 phosphorylation and ATP hydrolysis (Fig. 1B, right panel), signifying that both activities are intrinsic to the wild-type Asp1 protein.

3.3.3 Characterization of IP_6 kinase and ATPase activities

IP_6 kinase activity required exogenous magnesium; ATP hydrolysis (a low level of which was detectable in the absence of magnesium) was strongly stimulated by inclusion of magnesium (Fig. 1B, right panel, and Fig. 2A). Whereas ATP hydrolysis in the presence of IP_6 was optimal at 0.5 to 1 mM magnesium, IP_6 kinase activity required higher magnesium concentrations (Fig. 2A). IP_7 formation increased linearly with Mg^{2+} up to 2 mM and was optimal at 5 to 10 mM (Fig. 2A). The reasons for the higher Mg^{2+} requirement for IPP kinase activity versus ATPase can be surmised from the crystal structure of PPIP5K2 captured as a transition-state mimetic with ADP•MgF_3 and 5-IP_7 in the active site (14). This structure revealed two catalytic magnesium ions that engage the three ATP phosphates and stabilize the pentacoordinate phosphorane transition state of the γ-phosphate. The structure also disclosed two additional magnesium ions that are engaged to the IP_7 phosphate groups not directly involved in kinase reaction chemistry. One Mg^{2+} forms a hexa-hydrated complex that makes water-mediated contacts to the 2 and 3 phosphates of IP_7. Another Mg^{2+} forms a tetra-hydrated coordination complex that makes direct and water-mediated contacts to the 4 phosphate and 5 pyrophosphate groups of IP_7. These two noncatalytic Mg^{2+} complexes also make water-mediated contacts to the enzyme. We infer that the noncatalytic magnesium ions are important for productive binding of the inositol polyphosphate substrate to the kinase active site but may be irrelevant to the ATPase reaction.

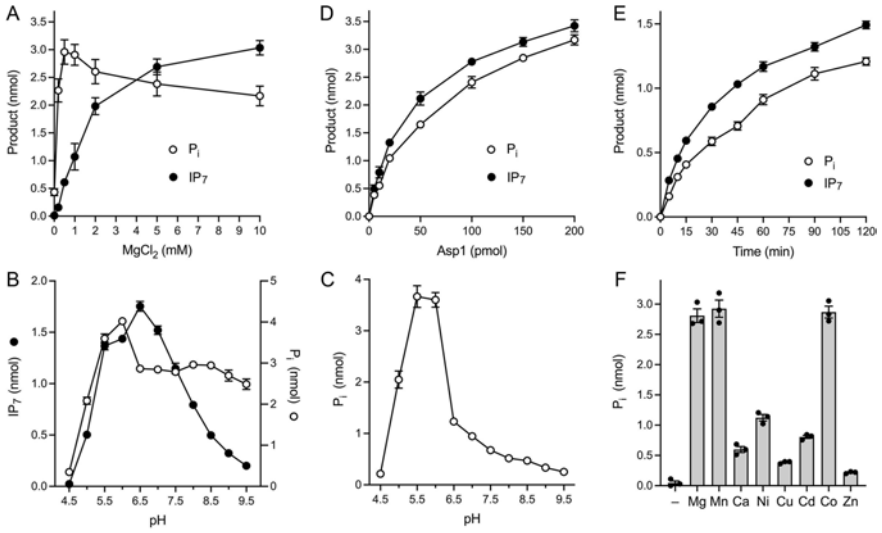

Figure 2. **Characterization of the Asp1 IP_6 kinase and ATPase activities. (A) Magnesium titration.** Reaction mixtures (20 µL) containing 30 mM Bis-Tris (pH 6.2), 50 mM NaCl, 0.5 mM (10 nmol) [γ^{32}P]ATP, 1 mM (20 nmol) IP_6, 5 µM (100 pmol) Asp1-(1-385), and magnesium as specified were incubated at 37°C for 90 min. The extents of IP_7 and P_i formation are plotted as a function of magnesium concentration. (B) pH profile. Reaction mixtures (20 µL) containing 30 mM Tris buffer (either Tris-acetate at pH 4.5, 5.0, 5.5, or 6.0; Tris-HCl at pH 6.5, 7.0, 7.5, 8.0, 8.5, 9.0, or 9.5), 50 mM NaCl, 2 mM $MgCl_2$, 0.5 mM (10 nmol) [γ^{32}P]ATP, 1 mM (20 nmol) IP_6, and 5 µM (100 pmol) Asp1-(1-385) were incubated at 37°C for 90 min. The extents of IP_7 and P_i formation are plotted as a function of pH. (C) pH profile of ATP hydrolysis in the absence of IP_6. Reaction mixtures (20 µL) containing 30 mM Tris buffer (either Tris-acetate at pH 4.5, 5.0, 5.5, or 6.0; Tris-HCl at pH 6.5, 7.0, 7.5, 8.0, 8.5, 9.0, or 9.5), 50 mM NaCl, 2 mM $MgCl_2$, 0.5 mM (10 nmol) [γ^{32}P]ATP, and 5 µM (100 pmol) Asp1-(1-385) were incubated at 37°C for 90 min. The extents of P_i formation are plotted as a function of pH. (D) Enzyme titration. Reaction mixtures (20 µL) containing 30 mM Bis-Tris (pH 6.2), 50 mM NaCl, 10 mM $MgCl_2$, 0.5 mM (10 nmol) [γ^{32}P]ATP, 1 mM (20 nmol) IP_6, and Asp1-(1-385) as specified were incubated at 37°C for 90 min. The extents of IP_7 and P_i formation are plotted as a function of input enzyme. (E) Kinetic profile. A reaction mixture (90 µL) containing 30 mM Bis-Tris (pH 6.2), 50 mM NaCl, 10 mM $MgCl_2$, 0.5 mM [γ^{32}P]ATP, 1 mM IP_6, and 5 µM Asp1-(1-385) was incubated at 37°C. At times specified, aliquots (10 µL; containing 5 nmol ATP, 10 nmol IP_6, and 50 pmol enzyme) were withdrawn and quenched immediately by adjustment to 45 mM EDTA. The extents of IP_7 and P_i formation are plotted as a function of time. (F) Divalent cation specificity for ATP hydrolysis. Reaction mixtures (20 µL) containing 30 mM Tris-acetate (pH 6.0), 50 mM NaCl, 0.5 mM (10 nmol) [γ^{32}P]ATP, 5 µM (100 pmol) Asp1-(1-385), and either no metal (–) or 2 mM the indicated divalent cation (as the chloride salt, except for $CdSO_4$) were incubated for 90 min at 37°C. The extents of P_i formation are plotted in bar graph format. All data in the graphs in panels A–F are the averages of three independent experiments ± SEM.

The effect of varying pH on the reaction of Asp-(1-385) with [γ^{32}P]ATP and IP_6 is shown in Fig. 2B. In this experiment, the Mg^{2+} concentration was adjusted to 2 mM to avoid the formation of an insoluble Mg^{2+}-IP_6 precipitate that occurred at pH ≥7.5 when the Mg^{2+} concentration was 5 mM or greater. IP_6 kinase activity displayed a bell-shaped pH curve with optimal activity between pH 5.5 and pH 7.0 in Tris buffer. ATP hydrolysis in the presence of IP_6 was optimal at pH 5.5 to 6.0 and plateaued between pH 6.5 and pH 9.5 on the alkaline side, while sharply falling off on the acidic side of the activity peak (Fig. 2B). ATPase activity in the absence of IP_6 displayed a sharper pH optimum peaking at pH 5.5 to 6.0 and tailing off steadily at higher pH values (Fig. 2C).

The extents of IP_7 and P_i product formation in IP_6-containing reactions with 10 mM Mg^{2+} at pH 6.2 increased in lockstep with the amount of Asp1-(1-385) protein added (Fig. 2D). At limiting enzyme, 5 pmol of Asp1-(1-385) generated 490 pmol of IP_7 and 390 pmol of P_i in 90 min, which translates into turnover numbers of ~1.1 min^{-1} and ~0.86 min^{-1} for kinase and ATPase activities, respectively. The kinetic profile of product formation by 5 μM Asp1-(1-385) affirmed that IP_7 and P_i accumulated in tandem (Fig. 2E). Taking the 5 min time point as indicative of initial rate, we calculated turnover numbers of 1.14 min^{-1} and 0.64 min^{-1} for the kinase and ATPase activities, respectively. At the 120 min time point in this experiment, 54% of the input [γ^{32}P]ATP substrate had been consumed and converted to IP_7 plus P_i products. Our apparent turnover number of 1.14 min^{-1} for the IP_6 kinase activity of the isolated kinase domain of fission yeast Asp1 is in the same range as the k_{cat} value of 0.6 min^{-1} reported for IP_6 kinase

activity of full length Asp1 (10) and the k_{cat} of 1.8 min^{-1} reported for IP_6 phosphorylation by the kinase domain of human PPIP5K2 (13).

To gauge the metal cofactor specificity of Asp1-(1-385), I tested various divalent cations at 2 mM concentration for their ability to support ATP hydrolysis at pH 6.0 in the absence of IP_6. (IP_6 was omitted in light of its propensity to form an insoluble precipitate in the presence of several of the transition metals that we planned to test.) Magnesium, manganese, and cobalt ions were equally adept at supporting ATPase activity (Fig. 2F). Other metal ions were less effective in descending order as follows: nickel, cadmium, calcium, copper, zinc (Fig. 2F).

3.3.4 NTP donor specificity of Asp1 kinase

To query the NTP requirement for the kinase reaction, I implemented an assay in which Asp1 was incubated for 90 min with 1 mM IP_6, 10 mM $MgCl_2$, and 5 mM cold nucleoside triphosphate (either ATP, GTP, UTP, CTP, or dATP). The reactions were quenched with EDTA and the products were analyzed by electrophoresis through a 36% polyacrylamide gel. The polyphosphorylated species were visualized by staining the gel with toluidine blue (20). Conversion of input IP_6 substrate to a slower-migrating IP_7 product depended on inclusion of both ATP (which migrated ahead of IP_6) and Asp1 kinase enzyme (Fig. 3). Whereas Asp1 kinase appeared equally adept at using 5 mM ATP and 5 mM dATP as phosphate donors, there was only scant formation of IP_7 in the presence of 5 mM GTP or CTP and no IP_7 generated in the presence of 5 mM UTP. The adenine nucleobase specificity of Asp1 kinase is consistent with the reported structure of the human PPIP5K2 homolog in complex with ATP, which highlights atomic

contacts of conserved glutamate and lysine side chains with the adenine N6 and N7 atoms, respectively (see Fig. 5B). Whereas a conserved aspartate makes bidentate hydrogen bonds to the adenosine 2′-OH and 3′-OH groups, our results anent dATP suggest that the 2′-OH interaction is not critical under the assay conditions employed (i.e., at high NTP concentration).

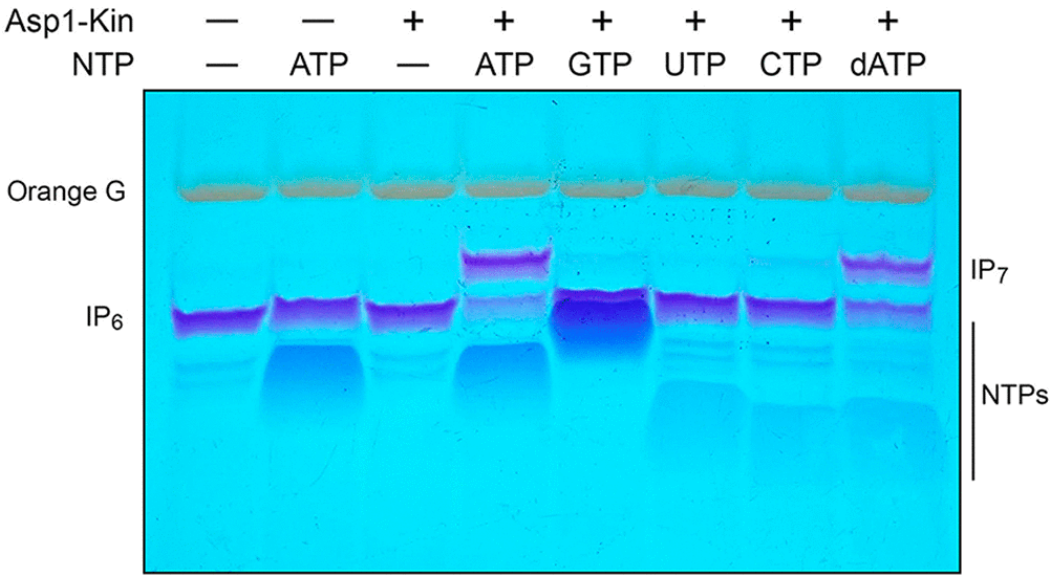

Figure 3. **NTP donor specificity of Asp1 kinase.** Reaction mixtures (20 µL) containing 30 mM Bis-Tris (pH 6.2), 50 mM NaCl, 10 mM $MgCl_2$, 1 mM IP_6, 5 µM Asp1-(1-385) (lanes +), and either no added NTP (–) or 5 mM ATP, GTP, UTP, CTP, or dATP as specified were incubated at 37°C for 90 min. Reaction products were analyzed by PAGE and detected by toluidine blue staining.

3.3.5 Asp1 kinase phosphorylates 5-IP7 but not 1-IP7

Asp1 kinase was reacted for 90 min with 2 mM ATP, 5 mM $MgCl_2$, and either 0.5 mM chemically synthesized 5-IP_7 or 1-IP_7 (21–23) or 0.5 mM IP_6. The Asp1 kinase products were analyzed by 36% PAGE (lanes + in Fig. 4A), in parallel with control samples containing the inositol polyphosphate substrate but lacking ATP and kinase (lanes –). Whereas Asp1 kinase catalyzed the conversion of 5-IP_7 into

a more slowly migrating IP_8 product, no such conversion was observed when the kinase was reacted with 1-IP_7 (Fig. 4A). These results affirm previous reports that Vip1/PPIP5K kinase enzymes are specific for phosphorylation at the 1-phosphate position (10, 14). (Note: the preparations of 5-IP_7 and 1-IP_7 contained additional toluidine blue-staining species as minor impurities, one of which is residual IP_6 [with which it comigrated during PAGE] and another, migrating slower than IP_7, that corresponds to an IP_7 species that was incompletely deprotected).

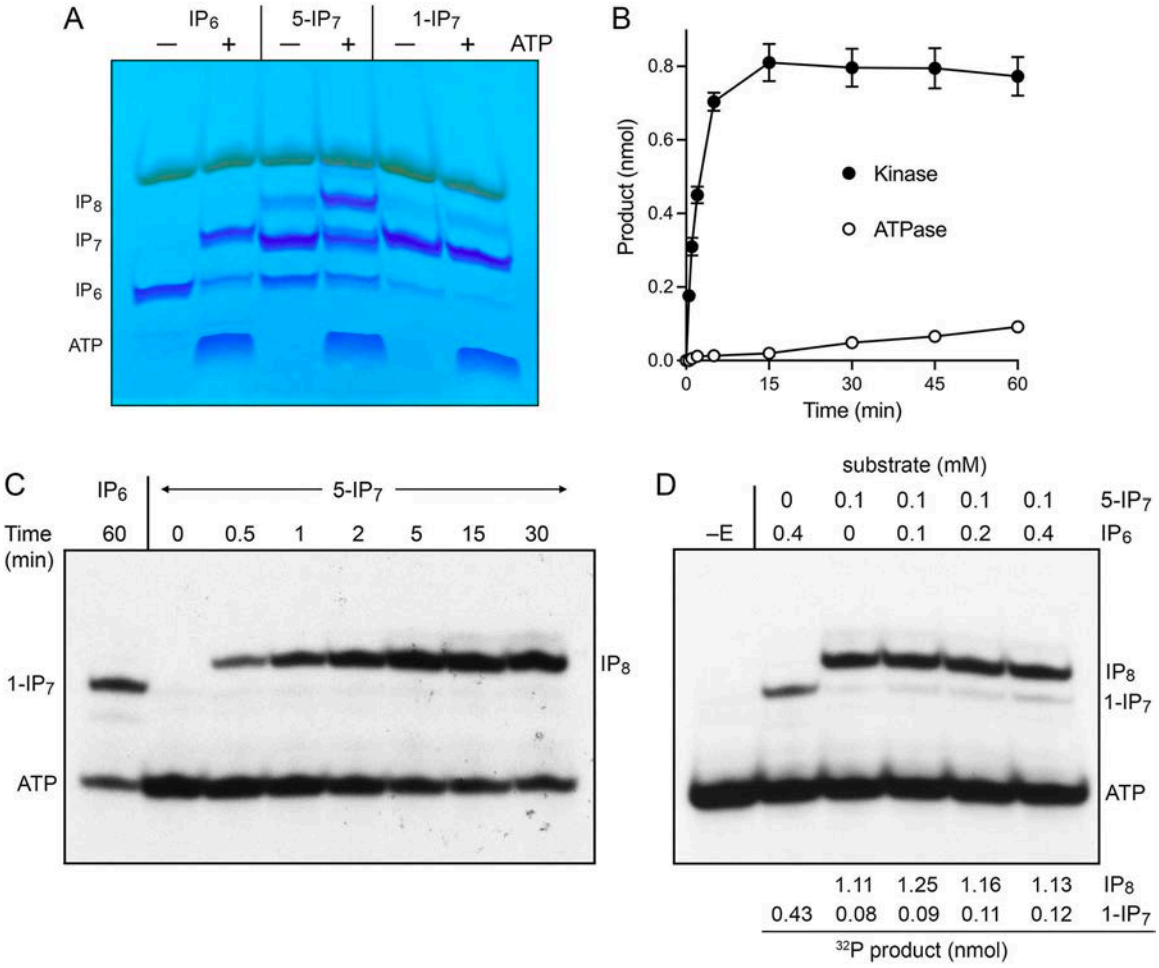

Figure 4. **5-IP_7 kinase activity.** (A) Reaction mixtures (20 µL) containing 30 mM Bis-Tris (pH 6.2), 50 mM NaCl, 5 mM $MgCl_2$, 2 mM ATP (in lanes labeled +), 0.5 mM IP_6, 5-IP_7, or 1-IP_7 as specified, and 5 µM Asp1-(1-385) were incubated at 37°C for 90 min. Reaction products were analyzed by PAGE and detected by toluidine blue staining. (B) Kinetic profile. A reaction mixture (50 µL) containing 30 mM Bis-Tris (pH 6.2), 50 mM NaCl, 5 mM $MgCl_2$, 0.25 mM [γ^{32}P]ATP, 0.5 mM 5-IP_7, and 2.5 µM Asp1-(1-385) was incubated at 37°C. At times specified, aliquots (5 µL; containing 1.25 nmol ATP, 2.5 nmol input 5-IP_7, and 12.5 pmol enzyme) were withdrawn and quenched immediately with EDTA. The products were analyzed by TLC. The extents of IP_8 formation (kinase) and P_i formation (ATPase) are plotted as a function of time. The data are averages of three independent experiments ± SEM. (C) A 5-IP_7 kinase reaction was performed as in panel B. Aliquots quenched at the times specified were analyzed by PAGE and the ^{32}P-labeled species were visualized by autoradiography. A control Asp1 kinase reaction with IP_6 as substrate was incubated for 60 min and analyzed in parallel. The positions of ^{32}P-labeled ATP substrate and the 1-IP_7 and IP_8 kinase products are indicated at left and right. (^{32}Pi runs off the bottom of the gel and is not visualized.) (D) Reaction mixtures (20 µL) containing 30 mM Bis-Tris (pH 6.2), 50 mM NaCl, 5 mM $MgCl_2$, 0.25 mM (5 nmol) [γ^{32}P]ATP, IP_6 and 5-IP_7 at the concentrations specified, and 2.5 µM (50 pmol) Asp1 kinase were incubated at 37°C for 15 min. Asp1 kinase was omitted from a control reaction (lane –E). Products were analyzed by PAGE; an autoradiograph of the gel is shown. The gel was scanned with a Typhoon FLA7000 imager and radioactivity was quantified with ImageQuant-TL. Yields of ^{32}P-labeled IP_8 and 1-IP_7 were calculated by normalizing their signal intensities to that of ATP in the no enzyme control.

To quantify Asp1 activity with 5-IP_7 as substrate, I tracked the kinetics of product formation in a reaction containing 0.5 mM 5-IP_7, 0.25 mM [γ^{32}P]ATP, 5 mM $MgCl_2$, and 2.5 µM Asp1 kinase. The products were analyzed by TLC and the extents of ATP hydrolysis to $^{32}P_i$ and of label transfer from ATP to form ^{32}P-IP_8 were plotted as a function of reaction time (Fig. 4B). Unlike the IP_6 kinetic profile documented in Fig. 2E, in which the reaction partitioned nearly equally between kinase and ATPase outcomes, the kinetic profile with 5-IP_7 was strongly biased in favor of the kinase reaction. At the 15 min time point, 65% of the input ATP was consumed in the kinase reaction versus 2% in the ATPase reaction (Fig. 4B). From the initial rate of the IP_7 kinase reaction, I calculated a turnover

number of 25.4 min^{-1}, a value 22-fold greater than the apparent rate of the IP_6 kinase reaction in Fig. 2E.

A separate analysis of the kinetic profile of the IP_7 kinase reaction was performed by subjecting the ^{32}P-labeled products to PAGE and visualization by autoradiography (Fig. 4C). This experiment showed clearly that the radiolabeled product of the IP_7 kinase reaction was IP_8, which migrated more slowly than the 1-IP_7 produced in a parallel reaction with IP_6 as the substrate (Fig. 4C).

Metabolic labeling with ^3H-inositol had revealed that the intracellular concentration of IP_6 in fission yeast is ~10-fold higher than that of 5-IP_7 (9). Therefore, it was of interest to gauge the product distribution of the Asp1 kinase reaction when the enzyme was presented with 0.25 mM [$\gamma^{32}P$]ATP and a mixture of 5-IP_7 and IP_6 as phosphate acceptors, versus 5-IP_7 or IP_6 alone. The yield of ^{32}P-IP_8 in a reaction containing 0.1 mM 5-IP_7 alone was 2.6-fold higher than the yield of ^{32}P-IP_7 in a reaction containing 0.4 mM IP_6 alone (Fig. 4D). The salient findings were that inclusion of 0.1, 0.2, or 0.4 mM IP_6 in reactions containing 0.1 mM 5-IP_7 had scant effect on the yield of ^{32}P-IP_8. To wit, 9.4-fold more IP_8 than 1-IP_7 was produced even when IP_6 was present in 4-fold excess over 5-IP_7. Thus, under competitive conditions, 5-IP_7 is the preferred kinase substrate and 1,5-IP_8 synthesis is the preferred reaction outcome.

3.3.6 Structure-function analysis by alanine scanning

I used a primary structure alignment of the human PPIP5K2 and fission yeast Asp1 kinase domains (Fig. 5A) and the atomic structure of a PPIP5K2 kinase transition state mimetic (Fig. 5B) (14) to guide an alanine scan of the Asp1 kinase

active site. The human and fission yeast kinases share 197 positions of amino acid side chain identity/similarity over the segment of Asp1 spanning aa 29 to 342 (Fig. 5A). A stereo view of the transition state structure of PPIP5K2 is shown in Fig. 5B with amino acid side chains numbered according to their identical counterparts in Asp1. The conserved active site residues that contact the ATP adenosine, the β-phosphate, and the MgF_3 mimetic of the γ-phosphate transition state are shaded gray, green, and cyan, respectively, in Fig. 5A. The amino acids that coordinate the catalytic magnesium ions and the IP_7 phosphates are shaded magenta and yellow, respectively in Fig. 5A. Here I introduced alanine in lieu of 12 Asp1-(1-385) amino acids that are predicted to engage the IP_7 phosphate acceptor, the ATP phosphate donor, and the catalytic magnesium ions. The Asp1 amino acids targeted, their counterparts in the human PPIP5K2, and their atomic contacts are compiled in Fig. 6. The recombinant Ala-mutants were produced in *E. coli* in parallel with the wild-type Asp1-(1-385). SDS-PAGE analysis of the respective peak Superdex-200 fractions is shown in Fig. 7A.

A

```
                . .  ..... .  . .... . .. ..         ... . ..... ..... .. ..
Spo   PTKRNVVGICAMDAKARSKPCRNILNRIIAEGEFEAIVFGDNMILDEAVENWPACDYLIC  88
Hsa   PERQIVVGICSMAKKSKSKPMKEILERISLFKYITVVVFEEEVILNEPVENWPLCDCLIS  99

                . . .... ..  .  .. .. ....  . .. ... . .. . .  .  .  ..
Spo   FYSSGFPLKKAEKYVELRKPFCVNDVVFQELLWDRRLVLNILDAIRVSTPQRLICSRD-G  147
Hsa   FHSKGFPLDKAVAYAKLRNPFVINDLNMQYLIQDRREVYSILQAEGILLPRYAILNRDPN  159

                 ..   ...                          .. . ... .  ........  ......
Spo   GPKINKVLEEKLRRKFGIEITEVPTPEVKMLDEDTLSVDGKIIKKPYVEKPVYGEDHNIY  207
Hsa   NPKECNLIE----------------------GEDHVEVNGEVFQKPFVEKPVSAEDHNVY  197

                .... . ...  .......  ... . ..    .. .........  .  .........
Spo   IYFPKSVGGGGRKLFRKVANKSSDYDPDLCAPRTEGSFIYEEFMNVDNAEDVKVYTVGPH  267
Hsa   IYYPTSAGGGSQRLFRKIGSRSSVYSPESNVRKT-GSYIYEEFMPTDGT-DVKVYTVGPD  255

                . ... .... ... . ..  ......   .   .. .. .. ... . .........  .
Spo   YSHAETRKSPVVDGIVRRNPHGKEIRFITNLSEEEKNMASKISIAFEQPVCGFDLLRVSG  327
Hsa   YAHAEARKSPALDGKVERDSEGKEVRYPVILNAREKLIAWKVCLAFKQTVCGFDLLRANG  315

                .... ..........   .... ....
Spo   QSYVIDVNGWSFVKDNNDYYDNAARIL  354
Hsa   QSYVCDVNGFSFVKNSMKYYDDCAKIL  342
```

B

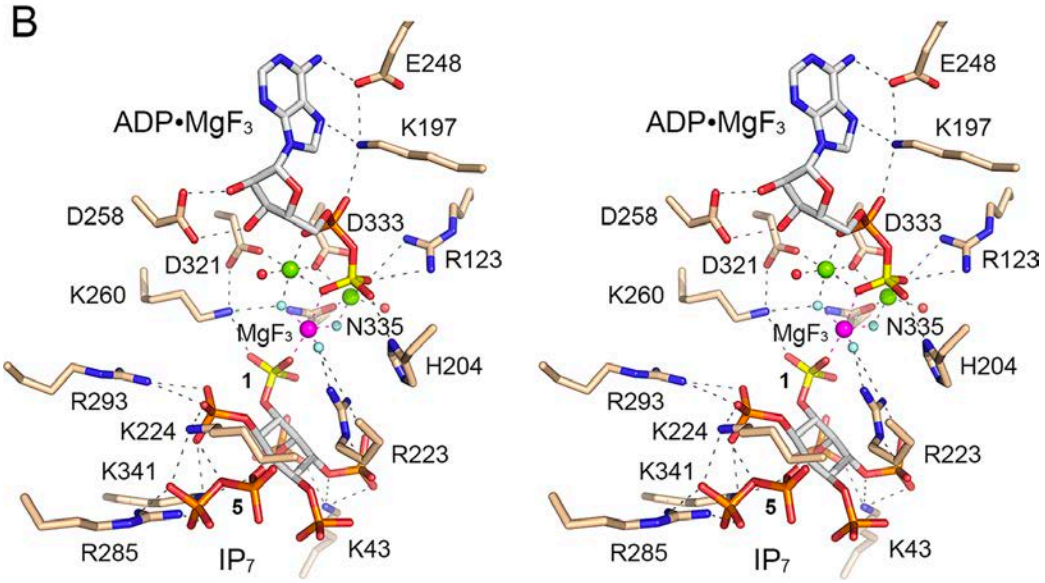

Figure 5. **Structural homology of fission yeast Asp1 and human PPIP5K2 kinase domains.** (A) The amino acid sequence of the *S. pombe* (Spo) Asp1 kinase domain is aligned to that of the *Homo sapiens* (Hsa) PPIP5K2 kinase domain. Positions of amino acid side chain identity/similarity are denoted by dots above the alignment. Gaps in the alignment are indicated by dashes. Amino acids in PPIP5K2 are highlighted in colored shading according to their contacts in the active site structure depicted in panel B. PPIPK2 residues that coordinate the two magnesium cofactors are highlighted in magenta. Residues that engage the adenosine nucleoside and the ADP β-phosphate are shaded in gray and green, respectively. Residues that coordinate the MgF_3 mimetic of the γ-phosphate transition state or the 1-phosphate of 5-IP_7 are shaded in cyan. Residues that contact the other phosphates of 5-IP_7 are highlighted in yellow. (B) Stereo view of the active site of PPIPK2 (from PDB 3T9E) as the ADP•MgF_3 transition state mimetic (MgF_3 rendered as atomic spheres with magnesium colored magenta and fluorines colored pale blue) in complex with 5-IP_7 (stick model with gray carbons) and two magnesium cofactors (green spheres). The ADP β-phosphorus and 5-IP_7 1-phosphorus atoms are colored yellow. Waters are depicted as red spheres. Amino acids are rendered as stick models with beige carbons. Amino acids are numbered according to their conserved counterparts in Asp1.

PPIP5K2	Asp1	Contacts
		IP_7
Lys54	Lys43	2-phosphate, 3-phosphate
Arg281	Arg293	6-phosphate
Lys214	Lys224	5-pyrophosphate, 6-phosphate
Arg273	Arg285	5-β-phosphate
Arg213	Arg223	3-phosphate
Lys329	Lys341	5-pyrophosphate, 6-phosphate
		ATP
His194	His204	β-phosphate
Arg134	Arg123	β-phosphate
		Mg^{2+} ions
Asp309	Asp321	Mg(1)
Asp321	Asp333	Mg(1), Mg(2)
Asn323	Asn335	Mg(2)
		Transition State
Lys248	Lys260	ATP γ-phosphate, inositol 1-phosphate
Arg213	Arg223	ATP γ-phosphate
Asn323	Asn335	ATP γ-phosphate

Figure 6. **Amino acids targeted for mutagenesis in Asp1 kinase and their conserved counterparts in human PPIP5K2.**

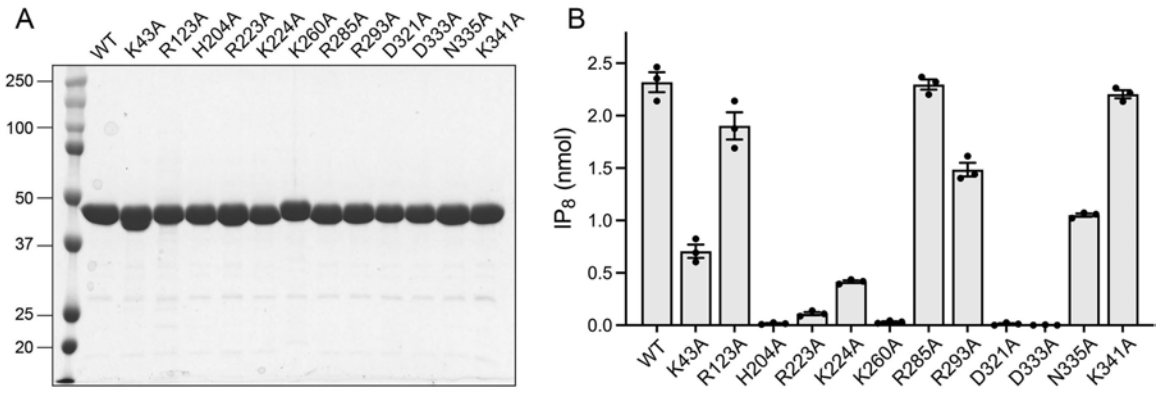

Figure 7. **Structure-guided alanine scanning mutagenesis of Asp1 kinase.** (A) Aliquots (8 µg) of wild-type Asp1 kinase domain and the indicated alanine mutants were analyzed by SDS–PAGE. The Coomassie-blue stained gel is shown. The positions and sizes (kDa) of marker polypeptides (leftmost lane) are indicated. (B) Kinase reaction mixtures (20 µL) containing 30 mM Bis-Tris (pH 6.2), 50 mM NaCl, 5 mM $MgCl_2$, 0.25 mM (5 nmol) [γ^{32}P]ATP, 0.5 mM (10 nmol) 5-IP_7, and 2.5 µM (50 pmol) of wild-type Asp1 kinase domain or the indicated alanine mutants were incubated at 37°C for 15 min. The products were analyzed by TLC. The extents of IP_8 formation are plotted for each enzyme. The data in the bar graph are the averages of three independent experiments ± SEM.

Equivalent amounts of wild-type and mutant proteins were assayed for activity with 5-IP_7 substrate (Fig. 7B). Three classes of mutational effects were observed: (i) those that eliminated IP_7 kinase activity or reduced product formation to less than 5% of wild type (H204A, R223A, K260A, D321A, and D333A); (ii) those that did not affect IP_7 kinase activity (R285A and K341A); and (iii) those that had displayed modestly reduced activity *vis-à-vis* wild type: R123A (82% of WT), R293A (64%), N335A (45%), K43A (30%), and K224A (18%) (Fig. 7B).

The essential Asp321 and Asp333 side chains are the enzymatic ligands for the two catalytic metal ions. The essential His204 coordinates the ATP β-phosphate in the human PPIP5K2 structure. The essential Lys260 coordinates the ATP γ-phosphate and the inositol 1-phosphate. The essential Arg223 coordinates the ATP γ-phosphate and the inositol 3-phosphate. It is noteworthy that Asn335,

which in the human PPIP5K2 structure coordinates the Mg(2) metal cofactor and the ATP γ-phosphate, is apparently not essential for catalysis by Asp1. Neither is Arg123, which contacts the ATP β-phosphate.

Other mutations that spare or moderately diminish Asp1 IP_7 kinase activity are mainly those that subtract predicted side chain contacts to the 5-IP_7 substrate remote from the 1-phosphate site at which chemistry occurs: Arg285, predicted to engage the 5-β-phosphate; Lys341, the 5-β-phosphate and 6-phosphate; Arg293, the 6-phosphate; Lys43, the 2- and 3-phosphates; and Lys224, the 5-β-phosphate and 6-phosphate. We suspect there is functional redundancy among the Asp1 amino acids that make atomic contacts to the same phosphate groups of the 5-IP_7 substrate. Also, the effects of subtracting a single remote phosphate contact on kinase activity (via a putative effect on affinity for 5-IP_7) might well be obscured by our assay conditions wherein the 5-IP_7 concentration (0.5 mM) greatly exceeds the reported K_m of 0.06 μM for human PPIP5K2 (13).

3.3.7 Asp1 kinase activity de-represses pho1 expression *in vivo*

Transcriptome profiling of IPP pyrophosphatase-defective *asp1-H397A* cells has delineated an IPP-responsive regulon comprising 30 protein-coding genes that were overexpressed when cellular IP_8 levels are increased (19). The "top hits" with respect to fold upregulation included the phosphate-regulated genes: *tgp1* (up 21-fold) and *pho1* (up 7-fold). Transcriptome profiling of the IPP-kinase defective *asp1-D333A* strain highlighted that phosphate homeostasis genes *pho1* and *pho84* were downregulated, by 20-fold and 14-fold, respectively, in the absence of cellular IP_8. Quantitative assay of cell surface-associated Pho1

acid phosphatase activity provides a convenient gauge of *pho1* gene expression under steady-state conditions, which recapitulates the derepression and hyper-repression of Pho1 activity in *asp1-H397A* and *asp1-D333A* mutants *vis-à-vis* wild-type cells (19). To gauge the impact of Asp1 kinase mutations *in vivo*, we established a Pho1 activity-based reporter system in which pTIN plasmids expressing wild-type or mutated versions of Asp1-(1-385) were introduced into *asp1*Δ cells. The pTIN expression vector (24) places the Asp1-(1-385) open reading frame under the transcriptional control of the *tgp1* promoter, which is situated adjacent to the transcription unit specifying the *nc-tgp1* lncRNA driven by the thiamine-repressible *nmt1* promoter. In the absence of thiamine, lncRNA transcription interferes with firing of the *tgp1* promoter. In the presence of thiamine, lncRNA synthesis is turned off and expression of the downstream mRNA—encoding Asp1-(1-385) in this case—is turned on (24).

The following experiments were performed by Dr. Angad Garg. The dynamic range of the assay was established by comparing Pho1 acid phosphatase activity of thiamine-replete *asp1*Δ cells bearing the pTIN-Asp1-(1-385) wild-type plasmid versus cells bearing the empty pTIN vector. Acid phosphatase activity was quantified by incubating suspensions of serial dilutions of the cells for 5 min with *p*-nitrophenylphosphate and assaying colorimetrically the formation of *p*-nitrophenol. Activity is expressed as the ratio of A_{410} (*p*-nitrophenol production) to A_{600} (input cells). *asp1*Δ cells with the empty pTIN vector had a Pho1 activity level of 0.6, whereas cells expressing the wild-type Asp1 kinase domain from the pTIN vector had an activity level of 157 (Fig. 8A). As a reference point, *asp1*$^{+}$ cells have a Pho1

activity level of 4.5 when grown in the same thiamine-replete ePMG liquid medium. Thus, expressing the isolated IPP kinase domain of Asp1 strongly de-repressed expression of the *pho1* gene from its native chromosomal locus.

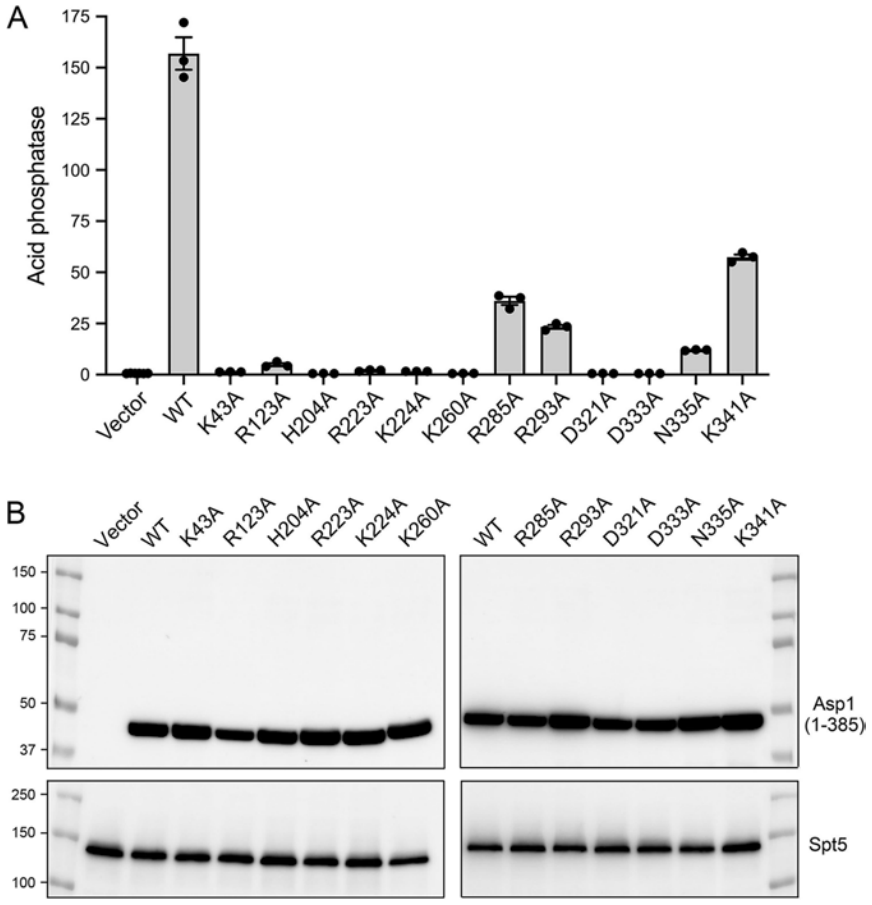

Figure 8. **Asp1 kinase activity derepresses *pho1* expression *in vivo*.** (A) Single colonies (≥20) of *asp1*Δ cells bearing either pTIN plasmids encoding wild-type or mutant Asp1 kinase domains or the empty pTIN vector were pooled and grown in Leu$^-$ ePMG with 15 μM thiamine. Aliquots of exponentially growing cultures were assayed for acid phosphatase activity. The data are averages (±SEM) of at least three independent biological replicates. (B) Western blots of whole-cell extracts prepared from *asp1*Δ cells bearing the indicated pTIN plasmids. The blots were probed with affinity-purified rabbit polyclonal antibodies recognizing Asp1 or Spt5 (as a loading control), as specified. The positions and sizes (kDa) of protein markers are indicated on the left.

3.3.8 Effect of Asp1 kinase domain mutations on pho1 expression

Western blotting of whole-cell extracts of *asp1*Δ fission yeast bearing wild-type or mutant pTIN-Asp1-(1-385) plasmids using affinity-purified anti-Asp1 antibody generated by Dr. Garg revealed that the steady-state levels of Asp1 kinase protein were similar in *asp1*Δ strains expressing wild-type and mutant Asp1 kinases, with the exception of R123A (Fig. 8B). As expected, there was no Asp1 kinase protein detected in *asp1*Δ cells bearing the empty pTIN vector (Fig. 8B). Assays of cell-surface acid phosphatase activity revealed that mutations H204A, R223A, K260A, D321A, and D333A, which abolished or nearly abolished IPP kinase activity, effaced the derepression of Pho1 when mutant proteins were expressed from pTIN plasmids (Fig. 8A). These results affirm that the IPP kinase function of Asp1 is what drives Pho1 de-repression *in vivo*.

Among the mutations that retained partial IP_7 kinase activity *in vitro*, K224A and K43A (with the lowest kinase activities) were unable to derepress Pho1 *in vivo*, whereas R285A, R293A, K341A, and N335A did derepress Pho1 (by 62-fold, 40-fold, 98-fold, and 21-fold, respectively compared to the vector control), albeit not to the degree achieved by wild-type Asp1 kinase (Fig. 8A). R123A retained partial kinase activity *in vitro* but derepressed Pho1 by only 8-fold when expressed with the pTIN system (Fig. 8A), an effect we would attribute to the apparently lower steady-state level of the R123A kinase polypeptide *vis-à-vis* wild-type and the other mutants (Fig. 8B).

3.3.9 Characterization of recombinant full-length Asp1

I produced full-length Asp1 in E. coli as a His_{10}Smt3 fusion and purified the protein from a soluble bacterial extract by sequential Ni-agarose, tag cleavage, second Ni-agarose, and gel filtration steps. The elution profile of the 105 kDa Asp1 polypeptide was consistent with it being predominantly a monomer in solution (Fig. 9). In parallel, I purified a mutated version of Asp1 in which the pyrophosphatase active site residue His397 was changed to alanine. SDS-PAGE analysis of the wild-type and H397A full-length Asp1 preparations (peak gel filtration fractions) is shown in Fig. 10A.

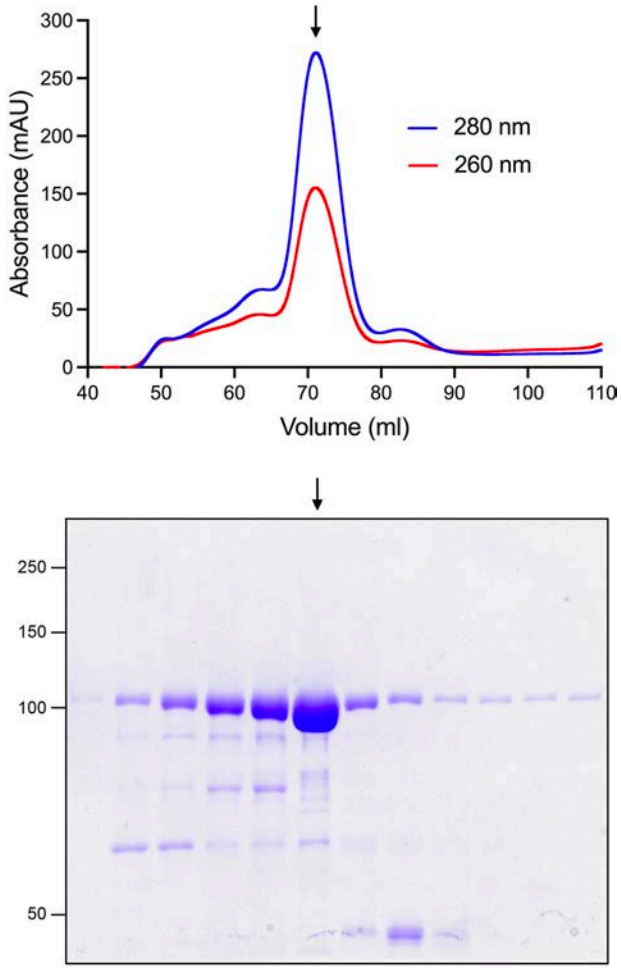

Figure 9. **Recombinant full-length Asp1.** Elution profile of wild-type Asp1 during Superdex-200 gel filtration. The top panel shows the absorbance at 280 nm (blue trace) and 260 nm (red trace) as a function of elution volume. The A_{260}=A_{280} peak at 50 mL demarcates the void volume. Aliquots (5 µL) of the fractions spanning and flanking the A_{280} peak were analyzed by SDS-PAGE. The Coomassie blue-stained gel is shown. The positions and sizes (kDa) of marker proteins are indicated on the left. The fraction corresponding to the A_{280} peak containing purified Asp1 is indicated by the vertical arrow.

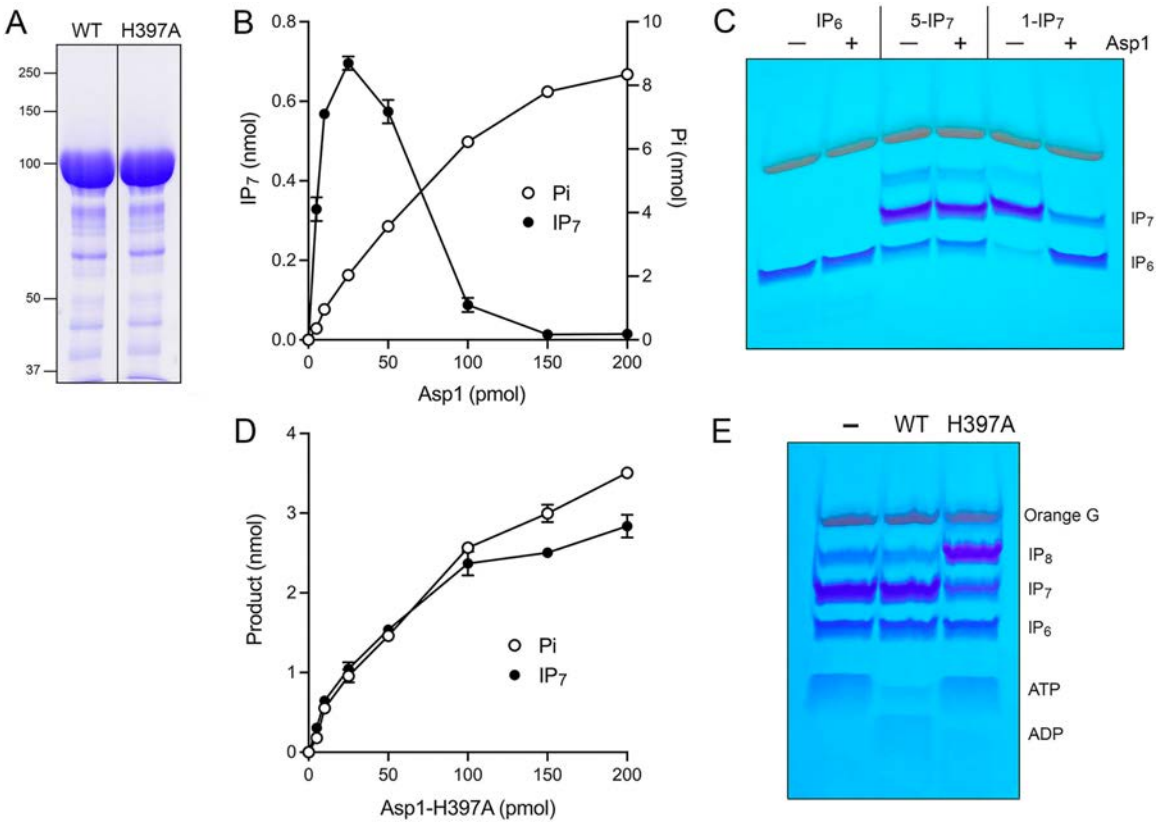

Figure 10. **Biochemical activities of full-length Asp1 and active site mutant.** (A) Aliquots (15 µg) of full-length wild-type Asp1 and H397A mutant were analyzed by SDS–PAGE. The Coomassie-blue stained gel is shown. The positions and sizes (kDa) of marker polypeptides are indicated on the left. (B) Reaction mixtures (20 µL) containing 30 mM Bis-Tris (pH 6.2), 50 mM NaCl, 10 mM $MgCl_2$, 0.5 mM (10 nmol) [γ^{32}P]ATP, 1 mM IP_6, and Asp1 as specified were incubated at 37°C for 90 min. Products were analyzed by TLC. The extents of IP_7 and P_i formation are plotted as a function of input enzyme. (C) Phosphatase reaction mixtures (20 µL) containing 30 mM Bis-Tris (pH 6.2), 50 mM NaCl, 2 mM $MgCl_2$, 0.5 mM IP_6, 5-IP_7 or 1-IP_7, and 5 µM wild-type Asp1 (lanes +) were incubated at 37°C for 30 min. Reaction products were analyzed by PAGE and detected by toluidine blue staining. (D) Kinase reaction mixtures (20 µL) containing 30 mM Bis-Tris (pH 6.2), 50 mM NaCl, 10 mM $MgCl_2$, 0.5 mM (10 nmol) [γ^{32}P]ATP, 1 mM IP_6, and Asp1-(H397A) as specified were incubated at 37°C for 90 min. The extents of IP_7 and P_i formation are plotted as a function of input enzyme. The data in panels B and D are averages of three independent experiments ± SEM. (E) IP_7 kinase reaction mixtures (20 µL) containing 30 mM Bis-Tris (pH 6.2), 50 mM NaCl, 5 mM $MgCl_2$, 0.5 mM 5-IP_7, 2 mM ATP, and 5 µM Asp1 WT or Asp1-(H397A) were incubated at 37°C for 30 min. Reaction products were analyzed by PAGE and detected by toluidine blue staining.

Assay of the wild-type Asp1 for kinase activity with IP_6 and [γ^{32}P]ATP revealed a distinctly different enzyme titration profile (Fig. 10B) compared to that of the isolated kinase domain (Fig. 2D). Formation of ^{32}P-IP_7 peaked at 25 pmol of input Asp1, at which point 7% of the input ATP ^{32}P-label was used in the kinase reaction (plotted on the left *y* axis scale in Fig. 10B) while 20% of the input ATP ^{32}P-label was converted to ^{32}P inorganic phosphate (plotted on the right *y* axis scale in Fig. 10B). Further increasing input Asp1 resulted in progressive reduction in the level of the kinase product (which was eliminated at ≥150 pmol of Asp1) as the extent of ^{32}P phosphate formation steadily increased, to 82% of the input ATP ^{32}P-label at 200 pmol Asp1 (Fig. 10B). We presume that the IPP pyrophosphatase activity resident in the C-terminal domain of Asp1 interferes with measurement of kinase activity because it effects the hydrolysis of the ^{32}P-labeled 1-IP_7 kinase reaction product.

To query the inositol pyrophosphatase activity of Asp1, I reacted the enzyme for 30 min with 0.5 mM IP_6, 5-IP_7, or 1-IP_7 in the absence of ATP. Product analysis by PAGE showed that Asp1 converted 1-IP_7 to IP_6 but did not modify either the 5-IP_7 or IP_6 substrates (Fig. 10C), thereby affirming previous findings that Asp1 is specific for hydrolysis of the phosphoanhydride bond at the 1-pyrophosphate position (25).

To evade the complications of pyrophosphatase activity on kinase detection, I assayed the Asp1-H397A pyrophosphatase mutant for kinase activity with IP_6 and [γ^{32}P]ATP and found that it generated approximately equal distributions of kinase and ATPase reaction products, both of which increased

steadily with input enzyme up to 200 pmol Asp1-H397A (Fig. 10D). PAGE-based assay of the wild-type and H397A full-length Asp1 proteins for 5-IP_7 kinase activity in the presence of excess cold ATP is shown in Fig. 10E. Wild-type Asp1 failed to produce IP_8 product and instead consumed most of the input ATP. (Note: ADP, the product of the kinase and ATPase reactions, is weakly stained by toluidine blue.) By contrast, Asp1-H397A did generate IP_8 without significantly depleting the input ATP (Fig. 10E). We surmise that full-length wild-type Asp1 churns unproductively through futile cycles of IP_8 synthesis by its kinase and decay by its pyrophosphatase.

3.3.10 Effect of inorganic phosphate on activity of full-length Asp1

Titration of full-length wild-type Asp1 for IP_7 kinase activity via TLC assay showed that formation of ^{32}P-IPP peaked at 5 pmol of input Asp1, at which point 19% of the input ATP ^{32}P-label was present as IPP while 31% of the input ATP ^{32}P-label was converted to ^{32}Pi (Fig. 11A). Increasing Asp1 progressively reduced in the level of the kinase product (which was eliminated at ≥25 pmol of Asp1) as the extent of ^{32}P phosphate formation steadily increased, to 89% of the input ATP ^{32}P-label at 50 pmol Asp1 (Fig. 11A). These results, and those in Fig. 10, suggest that net IPP synthesis by full-length Asp1 is thwarted by the action of its IPP pyrophosphatase domain. Thus, for net IP_8 synthesis by full-length Asp1 to be achieved in vivo, Asp1's IPP pyrophosphatase activity must be susceptible to modulation. In this vein, the Shears lab has reported that the pyrophosphatase activity of human PPIP5Ks was inhibited by 5 mM inorganic phosphate and that net IP_8 synthesis by PPIP5K2 was stimulated 2-fold by 5 mM P_i (26). By contrast,

IP_8 synthesis by the paralogous human IPP kinase/pyrophosphatase PPIP5K1 was insensitive to 5 mM P_i (26).

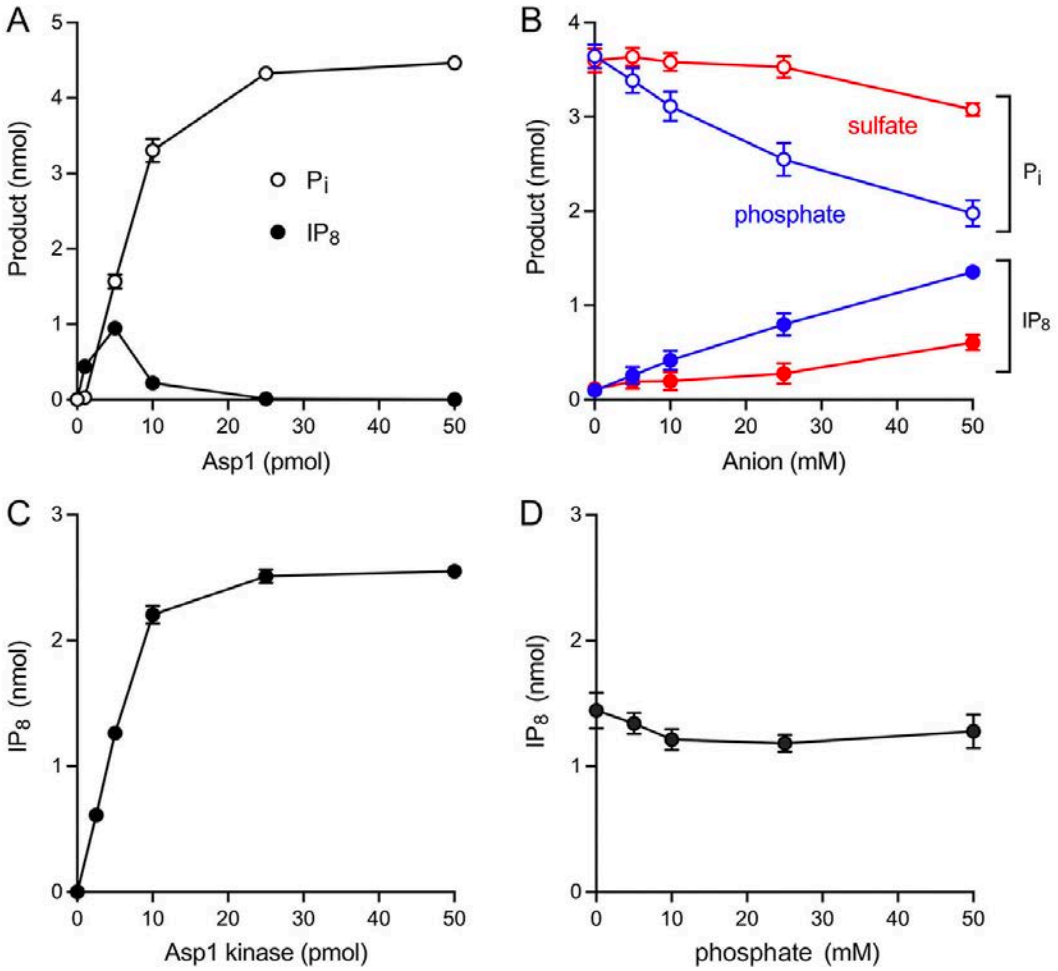

Figure 11. **Effect of inorganic phosphate on activity of full-length Asp1.** (A) Asp1 titration. Reaction mixtures (20 µL) containing 30 mM Bis-Tris (pH 6.2), 50 mM NaCl, 5 mM $MgCl_2$, 0.25 mM (5 nmol) [γ^{32}P]ATP, 0.5 mM 5-IP_7, and full-length Asp1 as specified were incubated at 37°C for 30 min. Products were analyzed by TLC. The extents of ^{32}P-IP_8 and $^{32}P_i$ formation are plotted as a function of input enzyme. (B) Effect of phosphate. Reaction mixtures (20 µL) containing 30 mM Bis-Tris (pH 6.2), 50 mM NaCl, 5 mM $MgCl_2$, 0.25 mM (5 nmol) [γ^{32}P]ATP, 0.5 mM 5-IP_7, 10 pmol full-length Asp1, and sodium phosphate (pH 6.4) or sodium sulfate (pH 6.4) as specified were incubated at 37°C for 30 min. Products were analyzed by TLC. The extents of ^{32}P-IP_8 formation (closed circles) and $^{32}P_i$ formation (open circles) are plotted as a function of phosphate or sulfate concentration. (C) Asp1 kinase titration. Reaction mixtures (20 µL) containing 30 mM Bis-Tris (pH 6.2), 50 mM NaCl, 5 mM $MgCl_2$, 0.25 mM (5 nmol) [γ^{32}P]ATP, 0.5 mM 5-IP_7, and Asp1 kinase as specified were incubated at 37°C for 15 min. Products were analyzed by TLC. The extent of ^{32}P-IP_8 formation is plotted as a function of input enzyme. The data in panels A, B, and C are averages of three independent experiments ± SEM. (D) Effect of phosphate on Asp1 kinase domain. Reaction mixtures (20 µL) containing 30 mM Bis-Tris (pH 6.2), 50 mM NaCl, 5 mM $MgCl_2$, 0.25 mM (5 nmol) [γ^{32}P]ATP, 0.5 mM 5-IP_7, 5 pmol Asp1 kinase domain, and sodium phosphate (pH 6.4) as specified were incubated at 37°C for 15 min. Products were analyzed by TLC. The extent of ^{32}P-IP_8 formation is plotted as a function of phosphate concentration. The data are the average of two independent experiments; error bars indicate the range of values.

Here I tested the effect of increasing phosphate on net synthesis of IP_8 by 10 pmol Asp1, an enzyme level at which product yield is biased toward $^{32}P_i$ versus ^{32}P-IPP. The instructive findings were that inorganic phosphate elicited a concentration-dependent shift in product formation in favor of net IPP synthesis (Fig. 11B). Compared to the no-phosphate control, supplementation with 5, 10, 25, and 50 mM phosphate increased the yields of IPP by factors of 2.7, 4.3, 8.3, and 14, respectively, concomitant with a concentration-dependent decrement in the formation of $^{32}P_i$ (Fig. 11B). Sulfate was less effective than phosphate in stimulating net IPP synthesis at the expense of P_i formation (Fig. 11B); to wit, IPP yield on addition of 10, 25, and 50 mM sulfate was 1.7-fold, 2.4-fold, and 5.3-fold that of the unsupplemented control. We regard the 8-fold stimulation of net

IP_8 synthesis by 25 mM phosphate to be physiologically relevant insofar as the intracellular concentration of inorganic phosphate in budding yeast is 23 to 25 mM (as determined by ^{31}P-NMR spectroscopy) (27).

To query the effect of phosphate on the IP_7 kinase activity of the isolated Asp1 kinase domain, I first titrated the kinase domain in reactions containing 0.25 mM [γ^{32}P]ATP and 0.5 mM 5-IP_7 to establish a suitably sensitive enzyme concentration (Fig. 11C). The yield of ^{32}P-IP_8 product during a 15 min reaction increased with input Asp1 kinase; from the slope of the titration curve, I calculated that 228 ± 5 pmol of IP_8 were formed per pmol of kinase. The effect of exogenous phosphate was assayed at 5 pmol of Asp1 kinase, a level at which half-maximal product formation was attained, thereby allowing for detection of either phosphate stimulation or inhibition of kinase activity. I found that inorganic phosphate had no impact on IP_8 product formation at up to 50 mM concentration (Fig. 11D).

3.3.11 Effect of full-length Asp1 on *pho1* expression

Dr. Angad Garg performed the following experiments. Expression of full-length wild-type Asp1 protein produced in *asp1Δ* cells via the pTIN system derepressed Pho1 activity, albeit only 57% as strongly as did the isolated kinase domain (Fig. 12A). This was to be expected given that the C-terminal IPP pyrophosphatase domain of Asp1 acts in opposition to the kinase domain and thus acts as a brake on the cellular accumulation of IP_8. Pyrophosphatase domain mutations R396A and H397A of full-length Asp1, which eliminate pyrophosphatase activity *in vitro* (9), restored Pho1 derepression to the level achieved by the isolated kinase domain (Fig. 12A). This is in keeping with my finding that the 5-

IP_7 kinase titration profile of the full-length Asp1-H397A protein (Fig. 12B) indicated a specific activity of 202 ± 8 pmol of IP_8 formed per pmol of enzyme, which was similar to the specific activity of the isolated kinase domain (Fig. 11C).

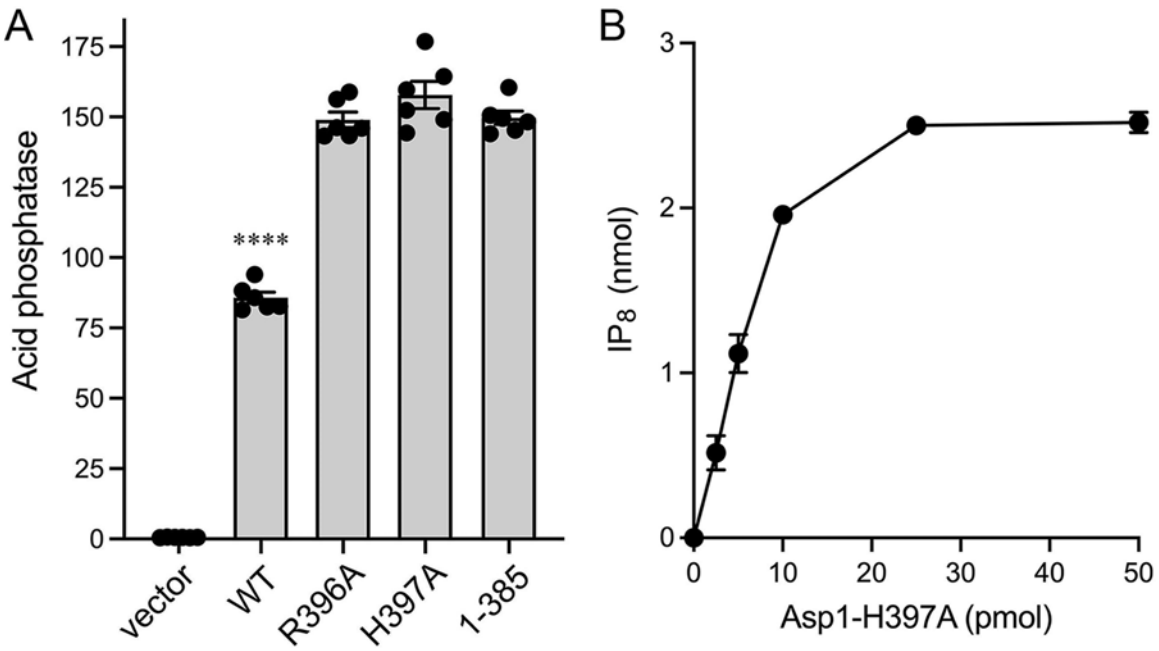

Figure 12. **Effect of full-length Asp1 on *pho1* expression.** (A) Single colonies (≥20) of *asp1*Δ cells bearing either the pTIN plasmids encoding full-length wild-type or mutant Asp1, the wild-type kinase domain (aa 1-385), or the empty pTIN vector were pooled and grown in Leu⁻ ePMG with 15 μM thiamine. Aliquots of exponentially growing cultures were assayed for acid phosphatase activity. The data are averages (± SEM) of six independent biological replicates. Whereas unpaired Welch's *t* tests of the full-length Asp1 data versus that of the kinase domain showed no significant differences between kinase domain and Asp1-H397A (*P* value 0.173) or Asp1-R396A (*P* value 0.846), the full-length wild-type Asp1 differed significantly (*P* value < 0.0001, denoted by ****). (B) 5-IP_7 kinase activity of Asp1-H397A. Reaction mixtures (20 μL) containing 30 mM Bis-Tris (pH 6.2), 50 mM NaCl, 5 mM $MgCl_2$, 0.25 mM (5 nmol) [γ^{32}P]ATP, 0.5 mM (10 nmol) 5-IP_7, and Asp1-H397A as specified were incubated at 37°C for 15 min. Products were analyzed by TLC. The extent of ^{32}P-IP_8 formation is plotted as a function of input enzyme. The data are averages of three independent experiments ± SEM.

3.4 Discussion

The results herein fortify and extend our understanding of the enzymatic properties of the bifunctional Asp1 IPP kinase-pyrophosphatase of fission yeast, an ortholog of budding yeast Vip1 and human PPIP5K. Two lines of investigation were especially informative. First, our characterization of the autonomous Asp1 N-terminal kinase domain highlighted starkly different reaction rates and outcomes when the enzyme is presented with IP_6 versus 5-IP_7 as the phosphate acceptor substrate. Second, our analysis of full-length Asp1 revealed that (i) IP_8 synthesis from 5-IP_7 is effectively futile in the face of IP_8 hydrolysis by the C-terminal pyrophosphatase component; and (ii) net synthesis of IP_8 is enabled by physiological concentrations of inorganic phosphate that selectively antagonize IP_8 turnover. As discussed below, our results have implications for IPP dynamics *in vivo* and the role of Asp1 in fission yeast phosphate homeostasis.

3.4.1 Asp1 kinase

I initiated biochemical studies of the recombinant kinase domain by utilizing commercially available IP_6 as the phosphate acceptor substrate and an assay protocol that followed the fate of the ^{32}P-labeled ATP γ-phosphate. We thereby discerned two reaction outcomes: formation of IP_7 and ATP hydrolysis, which comprise productive and unproductive modes of catalysis, respectively, with respect to IPP metabolism. Whereas the human PPIP5K2 kinase domain had been shown to hydrolyze ATP unproductively in the presence of a phosphate acceptor (13, 14), this property had not been documented previously for Asp1 (9,10). Under reaction conditions optimal for IP_6 kinase activity, we see that the Asp1 reaction

path is split almost equally between kinase and ATPase and that ATP hydrolysis does not depend on IP_6. By contrast, the ATPase of human PPIP5K2 kinase is strongly stimulated by the presence of IP_6 and other inositol phosphates (13, 14, 28). By implementing an electrophoretic assay of IP phosphorylation in the presence of cold nucleoside triphosphates, I demonstrated that Asp1 kinase is specific for ATP and dATP as the phosphate donor and either inactive or feebly active with GTP, CTP, and UTP. The adenine requirement of Asp1 is consistent with the adenine nucleobase-specific enzymatic contacts seen in the human PPIP5K crystal structure.

Key insights emerged when I deployed synthetic 5-IP_7 as the substrate for Asp1 kinase, in which case IP_8 synthesis was favored by >30-fold over the hydrolysis of ATP. Indeed, the rate of phosphorylation of 5-IP_7 by Asp1 kinase was 22-fold faster than the rate of IP_6 phosphorylation. This result resonates with findings for the human PPIP5K2 kinase domain, whereby the first-order rate constant for 5-IP_7 phosphorylation was 22-fold greater than the rate constant for IP_6 phosphorylation (14) and k_{cat}/K_m for 5-IP_7 phosphorylation was 29-fold greater than for IP_6 phosphorylation (13). I found that a strong preference of Asp1 kinase for 5-IP_7 versus IP_6 as the phosphate acceptor was maintained under competitive substrate conditions in which IP_6 was present in molar excess over 5-IP_7. My findings for Asp1 are consistent with the proposal by Shears and colleagues (29) that the synthetic path from IP_6 to IP_8 *in vivo* entails sequential conversion of IP_6 to 5-IP_7 by 5-kinases Kcs1/IP6K and phosphorylation of 5-IP_7 to IP_8 by 1-kinases Asp1/Vip1/PPIP5K.

3.4.1 Full-length Asp1

I show here that full-length Asp1 catalyzes futile cycles of 1-phosphate phosphorylation by its kinase component and 1-pyrophosphate hydrolysis by its pyrophosphatase component that result in unproductive net consumption of the ATP substrate. The H397A mutation in the pyrophosphatase active site restored net IP_8 synthesis by full-length Asp1-H397A to nearly the same specific activity as the isolated Asp1 kinase domain. A crucial finding here, inspired by studies of PPIP5K2, was that increasing concentrations of inorganic phosphate, the product of the IPP pyrophosphatase reaction, enabled net IP_8 synthesis *in vitro* by full-length wild-type Asp1. Significant activation of IP_8 synthesis was evident at 25 mM phosphate, which is the reported physiological intracellular concentration of orthophosphate in budding yeast grown in phosphate-replete medium (27). Phosphate was more effective than sulfate in reviving IP_8 synthesis by full-length Asp1. We attribute the phosphate effect to inhibition of Asp1's confounding pyrophosphatase activity, given that the IP_7 kinase activity of the isolated kinase domain was unaffected by up to 50 mM phosphate. Although we do not exclude the existence of other factors or metabolites that might regulate Asp1 activity in vivo, or of potential interdomain allostery, our findings anent phosphate *in vitro* provide a simple and plausible account of how the Asp1 can achieve net IP_8 synthesis in the cellular milieu.

3.4.1 Structure-guided mutagenesis with *in vitro* and *in vivo* readouts

Analyses of fission yeast strains bearing kinase-defective *asp1* mutant alleles (*asp1*Δ or *asp1-D333A*) that have no intracellular IP_8, and of cells with a

pyrophosphatase-defective *asp1-H397A* allele that have elevated levels of IP_8, implicate IP_8 in a variety of physiological events (9, 10, 19, 30–32). At the transcriptional level, IP_8 governs expression of the fission yeast phosphate regulon, such that Pho1 acid phosphatase is hyper-repressed in cells lacking IP_8 and overexpressed in cells with elevated IP_8 (19). Because cell surface Pho1 activity provides a quantitative gauge of the function of Asp1 kinase, we sought to correlate mutational effects on Asp1 5-IP_7 kinase activity *in vitro* with the derepression of Pho1 *in vivo* when the mutant kinase domains were expressed in *asp1*Δ cells. My alanine scan of the kinase, guided by the crystal structure of a human PPIP5K2 transition-state analog (14), identified Asp321, Asp333, Lys260, Arg223, and His204 as essential for Asp1 kinase activity *in vitro* and Pho1 derepression *in vivo*. The importance of these amino acids for catalysis is sensible insofar as the equivalent side chains in PPIP5K2 are those that bind the two metal ions, the inositol 1-phosphate, and the ATP phosphates in the transition state. Alanine scanning of PPIP5K2 had shown that Arg213 (Arg223 in Asp1) and Lys248 (Lys260 in Asp1) are essential for PPIP5K2's 5-IP_7 kinase activity (14). Dr. Garg found that expression of full-length wild-type Asp1 in *asp1*Δ cells was less potent than the Asp1 kinase domain in its extent of Pho1 derepression, presumably because the degree of IP_8 accumulation *in vivo* was attenuated by the pyrophosphate domain. Consistent with this idea, he saw that alanine mutations of pyrophosphatase active site constituents His397 and Arg396 restored derepression to the same level as the kinase domain.

Further mechanistic insights into Asp1 activity and its regulation will hinge on obtaining atomic structures of the component kinase and pyrophosphatase domains, and especially the full-length bifunctional enzyme, in complexes with reactants and products at discrete steps along the respective reaction pathways.

3.5 Materials and Methods

3.5.1 Recombinant Asp1 proteins

pET28b-His_{10}Smt3-Asp1-(1-385) plasmids encoding the Asp1 kinase domain (or alanine mutants thereof) fused to an N-terminal His_{10}Smt3 tag were transformed into *Escherichia coli* BL21(DE3). Cultures (3.2 liters for wild-type kinase or 800 mL for alanine mutants) amplified from single transformants were grown at 37°C in Terrific Broth containing 50 µg/mL kanamycin until A_{600} reached 0.8, then adjusted to 2% (vol/vol) ethanol and placed on ice for 30 min. Asp1 kinase expression was induced by adding isopropyl ß-D-1-thiogalactopyranoside (IPTG) to 0.5 mM and incubating the cultures overnight at 17°C with constant shaking. Cells were harvested by centrifugation and resuspended in buffer A (50 mM Tris-HCl pH 8.0, 500 mM NaCl, 10% glycerol) containing 10 mM imidazole and one cOmplete Protease Inhibitor Cocktail tablet (Roche) at a volume of 25 mL per L of culture. All subsequent purification procedures were performed at 4°C. Cell lysis was achieved by adding lysozyme to 0.5 mg/mL and incubating for 1 h, followed by sonication to reduce viscosity. The lysate was centrifuged at 38,000g for 45 min and the supernatant was mixed with 5 mL of Ni-NTA-agarose resin (Qiagen) that had been equilibrated in buffer A with 10 mM imidazole. After 1 h of mixing on a

nutator, the resin was recovered by centrifugation and washed twice with 50 mL of buffer A containing 20 mM imidazole. The washed resin was poured into a column and the bound protein was eluted with 250 mM imidazole in buffer A. The elution of His_{10}Smt3-Asp1-(1-385) protein was monitored by SDS-PAGE. The His_{10}Smt3 tag was cleaved by treatment with Ulp1 protease (100 µg Ulp1 per L of bacterial culture) during overnight dialysis against buffer A with 20 mM imidazole. Asp1-(1-385) proteins were separated from the His_{10}Smt3 tag by a second round of Ni-affinity chromatography, during which Asp1-(1-385) proteins were recovered in the flow-through fraction. Tag-free Asp1-(1-385) was concentrated to a volume of 5 mL by centrifugal ultrafiltration and then applied to a Hiload Superdex 200 pg 16/600 column (Cytiva Life Sciences) equilibrated in buffer B (30 mM HEPES, pH 6.8, 150 mM NaCl, 10% glycerol). The peak Superdex fraction of each Asp1-(1-385) preparation was concentrated by centrifugal ultrafiltration and stored at −80°C. Protein concentrations were determined by using the Bio-Rad dye reagent with BSA as the standard.

pET28b-His_{10}Smt3-Asp1 plasmids encoding the full-length Asp1 protein (or alanine mutants thereof) fused to an N-terminal His_{10}Smt3 tag were transformed into *Escherichia coli* BL21(DE3). IPTG induction of Asp1 expression and purification of Asp1 from soluble bacterial lysates was performed as described above for the Asp1 kinase domain.

3.5.2 TLC assay of Asp1 kinase and ATPase activity

Reaction mixtures containing 30 mM Bis-Tris (pH 6.2), 50 mM NaCl, $MgCl_2$, [γ^{32}P]ATP, IP_6 (phytic acid; Sigma P-8810-10G, lot BCBZ7573) or IP_7 (synthesized

as described in 21–23), and Asp1-(1-385) at concentrations specified in the figure legends were incubated at 37°C. Reactions were initiated by addition of Asp1 and quenched at the times specified by adjustment to 25 mM EDTA. Aliquots (2 µL) were applied to a PEI-cellulose TLC plate (Millipore-Sigma), and the products were resolved by ascending TLC with 1.7 M ammonium sulfate as the mobile phase. The radiolabeled ATP substrate and P_i and IPP products were visualized by autoradiography or visualized and quantified by scanning the TLC plate with a Typhoon FLA7000 imager and ImageQuant-TL software.

3.5.3 PAGE assay of Asp1 kinase activity

Reaction mixtures (20 µL) containing 30 mM Bis-Tris (pH 6.2), 50 mM NaCl, $MgCl_2$, ATP, and IP_6 or IP_7 as specified in the figure legends were incubated at 37°C. Reactions were terminated at the times specified by adjustment to 25 mM EDTA. The samples were mixed with an equal volume of 2× Orange G loading buffer (10 mM Tris-HCl, pH 7.0, 1 mM EDTA, 30% glycerol, 0.1% Orange G dye) and then analyzed by electrophoresis (at 4°C at 8 W constant power) through a 20-cm 36% polyacrylamide gel containing 80 mM Tris-borate, pH 8.3, 1 mM EDTA until the Orange G dye reached 2/3 of the length of the gel. The gel was briefly washed with water and then stained with a solution of 0.1% Toluidine blue (Sigma), 20% methanol, 2% glycerol, followed by destaining in 20% methanol.

3.5.4 pTIN-based expression of Asp1 in *asp1Δ* fission yeast

All *in vivo* expression assays were performed by and are presented with the permission of Angad Garg. pTIN plasmids (24) encoding the Asp1 kinase domain

(aa 1–385) or alanine mutants thereof were transfected by the lithium acetate method into *S. pombe asp1*Δ cells. Control transfection was performed with the empty pTIN vector. Transformants were selected on leu⁻ *e*nhanced *P*ombe *M*inimal *G*lutamate (ePMG) 2% agar medium with 15 µM thiamine. The recipe for 1 L of ePMG liquid medium contains the following ingredients: potassium hydrogen phthalate (3.0 g); anhydrous sodium phosphate dibasic (1.66 g); anhydrous sodium phosphate monobasic (0.46 g); glucose (20 g); adenine (0.25 g); uracil (0.25 g); glutamic acid (3.75 g); histidine (0.25 g); lysine (0.25 g); 1,000× vitamins (1 mL); 10,000× minerals (0.1 mL); 50× salts (20 mL); and Leu⁻ amino acid mix (2.5 g). The components of the vitamin, mineral, and salt stocks are as defined previously (33). The Leu⁻ amino acid mix is composed of alanine (2.8 g), arginine (1.3 g), asparagine (0.5 g), aspartic acid (2.65 g), cysteine (0.10 g), glutamine (0.1 g), glutamic acid (4.70 g), glycine (1.50 g), histidine (0.65 g), isoleucine (1.5 g), lysine (2.3 g) methionine (0.4 g), phenylalanine (1.3 g), proline (1.0 g), serine (0.8 g), threonine (0.8 g), tryptophan (0.25 g), tyrosine (0.60 g), and valine (1.75 g). The pH of ePMG is adjusted to 5.6 as needed by addition of NaOH.

3.5.5 Acid phosphatase activity

Acid phosphatase assays were performed by and are presented with the permission of Angad Garg. *S. pombe Δasp1* cells bearing pTIN plasmids were grown at 30°C in Leu⁻ ePMG liquid medium with 15 µM thiamine. Aliquots of exponentially growing cultures were harvested, washed with water, and resuspended in water. To quantify acid phosphatase activity, reaction mixtures

(200 µL) containing 100 mM sodium acetate (pH 4.2), 10 mM *p*-nitrophenylphosphate, and cells (ranging from 0.01 to 0.1 A_{600} units) were incubated for 5 min at 30°C. The reactions were quenched by addition of 1 mL of 1 M sodium carbonate, the cells were removed by centrifugation, and the absorbance of the supernatant at 410 nm was measured. Acid phosphatase activity is expressed as the ratio of A_{410} (*p*-nitrophenol production) to A_{600} (cells). The data are averages (±SEM) of at least three assays using cells from three independent cultures.

3.5.6 Asp1 antibody

The Asp1 antibody was purified by Angad Garg. These data are presented with his permission. Rabbit immunization with purified Asp1-(1–364) and preparation of antiserum were performed by Pocono Hills Rabbit Farm and Laboratory (Canadensis, PA) according to their Mighty Quick Protocol. Anti-Asp1 antibody was purified from rabbit serum by affinity chromatography as follows. Purified Asp1 kinase (4.5 mg) was dialyzed against coupling buffer (100 mM HEPES, pH 6.5, 500 mM NaCl, 5% glycerol) and then coupled to 4 mL of Affigel-10 resin (Bio-Rad) during overnight incubation at 4°C. The resin was washed serially with 100 mM Tris-HCl, pH 7.5; 200 mM glycine, pH 2.6; 1 M Tris-HCl, pH 7.5; and 20 mM Tris-HCl, pH 7.5, 150 mM NaCl. Asp1 kinase-coupled resin was then mixed with 8 mL of rabbit immune serum (adjusted to 10 mM Tris-HCl, pH 7.5) for 2 h at room temperature on a nutator. The resin was poured into a column and washed thoroughly with 10 mM Tris-HCl, pH 7.5, 150 mM NaCl until no further protein eluted, as gauged by Bio-Rad dye-binding assay of wash fractions. Bound

antibodies were eluted with 200 mM glycine, pH 2.6 while collecting fractions (1 mL) in tubes containing 100 µL of 1 M Tris-HCl, pH 7.5 to adjust the pH. Protein-containing eluate fractions were pooled, dialyzed against buffer containing 10 mM Tris-HCl, pH 7.5, 150 mM NaCl, and concentrated to 0.36 mg/mL.

3.5.7 Western blotting

Western blotting assays were performed by and are presented with the permission of Angad Garg. *S. pombe asp1Δ* cells bearing pTIN plasmids were grown at 30°C in Leu− ePMG liquid medium with 15 µM thiamine until A_{600} reached 0.6 to 0.9. Aliquots (8 A_{600} units) of cells were collected by centrifugation and resuspended in 200 µL 20% trichloroacetic acid, then supplemented with 0.7 g of 0.5 mm Zirconia beads (Biospec) and subjected to six 30-s cycles of treatment with a FastPrep-24 bead-beater (MP biomedical) at 6.5 m/s. Total acid-insoluble protein was recovered by centrifugation. The pellets were washed twice with ethanol, then air dried and resuspended in 300 µL 0.5 M Tris-HCl (pH 8.0). The samples were adjusted to 2% SDS, 10% glycerol, 10% β-mercaptoethanol and heated at 95°C for 5 min. Cell debris and insoluble material were removed by centrifugation. Aliquots of supernatant proteins (representative of 0.36 A_{600} units of cells) were resolved by electrophoresis through 8% polyacrylamide gels containing 0.1% SDS. Gel contents were transferred to a polyvinylidene difluoride (PVDF) membrane (Invitrogen). The blots were probed with affinity-purified rabbit polyclonal anti-Asp1 protein. Parallel blots were probed with anti-Spt5 antibody as a loading control. Immune complexes were detected using horseradish peroxidase-linked anti-rabbit IgG (Cytiva NA934V) and an ECL (enhanced

chemiluminescence) Western system (Cytiva) and visualized with an ImageQuant 800 apparatus (Amersham).

3.6 Permission to reprint

This chapter was published in the journal mBio under the following citation:

Benjamin B, Garg A, Jork N, Jessen HJ, Schwer B, Shuman S. Activities and Structure-Function Analysis of Fission Yeast Inositol Pyrophosphate (IPP) Kinase-Pyrophosphatase Asp1 and Its Impact on Regulation of *pho1* Gene Expression. mBio. 2022 Jun 28;13(3):e0103422. doi: 10.1128/mbio.01034-22. Epub 2022 May 10. PMID: 35536002; PMCID: PMC9239264.

Chapter 4: Crystal structure and mutational analysis of Asp1 illustrate determinants of substrate specificity and binding mechanism

4.1 Abstract

Eukaryotic phosphate homeostasis signaling is mediated by the small molecule 1,5-IP_8. The *Schizosaccharomyces pombe* enzyme Asp1 regulates levels of 1,5-IP_8 through an N-terminal kinase domain and a C-terminal phosphatase domain; Asp1 kinase activity generates 1,5-IP_8, while phosphatase activity catabolizes it. Here, we capture structural snapshots of the isolated N-terminal kinase in complex with different substrates and products. Each of our structures constitutes a 2-protomer asymmetric unit, with one protomer bound to substrate and the other protomer unbound. The unbound enzyme adopts an open conformation relative to the closed orientation observed in the pseudo-Michaelis complex, with the latter orientation more closely matching structures of Asp1 kinase's human homolog. The open and closed conformation differ in the position of two lid elements: a loop that is disordered in the apo protomer and a beta hairpin that moves 13 Å upon IPP binding. We demonstrate that the enzyme's nucleotide binding motif is flexible by capturing it in several conformations. Finally, we perform structure-guided mutagenesis of active site residues, identifying that Glu248 confers the enzyme's preference for ATP as a phosphate donor. These findings inform upon Asp1's mechanism of substrate capture and positioning, establishing a foundation for future studies into Asp1 regulation and cellular function.

4.2 Introduction

Fission yeast Asp1 is an inositol pyrophosphate (IPP) kinase/pyrophosphatase responsible for modifying cellular levels of inositol 1,5-pyrophosphate 2,3,4,6-tetrakisphosphate (1,5-IP_8). It belongs to an evolutionarily conserved family of bifunctional enzymes characterized by the presence of an N-terminal kinase domain that phosphorylates the IPP 5-IP_7 at the 1-phosphate position and a C-terminal pyrophosphatase that hydrolyzes the 1-pyrophosphate position of 1,5-IP_8 (1, 2). The cumulative effect of Asp1's kinase and pyrophosphatase activities is futile cycling between 5-IP_7 and 1,5-IP_8 with net consumption of ATP (3). The observation that 1,5-IP_8 levels fluctuate in response to environmental signals begets the inference that Asp1 must modulate its kinase and/or pyrophosphatase activities to increase or decrease 1,5-IP_8 abundance (4-7). However, mechanistic insight into regulation of Asp1 family enzymatic activity has thus far been limited.

Alternatively, the role of IPPs in cellular signaling has been thoroughly investigated. 5-IP_7 and 1,5-IP_8 are secondary messengers with pleiotropic functions, influencing apoptosis, cytoskeletal organization, and metabolism (8). Notably, phosphate homeostasis is subject to regulation by IPPs in a variety of eukaryotic organisms (7, 9, 10). In *Schizosaccharomyces pombe*, the phosphate homeostasis (*PHO*) gene program is actively repressed by transcription of upstream lncRNAs that occlude *PHO* gene promoters in cis (11). Disruption of Asp1 pyrophosphatase activity causes *PHO* lncRNAs to terminate upstream of *PHO* coding gene promoters, de-repressing the *PHO* regulon. Coupling Asp1

pyrophosphatase mutations with null mutations of cleavage and polyadenylation factors alleviates *PHO* dysregulation. Additionally, combining Asp1 pyrophosphatase mutations with other mutations that cause precocious termination is lethal. From these data, we formed a model in which cellular 1,5-IP_8 concentration tunes transcription termination sensitivity, with 1,5-IP_8 accumulation linked to precocious transcription termination and absence of 1,5-IP_8 associated with defective termination (9).

I recently performed a biochemical analysis of Asp1, with particular focus on the N-terminal 385 residues which contain the kinase activity (3). Consistent with a model proposed by Shears and colleagues in which Asp1 kinase is primarily responsible for the synthesis of 1-5-IP_8 rather than 1-IP_7 (2), we found that with 5-IP_7 served as a better phosphoacceptor substrate than did IP_6. We discerned an additional ATP phosphohydrolase activity roughly equivalent to the kinase activity against IP_6. I analyzed several putative active site mutations for *in vitro* kinase assay – these mutants were chosen based upon conservation to the kinase domain of Asp1's human homolog PPIP5K, for which several structures are available (12-14). These investigations were instructive but not exhaustive – lacking a structure of Asp1, we could not conclude that I had evaluated all relevant mutations. Furthermore, certain homologous mutations did not behave in the same manner reported by Shears and colleagues. For example, mutation to alanine of a putative phosphate-binding residue R293 resulted in roughly 40% reduction in kinase activity, whereas the analogous mutant in PPIP5K2 was effectively inactive

(activity <5% WT) (3, 12). Thus, independent solution of Asp1 kinase domain's structure can provide important insight into enzyme function.

Herein I describe six structures of Asp1 bound to a variety of substrates, substrate mimetics, and products. I find that Asp1 kinase adopts an ATP-grasp fold with a positively charged active site to accommodate negatively charged inositol phosphate ligands. The structures we solved each contained two protomers per asymmetric unit, one of which lacked bound substrates and adopted an open conformation that diverged from expectations. Our structures captured the enzyme with inositol phosphate ligands in different off-pathway orientations, which provide insight into Asp1 kinase and ATPase activities. Using these structures, I performed guided mutagenesis of additional substrate binding residues and engineered an enzyme with altered nucleotide utilization specificity.

4.3 Results

4.3.1 Crystal structure of Asp1 kinase domain in complex with IP_6, Mg^{2+}, and ADPNP

I previously performed a biochemical characterization of an Asp1 kinase domain consisting of residues 1-385. This protein readily crystallized in a variety of precipitant conditions when pre-incubated with inositol phosphate, metal, and nucleotide substrates. However, x-ray diffraction of these crystals demonstrated that they were highly mosaic and therefore unsuitable for structure solution. I therefore sought to minimize the crystallization construct by truncating unnecessary features from the N- and C-termini. Using a high confidence Phyre2

model of the Asp1 kinase domain templated on its human PPIP5K2 (pdb 3T9A), I generated a minimized kinase domain consisting of residues 31-364 (15). This protein expressed and purified well (Figure 1A), but was less soluble than its 1-385 kinase domain counterpart, the former precipitating out of solution when concentrated above 4 mg/mL as compared to the latter which tolerated concentration to at least 20 mg/ml. Both proteins demonstrated equal *in vitro* kinase activity using 5-IP_7 as a phosphoacceptor substrate (Figure 1B).

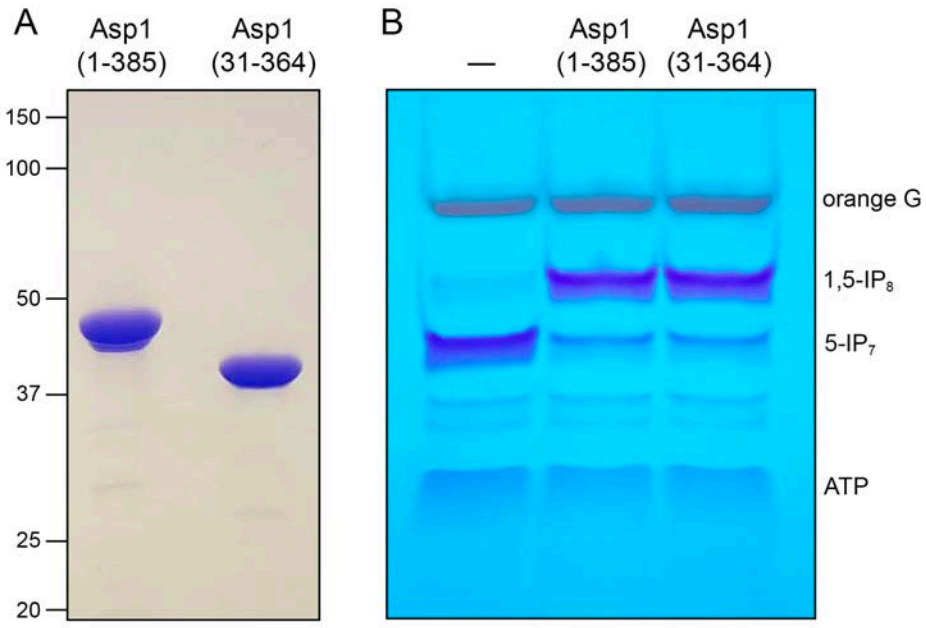

Figure 1. **Truncated Asp1 kinase domain phosphorylates 5-IP_7.** A, aliquots (5 µg) of the indicated Asp1 truncations were analyzed by SDS-PAGE. The Coomassie blue–stained gel is shown. The positions and sizes (kilodalton) of marker polypeptides are indicated on the left. B, IP_7 kinase reaction mixtures (20 µL) containing 30 mM Bis-Tris (pH 6.2), 50 mM NaCl, 5 mM $MgCl_2$, 0.5 mM 5-IP_7, 2 mM ATP, and 5 µM Asp1-(1-385) or Asp1-(31-364) were incubated at 37°C for 15 min. Reaction products were analyzed by native PAGE and detected by toluidine blue staining.

I grew crystals from a premixed solution of Asp1 kinase domain (residues 31-364) with 5 mM magnesium, 1 mM ADPNP, and 1 mM IP_6. The Asp1 crystals

diffracted X-rays to a resolution of 1.9 Å, were in space group $P2_1$, and contained two Asp1 protomers in the asymmetric unit (ASU). The structure was solved by Yehuda Goldgur as described under the Experimental procedures section and summarized in Supplemental Table 1. Phasing information was gained by molecular replacement (MR) using a Phyre2 model of Asp1 protein templated from the human homolog PPIP5K2 (pdb 4NZM) (15). The refined model (R/R_{free} = 0.197 / 0.226) comprised a continuous polypeptide from Asn33 to Glu362 in the first polypeptide and a disrupted polypeptide from Asn33–Arg274 and Ile295–Glu362.

The primary, secondary, and tertiary structures of Asp1 kinase bound to IP_6, ADPNP, and one Mg^{2+} ion are shown in Figure 2. Asp1 kinase is composed of 18 β-strands, 8 α helices, and four 3_{10} helices, which are displayed over the amino acid sequence. A protein topology map is presented in Figure 3 (16). The overall structure is that of a flattened disc of dimensions 74.1 Å x 53.3 Å x 36.7 Å. Asp1's core consists of two antiparallel β-sheets (with sheet 1 topology β12↑•β11↓•β10↑•β9↓•β13↑•β5↓ and sheet 2 topology β16↓•β15↑•β14↓•β17↑•β18↓, shown top to bottom, front to back according to orientation in Figure 2) characteristic of the ATP-grasp family. The fold is stabilized by several salt bridges (Lys275-Asp280, Lys260-Asp321, Arg123-Asp333, Glu196-Arg240, Lys197-Glu248, Lys228-Asp231, Lys220-Asp233, Glu302-Arg324). The entrance to the active site is rich with positively charged residues, as demonstrated by an electrostatic surface diagram (Figure 2, lower right panel).

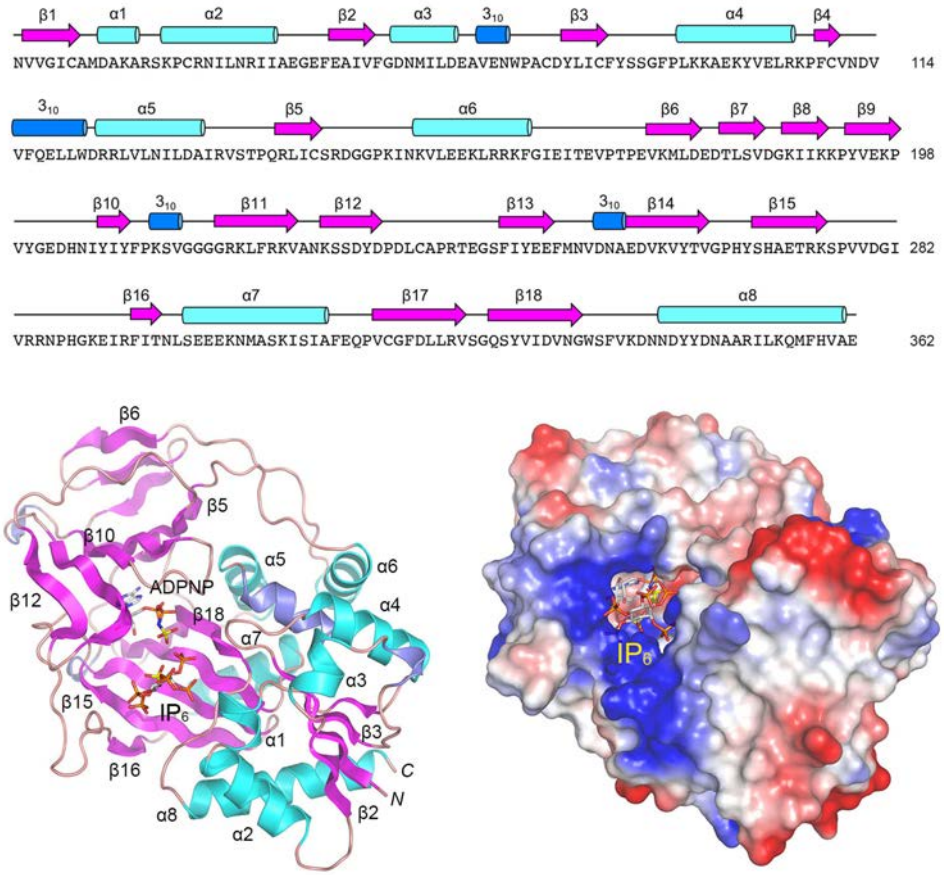

Figure 2. **Structure of Asp1 kinase bound to ADPNP, IP6, and Mg^{2+}.** (Upper panel) the amino acid sequence of Asp1 kinase, with the secondary structure elements displayed above. β-strands are depicted as *magenta arrows*, α-helices as *cyan cylinders*, and 3_{10} helices as *blue cylinders*. (Lower left panel) Asp1 kinase is depicted as a cartoon model, with secondary structure labels corresponding to primary structure shown above. (Lower right panel) surface electrostatic model of Asp1 kinase generated in Pymol, looking into the active-site pocket, in which IP_6 (stick model) is bound.

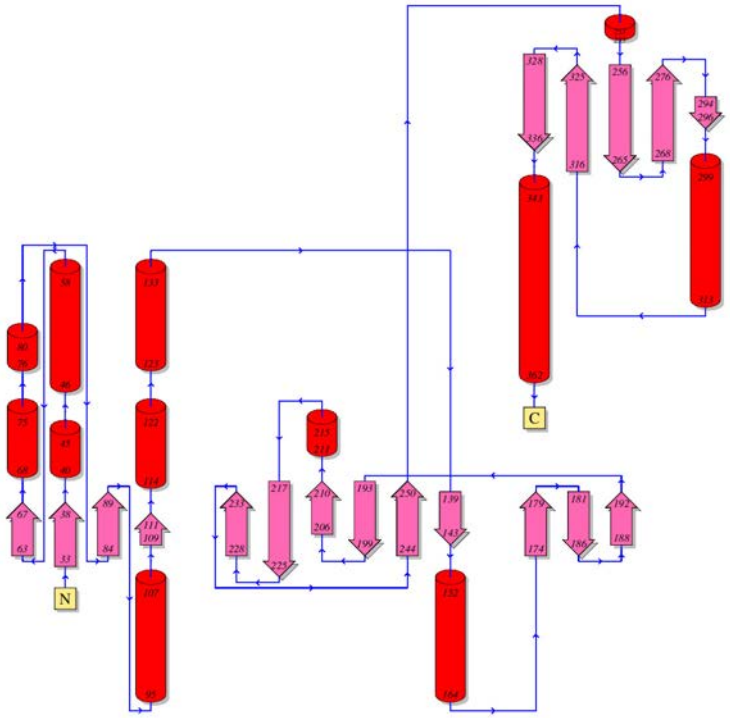

Figure 3. **Topology map of Asp1 kinase.** Topology was computed by PDBsum on Asp1 kinase (PDB ID 8E1V, complex with ADPNP, IP_6, and Mg^{2+}). Helices are depicted as red cylinders and sheets are depicted as pink arrows.

A DALI search of the pdb file returned several structures of ATP-grasp family proteins as closest matches (Table 1), the highest of which was a hPPIP5K2 structure (pdb 3t99) with a root mean square deviation (RMSD) of 1.5 Å over 304 Cα positions. Asp1 possesses an additional alpha helix (α6) not present in hPPIP5K2; it is separated from the core globular domain by two long loops (Ser144-Asn152 and Gly164-Glu174). This region constitutes the major primary structure divergence between Asp1 and PPIP5K2 kinase domains, which share 51% identity and 62% similarity within the resolved region. In place of α6, hPPIP5K2 possesses a shorter linker region containing an alpha helix and a beta strand.

Source	Description	pdb ID	Z score	% identity	Root mean square deviation	IP kinase?
Homo sapiens	INOSITOL PYROPHOSPHATE KINASE	3t99	40.3	51	1.5 at 304 Cα positions	✓
Escherichia coli K-12	RIBOSOMAL PROTEIN S6 MODIFICATION PROTEIN	4iwx	20.6	15	2.6 at 250 Cα positions	
Thermus thermophilus	RIBOSOMAL PROTEIN S6 MODIFICATION PROTEIN	3vpd	19.8	17	2.8 at 249 Cα positions	
Homo sapiens	INOSITOL-TETRAKISPHOSPHATE 1-KINASE	2qb5	19.6	15	2.9 at 251 Cα positions	✓
Streptomyces lavendulae	CYCLOSERINE BIOSYNTHESIS PROTEIN DCSG	6jil	18.2	14	3.3 at 250 Cα positions	
Rattus norvegicus	SYNAPSIN II	1i7l	17.8	11	3.1 at 242 Cα positions	
Leuconostoc mesenteroides	D-ALANINE:D-LACTATE LIGASE	1ehi	17	13	3.6 at 256 Cα positions	
Plesiocystis pacifica SIR-1	ATP-GRASP DOMAIN-CONTAINING PROTEIN	7drp	16.7	14	3.0 at 237 Cα positions	
Chryseobacterium gregarium DSM 19109	CDNC	7mgv	16.6	14	3.2 at 238 Cα positions	
Escherichia coli B	GLUTATHIONE SYNTHETASE	1gsa	16.4	13	2.9 at 237 Cα positions	
Pyrococcus horikoshii OT3	433AA LONG HYPOTHETICAL PHOSPHORIBOSYLGLYCINAMIDE	2dwc	16.4	13	3.2 at 241 Cα positions	
Burkholderia ambifaria MC40-6	PHOSPHORIBOSYLAMINOIMIDAZOLE CARBOXYLASE, ATPASE	4e4t	16.4	10	3.2 at 243 Cα positions	
Mycobacterium tuberculosis	D-ALANINE--D-ALANINE LIGASE	3lwb	16	12	3.6 at 250 Cα positions	
Methanosarcina barkeri str. Fusaro	PYLC	4ffl	15.4	12	3.4 at 227 Cα positions	

Table 1. **Closest structural homologs of Asp1 kinase.** The pdb coordinates of Asp1 kinase were used as a search template using the DALI structural homolog server. The top ten hits are listed according to z-score.

A cartoon depiction of the two protomers in the ASU is depicted in Figure 4A. Alignment of the two protomers in the ASU revealed key differences between the structures (Figure 4B). The continuous polypeptide, denoted Protomer A, contains clear density for nucleotide and inositol phosphate ligands. The discontinuous protomer, denoted protomer B, contains no ligands. Surface diagrams of the two protomers show that protomer A forms an active site cavity, while protomer B instead has an open crevice in the space where ligands would bind. We denote the two conformations of protomers A and B as closed and open, respectively.

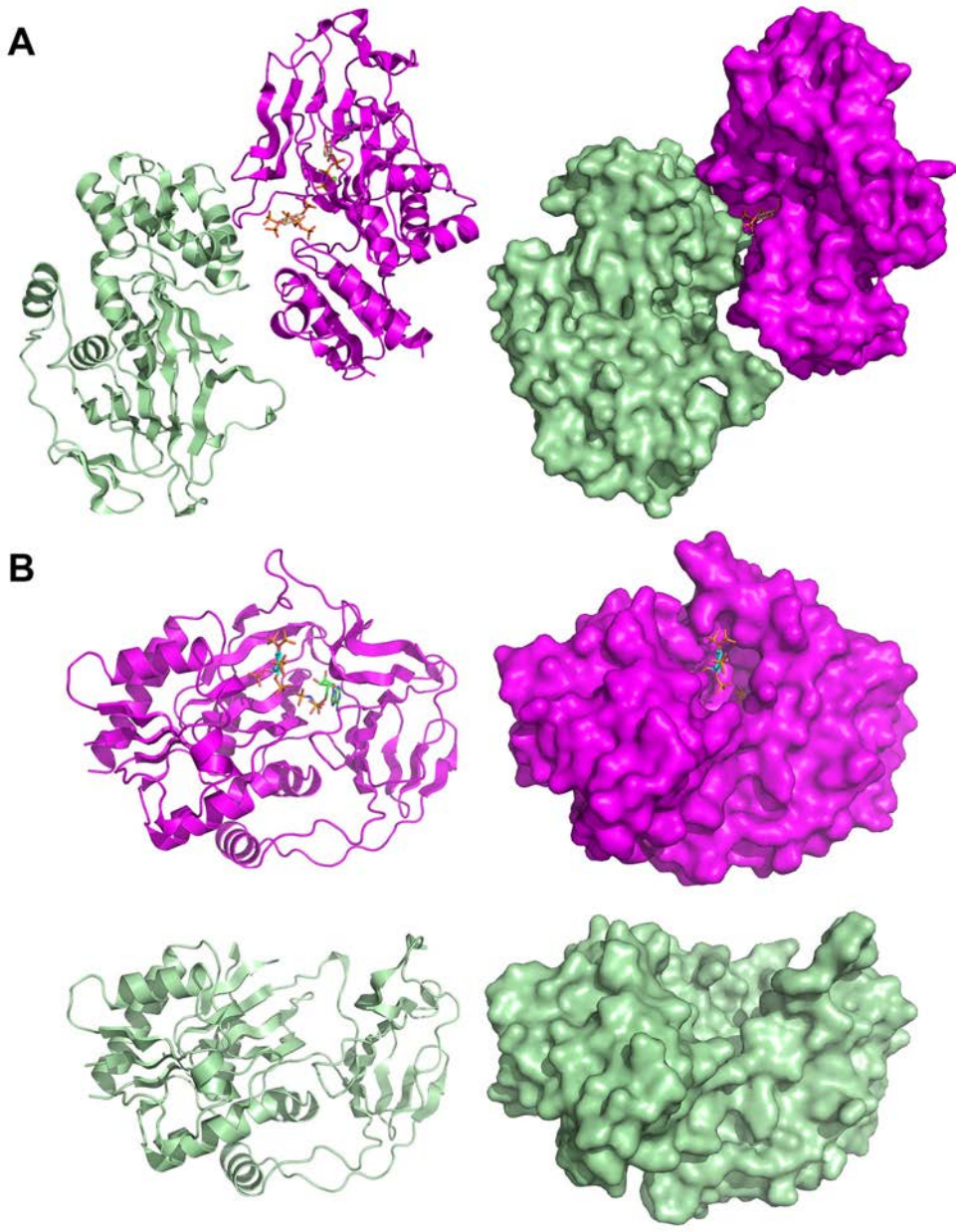

Figure 4. **Comparison of Asp1 closed and open conformations.** (A) Overall structure of two protomers in each ASU depicted as cartoon (left) or surface diagram (right). Protomer A with bound substrates is shown in magenta. Protomer B without substrates is shown in green. IP_6, Mg^{2+}, and ADPNP bound in protomer A's active site are depicted as sticks. (B) Isolated Asp1 kinase protomers were aligned and depicted individually as cartoon (left panels) or surface models (right panels). Protomer A with bound substrates is shown in magenta (upper panels). Protomer B without substrates is shown in green (lower panels).

The open conformation of protomer B relative to protomer A is due to two significant changes in protein tertiary structure. The first is the disordering of residues Lys275-Phe294, for which no electron density is observed in protomer B. This discontinuous stretch is resolved as a loop in protomer A (Figure 5A) and contains two residues (Lys290 and Arg293) that contact IP_6 phosphates in protomer A. We interpret this to mean that residues 275-294 are mobile in the absence of an IPP substrate. The second difference between protomer tertiary structure is the positioning of residues Phe222-Asp231. This module is a β-hairpin consisting of antiparallel β strands 11 and 12 connected by a short turn (residues Ala226-Asn227). In protomer A, this hairpin is flattened onto the active site like a lid, whereas in protomer B, it is peeled back from the active site (Figure 5B). The Asn227 Cα carbon is displaced by 13.1 Å during lid closure, whereas the side chains of catalytically-essential residues Arg223 and Lys224 swing inward 13.2 Å and 9.0 Å *vis-à-vis* their Cζ and Nζ respectively. Thus, lid closure moves key catalytic residues into position for IPP substrate engagement.

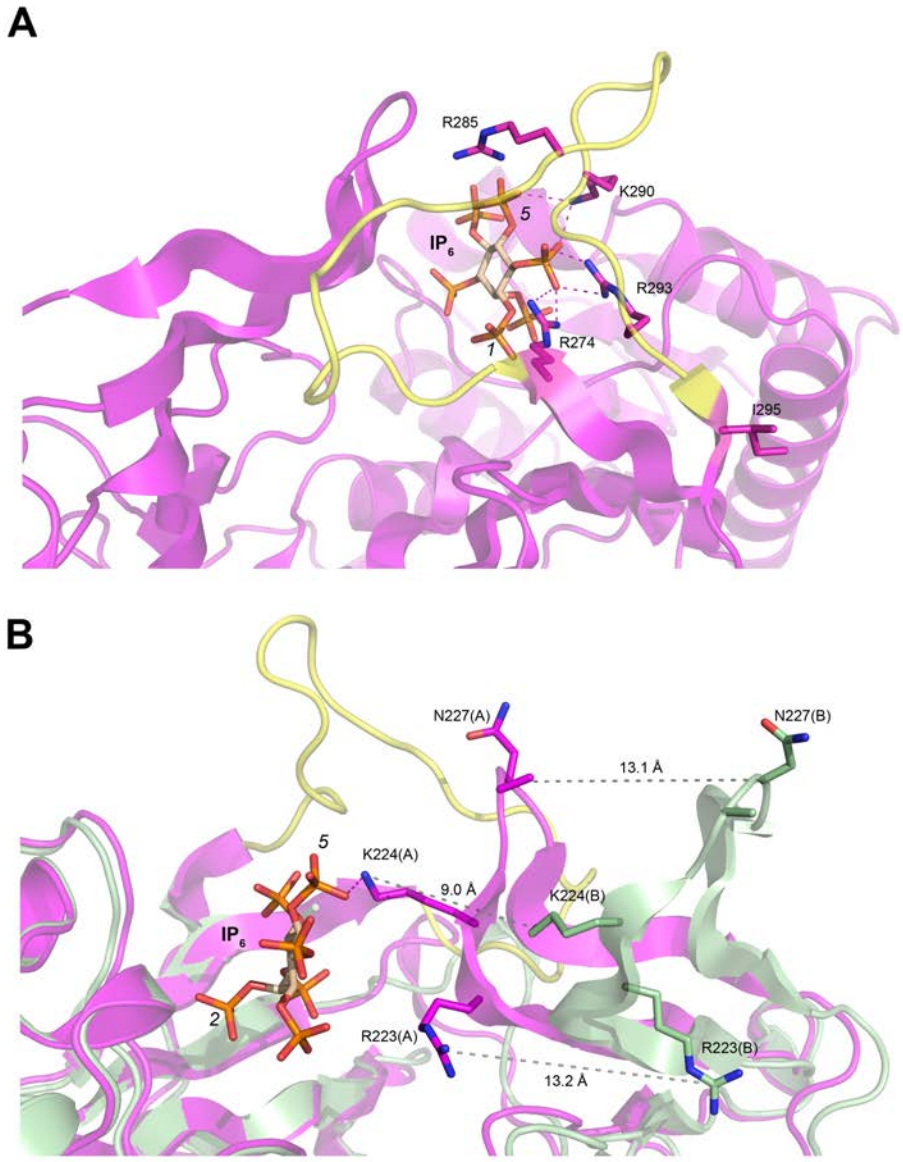

Figure 5. **Asp1 conformational changes upon substrate binding.** (A) Protomer A from structure of Asp1 with ADPNP, IP_6, and Mg^{2+} highlighting mobile loop motif that is disordered in protomer B. Peptide backbone is depicted as a magenta cartoon with mobile loop colored yellow. IP_6 is depicted as a stick model with beige carbons. Loop-resident IPP-binding residues and Ile295 are shown as sticks. Molecular contacts ≤ 3.5 Å with IP_6 are depicted as magenta dashed lines. IP_6 phosphates are labeled. (B) Overlaid protomers highlighting mobile hairpin motif. Protomer A and B are depicted as magenta and green cartoons, respectively. Side chains discussed in text are rendered as sticks. Parenthesized labels indicate protomer assignment. Distances between indicated residues of protomers are depicted as grey dashed lines.

Collectively, residues 275-294 (mobile loop) and residues 222-231 (mobile hairpin) constitute two flaps of a lid that covers the active site. The loop and hairpin are anchored on opposite sides of the active site cleft such that opening and closing is akin to the opening and closing of a box. The orientation of these mobile elements in protomer B places the enzyme in an open state that facilitates substrate access.

Crystal packing contacts with symmetry mates enable protomer B to adopt the open state despite the presence of saturating ligand. Protomer A α helix 6 inserts itself into the active site of protomer B from another ASU (Figure 6). Two salt bridges stabilize this interaction: 1) protomer B Asp233 – protomer A Arg134 (3.4 Å) and 2) protomer B Asp254 – protomer A Arg161 (2.8 Å). Asp254 is part of the nucleobase binding pocket; its involvement in salt bridges with symmetry mates may contribute to the stabilization of local structure deformations that occur during transient opening and closing of the active site. Mobile hairpin opening may be explained by interactions with protomer A C-terminal α helix 8. A salt bridge (protomer B Arg223 –protomer A Asp348 [3.0 Å]) stabilizes the hairpin in the open position (Figure 7). Arg223 is essential for Asp1 kinase activity – its engagement in interfacial salt bridges likely precludes it from coordinating IPPs into position for phosphoryl transfer. Thus, two factors, a) physical blocking of the active site by protomer A helix α6 and b) interfacial salt bridges involving protomer B active site residues, prevent protomer B from binding substrates and stabilize it in the open conformation.

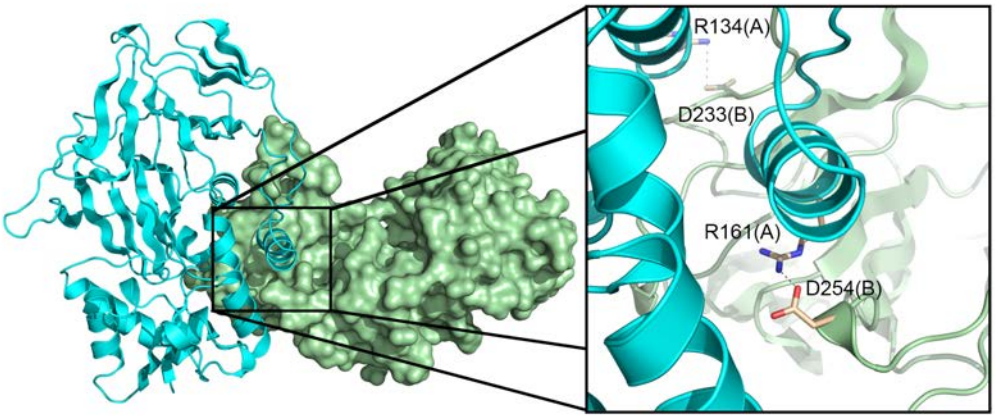

Figure 6. **Protomer B active site is occluded by symmetry mate protomer A helix α6, promoting open conformation.** Protomers A and B from the structure of Asp1 in complex with ADPNP, IP_6, and Mg^{2+} are depicted as cartoon and surface respectively, with protomer B of the primary ASU on right colored green and protomer A from a symmetrical ASU above colored cyan. (Inset) Both protomers are represented as cartoons. Side chains of residues involved in intermolecular salt bridges are represented as sticks with beige carbons. Molecular contacts ≤3.5 Å are shown as grey dashed lines.

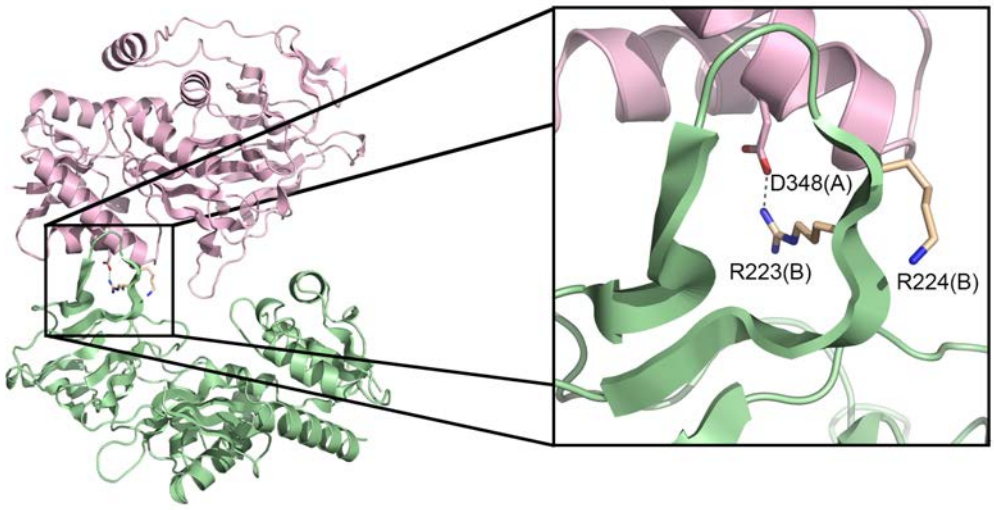

Figure 7. **Protomer B lid is stabilized in the open conformation *in crystallo* by interactions with symmetry mate protomer A.** Protomers A and B from the structure of Asp1 in complex with ADPNP, IP_6, and Mg^{2+} are depicted as cartoons, with protomer A colored pink and protomer B colored green. (Inset) Interfacial residues are depicted as sticks with beige carbons. Molecular contacts ≤3.5 Å are shown as grey dashed lines.

The non-hydrolysable ATP analog ADPNP is buried deep in the active site, with IP_6 closer to the mouth of the cavity. This orientation suggests that the substrates must bind and the products release in order with the nucleotide being first-in, last out (sequential bi-bi). The nucleotide is bound between two antiparallel β-sheets which define Asp1 as an ATP-grasp enzyme. Coordination of ligands within the active site is depicted in Figure 8. Asp321 and Asp333 coordinate a single magnesium ion which contacts each of the ADPNP α-, β-, and γ-phosphates. The ADPNP γ-phosphate is further coordinated by Asn335 and Lys260. Asp258 makes bidentate hydrogen bonds with the ribose 2' and 3' hydroxyls, while Glu248 and Lys197 contact the N^6 and N^7 moieties of the adenine nucleobase respectively. Adenine is caged by several bulky hydrophobic side chains, including Ile208, Phe250, Met251, Val253, Val278, and Leu323.

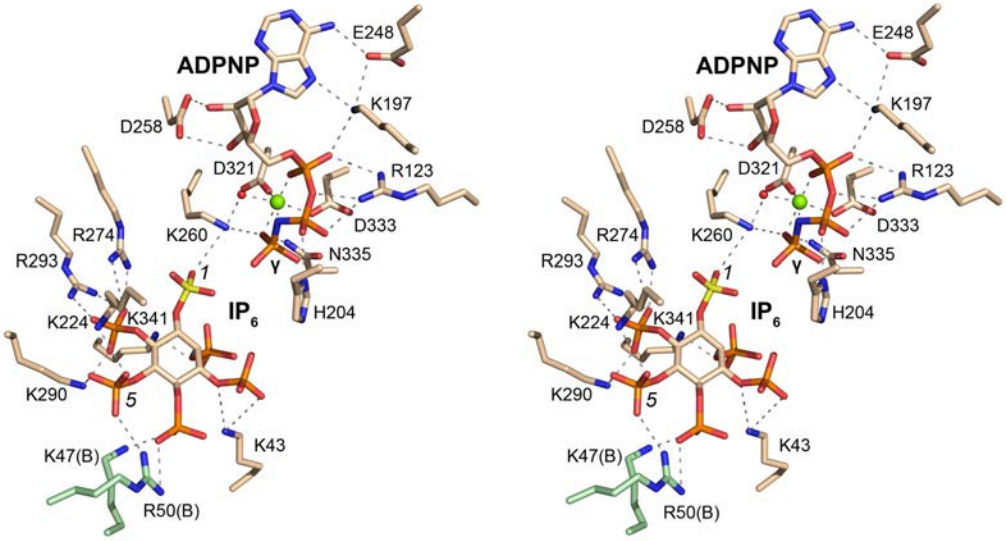

Figure 8. **Coordination of ADPNP and IP_6 by Asp1 active site residues and Mg^{2+}.** Stereo view of the active site of Asp1 in complex with ADPNP, IP_6 (stick models with beige carbons), and one magnesium cofactor (green sphere). The IP_6 1- and 5-phosphates are labeled; the 1-phosphorus atom is colored yellow. A single catalytic water is depicted as a red sphere. Active site side chains are rendered as stick models with beige carbons for protomer A, green carbons for protomer B. Molecular contacts ≤3.5 Å are depicted as dashed grey lines.

A 3_{10} helix-containing motif spanning residues Glu248-Asp258 defines the back of the active site's nucleobase binding pocket. These residues adopt a different position in protomer B, entailing a complete reorientation of the 3_{10} helix (Figure 9A). The side chains of Asn252, Val253, Asp254, and Asn255 each move more than 6 Å during this rotation, with the Cγ atom of Asp254 displaced by 11.4 Å (Figure 9B). Rotation of the nucleobase binding pocket during substrate binding creates space for the adenine base by shifting the peptide backbone, specifically the carbonyl of Glu249 and the amine of Met251, out of steric clash with adenine N^6 and N^5 respectively (Figure 9B). Further, binding induces a ~1 Å downward movement in Phe250 enabling Pi-cation stacking interaction with adenine. Thus, nucleotide binding is possible in the closed orientation due to relief of steric clash and creation of protein-base interaction.

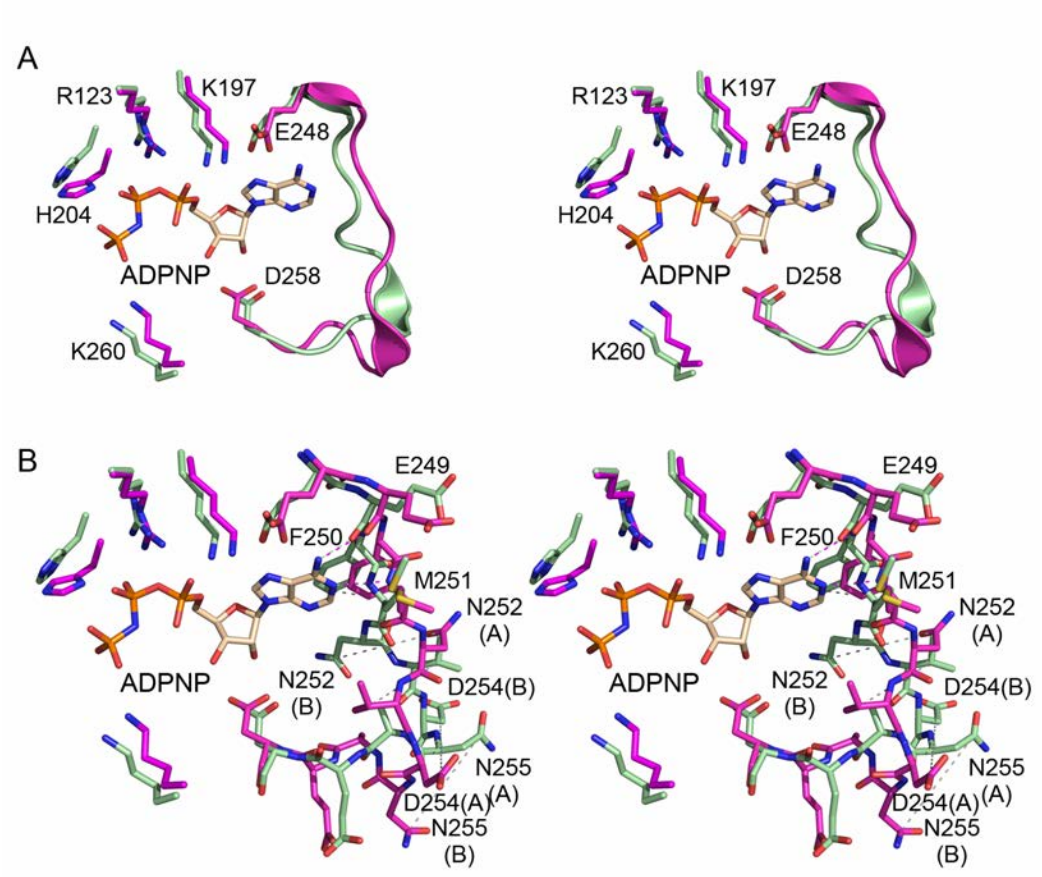

Figure 9. **Nucleobase binding motif rotation during ADPNP binding.** (A) Stereo image of overlaid protomers from structure of Asp1 with ADPNP, IP_6, and Mg^{2+} highlighting mobile nucleobase binding region and additional nucleotide coordinating residues. Peptide backbone is depicted as a cartoon, while ADPNP and protein side chains involved in NTP binding are depicted as sticks. Protomer A (substrate bound) is colored magenta, protomer B (unbound) is colored green, and ADPNP is shown with beige carbons. (B) Stereo image of the same region with protein depicted as sticks to highlight nucleobase-peptide backbone steric clashes and side chain rotation. Distances between atoms of protomers A and B are shown as grey dashed lines. Main chain atoms involved in steric clash are connected to the adenine via dashed lines with colors corresponding to the protomer involved.

Protomer A's active site entrance is shaped to accommodate the IPP ligand, with prongs formed by residues Lys43, Lys290, Lys224, and Arg223 defining the cavity's exterior shape. IP_6 is bound by seven positively charged residues: Lys43, Lys224, Lys260, Arg274, Lys290, Arg293, and Lys341 (Figure 8). A list of side

chain-phosphate interactions is provided in Supplemental Table 2A. Each of the six phosphate groups forms at least one salt bridge with a positively charged active site residue. Notably, the 4- and 5-phosphates form close hydrogen bonds with two non-catalytic residues of protomer B, Lys47 and Arg50 (Figures 8 and 10). This will be discussed at length later in this results section. The 1-phosphate nucleophile is pointed into the site of chemistry, with the closest oxygen 4.7 Å from the γ-phosphate (Figure 8). The angle formed between the nucleophilic oxygen, the ADPNP γ-phosphate, and the scissile γ-β oxygen is 141.2°. The distance and attack angle of the 1-phosphate are imperfect, providing insight into why IP_6 is a poor phosphoacceptor substrate for Asp1 kinase. His204 and Lys260 bridge the space between the IP_6 1-phosphate and ADPNP γ-phosphate, suggesting a role in stabilizing the phosphorane transition state as it transfers from ADPNP to IP_6 (Figure 8). It is worth noting that the pKa of histidine sits within the pH range of optimal Asp1 kinase activity, indicating that transient (de)protonation might be important during phosphoryl transfer.

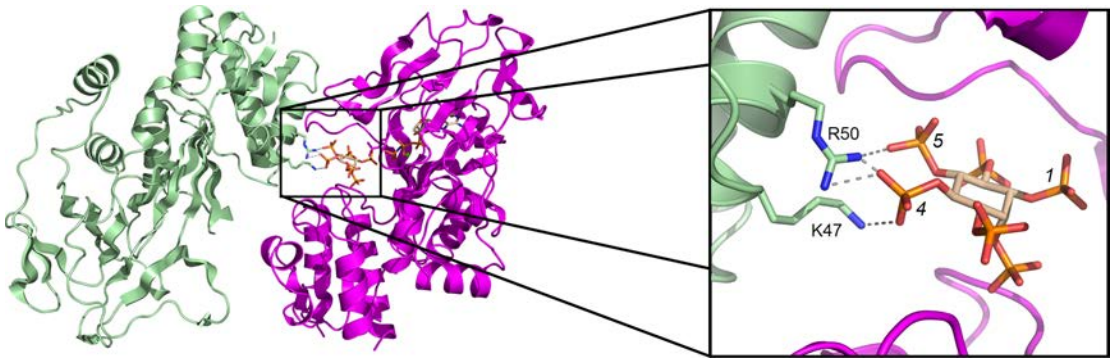

Figure 10. **Protomer B residues K47 and R50 interact with IP_6 in protomer A active site.** Protomers A and B from the structure of Asp1 in complex with ADPNP, IP_6, and Mg^{2+} are depicted as cartoons, with protomer B on left colored green and protomer A on right colored magenta. Substrates are depicted as sticks with beige carbons. The magnesium ion is shown as a green sphere. (Inset) Protomer B interfacial residues K47 and R50 are depicted as sticks. Molecular contacts ≤3.5 Å with the 4- and 5-phosphates of IP_6 bound to protomer A are shown as grey dashed lines. IP_6 1-, 4-, and 5-phosphates are labeled.

4.3.2 Crystal structure of Asp1 kinase domain in complex with IP_6, Mn^{2+}, and ADPNP

Crystal structures of the human homolog of Asp1 kinase showed at least two metal ions in the active site coordinating nucleotide phosphates (12). Our initial structure of Asp1 in complex with IP_6, Mg^{2+}, and ADPNP only showed one such metal which bridged each of the nucleotide's three phosphates. In order to definitively determine how many metal ions occupy the active site, I crystallized Asp1 kinase with IP_6, Mn^{2+}, and ADPNP. Using x-rays at the manganese absorption peak wavelength, Dr. Goldgur collected data which showed anomalous signal of intensity >20σ (data not shown), unambiguously establishing that two metal ions occupy the active site. We evaluated other crystals grown in the same well, one of which diffracted to resolution 1.9 Å, was of space group $P2_1$, and contained two protomers in the ASU (bound and apo). The protein and nucleotide of this structure superimposed perfectly onto that of Asp1 kinase with IP_6, Mg^{2+}, and ADPNP (Figure 11A and 11B). I interpret this finding as evidence that a second metal ion in the active site is not essential to position active site residues and nucleotide ligand into a position appropriate for catalysis. Alternatively, it is

possible that the structure with magnesium contained two metal ions, with one that could not be clearly differentiated from water.

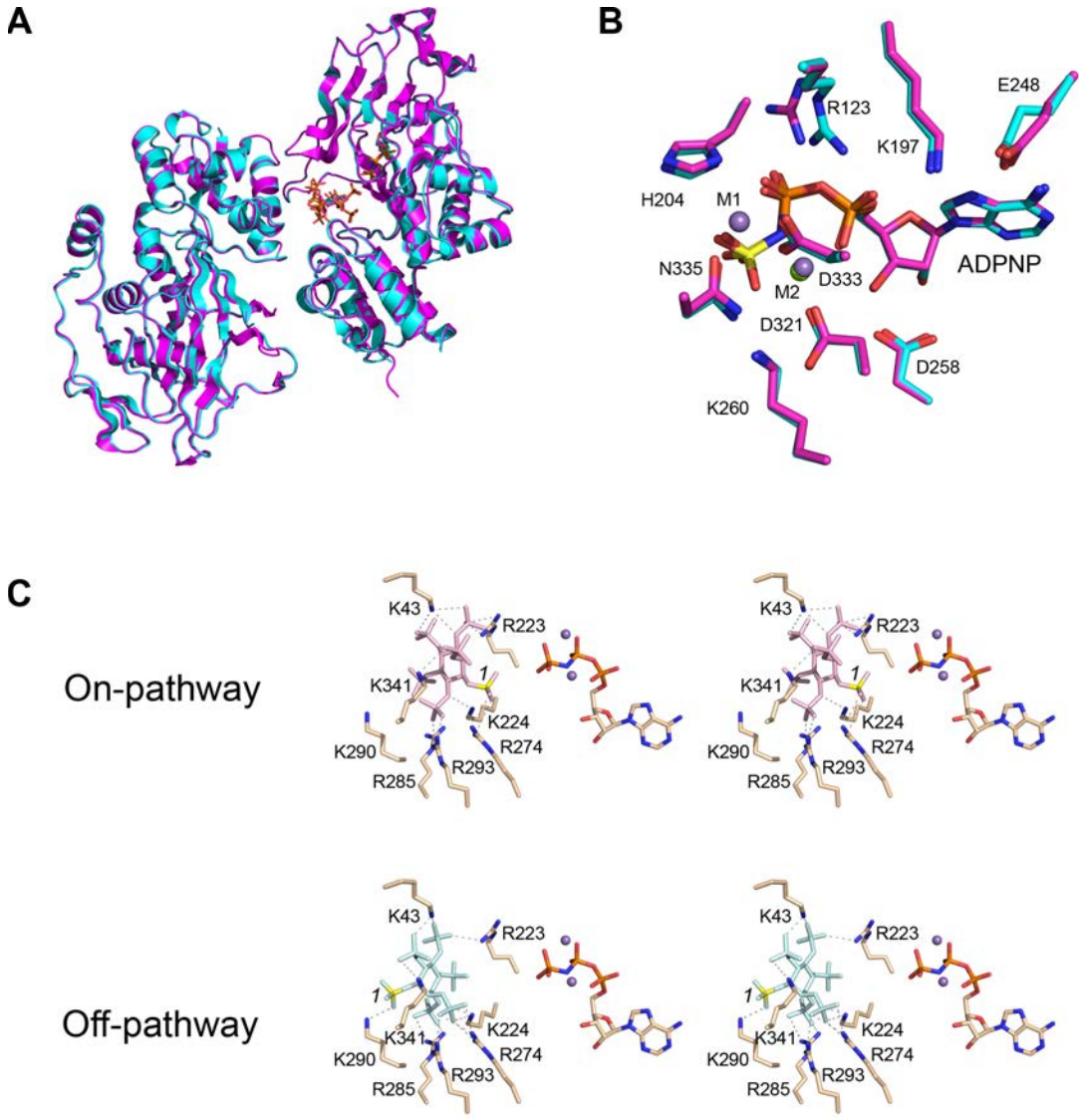

Figure 11. **Asp1 in complex with ADPNP, IP_6, and Mn^{2+}.** (A) Structures of Asp1 containing ADPNP, IP_6, and either Mn^{2+} (colored magenta) or Mg^{2+} (colored cyan) are depicted as cartoons and overlaid. (B) Close up view of ADPNP in the active site. Elements from Mn^{2+} or Mg^{2+} structure are colored as described. Mn^{2+} ions are depicted as purple spheres. The Mg^{2+} ion is depicted as a green sphere. (C) Stereo images of IP_6 in the active site coordinated into on-pathway (top) or off-pathway (bottom) orientation. The 1-phosphate phosphorus atom is colored yellow. IP_6 is colored pale pink in the on-pathway orientation and pale cyan in the off-pathway orientation.

The electron density at the mouth of the active site was more diffuse than the previous structure. We constructed a model in which IP_6 adopts two different positions that are occupied with equal frequency (Figure 11C). One orientation closely matches that of IP_6 in the magnesium-containing structure (on-pathway). In its other position, IP_6 is flipped such that 1-phosphate faces out of the active site (off-pathway). No IP_6 phosphate is closer than 8.1 Å away from the ADPNP γ-phosphate. The off-pathway position features a different pattern of side chain–IP_6 phosphate interactions. Notably, Arg223, Arg274, and Arg293 work in concert to point the 2-phosphate in toward the site of chemistry. Overall, IP_6 is well-coordinated in the off-pathway position, with only a single phosphate, the 4-phosphate, lacking contact to an active site side chain. A comparison between on- and off-pathway substrate coordination by active site residues is listed in Supplemental Table 2B. Collectively, we determine that Asp1 binds IP_6 in at least two orientations, only one of which promotes kinase activity.

4.3.3 Crystal structure of Asp1 kinase domain in complex with 5-IP_7, Mg^{2+}, and ADPNP

5-IP_7 is a better kinase substrate for Asp1 than is IP_6 (3). I thus sought to gain structural information on Asp1's coordination of 5-IP_7 with the non-hydrolysable ATP analog ADPNP. I obtained crystals of Asp1 kinase with 5-IP_7, Mg^{2+}, and ADPNP which diffracted to a resolution of 1.7 Å. The structure was solved by molecular replacement using Asp1 kinase in complex with IP_6, Mg^{2+}, and ADPNP as a reference model. Like others, this crystal was of space group $P2_1$ and

had two protomers in the ASU (bound and apo). The overall fold and side chain orientation was virtually identical to that of the reference structure.

Electron density for 5-IP_7 showed that the ligand is positioned in an off-pathway orientation (Figure 12). The 5-pyrophosphate moiety is pointed in toward the site of chemistry – it is 8.0 Å away from the ADPNP γ-phosphate with an attack angle nearly 90°, precluding any possibility that this orientation supports phosphoryl transfer. The 1-phosphate is pointed outward, hydrogen bonding with Lys290, Lys341, and protomer B Lys47. Two important catalytic residues do not form close contacts with the IPP: Lys260, whose on-pathway role is to bridge the IPP 1-phosphate to the ATP γ-phosphate, and Arg223, whose catalytic role will be explored later. However, other active site residues effectively neutralize the phosphate charges through extensive hydrogen bonding. The full map of IPP phosphate coordination is listed in Supplemental Table 2C. We conclude that 5-IP_7, like IP_6, can bind in an off-pathway orientation in Asp1 kinase's active site.

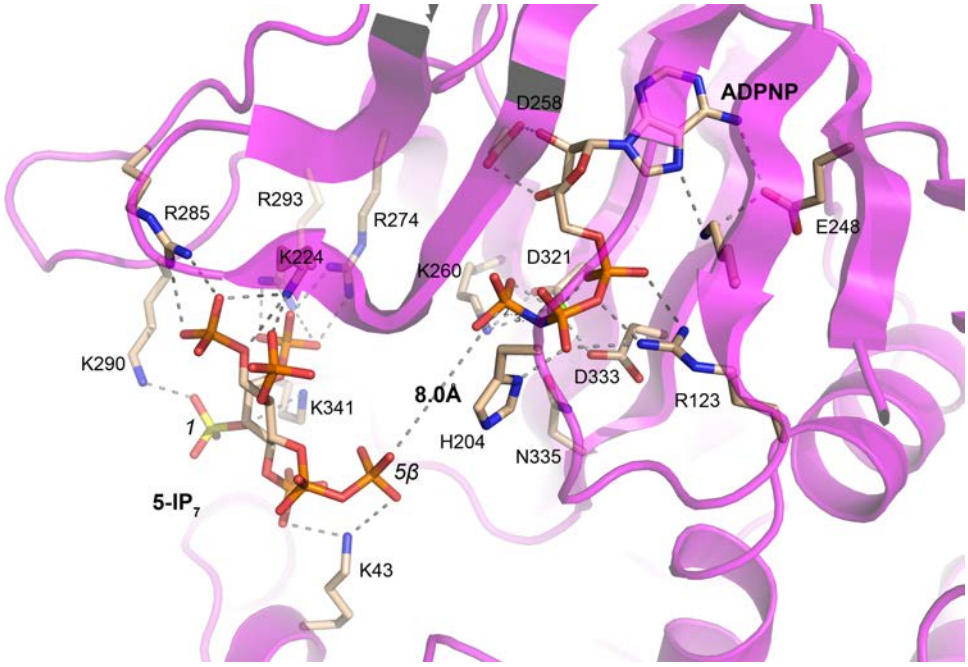

Figure 12. **ADPNP, 5-IP_7, and Mg^{2+} bound in the Asp1 active site.** The active site of Asp1 in complex with ADPNP, 5-IP_7 (stick models with beige carbons), and one magnesium cofactor (green sphere). The 5-IP_7 1-phosphorus atom is colored yellow. The Asp1 peptide backbone is depicted as a semitransparent magenta cartoon. Amino acid side chains are rendered as stick models with beige carbons. Molecular contacts ≤3.5 Å are depicted as dashed grey lines, except between 5-IP_7 5β-phosphate and ADPNP γ-phosphate as indicated.

4.3.4 Crystal structure of Asp1 kinase domain in complex with 5-IP_7, Mg^{2+}, and ADP

After obtaining several structures of Asp1 kinase with substrates, I sought to crystallize Asp1 with its different products. I grew crystals of a mixture of Asp1 kinase with 5-IP_7, Mg^{2+}, and ATP which diffracted to a resolution of 1.9 Å. The structure was solved by molecular replacement using Asp1 kinase in complex with IP_6, Mg^{2+}, and ADPNP as a reference model. This crystal was of space group $P2_1$ and had two protomers in the ASU (bound and apo). The overall fold and side chain orientation was virtually identical to that of the reference structure.

A cartoon depiction of substrate orientation in the bound protomer is shown in Figure 13. Electron density showed that the ATP had been replaced by ADP in the active site. The active site was also occupied by 5-IP_7 in an off-pathway orientation (phosphate coordination is detailed in Supplemental Table 2D). Three magnesium ions are present in the active site – two coordinating ADP phosphates and one bound between the 5-IP_7 5β-, 5α-, 4-, and 2-phosphates. The former two are octahedrally coordinated by active site contacts, ADP phosphates, and waters, while the lattermost magnesium makes only 4 close molecular contacts, each with IPP phosphates.

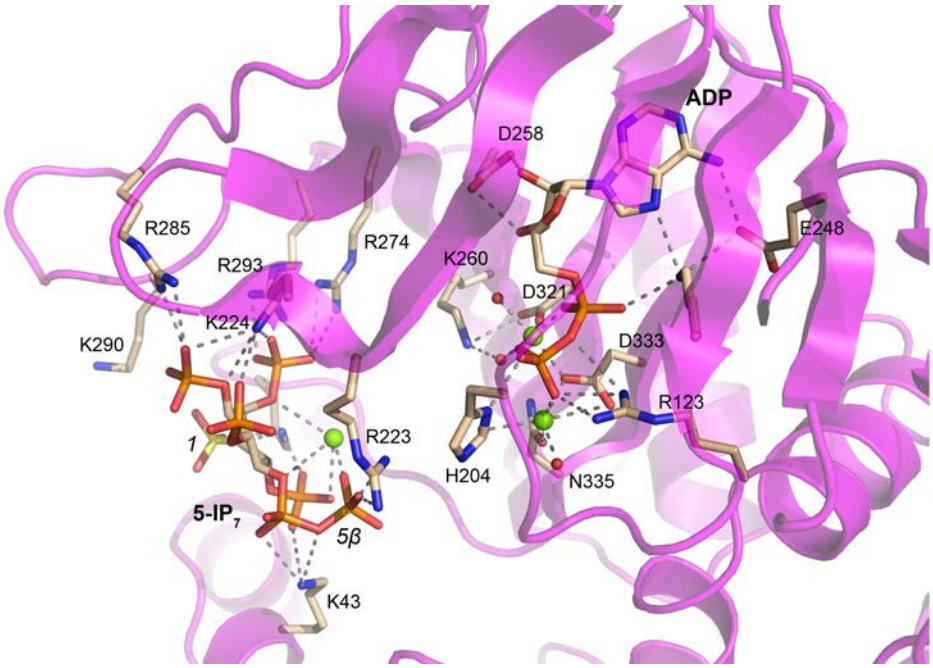

Figure 13. **ADP, 5-IP$_7$, and Mg^{2+} bound in the Asp1 active site.** The active site of Asp1 in complex with ADP, 5-IP$_7$ (stick models with beige carbons), and three magnesium cofactors (green spheres). The 5-IP$_7$ 1-phosphorus atom is colored yellow. The Asp1 peptide backbone is depicted as a semitransparent magenta cartoon. Amino acid side chains are rendered as stick models with beige carbons. Molecular contacts ≤3.5 Å are depicted as dashed grey lines.

This complex contains a mixture of reactants (5-IP$_7$) and products (ADP). I suspect that Asp1 catalyzed the reaction of 5-IP$_7$ + ATP → 1,5-IP$_8$ + ADP during complex preparation/crystallization and subsequently rebound 5-IP$_7$ (a substrate) and ADP (a product) after the reaction reached equilibrium. This begets the interpretation that Asp1 kinase is capable of binding both ATP and ADP. While it is possible that this crystal is a *bona fide* product complex of the ATP hydrolysis activity, this outcome is unlikely because no inorganic phosphate was observed in the closed structure and because ATP hydrolysis activity is weak in the presence of 5-IP$_7$.

4.3.5 Crystal structure of Asp1 kinase domain in complex with 1,5-IP_8

Asp1 prefers ATP over other nucleotides for use as a phosphate donor in its kinase activity (3). I asked whether it could accommodate a bulky ATP analog N^6-benzyl ATP (Figure 14A). I determined that Asp1 readily used N^6-benzyl ATP to phosphorylate 5-IP_7 *in vitro* (Figure 14B). This was surprising insofar as structures demonstrated that ATP fits snugly in the Asp1 binding pocket. I sought to gain structural insight into Asp1's utilization of a bulky ATP analog. I generated crystals from a solution containing Asp1 kinase with 5-IP_7, Mg^{2+}, and N^6-benzyl ATP which diffracted to a resolution of 1.6 Å. The structure was solved by molecular replacement using Asp1 kinase in complex with IP_6, Mg^{2+}, and ADPNP as a reference model. This crystal was of space group $P2_1$ and had two protomers in the ASU (bound and apo). The overall fold and side chain orientation was similar to that of the reference structure, with differences detailed below.

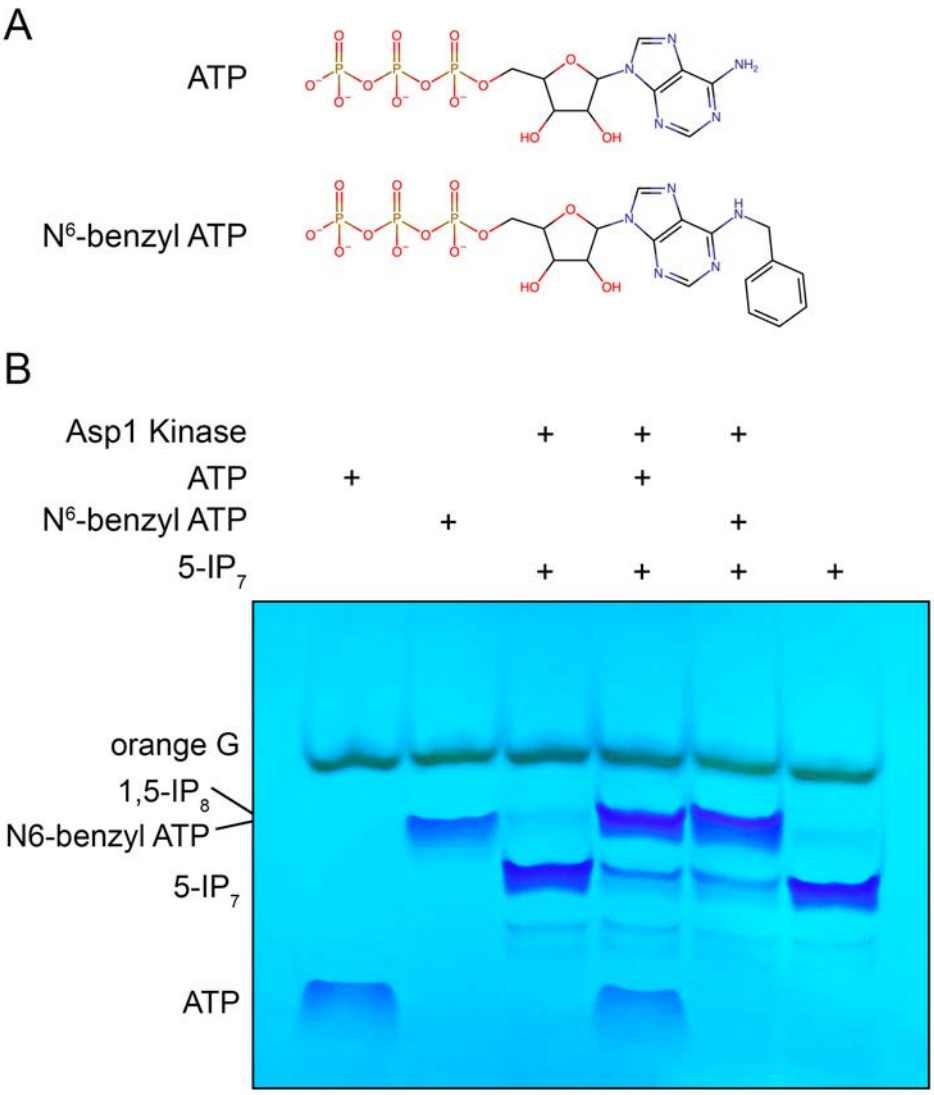

Figure 14. **N^6-benzyl ATP is a substrate for Asp1 kinase.** (A) Chemical structures of ATP and N^6-benzyl ATP. (B) 5-IP_7 kinase reaction mixtures (20 µL) containing 30 mM Bis-Tris (pH 6.2), 50 mM NaCl, 5 mM $MgCl_2$, 0.5 mM 5-IP_7, 2 mM ATP or N^6-benzyl ATP, and 2.5 µM (50 pmol) Asp1 kinase were incubated at 37°C for 15 min. Reaction products were analyzed by PAGE and detected by toluidine blue staining.

The crystal contained only a single ligand in the active site: the product of the kinase reaction 1,5-IP_8. This was surprising because all crystals up to now had demonstrated clear electron density for the nucleotide in the active site. Rather than providing information on the structural rationale for bulky ATP analog

utilization, this structure gave insight into the state of the enzyme with IP_8 bound in the absence of nucleotide. The IPP-bound protomer exhibited a disordered stretch from residues Asn252–Glu257; this region contains a 3_{10} helix motif that is part of Asp1's nucleobase binding module. Its disorder further suggests that this region is flexible and becomes rigid upon nucleotide binding. It is also worth noting that in the absence of this ordered module, the Asp1 active site is no longer a cavity but a channel. The opening in the backside of the active site is ~ 4 Å in diameter (Figure 15).

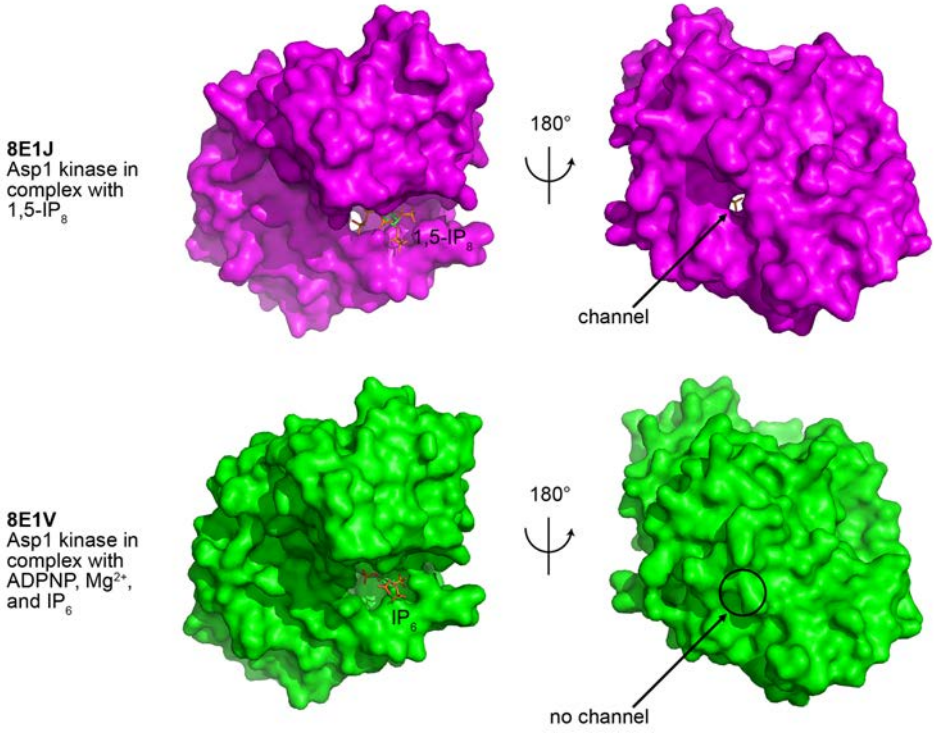

Figure 15. **Nucleobase binding loop is disordered when 1,5-IP_8 is bound without nucleotide.** Protomers with bound substrates from two structures (top: Asp1 with 1,5-IP_8, bottom: Asp1 with ADPNP, Mg^{2+}, and IP_6) are shown as surface models. Absence of modeled residues 252-257 in 1,5-IP_8 structure is visible as a channel through the active site indicated by an arrow. 1,5-IP_8, and IP_6 are depicted as sticks with green carbons.

Sharp electron density around the 1,5-IP_8 enabled us to determine its orientation without ambiguity (Figure 16). The IPP ligand is in an off-pathway orientation, with the 1-pyrophosphate pointing out toward solution and the 4-phosphate pointing inward toward the space normally occupied by nucleotide phosphate groups (Figure 17). Its orientation by active site sidechains is catalogued in Supplemental Table 2E. The bound protomer is in the closed position, suggesting that IPP binding is sufficient to lock down the active site lid. Since the shape of the active site precludes the possibility of nucleotide dissociation preceding IPP dissociation, 1,5-IP_8 must have been generated in solution and bound an empty Asp1 molecule.

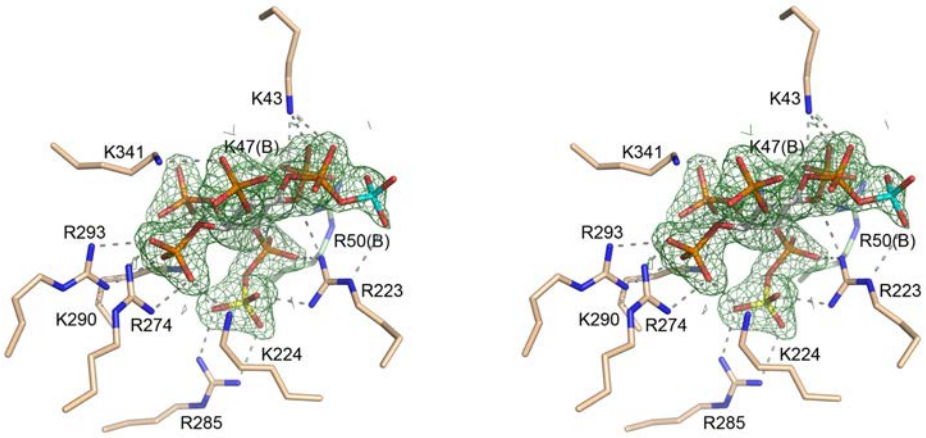

Figure 16. **Omit map of 1,5-IP_8 in the Asp1 active site.** Stereo images of Asp1 in complex with 1,5-IP_8 (stick models with grey carbons). The 1β and 5β phosphorus atoms are colored yellow and cyan, respectively. IPP-binding side chains are depicted as sticks with protomer A carbons colored beige, protomer B carbons colored green. Enzymic contacts ≤3.5 Å are depicted as dashed grey lines. Omit density ($2F_o–F_c$) for 1,5-IP_8, is depicted as green mesh contoured at 1σ and carved to 2.0 Å.

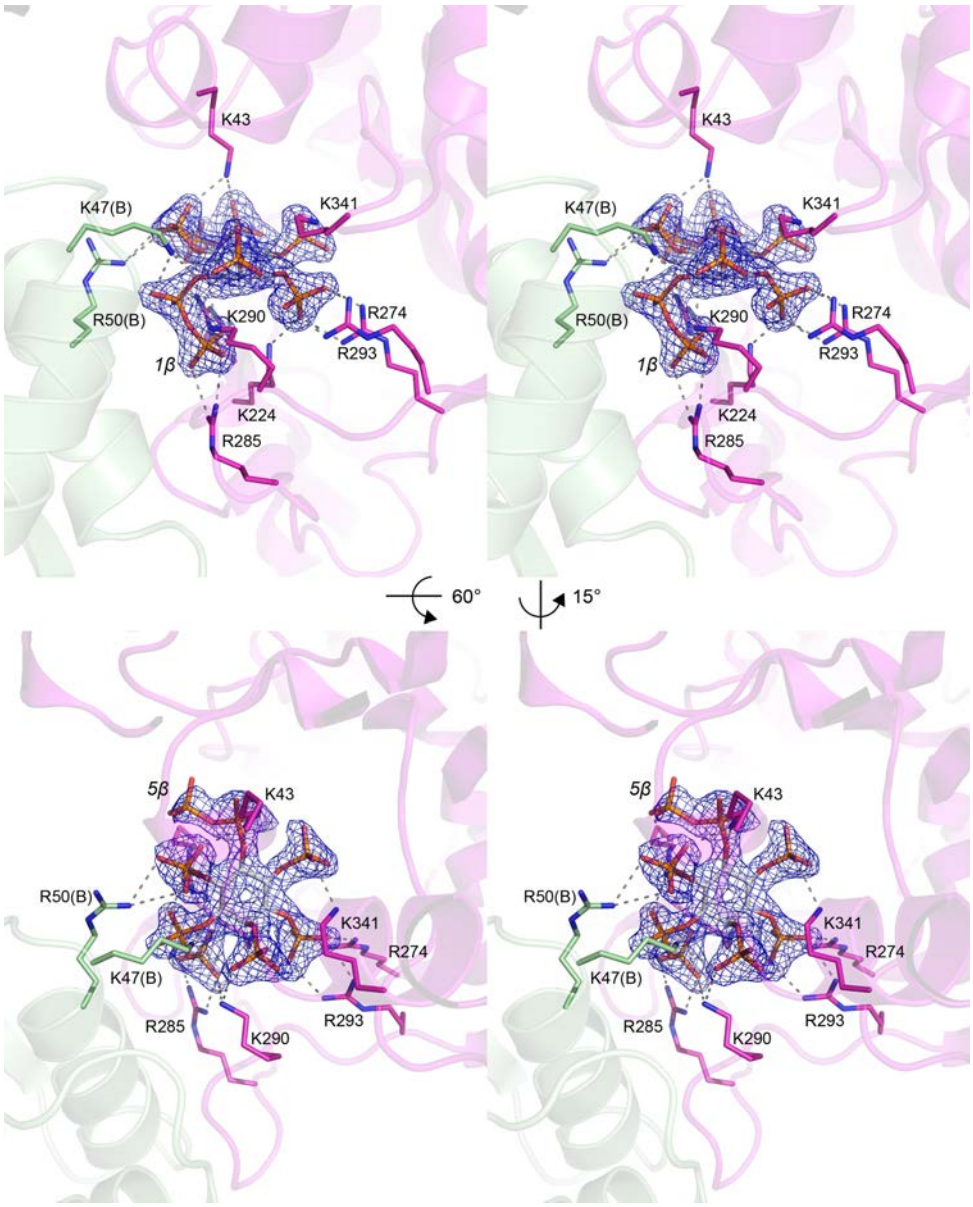

Figure 17. **1,5-IP$_8$ orientation in the Asp1 active site.** Stereo images of Asp1 in complex with 1,5-IP$_8$ (stick model with grey carbons). Peptide backbone is shown as a semitransparent cartoon with protomer A colored maroon and protomer B colored green. IPP-binding side chains are depicted as sticks with carbons colored by protomer. Enzymic contacts ≤3.5 Å are depicted as dashed grey lines. Omit density ($2F_o$–F_c) for 1,5-IP$_8$, is depicted as blue mesh contoured at 1σ and carved to 1.5 Å.

4.3.6 Crystal structure of Asp1 kinase domain in complex with 5-IP_7, Mg^{2+}, and ATP

The structure of Asp1 kinase with 5-IP_7 and ADPNP showed that the IPP 1-phosphate was positioned too far away from the nucleotide γ-phosphate for efficient phosphoryl transfer. Surface residues Lys47 and Arg50 from the unbound protomer formed close hydrogen bonds with the IPP phosphates in many of our structures, especially those with IPPs in off-pathway orientation. We hypothesized that this crystal packing artifact might contribute to the imperfect ligand position we observed. To test this, I mutated these residues to alanine and purified the double-mutant kinase. The recombinant mutant enzyme was as active as the truncated WT kinase *in vitro* (Figure 18). The mutant kinase crystallized under similar conditions to that of WT. I obtained crystals from many different mixes of substrates or substrate analogs and found that in most conditions, the IPP ligand was oriented out of ideal position for kinase chemistry (or was positioned in *bona fide* off-pathway orientation). However, a crystal containing Asp1 kinase with 5-IP_7, Mg^{2+}, and ATP in precipitant solution pH 7.8 contained 5-IP_7 with the 1-phosphate correctly oriented for nucleophilic attack on the ATP γ-phosphate. The crystal diffracted to a resolution of 2.0 Å and the structure was solved by molecular replacement using Asp1 kinase in complex with IP_6, Mg^{2+}, and ADPNP as a reference model. This crystal was of space group $P2_1$ and had two protomers in the ASU (bound and apo). The overall fold and side chain orientation was similar to that of the reference structure, with differences detailed below.

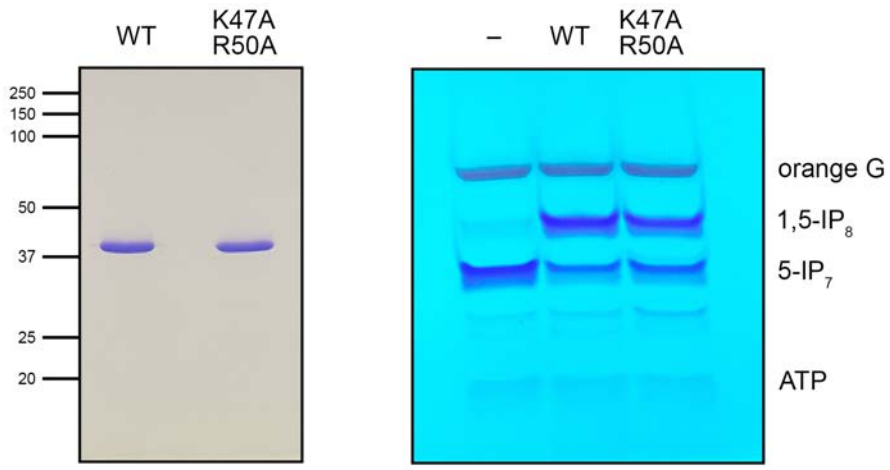

Figure 18. **Asp1 kinase-(31-364) K47A R50A purification and activity.** (Left panel) aliquots (3 μg) of the indicated Asp1 truncations were analyzed by SDS-PAGE. The Coomassie blue–stained gel is shown. The positions and sizes (kilodalton) of marker polypeptides are indicated on the left. (Right panel) IP_7 kinase reaction mixtures (20 μL) containing 30 mM Bis-Tris (pH 6.2), 50 mM NaCl, 5 mM $MgCl_2$, 0.5 mM 5-IP_7, 1 mM ATP, and 5 μM Asp1-(31-364) or Asp1-(31-364)-K47A-R50A were incubated at 37°C for 15 min. Reaction products were analyzed by PAGE and detected by toluidine blue staining.

Clear electron density of the ligand enabled us to determine that 5-IP_7 is positioned with the 1-phosphate facing in toward the ATP γ-phosphate (Figure 19A). The closest oxygen of the IPP 1-phosphate is 4.4 Å from the ATP γ-phosphate central phosphorus atom (Figure 19B). The attack angle between the IPP nucleophilic oxygen, the ATP γ-phosphate central phosphorus atom, and the scissile oxygen between ATP β- and γ-phosphates is 161.5°. These conditions are more likely to promote phosphoryl transfer than those observed in the structure of Asp1 with ADPNP and IP_6, which had a nucleophilic attack distance of 4.7 Å and attack angle of 141.2°.

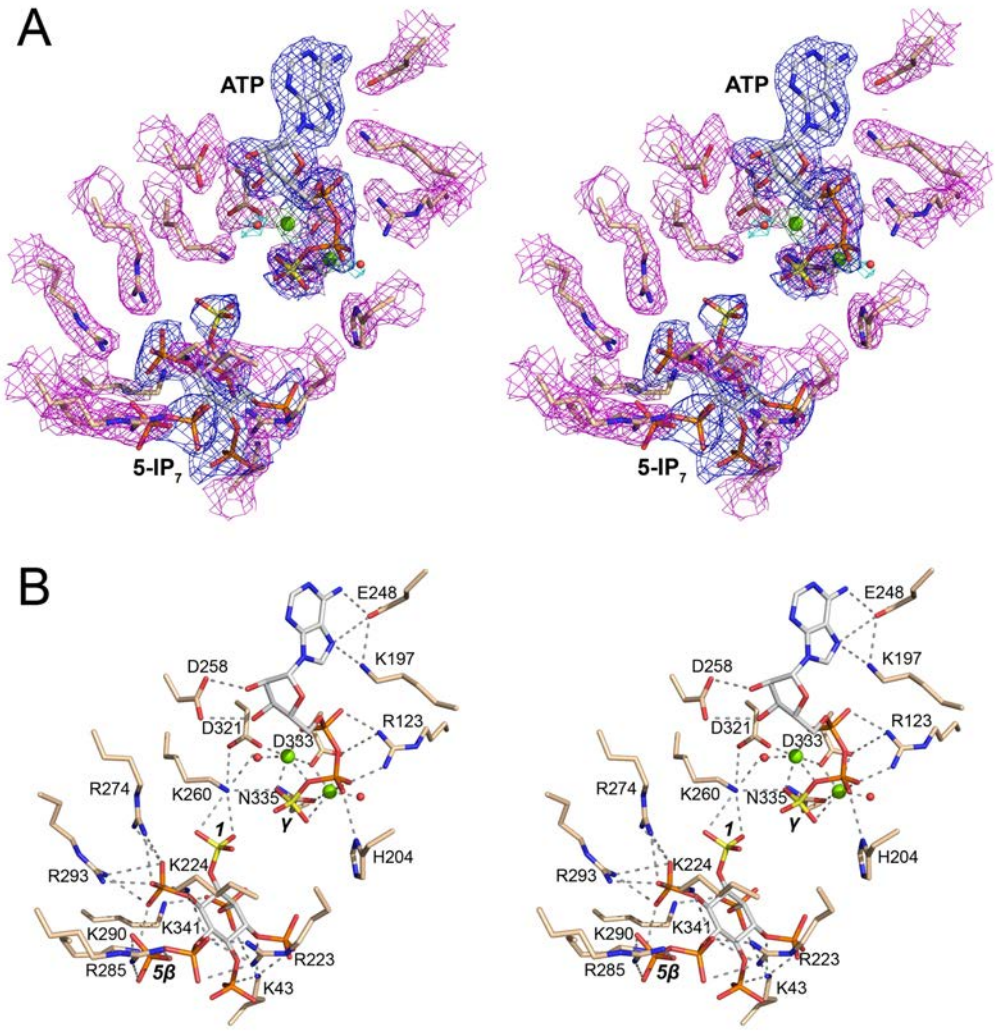

Figure 19. **Omit map and coordination of ATP, 5-IP$_7$, and Mg^{2+} in Asp1 active site.** (A) Stereo view of the active site of Asp1 in complex with ATP, 5-IP$_7$ (stick models with grey carbons), and two magnesium cofactors (green spheres). The 5-IP$_7$ 1-phosphorus and ATP γ-phosphate atoms are colored yellow. Waters are depicted as red spheres. Amino acid side chains are rendered as stick models with beige carbons. Enzymic contacts ≤3.5 Å are depicted as dashed grey lines. Omit density ($2F_o$–F_c) mesh is colored blue for ATP and 5-IP$_7$, cyan for water, and forest for Mg^{2+}. Model-biased density for side chains is colored magenta. Mesh is contoured at 1σ and carved to 2.0 Å. (B) Stereo image of Asp1 in complex with ATP, 5-IP$_7$, and magnesium with active side residues labeled. 5-IP$_7$ and ATP are depicted as sticks with grey carbons. The 5-IP$_7$ 1-phosphate and ATP γ-phosphate phosphorus atoms are colored yellow. Magnesium ions and waters are depicted as green and red spheres, respectively. Amino acid side chains are rendered as stick models with beige carbons. Molecular contacts ≤3.5 Å are depicted as dashed grey lines.

Two octahedrally coordinated magnesium ions are observed in the active site. M1 bridges the ATP β and γ phosphates and is further coordinated by active site residues Asp333 and Asn335, as well as an active site water. M2 is coordinated by the ATP α and γ phosphates, active site residues Asp321 and Asp333, and a water. Other than the water molecules coordinating the catalytic metals, the active site is devoid of water.

ATP is coordinated similarly to ADPNP of the reference structure, with residues Glu248 and Lys197 contacting the adenosine N^6 and N^7, respectively, Asp258 making bidentate contacts with the ribose 2' and 3' hydroxyl groups, and Arg123 and His204 contacting α and β phosphates, respectively. The nucleobase is further secured by the hydrophobic cage formed by Ile208, Phe250, Met251, Val253, Val278, and Leu323. Lys260 bridges the γ-phosphate to the 5-IP_7 1-phosphate and likely stabilizes the phosphorane transition state.

Each of the seven 5-IP_7 phosphates makes at least one contact to a positively charged active site side chain. Those residues are Lys43, Arg223, Lys224, Lys260, Arg274, Arg285, Lys290, Arg293, and Lys341 (Figure 20 and Supplemental Table 2F). Most are positioned in a similar orientation to that of the reference structure with IP_6 and ADPNP. One exception is Arg223, whose guanidium moiety moves ~6 Å relative to its position in the IP_6 structure to make new contacts with the 4- and 5α-phosphates. Arg285 makes bidentate contacts with the 5β-phosphate that were not present in previous structures. The movement of Arg223 stroking inward to form new contacts, coupled to pushing action of

Arg285 on the backside, may be responsible for the 1-phosphate inching ~0.3 Å closer to the ATP γ-phosphate and forming a more apical attack angle.

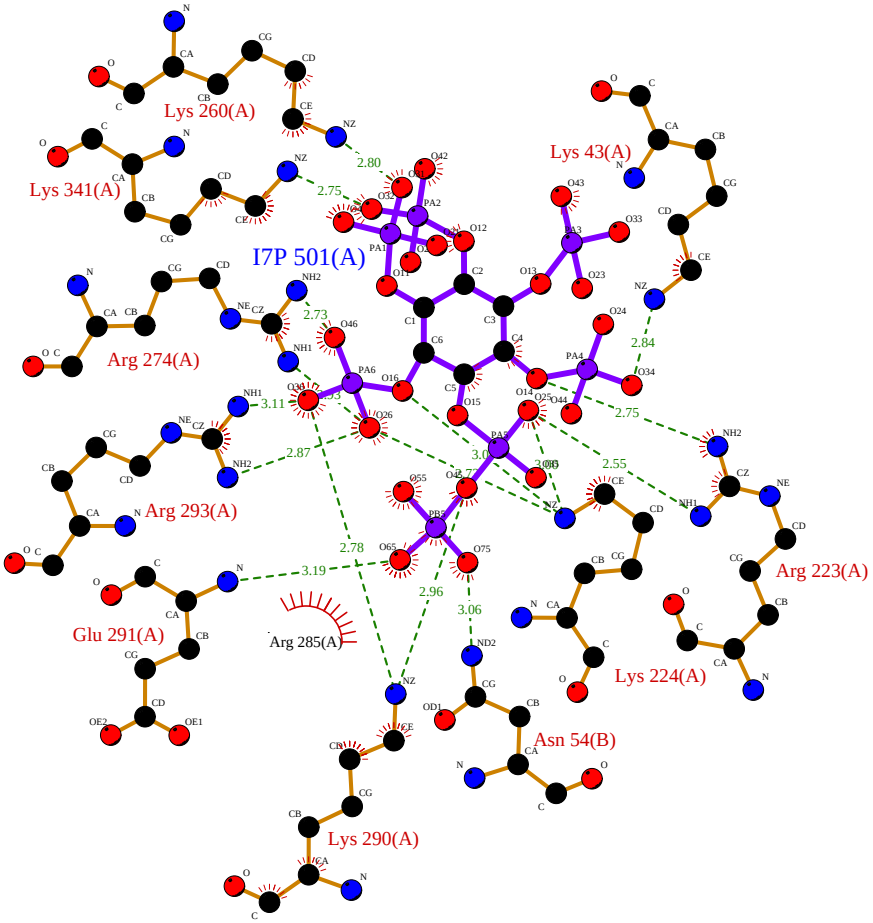

Figure 20. **Ligplot of 5-IP$_7$ in Asp1 active site.** Enzymic contacts were identified by PDBsum on Asp1 kinase PDB ID 8E1I (Asp1 kinase in complex with ATP, IP$_7$, and Mg^{2+}). Ionic and hydrogen bonds are depicted as green dashed lines. Hydrophobic interactions are depicted as red semicircles with red lines. Atoms are depicted as ball and line models with black carbon, blue nitrogen, red oxygen, and purple phosphorus.

The apo protomer in this crystal is held in the open conformation by two additional salt bridges not observed in the structure of Asp1 with ADPNP, IP$_6$, and Mg^{2+}. These salt bridges consist of the following residue pairs: 1) protomer B Arg274 and protomer A Glu157 (2.9 Å) (Figure 21A), 2) protomer B Lys224 and

protomer A Asp345 (3.0 Å) (Figure 21B). These contacts are significant because they include the IPP-binding residues Arg274 and Lys224, whose involvement in salt bridges excludes them from engaging IPP phosphates.

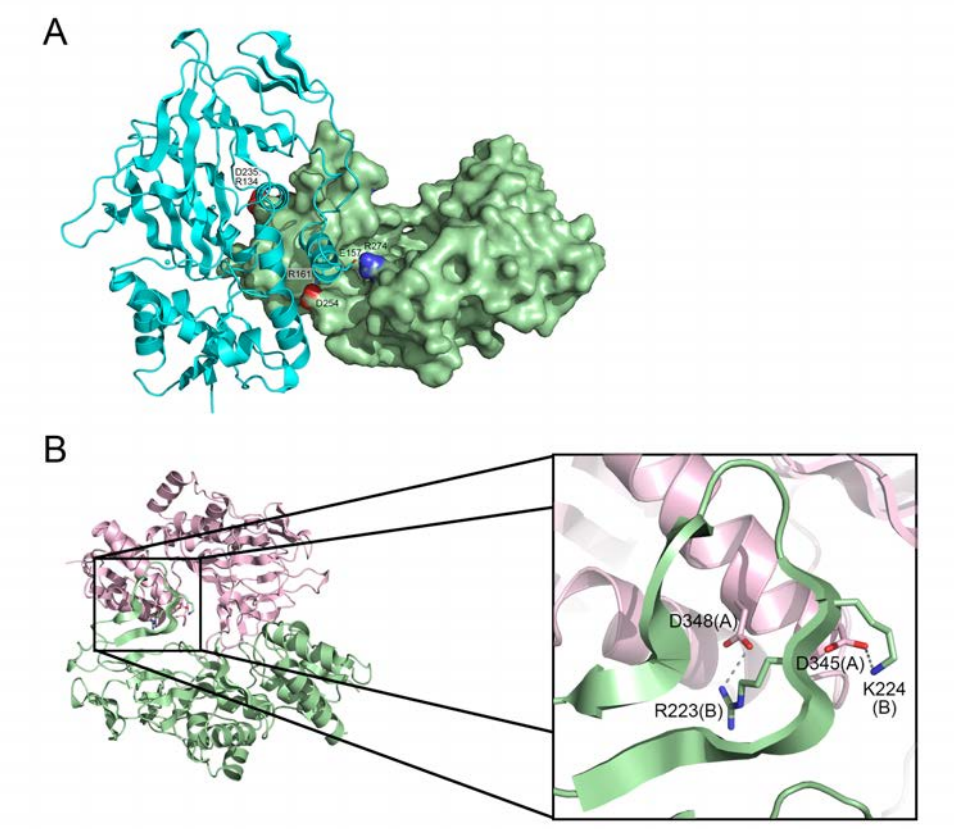

Figure 21. **Asp1 in complex with ATP, 5-IP$_7$, and Mg^{2+} features additional inter-protomer contacts that stabilize mobile lid elements in the open conformation.** (A) Protomers A and B from the structure of Asp1 in complex with ATP, 5-IP$_7$, and Mg^{2+} are depicted as cartoon and surface respectively, with protomer B of the primary ASU on right colored green and protomer A from a symmetry mate colored cyan. Side chains of residues involved in intermolecular salt bridges are represented as sticks with cyan carbons or as surfaces with oxygen highlighted red and nitrogen highlighted blue. Molecular contacts ≤3.5 Å are shown as grey dashed lines. (B) Protomers A and B from the structure of Asp1 in complex with ATP, 5-IP$_7$, and Mg^{2+} are depicted as cartoons, with protomer B of primary ASU on bottom colored green and protomer A from a symmetrical ASU above colored pale pink. (Inset) Interfacial residues are depicted as sticks. Molecular contacts ≤3.5 Å are shown as grey dashed lines.

4.3.7 Structure guided mutagenesis of adenosine-binding residues Lys197, Glu248, and Asp258

Structures of Asp1 in complex with nucleotides highlighted the role of the active site residues Lys197, Glu248, and Asp258 in coordinating the adenosine nucleobase. I sought to determine their contribution to kinase activity by mutating each to alanine. The recombinant Ala-mutants were produced in *E. coli* in parallel with the wild-type Asp1-(1-385). SDS-PAGE analysis of the respective peak Superdex-200 fractions is shown in Figure 22A.

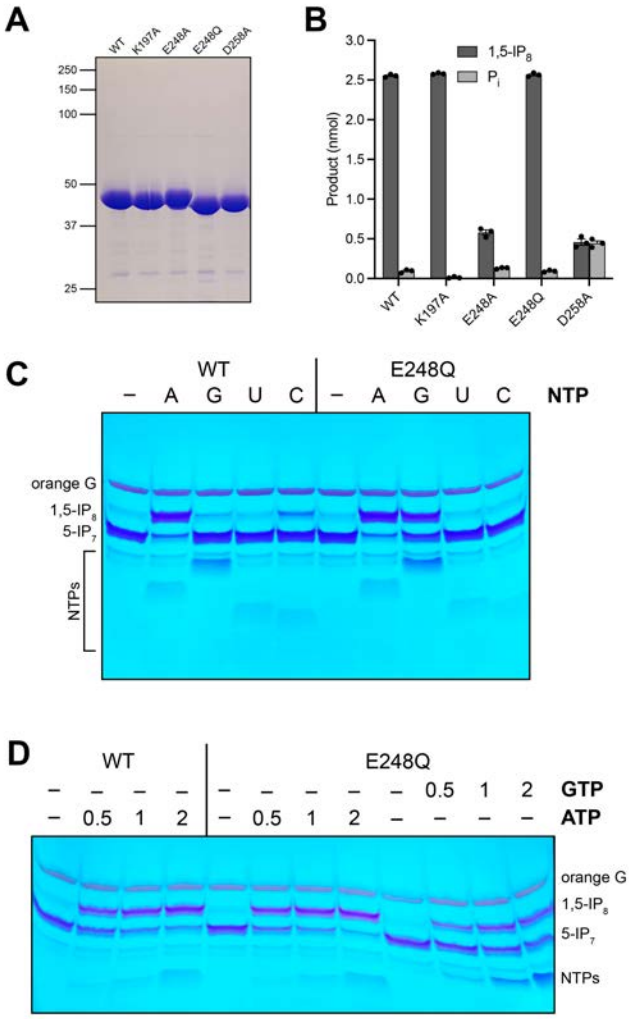

Figure 22. **Structure-guided mutagenesis of Asp1 NTP-binding residues.** (A) Aliquots (5 µg) of wild-type Asp1 kinase domain and the indicated mutants were analyzed by SDS–PAGE. The Coomassie-blue stained gel is shown. The positions and sizes (kDa) of marker polypeptides (leftmost lane) are indicated. (B) Kinase reaction mixtures (20 µL) containing 30 mM Bis-Tris (pH 6.2), 50 mM NaCl, 5 mM $MgCl_2$, 0.25 mM (5 nmol) [γ^{32}P]ATP, 0.5 mM (10 nmol) 5-IP_7, and 2.5 µM (50 pmol) of wild-type Asp1 kinase or the indicated mutants were incubated at 37°C for 15 min. The products were analyzed by TLC. The extents of P_i and 1,5-IP_8 formation are plotted for each enzyme. The data in the bar graph are the averages of three independent experiments ± SEM. (C) 5-IP_7 kinase reaction mixtures (20 µL) containing 30 mM Bis-Tris (pH 6.2), 50 mM NaCl, 5 mM $MgCl_2$, 0.5 mM 5-IP_7, 2 mM NTP as indicated, and 0.5 µM (10 pmol) Asp1 WT or -(E248Q) kinase were incubated at 37°C for 15 min. Reaction products were analyzed by PAGE and detected by toluidine blue staining. (D) 5-IP_7 kinase reaction mixtures (20 µL) containing 30 mM Bis-Tris (pH 6.2), 50 mM NaCl, 5 mM $MgCl_2$, 0.5 mM 5-IP_7, ATP or GTP at indicated concentration (mM), and 0.5 µM (10 pmol) Asp1 WT or -(E248Q) kinase were incubated at 37°C for 15 min. Reaction products were analyzed by PAGE and detected by toluidine blue staining.

Equivalent amounts of wild-type and mutant proteins were assayed for kinase activity with 5-IP_7 and [γ^{32}P]ATP substrates using a TLC-based assay to detect accumulation of radiolabeled 1,5-IP_8 (3). While Lys197Ala retained kinase activity comparable to that of WT, both Glu248Ala and Asp258Ala demonstrated ~80% reduced kinase activity (Figure 22B). These findings evince the essential roles of residues Glu248 and Asp258 in positioning the adenosine moiety.

Catalytically essential Glu248 hydrogen bonds with the adenosine N^6. I previously demonstrated that Asp1 kinase exhibits strong preference for ATP as a phosphate donor (3). We hypothesized that Glu248's negative charge contributed to Asp1 NTP specificity. To test this, I mutated Glu248 to a neutral isosteric residue glutamine. Asp1-(1-385)-Glu248Gln was assayed against WT Asp1 kinase using a PAGE-based assay to detect different IPP species. While WT Asp1 used only ATP to phosphorylate 5-IP_7 to 1,5-IP_8, Asp1 Glu248Gln used both ATP and GTP

(Figure 22C). Titrating NTP concentration, I determined that Asp1 Glu248Gln used ATP as efficiently as did WT (Figure 22D). Furthermore, Asp1 Glu248Gln used GTP less efficiently than ATP. Thus, while Glu248 confers Asp1 kinase's ATP preference, so long as the residue in position 248 can hydrogen bond the purine, negative charge is not necessary for efficient ATP utilization.

4.3.8 Structure guided mutagenesis of IPP-binding residue Lys290

I recently assayed the effect of mutating several predicted IPP-binding residues on Asp1 kinase activity (3). Residues were chosen based off their conservation to Asp1's human homolog PPIP5K2, for which structures were available. Structures of Asp1 showed that two additional residues, Arg274 and Lys290, contact IPP phosphates. In our structure of Asp1 kinase in complex with ATP, 5-IP_7, and Mg^{2+}, Arg274 makes bidentate contact with the 5-IP_7 6-phosphate, while Lys290 contacts both the 5α- and 6-phosphates.

I produced recombinant Ala-mutants in *E. coli* (Figure 23A). Arg274Ala expressed poorly and was not pure enough to evaluate. Lys290Ala was assayed for kinase activity and determined to be as active as WT (Figure 23B). Considering its proximity to the IPP 5-phosphate moiety, I considered that it might play a redundant role with another 5-phosphate binding residue, Arg285, in providing 5-IP_7 substrate specificity. I therefore generated a recombinant Arg285Ala-Lys290Ala double mutant. This mutant demonstrated diminished but still significant 5-IP_7 kinase activity (Figure 23B). Furthermore, while Arg285Ala and Lys290Ala each exhibited slightly higher IP_6 kinase activity than WT (Figure 23B), Arg285Ala-Lys290Ala's IP_6 kinase activity was the same as WT, undermining my

hypothesis that these residues act to block IP_6 utilization in favor of 5-IP_7. I conclude that Arg285 and Lys290 are not essential for Asp1 kinase activity nor are they essential for recognizing the 5β-moiety that distinguishes 5-IP_7 from IP_6.

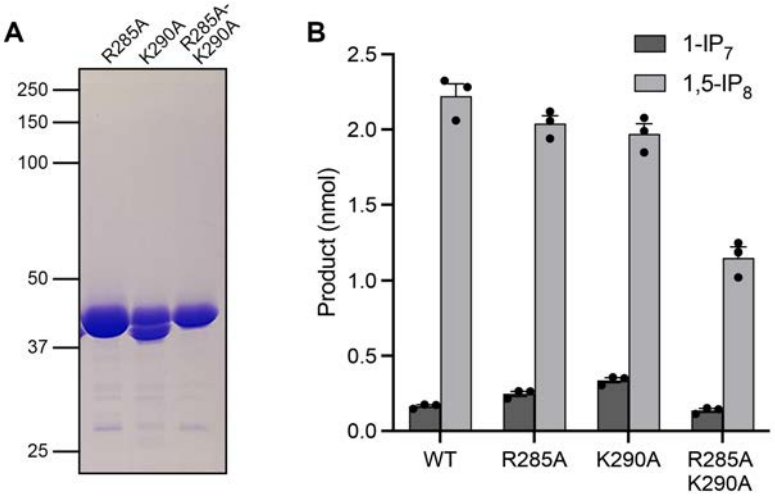

Figure 23. **Structure-guided mutagenesis of Asp1 5-phosphate binding residues.** (A) Aliquots (5 µg) of wild-type Asp1 kinase domain and the indicated alanine mutants were analyzed by SDS–PAGE. The Coomassie-blue stained gel is shown. The positions and sizes (kDa) of marker polypeptides (leftmost lane) are indicated. (B) Kinase reaction mixtures (20 µL) containing 30 mM Bis-Tris (pH 6.2), 50 mM NaCl, 5 mM $MgCl_2$, 0.25 mM (5 nmol) [γ^{32}P]ATP, 0.5 mM (10 nmol) IP_6 or 5-IP_7, and 0.5 µM (10 pmol) of wild-type Asp1 kinase or the indicated mutants were incubated at 37°C for 15 min. The products were analyzed by TLC. The extents of 1-IP_7 formation (in the cases where IP_6 was used as substrate) and 1,5-IP_8 formation (in cases where 5-IP_7 was used as substrate) are plotted for each enzyme. The data in the bar graph are the averages of three independent experiments ± SEM.

4.4 Discussion

Inositol pyrophosphates are signaling molecules utilized by diverse eukaryotic organisms to regulate a variety of cellular processes. Our interest in Asp1 kinase stemmed from our discovery that fission yeast *PHO* gene expression is tuned by inositol pyrophosphate levels through a transcription termination-centric mechanism. Asp1 pyrophosphatase mutations that efface 1,5-IP_8

catabolism de-repress *PHO* genes by causing Pol II to terminate precociously upstream of *PHO* gene promoters. These findings led us to two overarching questions: 1) what is the mechanism linking elevated 1,5-IP_8 concentration to precocious Pol II termination, and 2) does intracellular 1,5-IP_8 flux serve as a means of coupling inorganic phosphate availability to regulation of *PHO* gene expression, and if so, how do cells alter 1,5-IP_8 concentration in response to extracellular inorganic phosphate fluctuations?

Our recent biochemical analysis of Asp1 kinase activity began to answer this second question. While significant information was gleaned from this exercise, our understanding of the enzyme was incomplete due to the absence of structural data. Hints to Asp1 kinase's structure were provided through comparison to its human homolog published by the Shears group (12). Our present report reinforces many of the findings of the initial Shears study, namely the overall fold of the enzyme and the positioning of substrates in the active site, alluding to a one-step mechanism of direct phosphoryl transfer of the ATP γ-phosphate to the IPP 1-phosphate. Asp1 structures increase our understanding of this class of enzymes by contributing key insights into distinct conformational states of the substrate-bound and unbound enzyme, as well as the positioning of the IPP within the active site, thereby informing upon the enzyme's mechanism of substrate binding and how specificity for the 1-phosphate position is achieved.

4.4.1 Asp1 has a mobile lid that closes upon substrate binding

Each of the six structures presented in this study contain two protomers per ASU – one with ligand and one without. This serendipitous finding enabled us to

evaluate differences between the enzyme in substrate-bound and apo states. Two protein features, a 21 amino acid loop and a β-hairpin, constitute a lid over the active site. In the unbound enzyme, the loop is disordered and the hairpin is peeled back, exposing the active site interior to the solvent environment. The mobility of these lid elements enables substrates to easily access their positions for chemistry.

This finding could not have been anticipated from comparison to structures of Asp1's human homolog PPIP5K2. All previously published structures of this enzyme contain ligands and show the enzyme in a closed conformation (12-14). Researchers naturally asked how substrates accessed the active site through such a tight aperture. The Shears group proposed a model in which the IPP substrate would be caught by positively charged residues on the outer rim of the active site, then passed through the opening to the enzyme's interior through the concerted action of several external and internal residues. They based this model off structures in which IPP substrate analogs were captured on the exterior of the active site (14). Molecular dynamics modeling provided further support that this "catch and pass" mechanism was a viable model for IPP active site positioning (13). However, this model also had several inconsistencies and complications. It did not provide an explanation for how nucleotides access the active site. Several residues purported to be involved in the catch and pass process are not conserved in fission yeast Asp1: hsPPIP5K2 Lys53 corresponds to spAsp1 Ala42, hsPPIP5K2 His101 corresponds to spAsp1 Tyr90, and hsPPIP5K2 Lys103 corresponds to spAsp1 Ser92. Finally, only one of several molecular dynamics

simulations demonstrated successful passing of the IPP substrate through the tight aperture of the closed enzyme, presumably because this event is thermodynamically unfavorable. Thus, the “catch and pass” mechanism is an imperfect explanation for how Asp1 binds substrates.

I believe that Asp1’s open conformation is a physiologically relevant orientation rather than an artifact of crystal packing. While proteins may adopt unnatural conformations *in crystallo*, the Asp1 open orientation makes sense mechanistically, filling a gap in our understanding of how substrates access the active site. While certain mobile elements, such as the β11-12 hairpin and nucleobase binding loop, are stabilized in the open orientation by interactions with symmetry mates, their capture in these orientations demonstrates that they are inherently mobile enough to reach the position to form these quaternary interactions. Conversely, the loop defined by residues 275-294 cannot be resolved in the apo conformation, presumably because it is mobile in solution and does not form contacts with crystallographic symmetry mates. No obvious salt bridges or hydrogen bonds exist between the two mobile elements in the closed orientation, decreasing the likelihood that the reorientation of the mobile hairpin causes disordering of the mobile loop. Taken together, we propose that Asp1 adopts distinct open and closed conformations in nature, with the open form enabling substrates to access the active site, and the closed conformation locking substrates in to promote catalysis.

I envision two possible scenarios for how inositol phosphate substrate binding induces transition from open to closed conformation. One possibility is that

the substrate binds to the immobile active site residues Lys43, Lys260, and Lys341 in position for catalysis. Binding creates electrostatic interaction opportunity between the negatively charged phosphates and positively charged residues of the mobile lid, stimulating lid closure. A second possibility is that the mobile elements survey the environment for substrate like the fan of a barnacle. Upon catching the IPP, the mobile elements swing shut, pulling the IPP into catalytic position. Neither model addresses how the closed conformation opens to release products after catalysis, providing a goal for future investigations of this class of enzyme's mechanism of action.

4.4.2 Asp1 kinase binds IPP substrates in a variety of orientations

IP_6 is a symmetrical molecule with a plane of symmetry along its 2-5 carbon axis. The axial 2-phosphate is the only feature keeping this molecule from having 6 axes of symmetry. While this symmetry leads other inositol phosphate kinases and phosphatases to promiscuously (de)phosphorylate several positions around the inositol ring (17-19), Asp1 kinase specifically phosphorylates the 1-phosphate position of IP_6 or 5-IP_7. Our observation that Asp1 binds IPPs in a variety of on- and off-pathway orientations speaks to the challenge the enzyme faces in properly positioning the inositol ring in the appropriate position for catalysis. Our structures are consistent with suppositions made by the Shears group that through concerted flexing movement, active site residues move and rotate the IPP so that the 1-phosphate faces the ATP γ-phosphate (14). I interpret the diffuse electron density we frequently observe around the IPP to mean that we are crystallizing millions of subtly different conformations of IPP as it moves into position for catalysis.

That the IPP rotates within the active site provides an intuitive explanation for why 5-IP_7 is a better phosphoacceptor substrate than is IP_6. While the equatorial orientation of the 2-phosphate provides a single 'handle' for the active site to determine the position of the 1-phosphate, having a second handle in the form of a 5-pyrophosphate moiety likely facilitates positioning of the 1-phosphate into the correct orientation for catalysis. Indeed, only when 5-IP_7 was crystallized in a pseudo-Michaelis complex did we observe each of the IPP phosphates neutralized by each of the nine IPP binding residues. Any off-pathway orientation or IP_6-containing crystal showed at least one IPP phosphate or IPP-binding side chain lacking a complementary charged binding mate. Thus, correct orientation of 5-IP_7 for catalysis entails maximum charge neutralization.

4.5 Materials and Methods

4.5.1 Recombinant Asp1 proteins

Asp1-(31-364) was cloned into the pET28b-His_{10}Smt3 vector and transformed into BL21(DE3) cells. A 3.2 liter culture amplified from single transformants was grown at 37°C in Terrific Broth containing 50 μg/mL kanamycin until A_{600} reached 0.8, then adjusted to 2% (vol/vol) ethanol and placed on ice for 30 min. Asp1 kinase expression was induced by adding isopropyl ß-D-1-thiogalactopyranoside (IPTG) to 0.25 mM and incubating the cultures overnight at 17°C with constant shaking. Cells were harvested by centrifugation and resuspended in buffer A (50 mM Tris-HCl pH 8.0, 500 mM NaCl, 10% glycerol) containing 10 mM imidazole and one cOmplete Protease Inhibitor Cocktail tablet

(Roche) at a volume of 25 mL per L of culture. All subsequent purification procedures were performed at 4°C. Cell lysis was achieved by adding lysozyme to 0.5 mg/mL and incubating for 1 h, followed by sonication to reduce viscosity. The lysate was centrifuged at 38,000g for 45 min and the supernatant was mixed with 5 mL of Ni-NTA-agarose resin (Qiagen) that had been equilibrated in buffer A with 10 mM imidazole. After 1 h of mixing on a nutator, the resin was recovered by centrifugation and washed twice with 50 mL of buffer A containing 20 mM imidazole. The washed resin was poured into a column and the bound protein was eluted with 250 mM imidazole in buffer A. The elution of His_{10}Smt3-Asp1-(31-364) protein was monitored by SDS-PAGE. The His_{10}Smt3 tag was cleaved by treatment with Ulp1 protease (100 µg Ulp1 per L of bacterial culture) during overnight dialysis against buffer A with 20 mM imidazole. Asp1-(31-364) was separated from the His_{10}Smt3 tag by a second round of Ni-affinity chromatography, during which Asp1-(31-364) was recovered in the flow-through fraction. Tag-free Asp1 kinase was concentrated to a volume of 5 mL by centrifugal ultrafiltration and then applied to a Hiload Superdex 200 pg 16/600 column (Cytiva Life Sciences) equilibrated in buffer B (30 mM HEPES, pH 6.8, 150 mM NaCl, 1 mM DTT). The peak Superdex fractions of Asp1-(31-364) were concentrated by centrifugal ultrafiltration and stored at −80°C. Protein concentrations were determined by using the Bio-Rad dye reagent with BSA as the standard.

The coding sequences for Asp1 mutants were generated by tandem overlap PCR and cloned into the pET28b-His_{10}Smt3 vector. The presence of the desired mutations and lack of additional mutations was confirmed by Sanger sequencing.

IPTG induction of mutant kinase expression and purification from soluble bacterial lysates was performed as described above for Asp1-(31-364).

4.5.2 Crystallization

4.5.2.1 Asp1 kinase • ADPNP • $MgCl_2$ • IP_6

A solution containing 4 mg/mL protein, 5 mM $MgCl_2$, 1 mM ADPNP, and 1 mM IP_6 was preincubated on ice for 30 minutes. Aliquots (3 µL) were then mixed with 3 µL of precipitant solution containing 0.1 M bis-tris (pH 5.5), 0.1 M NH_4OAc, 17% PEG 10,000. Crystals were grown by sitting drop vapor diffusion at room temperature. Crystals grew over one week and were harvested within one week of observation. Crystals were cryoprotected in precipitant solution supplemented with 25% ethylene glycol for one minute and then flash-frozen in liquid nitrogen.

4.5.2.2 Asp1 kinase • ADPNP• $MnCl_2$ • IP_6

A solution containing 4 mg/mL protein, 5 mM $MnCl_2$, 1 mM ADPNP, and 1 mM IP_6 was preincubated on ice for 30 minutes. Aliquots (3 µL) were then mixed with 3 µL of precipitant solution containing 0.1 M bis-tris (pH 5.9), 0.025 M NH_4OAc, and 17% PEG 10,000. Crystals were grown by sitting drop vapor diffusion at room temperature. A single crystal grew over one week. That crystal was manually crushed during harvesting and the well was re-sealed. Additional crystals seeded from crushed crystal shards grew and were harvested over the next week. Crystals were cryoprotected in precipitant solution supplemented with 25% ethylene glycol and 5 mM $MnCl_2$ for one minute and then flash-frozen in liquid nitrogen.

4.5.2.3 Asp1 kinase • ADP • $MgCl_2$ • 5-IP_7

A solution containing 4 mg/mL protein, 5 mM $MgCl_2$, 1 mM ATP, and 1 mM 5-IP_7 (chemically synthesized) was preincubated on ice for 30 minutes. Aliquots (2 µL) were then mixed with 2 µL of precipitant solution containing 0.1 M bis-tris propane (pH 8.1), 0.15 M NaF, and 20% PEG 3,350. Crystals were grown by sitting drop vapor diffusion at room temperature. Crystals grew over one week and were harvested within one week of observation. Crystals were cryoprotected in precipitant solution supplemented with 25% glycerol, 5 mM $MgCl_2$, 1 mM 5-IP_7, 1 mM ATP for one minute and then flash-frozen in liquid nitrogen.

4.5.2.4 Asp1 kinase • ADPNP • $MgCl_2$ • 5-IP_7

A solution containing 4 mg/mL protein, 5 mM $MgCl_2$, 1 mM ADPNP, and 1 mM 5-IP_7 (chemically synthesized) was preincubated on ice for 30 minutes. Aliquots (2 µL) were then mixed with 2 µL of precipitant solution containing 0.1 M bis-tris propane (pH 8.4), 0.15 M NaF, and 20% PEG 3,350. Crystals were grown by sitting drop vapor diffusion at room temperature. Crystals grew over one week and were harvested within one week of observation. Crystals were cryoprotected in precipitant solution supplemented with 25% glycerol, 5 mM $MgCl_2$, 1 mM 5-IP_7, 1 mM ADPNP for one minute and then flash-frozen in liquid nitrogen.

4.5.2.5 Asp1 kinase • IP_8

A solution containing 4 mg/mL protein, 10 mM $MgCl_2$, 1 mM N^6-benzyl ATP (Jena Biosciences), and 1 mM 5-IP_7 (chemically synthesized) was preincubated at room temperature for 30 minutes. Aliquots (2 µL) were then mixed with 2 µL of

precipitant solution containing 0.1 M bis-tris propane (pH 6.9), 0.3 M NaF, and 20% PEG 3,350. Crystals were grown by sitting drop vapor diffusion at room temperature. Crystals grew over one week and were harvested within one week of observation. Crystals were cryoprotected in 0.05 M bis-tris propane (pH 6.6), 0.1 M NaF, 10 mM $MgCl_2$, 20% PEG 3,350, and 25% ethylene glycol for one minute and then flash-frozen in liquid nitrogen.

4.5.2.6 Asp1 kinase K47A R50A • ATP • MgCl2 • 5-IP7

A solution containing 6 mg/mL protein, 10 mM $MgCl_2$, 1 mM ATP, and 1 mM 5-IP_7 (chemically synthesized) was preincubated at room temperature for 30 minutes. Aliquots (2 µL) were then mixed with 2 µL of precipitant solution containing 0.05 M bis-tris propane (pH 7.8), 0.1 M NaF, and 20% PEG 3,350. Crystals were grown by sitting drop vapor diffusion at room temperature. Crystals grew over one week and were harvested within one week of observation. Crystals were cryoprotected in precipitant solution at pH 6.6 supplemented with 25% ethylene glycol and 10 mM $MgCl_2$ for one minute and then flash-frozen in liquid nitrogen.

4.5.3 Structure determination

Structure determination was performed by or under the supervision of Yehuda Goldgur. X-ray diffraction data was collected from a single crystal at APS beamline 24ID-E. The data were integrated with HKL2000 (20). Phases were obtained in Phenix (21) by molecular replacement using the Phyre2 model based on the structure of the catalytic domain of the catalytic domain of PPIP5K2 (pdb ID

4NZM) as the search probe (14). Iterative model building into electron density was performed with O (22). Refinement was accomplished with Phenix (21). Data collection and refinement statistics are presented in Supplementary Table 1.

4.5.4 TLC assay of Asp1 kinase and ATPase activity

Reaction mixtures (20 µL) containing 30 mM Bis-Tris (pH 6.2), 50 mM NaCl, 5 mM $MgCl_2$, 0.25 mM [γ^{32}P]ATP, 0.5 mM IP_6 (phytic acid; Sigma P-8810-10G, lot BCBZ7573) or 5-IP_7 (synthesized as described (23-25)) at concentrations specified in the figure legends were incubated at 37°C. Reactions were initiated by addition of Asp1 and quenched at the times specified by adjustment to 25 mM EDTA. Aliquots (2 µL) were applied to a PEI-cellulose TLC plate (Millipore-Sigma), and the products were resolved by ascending TLC with 1.7 M ammonium sulfate as the mobile phase. The radiolabeled ATP substrate and P_i and IPP products were visualized by autoradiography or visualized and quantified by scanning the TLC plate with a Typhoon FLA7000 imager and ImageQuant-TL software.

4.5.5 PAGE assay of Asp1 kinase activity

Reaction mixtures (20 µL) containing 30 mM Bis-Tris (pH 6.2), 50 mM NaCl, 5 mM $MgCl_2$, ATP, and IP_6 or 5-IP_7 as specified in the figure legends were incubated at 37°C. Reactions were initiated by addition of Asp1 and terminated after 15 minutes by adjustment to 25 mM EDTA. The samples were mixed with an equal volume of 2× Orange G loading buffer (10 mM Tris-HCl, pH 7.0, 1 mM EDTA, 30% glycerol, 0.1% Orange G dye) and then analyzed by electrophoresis (at 4°C at 8 W constant power) through a 20-cm 36% polyacrylamide gel containing 80 mM

Tris-borate, pH 8.3, 1 mM EDTA until the Orange G dye reached 2/3 of the length of the gel. The gel was briefly washed with water and then stained with a solution of 0.1% Toluidine blue (Sigma), 20% methanol, 2% glycerol, followed by destaining in 20% methanol.

4.6 Supporting information

4.6.1 Supplemental Table 1: Crystallographic data and refinement statistics

Supplemental Table 1: Crystallographic data and refinement statistics

	AMPPNP•Mg•IP6	AMPPNP•Mg•5-IP7	AMPPNP•[Mn,Mn]•IP6	ADP•[Mg,Mg]•5-IP7	IP8	K47A R50A IP7 ATP Mg
Beamline	24ID-E 03/22 66-5	24ID-E 04/26 3-8	24ID-E 04/13 I/7-15	24ID-E 04/26 2-11	24ID-C 07/31 5-15	24ID-C 07/31 1-13
Space group	$P2_1$	$P2_1$	$P2_1$	$P2_1$	$P2_1$	$P2_1$
Cell dimensions a, b, c (Å) α, β, γ (°)	47.56, 86.99, 86.29 90, 95.2, 90	47.60, 87.51, 85.99 90, 94.8, 90	48.08, 87.78, 86.05 90, 94.9, 90	47.60, 87.12, 86.03 90, 94.7, 90	47.86, 88.00, 86.18 90, 94.2, 90	47.78, 88.50, 86.60 90, 94.8, 90
Resolution (Å)	50-1.9 (1.93-1.90)	50-1.7 (1.74-1.70)	50-1.7 (1.74-1.70)	50-1.9 (1.93-1.90)	50-1.6 (1.63-1.60)	50-2.0 (2.03-2.0)
Wavelength (Å)	0.9792	0.9792	0.9792	0.9792	0.9792	0.9792
R_{sym}	0.040 (0.334)	0.033 (0.278)	0.035 (0.380)	0.052 (0.346)	0.031 (0.333)	0.031 (0.401)
CC(1/2)	0.993 (0.543)	0.995 (0.784)	0.996 (0.601)	0.994 (0.804)	0.995 (0.732)	0.998 (0.697)
<I>/<σI>	26.6 (2.2)	29.1 (3.2)	31.3 (2.0)	25.2 (2.6)	38.3 (2.5)	32.2 (2.6)
Completeness (%)	98.7 (99.3)	95.9 (87.8)	97.7 (69.8)	95.2 (97.6)	98.0 (97.8)	98.6 (98.9)
Redundancy	4.0 (3.9)	3.9 (3.7)	4.2 (3.4)	2.9 (2.6)	4.2 (4.3)	4.3 (4.4)
Unique reflections	54255	72264	75427	52215	91920	48016
Refinement						
R_{work} / R_{free}	0.197 / 0.226	0.182 / 0.213	0.176 / 0.205	0.197 / 0.234	0.193 / 0.219	0.195 / 0.235
B-factors (Å^2) Average/Wilson	34.6 / 26.9	25.7/ 18.8	27.5 / 20.8	36.7 / 29.6	28.8 / 22.4	39.2 / 31.8
RMS deviations bond lengths (Å) bond angles (°)	0.010 1.15	0.007 1.026	0.008 1.09	0.008 1.06	0.008 1.06	0.010 1.06
Ramachandran % favored % allowed outliers	97.6 2.4 0	98.3 1.7 0	98.8 1.2 0	98.6 1.4 0	98.7 1.3 0	97.7 2.3 0
Model contents						
Protomers/ASU	2	2	2	2	2	2
Protein residues	640	647	647	647	641	646
Ions	1	1	2	3	0	2
Ligands	2	2	2	2	1	2
Water	460	661	725	416	710	419
PDB ID	8E1V	8E1T	8E1S	8E1H	8E1J	8E1I

4.6.2 Supplemental Table 2: Coordination distances of IPPs by Asp1 active site residues.

A

8E1V - Asp1 + ADPNP, IP6, and Mg2+		
Active site residue	**IP6 phosphate contact**	**Distance (Å)**
K43	3	3.4
K43	3	3.5
K224	5	3
K260	1	3.3
R274ηN1	6	2.6
K290	5	3.2
K290	6	2.5
R293ηN1	6	2.7
R293ηN2	6	2.9
K341	2	3.3
apo-K47	4	3.3
apo-R50ηN1	4	2.8
apo-R50ηN2	5	2.9
Attack distance	4.7Å	
Attack angle	141.2°	

B

		8E1S - Asp1 + ADPNP, IP6, and Mn2+				
On-pathway				**Off-pathway**		
Active site residue	**IP6 phosphate contact**	**Distance (Å)**		**Active site residue**	**IP6 phosphate contact**	**Distance (Å)**
K43	3	3.4		K43	6	2.4
K43	3	3.4		K43	5	3.5
K43	4	3.4		R223	5	3
R223	3	2.6		K224	2	2.8
R223	3	3.4		K224	3	3.3
K224	6	3.3		R274ηN1	2	2.8
R274ηN1	1	3.3		R274ηN2	2	3
R274ηN2	1	3.5		R274ηN2	2	3.4
R293ηN1	6	2.8		R285ηN1	3	2.8
R293ηN2	6	3.2		R285ηN2	3	3.4
K341	2	3.2		K290	1	3
				R293ηN1	2	3
	Attack distance	4.9Å		K341	6	3.5
	Attack angle	155.5°				

C

8E1T - Asp1 + ADPNP, 5-IP7, and Mg2+		
Active site residue	**5-IP7 phosphate contact**	**Distance (Å)**
K43	5β	3.3
K43	6	2.9
K224	3	2.8
K224	3	3
K224	4	2.3
R274ηN1	2	2.9
R274ηN2	2	2.9
R285ηN1	3	3
R285ηN2	3	3.3
K290	1	2.3
K290	6	2.5
R293ηN1	2	2.8
R293ηN2	2	3.4
K341	1	3.4
apo-K47	1	3.4

D

8E1H - Asp1 + ADP, 5-IP7, and Mg2+		
Active site residue	**5-IP7 phosphate contact**	**Distance (Å)**
K43	5α	3.3
K43	5α	3.3
K43	6	3.5
R223ηN1	5β	2.3
R223ηN2	5β	2.8
K224	2	3
K224	3	3.1
K224	3	3.1
K224	4	2.8
R274ηN1	2	3
R274ηN2	2	3.4
R285ηN1	3	2.9
R285ηN2	3	3.2
R293	2	3.2
K341	1	2.7
K341	1	2.8
K341	6	2.6
apo-K47	1	2.8

E

8E1J - Asp1 + 1,5-IP8		
Active site residue	**IP8 phosphate contact**	**Distance (Å)**
K43	5	3
K43	5	3.1
K43	6	2.7
R223ηN1	1α	2.5
R223ηN2	1β	2.8
R223εN	5β	3.2
K224	1β	2.8
K224	3	2.6
R274ηN1	3	2.3
R274ηN2	3	2.7
R285ηN1	1β	2.9
R285ηN2	1β	3
K290	1β	3
K290	2	3
R285ηN1	3	2.9
R285ηN2	3	3.1
K341	3	3.5
K341	4	3.1
apo-K47	1α	2.6
apo-K47	1α	2.8
apo-K47	2	2.7
apo-K47	6	2.8
apo-R50ηN1	6	3
apo-R50ηN1	6	3.4

F

8E1I - Asp1 K47A R50A + ATP, 5-IP7, and Mg2+		
Active site residue	**5-IP7 phosphate contact**	**Distance (Å)**
K43	2	3.3
K43	3	2.8
K43	4	2.8
R223ηN1	4	2.8
R223ηN1	5α	3.3
R223ηN2	5α	2.5
K224	5α	3
K224	6	2.7
K260	1	2.8
K260	1	3.2
R274ηN1	6	2.7
R274ηN2	6	2.9
R285ηN1	5β	3
R285ηN2	5β	3.4
K290	5α	3
K290	6	2.8
R293ηN1	6	2.9
R293ηN1	6	3.1
K341	2	2.7
Attack distance	4.4 Å	
Attack angle	141.2°	

Supplemental Table 2. **Coordination distances of IPPs by Asp1 active site side residues.** Asp1 active site residues that bind IPP phosphates at a distance of ≤3.5 Å are listed next to IPP phosphates they bind and the distance of the interaction.

Chapter 5: Activity of Asp1 Pyrophosphatase

5.1 Abstract

Inositol pyrophosphates are signaling molecules with pleiotropic roles in a variety of cellular processes. In fission yeast, 1,5-IP_8 flux changes phosphate homeostasis gene expression by influencing RNA Polymerase II termination behavior. 1,5-IP_8 levels are determined by Asp1, a bifunctional enzyme whose N-terminal kinase catalyzes the phosphorylation of 5-IP_7 to 1,5-IP_8 and C-terminal pyrophosphatase (PPase) dephosphorylates 1,5-IP_8 back to 5-IP_7. Deactivation of the PPase reduces 1,5-IP_8 catabolism, leading to its accumulation. I set out to biochemically characterize the Asp1 PPase domain. Using recombinant Asp1 PPase proteins, I demonstrate that the PPase activity is specific to the 1-phosphate position of 1,5-IP_8 or 1-IP_7. PPase activity is metal independent and resistant to EDTA treatment. Consistent with expectations that the enzyme is a histidine acid phosphatase, the activity was optimal between pH 4.5-5.0.

5.2 Introduction

Asp1 is the sole agent of 1,5-IP_8 biosynthesis in fission yeast (1, 2). Its N-terminal kinase converts 5-IP_7 to 1,5-IP_8 by pyrophosphorylating the phosphate at position ‘1’ on the inositol ring (3, 4). 1,5-IP_8 is catabolized by dephosphorylation of the β-phosphate at either the 5-phosphate position by the Nudix-family hydrolase Aps1 or the 1-phosphate position by Asp1’s C-terminal PPase (2, 3). Mutations that efface Asp1 PPase activity dysregulate phosphate homeostasis, suggesting a role of 1,5-IP_8 in these processes (5, 6).

The fission yeast phosphate homeostasis regulon (*PHO*) is controlled by transcriptional interference (7). During phosphate rich conditions, transcription of lncRNAs upstream of the three *PHO*-responsive genes blocks RNA polymerase II (Pol2) from accessing the promoters of protein-coding genes, keeping their expression low. During phosphate starvation, *PHO* lncRNA transcription shuts off, enabling Pol2 to transcribe *PHO* mRNAs, resulting in accumulation of proteins involved in extracellular phosphate scavenging.

PHO gene expression can be used as a gauge of transcription termination efficacy (8). Mutations that cause precocious *PHO* lncRNA transcription termination upregulate *PHO* genes (5, 9). Conversely, mutations that decrease *PHO* lncRNA termination downregulate *PHO* genes. This connection enabled us to uncover a link between cellular 1,5-IP_8 concentration and Pol2 termination efficiency. High levels of 1,5-IP_8 cause precocious termination, while low 1,5-IP_8 causes defective termination. Combining 1,5-IP_8 PPase mutations in the presence of an active Asp1 kinase was lethal, presumably due to the toxic accumulation of 1,5-IP_8 (6). This lethality could be relieved by mutating inessential components of the mRNA cleavage and polyadenylation factor (CPF), indicating that 1,5-IP_8's lethality is linked to its ability to promote precocious transcription termination.

We became interested in the biochemistry of Asp1, which is an intriguing enzyme by virtue of its unique domain structure (oppositional N-terminal kinase and C-terminal PPase) and the lack of understanding of its regulation (for 1,5-IP_8 levels to fluctuate in response to environmental signals, the kinase or PPase activities must be themselves tunable). I performed a structure-function analysis

of the kinase domain and began to evaluate the full-length enzyme, demonstrating that in the full-length context, PPase activity is inhibited by physiologically relevant concentrations of inorganic phosphate. In the present report, I begin to characterize the isolated PPase domain.

5.3 Results

5.3.1 Purification of recombinant Asp1 pyrophosphatase

We performed an in-silico analysis of Asp1's PPase domain; it is predicted to belong to the histidine acid phosphatase family of enzymes, which encompasses other inositol phosphate phosphatases (phytases) (3, 4, 10, 11). Using a predicted structure of the full-length enzyme generated by Alphafold (12, 13), I chose residue 383 as an N-terminal demarcation for a PPase construct. I produced the C-terminal PPase domain of Asp1 (aa 383–920) in *E. coli* as a His_{10}Smt3 fusion and isolated the protein from a soluble bacterial extract by adsorption to a Ni-agarose column and elution with imidazole. I did not use any protease inhibitors during protein purification because chloromethylketones present in commercial protease inhibitor cocktails may inhibit 1-PPase activity (3); yield was sufficient that inclusion of protease inhibitors was unnecessary. The His_{10}Smt3 was removed by treatment with the Smt3 protease Ulp1 and the tag-free native Asp1 PPase protein was separated from the tag during a second round of Ni-affinity chromatography. Final purification was achieved by Superdex-200 gel filtration (Figure 1). The elution profile of the PPase polypeptide (62 kDa) was consistent with it being a monomer in solution. It appeared rusty brown in solution

during purification, consistent with reports that Asp1 PPase hosts a [2Fe•2S] cluster (14, 15).

I also produced a longer PPase construct, 365-920, in tandem. This protein lacked PPase activity, so I did not pursue it further (data not shown).

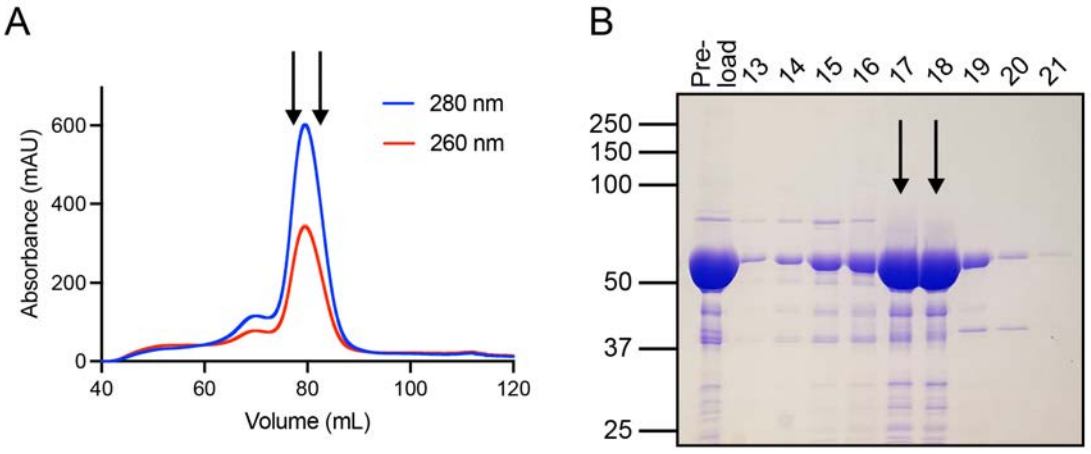

Figure 1. **Recombinant Asp1 pyrophosphatase.** (A) Elution profile of Asp1-(383-920) during Superdex-200 gel filtration, with absorbance at 280 nm (blue trace) and 260 nm (red trace) as a function of elution volume. The A_{260}=A_{280} peak at 50 mL demarcates the void volume. (B) Aliquots (4 µL) of the fractions spanning and flanking the A_{280} peak were analyzed by SDS-PAGE. The Coomassie blue-stained gel is shown. The positions and sizes (kDa) of marker proteins are indicated on the left. The fractions corresponding to the A_{280} peak containing purified Asp1 pyrophosphatase is indicated by vertical arrows.

5.3.2 Characterization of pyrophosphatase activity

I evaluated Asp1 PPase inositol pyrophosphate (IPP) substrate specificity using a PAGE-based assay capable of separating different IPP species (16). Recombinant protein was incubated for 30 min with 0.5 mM IPP and 2 mM Mg^{2+} at pH 5.0. Reactions were then immediately analyzed by 36% PAGE and products

were visualized by toluidine blue staining. Full-length Asp1 was included as a positive control. Asp1 PPase robustly converted 1,5-IP_8 to IP_7, with a small amount of IP_6 being produced (Figure 2). Activity was weaker yet still significant using 1-IP_7. Only feeble PPase activity was exhibited toward 5-IP_7. Activity of the isolated PPase domain and full-length Asp1 were comparable. These data show that Asp1 PPase is more active toward the IPP 1-pyrophosphate position than the 5-pyrophosphate position.

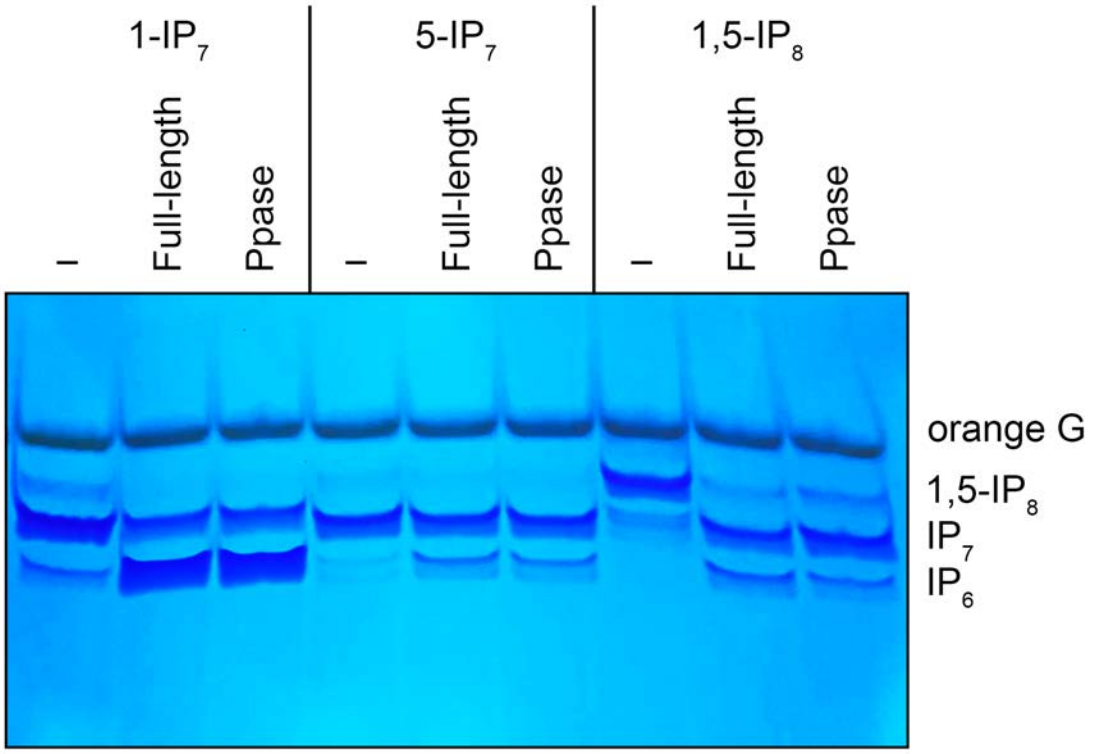

Figure 2. **PPase activity against different IPP species.** Phosphatase reaction mixtures (20 µL) containing 30 mM Tris-Acetate (pH 5.0), 50 mM NaCl, 2 mM $MgCl_2$, 0.25 mM 1-IP_7 5-IP_7, or 1,5-IP_8, and 2.5 µM indicated Asp1 enzyme were incubated at 37°C for 30 min. Reaction products were analyzed by PAGE and detected by toluidine blue staining.

I next titrated Asp1 PPase. Dephosphorylation of 1-IP_7 to IP_6 correlated with protein concentration (Figure 3). The nature of the PAGE-based assay precludes

quantitative assessment of product formation, thereby preventing determination of enzyme kinetics. However, the 30-minute reaction containing 0.25 mM substrate appeared to saturate at a concentration of 1.25 μM enzyme.

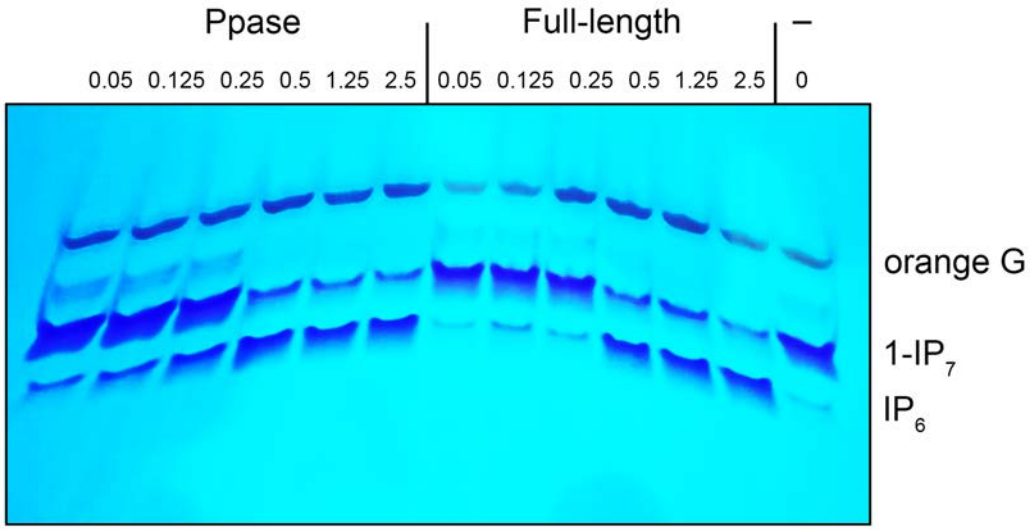

Figure 3. **Pyrophosphatase and full-length titration.** Phosphatase reaction mixtures (20 μL) containing 30 mM Tris-Acetate (pH 5.0), 50 mM NaCl, 2 mM $MgCl_2$, 0.25 mM 1-IP_7, and Asp1 PPase or full-length enzyme at the indicated concentration (μM) were incubated at 37°C for 30 min. Reaction products were analyzed by PAGE and detected by toluidine blue staining.

I performed a pH curve to evaluate the effect of varying pH on Asp1 PPase's activity against 1-IP_7. Dephosphorylation occurred within a window between pH 4.5-6.5, with peak activity at 4.5-5.0 (Figure 4). These findings are consistent with the expectation that Asp1 PPase is a histidine acid phosphatase, which are optimally active below pH 7.0 (17).

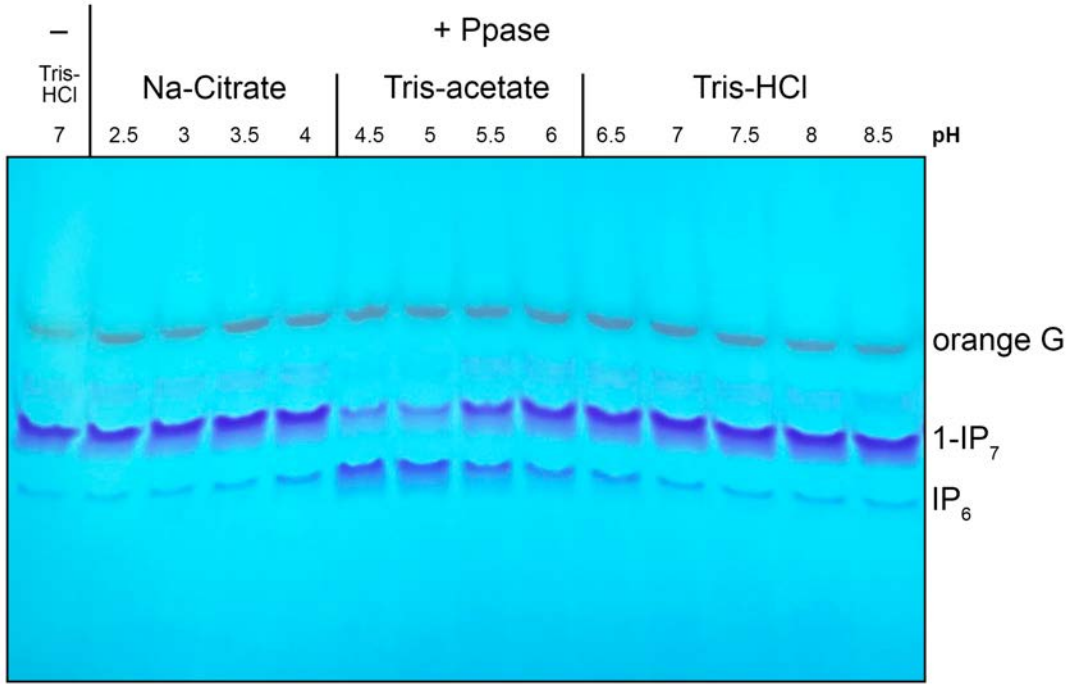

Figure 4. **pH profile.** Phosphatase reaction mixtures (10 µL) containing 30 mM buffer at indicated pH, 50 mM NaCl, 2 mM $MgCl_2$, 0.5 mM 1-IP_7, and 1 µM Asp1 PPase (or no enzyme) were incubated at 37°C for 30 min. Reaction products were analyzed by PAGE and detected by toluidine blue staining.

I next evaluated whether Asp1 PPase required a metal cofactor for catalysis. I first tested Asp1 PPase activity against 1-IP_7 in the absence of exogenously supplied metal. Asp1 PPase was as active without Mg^{2+} as it was with Mg^{2+}, indicating that the activity does not require exogenous metal ions (Figure 5A). To rule out the possibility that Asp1 PPase retained a metal cofactor acquired during *E. coli* expression, I repeated the assay including EDTA. PPase activity was insensitive to EDTA treatment, suggesting that the activity is metal independent (Figure 5B). As EDTA should also chelate iron, this assay further demonstrates that Asp1's [2Fe•2S] cluster is inessential for PPase activity *in vitro*.

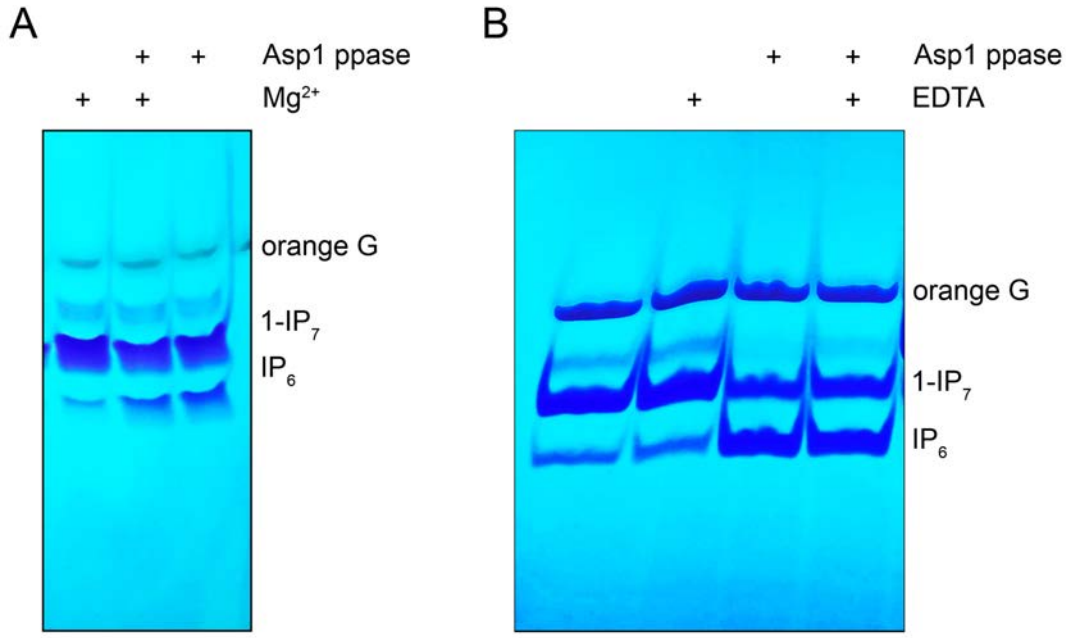

Figure 5**. Metal independence.** (A) Phosphatase reaction mixtures (10 µL) containing 30 mM tris-acetate pH 5.0, 50 mM NaCl, 2 mM $MgCl_2$ where indicated, 0.5 mM 1-IP_7, and 1 µM Asp1 ppase (or no enzyme) were incubated at 37°C for 30 min. Reaction products were analyzed by PAGE and detected by toluidine blue staining. (B) Phosphatase reaction mixtures (20 µL) containing 30 mM tris-acetate pH 5.0, 50 mM NaCl, 5 mM EDTA where indicated, 0.5 mM 1-IP_7, and 1 µM Asp1 PPase (or no enzyme) were incubated at 37°C for 15 min. Reaction products were analyzed by PAGE and detected by toluidine blue staining.

5.4 Discussion

Asp1's two enzymatic activities, 1-phosphate kinase and 1-pyrophosphate PPase, are inherently oppositional. After performing a thorough biochemical and structural evaluation of the kinase activity in the isolated kinase domain, it was natural to investigate the activity of the isolated PPase domain. All evidence supports the idea that Asp1 PPase is a histidine acid phosphatase specific for the 1-pyrophosphate of 1,5-IP_8 and 1-IP_7, although weak activity against 5-

pyrophosphate position demonstrates some positional flexibility in substrate utilization.

Further investigation will evaluate whether this domain possesses ATP hydrolase activity, determine the binding kinetics of different substrates into the PPase active site, and gauge the effect of mutating individual active site residues on kinase activity. While mechanistic insight provided from structures of the PPase domain or full-length kinase/PPase protein would shed light upon this enzyme's mechanism of action, those enzymes have resisted crystallization. Structure solution, perhaps by cryogenic electron microscopy, of the full-length enzyme would inform upon the physical relationship between PPase and kinase. As kinase and/or PPase activity must be modulated to enable net accumulation of 1,5-IP_8, structures of the PPase would also provide researchers with clues into the nature of PPase regulation.

5.5 Materials and Methods

5.5.1 Recombinant Asp1 pyrophosphatase

Asp1-(383-920) was cloned into the pET28b-His_{10}Smt3 vector and transformed into BL21(DE3) cells. A 1.6 liter culture amplified from a single transformant was grown at 37°C in Terrific Broth containing 50 µg/mL kanamycin until A600 reached 0.8, then adjusted to 2% (vol/vol) ethanol and placed on ice for 30 min. Asp1 PPase expression was induced by adding isopropyl ß-D-1-thiogalactopyranoside (IPTG) to 0.25 mM and incubating the culture overnight at 17°C with constant shaking. Cells were harvested by centrifugation and

resuspended in 40 mL of buffer A (50 mM Tris-HCl pH 8.0, 500 mM NaCl, 10% glycerol) containing 10 mM imidazole. All subsequent purification procedures were performed at 4°C. Cell lysis was achieved by adding lysozyme to 0.5 mg/mL and incubating for 1 h, followed by sonication to reduce viscosity. The lysate was centrifuged at 38,000g for 45 min and the supernatant was mixed with 5 mL of Ni-NTA-agarose resin (Qiagen) that had been equilibrated in buffer A with 10 mM imidazole. After 1 h of mixing on a nutator, the resin was recovered by centrifugation and washed twice with 50 mL of buffer A containing 20 mM imidazole. The washed resin was poured into a column and the bound protein was eluted with 250 mM imidazole in buffer A. The elution of His_{10}Smt3-Asp1 PPase protein was monitored by SDS-PAGE. The His_{10}Smt3 tag was cleaved by treatment with Ulp1 protease (100 µg) during overnight dialysis against buffer A with 20 mM imidazole. Asp1 PPase was separated from the His_{10}Smt3 tag by a second round of Ni-affinity chromatography, during which Asp1 PPase was recovered in the flow-through fraction. Tag-free Asp1 PPase was concentrated to a volume of 5 mL by centrifugal ultrafiltration and then applied to a Hiload Superdex 200 pg 16/600 column (Cytiva Life Sciences) equilibrated in buffer B (30 mM HEPES, pH 6.8, 150 mM NaCl, 1 mM DTT). The peak Superdex fractions of Asp1 PPase were concentrated by centrifugal ultrafiltration and stored at −80°C. Protein concentrations were determined by using the Bio-Rad dye reagent with BSA as the standard.

5.5.2 PAGE assay of Asp1 PPase activity

Reaction mixtures (20 µL) containing 30 mM Tris-acetate (pH 5.0), 50 mM NaCl, $MgCl_2$, IPP (synthesized as described (18-20)), and Asp1 PPase as specified in the figure legends were incubated at 37°C for the indicated amount of time. The samples were then mixed with an equal volume of 2× Orange G loading buffer (10 mM Tris-HCl, pH 7.0, 1 mM EDTA, 30% glycerol, 0.1% Orange G dye) and immediately analyzed by electrophoresis (at 4°C at 8 W constant power) through a 20-cm 36% polyacrylamide gel containing 80 mM Tris-borate, pH 8.3, 1 mM EDTA until the Orange G dye reached 2/3 of the length of the gel. The gel was briefly washed with water and then stained with a solution of 0.1% Toluidine blue (Sigma), 20% methanol, 2% glycerol, followed by destaining in 20% methanol.

Chapter 6: Concluding Remarks

6.1 Impact of this dissertation

Proper execution of transcription termination ensures appropriate gene expression (e.g. fission yeast *PHO* genes), prevents generation of prematurely truncated RNAs, and limits the impact of harmful read-through transcription. The study of the proteins and metabolites which tune transcription termination therefore has widespread impact. This dissertation presents structure/function analyses of two fission yeast proteins with roles in regulating transcription termination and the expression of *PHO* genes. By dissecting Ppn1 primary structure, I identified several functional components of this protein. Through biochemical and structural evaluation of Asp1, I gained insight into substrate preference and mechanisms of ligand binding. I hope that these studies can serve as a springboard for future research into the mechanisms by which Ppn1 and Asp1 (and Asp1 kinase's product 1,5-IP_8) influence Pol2 termination site utilization.

6.1.1 Chapter 2: Structure-function analysis of fission yeast cleavage and polyadenylation factor (CPF) subunit Ppn1 and its interactions with Dis2 and Swd22

Fission yeast CPF contains 13 protein factors and enzymes that carry out a variety of functions related to mRNA 3' end processing and transcription termination. Two of these proteins, Dis2 and Ssu72, are phosphatases that dephosphorylate the Pol2 CTD (1). These phosphatases are functionally redundant – while mutational deletion or abrogation of phosphatase activity of one

phosphatase is tolerated, removal of both phosphatase activities is lethal (2). Dis2 is part of a 3-protein CPF submodule consisting of a regulatory protein Ppn1 and a WD-repeat protein Swd22 termed “DPS” (3). Given that deletion of Ppn1 or Swd22 phenocopied Dis2 with regards to Ssu72 synthetic lethality, we wondered whether the entire DPS function is tied to Dis2 activity. Surprisingly, Ppn1 and Swd22 genetic relationships diverged from those of Dis2 when mutations were combined with deletion of other CPF members or mutations to the Pol2 CTD (2). This left us to wonder whether Ppn1•Swd22 might have an independent role in transcription termination.

As a WD-repeat protein, Swd22’s structure could be predicted with high confidence. This class of proteins frequently function to promote protein-protein interaction (4). Indeed, Vanoosthuyse et al reported that while Ppn1 can form independent binary complexes with both Dis2 and Swd22, Swd22 is required for DPS association with the CPF core (3). Armed with this knowledge, I focused on exploring the nature of Ppn1 function. Ppn1 contains a conserved core sequence that is homologous to mammalian TFIIS. Flanking this core are regions whose functions were unknown and lacked strong conservation to Ppn1 from other fission yeast species.

To establish the role of these regions, I truncated Ppn1 at strategic locations along its primary structure to generate N-, C-, and N/C-terminally truncated Ppn1 proteins that were expressed from Ppn1’s endogenous genomic locus. I found that truncating Ppn1’s intrinsically disordered N-terminus increased protein abundance, suggesting that this region may decrease stability or increase

susceptibility to targeted degradation. I found that the TFIIS-like core, as well as the extreme C-terminus of the protein were unnecessary in contexts where Ppn1 activity was essential, but functional insofar as these mutations dysregulated efficient termination of *PHO* lncRNA. The essential components of Ppn1 consist of a ~200aa region that contains Ppn1's Dis2- and Swd22-binding motifs. Mapping these motifs to short regions, we identified point mutants that could selectively disrupt one interaction while retaining the other. Using these point mutations, I found that Ppn1 mutants that lacked the ability to bind Dis2 behaved identically to the Ppn1 null strain. This contrasted with genetic evidence which had suggested a Dis2-independent role for Ppn1. We hypothesized that in the absence of Dis2, Ppn1 might be able to coopt a Dis2 paralog, Sds21, into Dis2's essential role. Using yeast two-hybrid assays, I confirmed that Ppn1 strongly binds Sds21, and point mutants that disrupt Ppn1•Dis2 interaction also efface Ppn1•Sds21 interaction. These findings supported our hypothesis that Ppn1's essential role depends on its ability to coordinate a phosphatase, either Dis2 or Sds21, into the CPF to play a role in transcription termination and/or mRNA 3' end processing.

These findings were published in the journal Plos Genetics in 2021 under the DOI 10.1371/journal.pgen.1009452. Reviewers praised the study, calling it "a clear extension of prior work that provides novel insights into the molecular underpinnings of the DPS complex interactions and molecular dependencies," while also noting that the experiments were "meticulously executed." The study has already been cited, indicating its utility to the study of transcription and the CPF. To facilitate access to the information reported in this study, I uploaded its

findings to Pombase, an online database of Schizosaccharomyces pombe resources (5).

6.1.2 Chapter 3: Activities and Structure-Function Analysis of Fission Yeast Inositol Pyrophosphate (IPP) Kinase-Pyrophosphatase Asp1 and Its Impact on Regulation of pho1 Gene Expression

Genetic studies found that inositol pyrophosphate (IPP) metabolism was linked to fission yeast phosphate homeostasis (6-8). Asp1 stood out among the many players involved in IPP metabolism because of its unique domain structure, consisting of an N-terminal IPP kinase and a C-terminal IPP phosphatase. Asp1 is the sole agent of 1,5-IP_8 synthesis, but also is responsible for catabolizing 1,5-IP_8 back to 5-IP_7. Our lab demonstrated that unrestricted accumulation of 1,5-IP_8 results in dysregulation of *PHO* gene expression in a *PHO* lncRNA termination-dependent manner (7, 8). This finding led us to a model in which 1,5-IP_8 promotes transcription termination; too much causes precocious termination, too little causes defective termination. Whether and how cells temper 1,5-IP_8 levels to regulate transcription termination site utilization is currently unclear.

We sought to characterize the enzymatic activity responsible for the generation of 1,5-IP_8. To do so, I expressed and purified recombinant Asp1 kinase (1-385). Asp1's human homolog possesses both kinase and ATP hydrolase activity in its N-terminal domain. We were interested in assessing whether Asp1 exhibited one or both of these activities. Rather than use the established technique of assaying IPP kinase activity, HPLC scintillation counting of H^3-labeled IPP precursor, I developed a new assay which would simultaneously evaluate kinase

and ATPase activities. Combining γ[^{32}P]-ATP, an inositol phosphate phosphoacceptor substrate, and Asp1 kinase, I tracked the fate of the radiolabel in a one-pot thin layer chromatography assay. I first assayed Asp1 kinase's activity against the commercially available inositol phosphate IP_6. I found that in the presence of IP_6, Asp1 kinase indeed exhibited both kinase and ATPase activities, which were equally partitioned. I thoroughly characterized these activities, determining metal cofactor preference, optimal metal concentration, and pH profiles.

We made a breakthrough by opening a collaboration with the synthetic chemist Henning Jessen of the University of Freiburg. Dr. Jessen shared with us 5-IP_7, 1-IP_7, and 1,5-IP_8 synthesized in his lab. 5-IP_7 proved to be a much better Asp1 kinase substrate than IP_6, with a 22-fold higher initial reaction rate (mirroring the rate difference observed in Asp1 kinase's human homolog). In a competitive assay containing both IP_6 and 5-IP_7, Asp1 exclusively used 5-IP_7 as a phosphoacceptor, even when IP_6 was in 4-fold molar excess. Furthermore, ATPase activity was diminished in the presence of 5-IP_7 compared to IP_6. These experiments demonstrated Asp1's inherent preference for 5-IP_7, supporting a model in which Asp1's cellular role is to synthesize 1,5-IP_8 rather than 1-IP_7. I then turned to study the kinase active site by mutating several residues predicted to be involved in binding catalytic metal, IPP, nucleotide, or transition-state stabilization, each of which provided insight into the role of those functions on kinase activity.

I proceeded to use our collection of IPPs to evaluate full-length Asp1. When provided with 5-IP_7 and ATP, Asp1 generates ADP and P_i. Titrating Asp1 enabled

us to observe that at low enzyme concentrations, a small amount of 1,5-IP_8 accumulates, suggesting that 1,5-IP_8 is a transient intermediate that is generated by the kinase and dephosphorylated by the pyrophosphatase. Using a pyrophosphatase-dead mutant, I demonstrated that full-length Asp1 kinase activity is equal to that of the isolated kinase domain. I also show the pyrophosphatase activity is specific for the 1-pyrophosphate position. Finally, I showed that cellular levels of P_i inhibit the pyrophosphatase activity and enable accumulation of the kinase product with altering kinase activity.

This chapter was recently published as an article by the journal mBio (a publication of the American Society of Microbiology). Drs. Ursula Fleig and Adolfo Saiardi, two foremost experts on IPP biology, served as referees of peer review; both expressed that the article was in the top 10% of its field and recommended its publication. Dr. Fleig praised its “strong and thorough biochemical approach,” and Dr. Saiardi noted that our ‘one pot’ assay design was “particularly clever.”

The final note in the discussion of this chapter hints that atomic structures are required to further explore the mechanism and regulation of Asp1 and its constituent kinase and pyrophosphatase domains. Indeed, an essential contribution of this study was its establishment of assay systems and expertise that enabled my follow-up study on crystal structures of the kinase domain that is reported as Chapter 4 in this dissertation.

6.1.3 Chapter 4: Crystal structure and mutational analysis of Asp1 illustrate determinants of substrate specificity and binding mechanism

Through rigorous genetic and biochemical approaches, including those detailed in Chapter 3, our lab established that both Asp1 kinase and pyrophosphatase activity influence Pol2 termination behavior (7, 8). Inherent in Asp1's domain organization is a futilely balanced activity that consumes ATP without altering the IPP substrate. Under normal conditions, cells contain ~10-fold greater 5-IP_7 than 1-5-IP_8, suggesting that Asp1's pyrophosphatase activity dominates (9). I subscribe to the belief that Asp1 responds to cellular cues to modulate the ratio of the kinase and pyrophosphatase activity to enable accumulation of 1,5-IP_8. The generation of atomic structures of Asp1 is an essential step in the process of understanding the mechanisms of Asp1 regulation.

The structures reported in Chapter 4 should provide the field of IPP metabolism research with a rich template of study. In many ways, they affirmed our expectations about the overall fold of the enzyme (ATP grasp), the positioning of the nucleotide and IPP substrates relative to each other within the active site, and the constellation of active site side chains which bind substrates to align the IPP 1-phosphate to the ATP γ-phosphate. However, we also generated meaningful novel information. We implicated two additional residues, Arg274 and Lys290 in IPP binding. We also clarified the role of Arg223, a mobile residue whose counterpart in Asp1's human homolog appears to play a different catalytic role. Most significant, however, was the generation of structures lacking ligand, which

suggests that the enzyme undergoes macro-scale structural reorganization to transition between substrate capture (open) and catalytic (closed) modes.

Ironically, this discovery was strictly serendipitous; I failed in my many attempts to generate high-quality crystals of Asp1 kinase without ligand. The unbound structure was found only as an unexpected interloper within enzyme-substrate cocrystals. Thus, it is by Asp1's unique surface residue composition, notably the existence of helix α6 which is unique relative to its human homolog, that two Asp1 protomers stabilize each other *in crystallo*, one with IPP substrate bound and the other lacking substrate.

The Shuman/Schwer lab will continue to explore Asp1 structures – ongoing attempts to generate structures of the full-length enzyme encompassing kinase and pyrophosphatase domain using cryo-EM appear promising. In combining structural information (provided in this dissertation and generated in the future) with other approaches such as phospho-proteomics, live-cell microscopy, and high-throughput sequencing, I hope that ongoing research will one day reveal Asp1's regulatory features, the mechanisms by which it responds to cellular signals, and its function in cellular physiology.

6.1.4 Chapter 5: Activity of Asp1 Pyrophosphatase

While Asp1 kinase activity is responsible for generation of 1,5-IP_8, the metabolite that influences Pol2 termination site utilization, it is likely that any regulation of Asp1 which promotes net accumulation of 1,5-IP_8 depends on inhibition of pyrophosphatase activity rather than stimulation of kinase activity. I base this position upon the following observations: 1) full length, pyrophosphatase

dead Asp1 exhibits robust kinase activity, 2) pyrophosphatase activity responds to fluctuations in a related metabolite, inorganic phosphate (P_i). The mechanism by which P_i inhibits Asp1 pyrophosphatase is *tabula rasa*. Biochemical characterization of the isolated pyrophosphatase domain therefore serves as a logical first step toward understanding the mechanisms underpinning its regulation. To this end, I generated an active pyrophosphatase domain consisting of Asp1 residues 383-920 and performed preliminary exploration of its enzymatic properties and activity against different IPP substrates. These experiments lay the groundwork for future structural and biochemical evaluation of Asp1 pyrophosphatase with an eye toward exposing the means by which it is regulated.

6.2 Perspective

It is easy to take the complexity of gene expression for granted. Cells integrate myriad intra- and extracellular signals to marshal an army of protein and metabolic factors which coordinate the recruitment of Pol2 to specific genomic loci. Pol2 in turn interprets many levels of *cis* and *trans* signaling elements to terminate at just the right location on the genome. Failure to properly execute transcription termination results in prematurely truncated RNA or dangerous read-through that threatens genomic integrity. Exploration of this process could satisfy innumerable theses – this study attempts to scratch the surface by providing structure/function analyses of just two of the many proteins involved in ensuring proper spatial regulation of transcription.

7: Bibliography

7.1 Chapter 1

1. Shuman S. Transcriptional interference at tandem lncRNA and protein-coding genes: an emerging theme in regulation of cellular nutrient homeostasis. Nucleic Acids Research. 2020;48(15):8243-54.

2. Carter-O'Connell I, Peel MT, Wykoff DD, O'Shea EK. Genome-Wide Characterization of the Phosphate Starvation Response in Schizosaccharomyces pombe. BMC Genomics. 2012;13(1):697.

3. Henry TC, Power JE, Kerwin CL, Mohammed A, Weissman JS, Cameron DM, et al. Systematic screen of Schizosaccharomyces pombe deletion collection uncovers parallel evolution of the phosphate signal transduction pathway in yeasts. Eukaryot Cell. 2011;10(2):198-206.

4. Sanchez AM, Shuman S, Schwer B. Poly(A) site choice and Pol2 CTD Serine-5 status govern lncRNA control of phosphate-responsive tgp1 gene expression in fission yeast. RNA (New York, NY). 2018;24(2):237-50.

5. Lee Nathan N, Chalamcharla Venkata R, Reyes-Turcu F, Mehta S, Zofall M, Balachandran V, et al. Mtr4-like Protein Coordinates Nuclear RNA Processing for Heterochromatin Assembly and for Telomere Maintenance. Cell. 2013;155(5):1061-74.

6. Shah S, Wittmann S, Kilchert C, Vasiljeva L. lncRNA recruits RNAi and the exosome to dynamically regulate pho1 expression in response to phosphate levels in fission yeast. Genes & development. 2014;28(3):231-44.

7. Chatterjee D, Sanchez AM, Goldgur Y, Shuman S, Schwer B. Transcription of lncRNA prt, clustered prt RNA sites for Mmi1 binding, and RNA polymerase II CTD phospho-sites govern the repression of pho1 gene expression under phosphate-replete conditions in fission yeast. RNA (New York, NY). 2016;22(7):1011-25.

8. Ard R, Tong P, Allshire RC. Long non-coding RNA-mediated transcriptional interference of a permease gene confers drug tolerance in fission yeast. Nature communications. 2014;5(1):5576.

9. Garg A, Sanchez AM, Shuman S, Schwer B. A long noncoding (lnc)RNA governs expression of the phosphate transporter Pho84 in fission yeast and has cascading effects on the flanking prt lncRNA and pho1 genes. Journal of Biological Chemistry. 2018;293(12):4456-67.

10. Martens JA, Wu P-YJ, Winston F. Regulation of an intergenic transcript controls adjacent gene transcription in Saccharomyces cerevisiae. Genes & Development. 2005;19(22):2695-704.

11. Castro Alvarez JJ, Revel M, Carrasco J, Cléard F, Pauli D, Hilgers V, et al. Repression of the Hox gene abd-A by ELAV-mediated Transcriptional Interference. PLoS genetics. 2021;17(11):e1009843.

12. Schwer B, Bitton DA, Sanchez AM, Bähler J, Shuman S. Individual letters of the RNA polymerase II CTD code govern distinct gene expression programs in fission yeast. Proceedings of the National Academy of Sciences. 2014;111(11):4185-90.

13. Schwer B, Sanchez AM, Shuman S. RNA polymerase II CTD phospho-sites Ser5 and Ser7 govern phosphate homeostasis in fission yeast. RNA (New York, NY). 2015;21(10):1770-80.

14. Sanchez AM, Shuman S, Schwer B. RNA polymerase II CTD interactome with 3' processing and termination factors in fission yeast and its impact on phosphate homeostasis. Proceedings of the National Academy of Sciences of the United States of America. 2018.

15. Vanoosthuyse V, Legros P, van der Sar SJ, Yvert G, Toda K, Le Bihan T, et al. CPF-associated phosphatase activity opposes condensin-mediated chromosome condensation. PLoS genetics. 2014;10(6):e1004415.

16. Eick D, Geyer M. The RNA Polymerase II Carboxy-Terminal Domain (CTD) Code. Chemical reviews. 2013;113(11):8456-90.

17. Shuman S. Capping enzyme in eukaryotic mRNA synthesis. Prog Nucleic Acid Res Mol Biol. 1995;50:101-29.

18. Bentley DL. Coupling mRNA processing with transcription in time and space. Nature reviews Genetics. 2014;15(3):163-75.

19. Schwer B, Shuman S. Deciphering the RNA polymerase II CTD code in fission yeast. Molecular cell. 2011;43(2):311-8.

20. Pei Y, Hausmann S, Ho CK, Schwer B, Shuman S. The Length, Phosphorylation State, and Primary Structure of the RNA Polymerase II Carboxyl-terminal Domain Dictate Interactions with mRNA Capping Enzymes. Journal of Biological Chemistry. 2001;276(30):28075-82.

21. Kecman T, Kus K, Heo DH, Duckett K, Birot A, Liberatori S, et al. Elongation/Termination Factor Exchange Mediated by PP1 Phosphatase Orchestrates Transcription Termination. Cell reports. 2018;25(1):259-69.e5.

22. Parua PK, Booth GT, Sanso M, Benjamin B, Tanny JC, Lis JT, et al. A Cdk9-PP1 switch regulates the elongation-termination transition of RNA polymerase II. Nature. 2018;558(7710):460-4.

23. Suh H, Scott, Kang U-B, Chun Y, Jarrod, Buratowski S. Direct Analysis of Phosphorylation Sites on the Rpb1 C-Terminal Domain of RNA Polymerase II. Molecular cell. 2016;61(2):297-304.

24. Schüller R, Forné I, Straub T, Schreieck A, Texier Y, Shah N, et al. Heptad-Specific Phosphorylation of RNA Polymerase II CTD. Molecular cell. 2016;61(2):305-14.

25. Ho CK, Shuman S. Distinct roles for CTD Ser-2 and Ser-5 phosphorylation in the recruitment and allosteric activation of mammalian mRNA capping enzyme. Molecular cell. 1999;3(3):405-11.

26. Kim M, Krogan NJ, Vasiljeva L, Rando OJ, Nedea E, Greenblatt JF, et al. The yeast Rat1 exonuclease promotes transcription termination by RNA polymerase II. Nature. 2004;432(7016):517-22.

27. Fabrega C, Shen V, Shuman S, Lima CD. Structure of an mRNA Capping Enzyme Bound to the Phosphorylated Carboxy-Terminal Domain of RNA Polymerase II. Molecular cell. 2003;11(6):1549-61.

28. Garg A, Shuman S, Schwer B. A genetic screen for suppressors of hyper-repression of the fission yeast PHO regulon by Pol2 CTD mutation T4A implicates inositol 1-pyrophosphates as agonists of precocious lncRNA transcription termination. Nucleic acids research. 2020;48(19):10739-52.

29. Krishnamurthy S, He X, Reyes-Reyes M, Moore C, Hampsey M. Ssu72 Is an RNA Polymerase II CTD Phosphatase. Molecular cell. 2004;14(3):387-94.

30. Terrak M, Kerff F, Langsetmo K, Tao T, Dominguez R. Structural basis of protein phosphatase 1 regulation. Nature. 2004;429(6993):780-4.

31. Schreieck A, Easter AD, Etzold S, Wiederhold K, Lidschreiber M, Cramer P, et al. RNA polymerase II termination involves C-terminal-domain tyrosine dephosphorylation by CPF subunit Glc7. Nature structural & molecular biology. 2014;21(2):175-9.

32. Parua PK, Kalan S, Benjamin B, Sansó M, Fisher RP. Distinct Cdk9-phosphatase switches act at the beginning and end of elongation by RNA polymerase II. Nature communications. 2020;11(1):4338.

33. Usheva A, Maldonado E, Goldring A, Lu H, Houbavi C, Reinberg D, et al. Specific interaction between the nonphosphorylated form of RNA polymerase II and the TATA-binding protein. Cell. 1992;69(5):871-81.

34. Schwer B, Ghosh A, Sanchez AM, Lima CD, Shuman S. Genetic and structural analysis of the essential fission yeast RNA polymerase II CTD phosphatase Fcp1. RNA (New York, NY). 2015;21(6):1135-46.

35. Choy MS, Hieke M, Kumar GS, Lewis GR, Gonzalez-Dewhitt KR, Kessler RP, et al. Understanding the antagonism of retinoblastoma protein dephosphorylation by PNUTS provides insights into the PP1 regulatory code. Proceedings of the National Academy of Sciences. 2014;111(11):4097-102.

36. Sanchez AM, Garg A, Shuman S, Schwer B. Genetic interactions and transcriptomics implicate fission yeast CTD prolyl isomerase Pin1 as an agent of RNA 3′ processing and transcription termination that functions via its effects on CTD phosphatase Ssu72. Nucleic Acids Research. 2020;48(9):4811-26.

37. Jasnovidova O, Krejcikova M, Kubicek K, Stefl R. Structural insight into recognition of phosphorylated threonine-4 of RNA polymerase II C-terminal domain by Rtt103p. EMBO reports. 2017;18(6):906-13.

38. Werner-Allen JW, Lee C-J, Liu P, Nicely NI, Wang S, Greenleaf AL, et al. cis-Proline-mediated Ser(P)5 Dephosphorylation by the RNA Polymerase II C-terminal Domain Phosphatase Ssu72. Journal of Biological Chemistry. 2011;286(7):5717-26.

39. Bennett M, Onnebo SMN, Azevedo C, Saiardi A. Inositol pyrophosphates: metabolism and signaling. Cellular and Molecular Life Sciences. 2006;63(5):552-64.

40. Shears SB. Inositol pyrophosphates: Why so many phosphates? Advances in Biological Regulation. 2015;57:203-16.

41. Lee Y-S, Huang K, Quiocho FA, O'Shea EK. Molecular basis of cyclin-CDK-CKI regulation by reversible binding of an inositol pyrophosphate. Nature chemical biology. 2008;4(1):25-32.

42. Lee Y-S, Mulugu S, York JD, O'Shea EK. Regulation of a Cyclin-CDK-CDK Inhibitor Complex by Inositol Pyrophosphates. Science (New York, NY). 2007; 16(5821):109-12.

43. Sanchez AM, Garg A, Shuman S, Schwer B. Inositol pyrophosphates impact phosphate homeostasis via modulation of RNA 3' processing and transcription termination. Nucleic acids research. 2019;47(16):8452-69.

44. Murthy PPN. Structure and Nomenclature of Inositol Phosphates, Phosphoinositides, and Glycosylphosphatidylinositols. Springer US. p. 1-19.

45. Barnett JEG, Corina DL. The mechanism of glucose 6-phosphate-D-myo-inositol 1-phosphate cyclase of rat testis. The involvement of hydrogen atoms. Biochemical Journal. 1968;108(1):125-9.

46. Blunsom NJ, Cockcroft S. Phosphatidylinositol synthesis at the endoplasmic reticulum. Biochimica et Biophysica Acta (BBA) - Molecular and Cell Biology of Lipids. 2020;1865(1):158471.

47. Hemmings BA, Restuccia DF. PI3K-PKB/Akt Pathway. Cold Spring Harbor Perspectives in Biology. 2012;4(9):a011189-a.

48. Putney JW, Tomita T. Phospholipase C signaling and calcium influx. Advances in Biological Regulation. 2012;52(1):152-64.

49. Streb H, Irvine RF, Berridge MJ, Schulz I. Release of Ca2+ from a nonmitochondrial intracellular store in pancreatic acinar cells by inositol-1,4,5-trisphosphate. Nature. 1983;306(5938):67-9.

50. Guérin R, Beauregard PB, Leroux A, Rokeach LA. Calnexin Regulates Apoptosis Induced by Inositol Starvation in Fission Yeast. PLoS ONE. 2009;4(7):e6244.

51. Belde PJM, Vossen JH, Borst-Pauwels GWFH, Theuvenet APR. Inositol 1,4,5-trisphosphate releases Ca2+from vacuolar membrane vesicles of Saccharomyces cerevisiae. FEBS Letters. 1993;323(1-2):113-8.

52. Thota SG, Bhandari R. The emerging roles of inositol pyrophosphates in eukaryotic cell physiology. Journal of Biosciences. 2015;40(3):593-605.

53. Shears SB. A Short Historical Perspective of Methods in Inositol Phosphate Research. Springer US; 2020. p. 1-28.

54. Shears SB, Wang H. Inositol phosphate kinases: Expanding the biological significance of the universal core of the protein kinase fold. Adv Biol Regul. 2019;71:118-27.

55. Schlemmer U, Frølich W, Prieto RM, Grases F. Phytate in foods and significance for humans: food sources, intake, processing, bioavailability, protective role and analysis. Mol Nutr Food Res. 2009;53 Suppl 2:S330-75.

56. Macbeth MR, Schubert HL, Vandemark AP, Lingam AT, Hill CP, Bass BL. Inositol Hexakisphosphate Is Bound in the ADAR2 Core and Required for RNA Editing. Science (New York, NY). 2005;309(5740):1534-9.

57. Dick RA, Zadrozny KK, Xu C, Schur FKM, Lyddon TD, Ricana CL, et al. Inositol phosphates are assembly co-factors for HIV-1. Nature. 2018;560(7719):509-12.

58. Kim Y-K, Lee KJ, Jeon H, Yu YG. Protein Kinase CK2 Is Inhibited by Human Nucleolar Phosphoprotein p140 in an Inositol Hexakisphosphate-dependent Manner. Journal of Biological Chemistry. 2006;281(48):36752-7.

59. Lee W-K, Son SH, Jin B-S, Na J-H, Kim S-Y, Kim K-H, et al. Structural and functional insights into the regulation mechanism of CK2 by IP6 and the intrinsically disordered protein Nopp140. Proceedings of the National Academy of Sciences. 2013;110(48):19360-5.

60. Shears SB. Intimate connections: Inositol pyrophosphates at the interface of metabolic regulation and cell signaling. Journal of Cellular Physiology. 2018;233(3):1897-912.

61. Secco D, Wang C, Arpat BA, Wang Z, Poirier Y, Tyerman SD, et al. The emerging importance of the SPX domain-containing proteins in phosphate homeostasis. New Phytologist. 2012;193(4):842-51.

62. Wild R, Gerasimaite R, Jung J-Y, Truffault V, Pavlovic I, Schmidt A, et al. Control of eukaryotic phosphate homeostasis by inositol polyphosphate sensor domains. Science (New York, NY). 2016;352(6288):986-90.

63. Guan Z, Zhang Q, Zhang Z, Zuo J, Chen J, Liu R, et al. Mechanistic insights into the regulation of plant phosphate homeostasis by the rice SPX2 – PHR2 complex. Nature communications. 2022;13(1).

64. Ried MK, Wild R, Zhu J, Pipercevic J, Sturm K, Broger L, et al. Inositol pyrophosphates promote the interaction of SPX domains with the coiled-coil motif of PHR transcription factors to regulate plant phosphate homeostasis. Nature communications. 2021;12(1).

65. Furkert D, Hostachy S, Nadler-Holly M, Fiedler D. Triplexed Affinity Reagents to Sample the Mammalian Inositol Pyrophosphate Interactome. Cell chemical biology. 2020;27(8):1097-108.e4.

66. Saiardi A, Bhandari R, Resnick AC, Snowman AM, Snyder SH. Phosphorylation of proteins by inositol pyrophosphates. Science (New York, NY). 2004;306(5704):2101-5.

67. Bhandari R, Saiardi A, Ahmadibeni Y, Snowman AM, Resnick AC, Kristiansen TZ, et al. Protein pyrophosphorylation by inositol pyrophosphates is a posttranslational event. Proceedings of the National Academy of Sciences. 2007;104(39):15305-10.

68. Szijgyarto Z, Garedew A, Azevedo C, Saiardi A. Influence of inositol pyrophosphates on cellular energy dynamics. Science (New York, NY). 2011;334(6057):802-5.

69. Feoktistova A, McCollum D, Ohi R, Gould KL. Identification and Characterization of Schizosaccharomyces pombe asp1+, a Gene That Interacts with Mutations in the Arp2/3 Complex and Actin. Genetics. 1999;152(3):895-908.

70. Saiardi A, Erdjument-Bromage H, Snowman AM, Tempst P, Snyder SH. Synthesis of diphosphoinositol pentakisphosphate by a newly identified family of higher inositol polyphosphate kinases. Current Biology. 1999;9(22):1323-6.

71. Mulugu S, Bai W, Fridy PC, Bastidas RJ, Otto JC, Dollins DE, et al. A conserved family of enzymes that phosphorylate inositol hexakisphosphate. Science (New York, NY). 2007;316(5821):106-9.

72. Dollins DE, Bai W, Fridy PC, Otto JC, Neubauer JL, Gattis SG, et al. Vip1 is a kinase and pyrophosphatase switch that regulates inositol diphosphate signaling. Proceedings of the National Academy of Sciences. 2020;117(17):9356-64.

73. Pascual-Ortiz M, Saiardi A, Walla E, Jakopec V, Künzel NA, Span I, et al. Asp1 Bifunctional Activity Modulates Spindle Function via Controlling Cellular Inositol Pyrophosphate Levels in Schizosaccharomyces pombe. Molecular and cellular biology. 2018;38(9).

74. Pöhlmann J, Fleig U. Asp1, a conserved 1/3 inositol polyphosphate kinase, regulates the dimorphic switch in Schizosaccharomyces pombe. Molecular and cellular biology. 2010;30(18):4535-47.

75. Pöhlmann J, Risse C, Seidel C, Pohlmann T, Jakopec V, Walla E, et al. The Vip1 Inositol Polyphosphate Kinase Family Regulates Polarized Growth and Modulates the Microtubule Cytoskeleton in Fungi. PLoS genetics. 2014;10(9):e1004586.

76. Fawaz MV, Topper ME, Firestine SM. The ATP-grasp enzymes. Bioorganic Chemistry. 2011;39(5-6):185-91.

77. Rao VD, Misra S, Boronenkov IV, Anderson RA, Hurley JH. Structure of Type IIβ Phosphatidylinositol Phosphate Kinase. Cell. 1998;94(6):829-39.

78. Grishin NV. Phosphatidylinositol phosphate kinase: a link between protein kinase and glutathione synthase folds. J Mol Biol. 1999;291(2):239-47.

79. Wang H, Falck JR, Hall TMT, Shears SB. Structural basis for an inositol pyrophosphate kinase surmounting phosphate crowding. Nature chemical biology. 2012;8(1):111-6.

80. Yao MZ, Zhang YH, Lu WL, Hu MQ, Wang W, Liang AH. Phytases: crystal structures, protein engineering and potential biotechnological applications. Journal of Applied Microbiology. 2012;112(1):1-14.

81. Gu C, Nguyen H-N, Hofer A, Jessen HJ, Dai X, Wang H, et al. The Significance of the Bifunctional Kinase/Phosphatase Activities of Diphosphoinositol Pentakisphosphate Kinases (PPIP5Ks) for Coupling Inositol Pyrophosphate Cell Signaling to Cellular Phosphate Homeostasis. Journal of Biological Chemistry. 2017;292(11):4544-55.

82. Weaver JD, Wang H, Shears SB. The kinetic properties of a human PPIP5K reveal that its kinase activities are protected against the consequences of a deteriorating cellular bioenergetic environment. Biosci Rep. 2013;33(2):e00022.

83. Gu C, Wilson MSC, Jessen HJ, Saiardi A, Shears SB. Inositol Pyrophosphate Profiling of Two HCT116 Cell Lines Uncovers Variation in InsP8 Levels. PLOS ONE. 2016;11(10):e0165286.

84. Onnebo SM, Saiardi A. Inositol pyrophosphates modulate hydrogen peroxide signalling. Biochem J. 2009;423(1):109-18.

85. An Y, Jessen HJ, Wang H, Shears SB, Kireev D. Dynamics of Substrate Processing by PPIP5K2, a Versatile Catalytic Machine. Structure. 2019;27(6):1022-8.e2.

7.2 Chapter 2

1. Vanoosthuyse V, Legros P, van der Sar SJ, Yvert G, Toda K, Le Bihan T, et al. CPF-associated phosphatase activity opposes condensin-mediated chromosome condensation. PLoS Genet. 2014; 10: e1004415. pmid:24945319

2. Clerici M, Faini M, Meckenfuss LM, Aebersold R, Jinek M. Structural basis of AAUAAA polyadenylation signal recognition by the human CPSF complex. Nat Struct Mol Biol. 2018; 25:135–138. pmid:29358758

3. Casañal A, Kumar A, Hill CH, Easter AD, Emsley P, Degliesposti G, et al. Architecture of eukaryotic mRNA 3'-end processing machinery. Science. 2017; 358:1056–1059. pmid:29074584

4. Hill CH, Boreikaitė V, Kumar A, Casañal A, Kubík P, Degliesposti G, et al. Activation of the endonuclease that defines mRNA 3' ends requires incorporation into an 8-subunit core cleavage and polyadenylation factor complex. Mol Cell. 2019; 73:1217–1231. pmid:30737185

5. Zhang Y, Sun Y, Shi Y, Walz T, Tong L. Structural insights into the human pre-mRNA 3'-end processing machinery. Mol Cell. 2020; 77:800–809. pmid:31810758

6. Sanchez AM, Shuman S, Schwer B. RNA polymerase II CTD interactome with 3' processing and termination factors in fission yeast and its impact on phosphate homeostasis. Proc Natl Acad Sci USA. 2018; 115:E10652–E10661. pmid:30355770

7. Sanchez AM, Garg A, Shuman S, Schwer B. Inositol pyrophosphates impact phosphate homeostasis via modulation of RNA 3' processing and transcription termination. Nucleic Acids Res 2019; 47:8452–8469. pmid:31276588

8. Eick D, Geyer M. The RNA polymerase II carboxy-terminal domain (CTD) code. Chem Rev. 2013; 113:8456–8490. pmid:23952966

9. Corden JL. RNA polymerase II C-terminal domain: tethering transcription to transcript and template. Chem Rev. 2013; 113:8423–8455. pmid:24040939

10. Jeronimo C, Bataille AR, Robert F. The writers, readers, and functions of the RNA polymerase II C-terminal domain code. Chem Rev. 2013; 113:8491–522. pmid:23837720

11. Schwer B, Shuman S. Deciphering the RNA polymerase II CTD code in fission yeast. Mol Cell. 2011; 43:311–318. pmid:21684186

12. Schwer B, Sanchez AM, Shuman S. Punctuation and syntax of the RNA polymerase II CTD code in fission yeast. Proc Natl Acad Sci USA. 2012; 109:18024–18029. pmid:23071310

13. Kecman T, Kuś K, Heo DH, Duckett K, Birot A, Liberatori S, et al. Elongation/termination factor exchange mediated by PP1 phosphatase orchestrates transcription termination. Cell Rep. 2018; 25:259–269. pmid:30282034

14. Sanchez AM, Garg A, Shuman S, Schwer B. Genetic interactions and transcriptomics implicate fission yeast CTD prolyl isomerase Pin1 as an agent of RNA 3' processing and transcription termination that functions via its effects on CTD phosphatase Ssu72. Nucleic Acids Res. 2020; 48:4811–4826. pmid:32282918

15. Allen PB, Kown YG, Nairn AC, Greengard P. Isolation and characterization of PNUTS, a putative protein phosphatase 1 nuclear targeting subunit. J Biol Chem. 1998; 273:4089–4095. pmid:9461602

16. Kim YM, Watanabe T, Allen PB, Kim YM, Lee SJ, Greengard P, et al. PNUTS, a protein phosphatase 1 (PP1) nuclear targeting subunit:

characterization of its PP1- and RNA-binding domains and regulation by phosphorylation. J Biol Chem. 2003; 278:13819–13828. pmid:12574161

17. Shuman S. Transcriptional interference at tandem lncRNA and protein-coding genes: an emerging theme in regulation of cellular nutrient homeostasis. Nucleic Acids Res. 2020; 48:8243–8254. pmid:32720681

18. Mészáros B, Erdős G, Dosztányi Z. IUPred2A: context-dependent prediction of protein disorder as a function of redox state and protein binding. Nucleic Acids Res. 2018; 46:W329–W337. pmid:29860432

19. Kelley LA, Mezulis S, Yates CM, Wass MN, Sternberg MJE. The Phyre2 web portal for protein modeling, prediction and analysis. Nature Protocols. 2015; 10:845–858. pmid:25950237

20. Lemak A, Wei Y, Duan S, Houliston S, Penn LZ, Arrowsmith CH. Solution NMR structure of the N-terminal domain of the serine/threonine-protein phosphatase 1 regulatory subunit 10, PPP1R10. Protein Data Bank. 2020; Available from: www.rcsb.org/structure/6VTI

21. Schwer B, Bitton DA, Sanchez AM, Bähler J, Shuman S. Individual letters of the RNA polymerase II CTD code govern distinct gene expression programs in fission yeast. Proc Natl Acad Sci USA. 2014; 111:4185–4190. pmid:24591591

22. Schwer B, Sanchez AM, Shuman S. RNA polymerase II CTD phospho-sites Ser5 and Ser7 govern phosphate homeostasis in fission yeast. RNA. 2015; 21:1770–1780. pmid:26264592

23. Carter-O'Connell I, Peel MT, Wykoff DD, O'Shea EK. Genome-wide characterization of the phosphate starvation response in *Schizosaccharomyces pombe*. BMC Genomics. 2012; 13:697. pmid:23231582

24. Chatterjee D, Sanchez AM, Goldgur Y, Shuman S, Schwer B. Transcription of lncRNA *prt*, clustered *prt* RNA sites for Mmi1 binding, and RNA polymerase II CTD phospho-sites govern the repression of *pho1* gene expression under phosphate-replete conditions in fission yeast. RNA. 2016; 22:1011–1025. pmid:27165520

25. Sanchez AM, Shuman S, Schwer B. Poly(A) site choice and Pol2 CTD Serine-5 status govern lncRNA control of phosphate-responsive *tgp1* gene expression in fission yeast. RNA. 2018; 24:237–250. pmid:29122971

26. Garg A, Sanchez AM, Shuman S, Schwer B. A long noncoding (lnc) RNA governs expression of the phosphate transporter Pho84 in fission yeast and has cascading effects on the flanking *prt* lncRNA and *pho1* genes. J Biol Chem. 2018; 293:4456–4467. pmid:29414789

27. Shah S, Wittmann S, Kilchert C, Vasiljeva L. lncRNA recruits RNAi and the exosome to dynamically regulate *pho1* expression in response to phosphate levels in fission yeast. Genes Dev. 2014; 28:231–244. pmid:24493644

28. Lee NN, Chalamcharia VR, Reyes-Turce F, Mehta S, Zofall M, Balachandran V, et al. Mtr4-like protein coordinates nuclear RNA processing for heterochromatin assembly and for telomere maintenance. Cell. 2013; 155:1061–1074. pmid:24210919

29. Ard R, Tong P, Allshire RC. Long non-coding RNA-mediate transcriptional interference of a permease gene confers drug tolerance in fission yeast. Nature Comm. 2014; 5:5576.

30. Pascual-Ortiz M, Saiardi A, Walla E, Jakopec V, Künzel NA, Span I, et al. Asp1 bifunctional activity modulates spindle function via controlling cellular inositol pyrophosphate levels in *Schizosaccharomyces pombe*. Mol Cell Biol. 2018; 38:e00047–18. pmid:29440310

31. Dollins DE, Bai W, Fridy PC, Otto JC, Neubauer JL, Gattis SG, et al. Vip1 is a kinase and pyrophosphatase switch that regulates inositol diphosphate signaling. Proc Natl Acad Sci USA. 2020; 117:9356–9364. pmid:32303658

32. Egloff MP, Johnson DF, Moorhead G, Cohen PT, Cogen P, Barford D. Structural basis for the recognition of regulatory subunits by the catalytic subunit of protein phosphatase 1. EMBO J. 1997; 16:1876–1887. pmid:9155014

33. Terrak M, Kerff F, Langsetmo K, Tao T, Dominguez D. Structural basis of protein phosphatase 1 recognition. Nature. 2004; 429:780–784. pmid:15164081

34. Choy MS, Hieke M, Kumar GS, Lewis GR, Gonzales-DeWhitt KR, Kessler RP, et al. Understanding the antagonism of retinoblastoma protein dephosphorylation by PNUTS provides insights into the PP1 regulatory code. Proc Natl Acad Sci USA. 2014; 111:4097–4102. pmid:24591642

35. Yu J, Deng T, Xiang S. Structural basis for protein phosphatase 1 recruitment by glycogen-targeting subunits. FEBS J. 2018; 285:4646–4659. pmid:30422398

36. Ohkura H, Kinoshita N, Miyatani S, Toda T, Yanagida M. The fission yeast *dis2*$^{+}$ gene required for chromosome disjoining encodes one of two putative type 1 protein phosphatases. Cell. 1989; 57:997–1007. pmid:2544298

37. Alvarez-Tabarés I, Grallert A, Ortiz JM, Hagan IM. *Schizosaccharomyces pombe* protein phosphatase 1 in mitosis, endocytosis and a partnership

with Wsh3/Tea4 to control polarized growth. J Cell Sci. 2007; 120:3859–3601. pmid:17940068

38. Yamano H, Oshii K, Yanagida M. Phosphorylation of dis2 protein phosphatase at the cdc2 consensus and its potential role in cell cycle regulation. EMBO J. 1994; 13:5310–5318. pmid:7957097

39. Parua PK, Booth GT, Sansó M, Benjamin B, Tanny JC, Lis JT, et al. A Cdk9-PP1 switch regulates the elongation-termination transition of RNA polymerase II. Nature. 2018; 558:460–464. pmid:29899453

40. Cortazar MA, Sheridan RM, Erickson B, Fong N, Glover-Cutter K, Brannan K, et al. Control of RNA pol II speed by PNUTS-PP1 and Spt5 dephosphorylation facilitates termination by a "sitting duck torpedo" mechanism. Mol Cell. 2019; 76:896–908. pmid:31677974

41. Kim D, Langmead B, Salzberg S.L. HISAT: a fast spliced aligner with low memory requirements. Nature Methods. 2015; 12:357 pmid:25751142

42. Li H, Handsaker B, Wysoker A, Fennell T, Ruan J, Homer N, et al. The Sequence Alignment/Map format and SAMtools. Bioinformatics. 2009; 25:2078–2079 pmid:19505943

43. Anders S, Pyl PT, Huber W. HTSeq—a Python framework to work with high-throughput sequencing data. Bioinformatics. 2015; 31:166–169 pmid:25260700

44. Love MI, Huber W, Anders S. Moderated estimation of fold change and dispersion for RNA-seq data with DESeq2. Genome Biology. 2014; 15:550. pmid:25516281

45. Pei Y, Hausmann S, Ho CK, Schwer B, Shuman S. The length, phosphorylation state, and primary structure of the RNA polymerase II carboxyl-terminal domain dictate interactions with mRNA capping enzymes. J Biol Chem. 2001; 276:28075–28082. pmid:11387325

7.3 Chapter 3

1. Shears SB. 2018. Intimate connections: inositol pyrophosphates at the interface of metabolic regulation and cell signaling. J Cell Physiol 233:1897–1912. Crossref. PubMed. ISI.

2. Azevedo C, Saiardi A. 2017. Eukaryotic phosphate homeostasis: the inositol pyrophosphate perspective. Trends Biochem Sci 42:219–231. Crossref. PubMed. ISI.

3. Wild R, Gerasimaite R, Jung J-Y, Truffault V, Pavlovic I, Schmidt A, Saiardi A, Jessen HJ, Poirier Y, Hothorn M, Mayer A. 2016. Control of eukaryotic phosphate homeostasis by inositol polyphosphate sensor domains. Science 352:986–990. Crossref. PubMed. ISI.

4. Dong J, Ma G, Sui L, Wei M, Satheesh V, Zhang R, Ge S, Li J, Zhang TE, Wittwer C, Jessen HJ, Zhang H, An GY, Chao DY, Liu D, Lei M. 2019. Inositol pyrophosphate $InsP_8$ acts as an intracellular phosphate signal in *Arabidopsis*. Mol Plant 12:1463–1473. Crossref. PubMed.

5. Zhu J, Lau K, Puschmann R, Harmel RK, Zhang Y, Pries V, Gaugler P, Broger L, Dutta AK, Jessen HJ, Schaaf G, Fernie AR, Hothorn LA, Fiedler D, Hothorn M. 2019. Two bifunctional inositol pyrophosphate kinases/phosphatases control plant phosphate homeostasis. Elife 8:e43582. Crossref. PubMed. ISI.

6. Lee S, Kim MG, Ahn H, Kim S. 2020. Inositol pyrophosphates: signaling molecules with pleiotropic actions in mammals. Molecules 25:2208. Crossref. ISI.

7. Shears SB, Wang H. 2019. Inositol phosphate kinases: expanding the biological significance of the universal core of the protein kinase fold. Adv Biol Regul 71:118–127. Crossref. PubMed.

8. Randall TA, Gu C, Li X, Wang H, Shears SB. 2020. A two-way switch for inositol pyrophosphate signaling: evolutionary history and biological significance of a unique, bifunctional kinase/phosphatase. Adv Biol Regul 75:100674. Crossref. PubMed.

9. Pascual-Ortiz M, Saiardi A, Walla E, Jakopec V, Künzel NA, Span I, Vangala A, Fleig U. 2018. Asp1 bifunctional activity modulates spindle function via controlling cellular inositol pyrophosphate levels in *Schizosaccharomyces pombe*. Mol Cell Biol 38:e00047-18. Crossref. PubMed. ISI.

10. Dollins DE, Bai W, Fridy PC, Otto JC, Neubauer JL, Gattis SG, Mehta KP, York JD. 2020. Vip1 is a kinase and pyrophosphatase switch that regulates inositol diphosphate signaling. Proc Natl Acad Sci USA 117:9356–9364. Crossref. PubMed. ISI.

11. Fridy PC, Otto JC, Dollins DE, York JD. 2007. Cloning and characterization of two human *VIP1*-like inositol hexakisphosphate and diphosphoinositol pentakisphosphate kinases. J Biol Chem 282:30754–30762. Crossref. PubMed. ISI.

12. Mulugu S, Bai W, Fridy PC, Bastidas RJ, Otto JC, Dollins DE, Haystead TA, Ribeiro AA, York JD. 2007. A conserved family of enzymes that

phosphorylate inositol hexakisphosphate. Science 316:106–109. Crossref. PubMed. ISI.

13. Weaver JD, Wang H, Shears SB. 2013. The kinetic properties of a human PPIP5K reveal that its kinase activities are protected against the consequences of a deteriorating cellular bioenergetic environment. Biosci Rep 33:e00022. Crossref. PubMed. ISI.

14. Wang H, Falck JR, Tanaka Hall TM, Shears SB. 2011. Structural basis for an inositol pyrophosphate kinase surmounting phosphate crowding. Nat Chem Biol 8:111–116. Crossref. PubMed. ISI.

15. Carter-O'Connell I, Peel MT, Wykoff DD, O'Shea EK. 2012. Genome-wide characterization of the phosphate starvation response in *Schizosaccharomyces pombe*. BMC Genomics 13:697. Crossref. PubMed. ISI.

16. Shuman S. 2020. Transcriptional interference at tandem lncRNA and protein-coding genes: an emerging theme in regulation of cellular nutrient homeostasis. Nucleic Acids Res 48:8243–8254. Crossref. PubMed. ISI.

17. Sanchez AM, Shuman S, Schwer B. 2018. RNA polymerase II CTD interactome with 3' processing and termination factors in fission yeast and its impact on phosphate homeostasis. Proc Natl Acad Sci USA 115:E10652–E10661. Crossref. PubMed. ISI.

18. Sanchez AM, Shuman S, Schwer B. 2018. Poly(A) site choice and Pol2 CTD Serine-5 status govern lncRNA control of phosphate-responsive *tgp1* gene expression in fission yeast. RNA 24:237–250. Crossref. PubMed. ISI.

19. Sanchez AM, Garg A, Shuman S, Schwer B. 2019. Inositol pyrophosphates impact phosphate homeostasis via modulation of RNA 3’ processing and transcription termination. Nucleic Acids Res 47:8452–8469. Crossref. PubMed. ISI.

20. Losito O, Szijgyarto Z, Resnick AC, Saiardi A. 2009. Inositol pyrophosphates and their unique metabolic complexity: analysis by gel electrophoresis. PLoS One 4:e5580. Crossref. PubMed. ISI.

21. Capolicchio S, Thakor DT, Linden A, Jessen HJ. 2013. Synthesis of unsymmetric diphospho-inositol polyphosphates. Angew Chem Int Ed Engl 52:6912–6916. Crossref. PubMed. ISI.

22. Capolicchio S, Wang H, Thakor DT, Shears SB, Jessen HJ. 2014. Synthesis of densely phosphorylated bis-1,5-diphospho-*myo*-insoitol tetrakisphosphate and its enantiomers by bidirectional P-anhydride formation. Angew Chem Int Ed Engl 53:9508–9511. Crossref. PubMed. ISI.

23. Pavlovic I, Thakor DT, Vargas JR, McKinlay CJ, Hauke S, Anstaett P, Camuña RC, Bigler L, Gasser G, Schultz C, Wender PA, Jessen HJ. 2016. Cellular delivery and photochemical release of a caged inositol-pyrophosphate induces PH-domain translocation *in cellulo*. Nat Commun 7:10622. Crossref. PubMed.

24. Garg A. 2020. A lncRNA-regulated gene expression system with rapid induction kinetics in the fission yeast *Schizosaccharomyces pombe*. RNA 26:1743–1752. Crossref. PubMed. ISI.

25. Wang H, Nair VS, Holland AA, Capolicchio S, Jessen HJ, Johnson MK, Shears SB. 2015. Asp1 from *Schizosaccharomyces pombe* binds a [2Fe-2S]$^{2+}$ cluster which inhibits inositol pyrophosphate 1-phosphatase activity. Biochemistry 54:6462–6474. Crossref. PubMed. ISI.

26. Gu C, Nguyen HN, Hofer A, Jessen HJ, Dai X, Wang H, Shears SB. 2017. The significance of the bifunctional kinase/phosphatase activities of diphosphoinositol pentakisphosphate kinases (PPIP5Ks) for coupling inositol pyrophosphate cell signaling to cellular phosphate homeostasis. J Biol Chem 292:4544–4555. Crossref. PubMed. ISI.

27. Auesukaree C, Homma T, Tochio H, Shirakawa M, Kaneko Y, Harashima S. 2004. Intracellular phosphate serves as a signal for the regulation of the *PHO* pathway in *Saccharomyces cerevisiae*. J Biol Chem 279:17289–17294. Crossref. PubMed. ISI.

28. Wang H, Godage HY, Riley AM, Weaver JD, Shears SB, Potter BV. 2014. Synthetic inositol phosphate analogs reveal that PPIP5K2 has a surface-mounted substrate capture site that is a target for drug discovery. Chem Biol 21:689–699. Crossref. PubMed. ISI.

29. Shears SB, Baughman BM, Gu C, Nair VS, Wang H. 2017. The significance of the 1-kinase/1-phosphatase activities of the PPIP5K family. Adv Biol Regul 63:98–106. Crossref. PubMed.

30. Pöhlmann J, Fleig U. 2010. Asp1, a conserved 1/3 inositol polyphosphate kinase, regulates the dimorphic switch in *Schizosaccharomyces pombe*. Mol Cell Biol 30:4535–4537. Crossref. PubMed. ISI.

31. Topolski B, Jakopec J, Künzel NA, Fleig U. 2016. Inositol pyrophosphate kinase Asp1 modulates chromosome segregation fidelity and spindle function in *Schizosaccharomyces pombe*. Mol Cell Biol 36:3128–3140. Crossref. PubMed. ISI.

32. Pascual-Ortiz M, Walla E, Fleig U, Saiardi A. 2021. The PPIP5K family member Asp1 controls inorganic polyphosphate metabolism in *S. pombe*. JoF 7:626. Crossref. ISI.

33. Sabatinos SA, Forsburg SL. 2010. Molecular genetics of *Schizosaccharomyces pombe*. Methods Enzymol 470:759–795. Crossref. PubMed. ISI.

7.4 Chapter 4

1. Mulugu S, Bai W, Fridy PC, Bastidas RJ, Otto JC, Dollins DE, et al. A conserved family of enzymes that phosphorylate inositol hexakisphosphate. Science (New York, NY). 2007;316(5821):106-9.

2. Shears SB, Baughman BM, Gu C, Nair VS, Wang H. The significance of the 1-kinase/1-phosphatase activities of the PPIP5K family. Adv Biol Regul. 2017;63:98-106.

3. Benjamin B, Garg A, Jork N, Jessen HJ, Schwer B, Shuman S. Activities and Structure-Function Analysis of Fission Yeast Inositol Pyrophosphate (IPP) Kinase-Pyrophosphatase Asp1 and Its Impact on Regulation of pho1 Gene Expression. mBio. 2022;13(3):e0103422.

4. Li X, Gu C, Hostachy S, Sahu S, Wittwer C, Jessen HJ, et al. Control of XPR1-dependent cellular phosphate efflux by $InsP_8$ is an exemplar for functionally-exclusive inositol pyrophosphate signaling. Proceedings of the National Academy of Sciences. 2020;117(7):3568-74.

5. Weaver JD, Wang H, Shears SB. The kinetic properties of a human PPIP5K reveal that its kinase activities are protected against the consequences of a deteriorating cellular bioenergetic environment. Biosci Rep. 2013;33(2):e00022.

6. Pesesse X, Choi K, Zhang T, Shears SB. Signaling by Higher Inositol Polyphosphates: SYNTHESIS OF BISDIPHOSPHOINOSITOL TETRAKISPHOSPHATE (“InsP8”) IS SELECTIVELY ACTIVATED BY HYPEROSMOTIC STRESS*. Journal of Biological Chemistry. 2004;279(42):43378-81.

7. Gu C, Nguyen H-N, Hofer A, Jessen HJ, Dai X, Wang H, et al. The Significance of the Bifunctional Kinase/Phosphatase Activities of Diphosphoinositol Pentakisphosphate Kinases (PPIP5Ks) for Coupling Inositol Pyrophosphate Cell Signaling to Cellular Phosphate Homeostasis. Journal of Biological Chemistry. 2017;292(11):4544-55.

8. Shears SB. Intimate connections: Inositol pyrophosphates at the interface of metabolic regulation and cell signaling. Journal of Cellular Physiology. 2018;233(3):1897-912.

9. Sanchez AM, Garg A, Shuman S, Schwer B. Inositol pyrophosphates impact phosphate homeostasis via modulation of RNA 3' processing and transcription termination. Nucleic acids research. 2019;47(16):8452-69.

10. Secco D, Wang C, Arpat BA, Wang Z, Poirier Y, Tyerman SD, et al. The emerging importance of the SPX domain-containing proteins in phosphate homeostasis. New Phytologist. 2012;193(4):842-51.

11. Shuman S. Transcriptional interference at tandem lncRNA and protein-coding genes: an emerging theme in regulation of cellular nutrient homeostasis. Nucleic Acids Research. 2020;48(15):8243-54.

12. Wang H, Falck JR, Hall TMT, Shears SB. Structural basis for an inositol pyrophosphate kinase surmounting phosphate crowding. Nature chemical biology. 2012;8(1):111-6.

13. An Y, Jessen HJ, Wang H, Shears SB, Kireev D. Dynamics of Substrate Processing by PPIP5K2, a Versatile Catalytic Machine. Structure. 2019;27(6):1022-8.e2.

14. Wang H, Godage Himali Y, Riley Andrew M, Weaver Jeremy D, Shears Stephen B, Potter Barry VL. Synthetic Inositol Phosphate Analogs Reveal that PPIP5K2 Has a Surface-Mounted Substrate Capture Site that Is a Target for Drug Discovery. Chemistry & Biology. 2014;21(5):689-99.

15. Kelley LA, Mezulis S, Yates CM, Wass MN, Sternberg MJE. The Phyre2 web portal for protein modeling, prediction and analysis. Nature Protocols. 2015;10(6):845-58.

16. Laskowski RA, Jabłońska J, Pravda L, Vařeková RS, Thornton JM. PDBsum: Structural summaries of PDB entries. Protein Science. 2018;27(1):129-34.

17. Shears SB. A Short Historical Perspective of Methods in Inositol Phosphate Research. Springer US; 2020. p. 1-28.

18. Wang H, Derose EF, London RE, Shears SB. IP6K structure and the molecular determinants of catalytic specificity in an inositol phosphate kinase family. Nature communications. 2014;5(1).

19. Dollins DE, Bai W, Fridy PC, Otto JC, Neubauer JL, Gattis SG, et al. Vip1 is a kinase and pyrophosphatase switch that regulates inositol diphosphate signaling. Proceedings of the National Academy of Sciences. 2020;117(17):9356-64.

20. Otwinowski Z, Minor W. Processing of X-ray diffraction data collected in oscillation mode. Methods Enzymol. 1997;276:307-26.

21. Adams PD, Afonine PV, Bunkóczi G, Chen VB, Davis IW, Echols N, et al. PHENIX: a comprehensive Python-based system for macromolecular structure solution. Acta Crystallographica Section D: Biological Crystallography. 2010;66(2):213-21.

22. Jones TA, Zou J-Y, Cowan S, Kjeldgaard M. Improved methods for building protein models in electron density maps and the location of errors in these models. Acta Crystallographica Section A: Foundations of Crystallography. 1991;47(2):110-9.

23. Capolicchio S, Thakor DT, Linden A, Jessen HJ. Synthesis of unsymmetric diphospho-inositol polyphosphates. Angew Chem Int Ed Engl. 2013;52(27):6912-6.

24. Capolicchio S, Wang H, Thakor DT, Shears SB, Jessen HJ. Synthesis of densely phosphorylated bis-1,5-diphospho-myo-inositol tetrakisphosphate and its enantiomer by bidirectional P-anhydride formation. Angew Chem Int Ed Engl. 2014;53(36):9508-11.

25. Pavlovic I, Thakor DT, Vargas JR, McKinlay CJ, Hauke S, Anstaett P, et al. Cellular delivery and photochemical release of a caged inositol-pyrophosphate induces PH-domain translocation in cellulo. Nature communications. 2016;7:10622.

7.5 Chapter 5

1. Shears SB, Baughman BM, Gu C, Nair VS, Wang H. The significance of the 1-kinase/1-phosphatase activities of the PPIP5K family. Adv Biol Regul. 2017;63:98-106.

2. Pöhlmann J, Fleig U. Asp1, a conserved 1/3 inositol polyphosphate kinase, regulates the dimorphic switch in Schizosaccharomyces pombe. Molecular and cellular biology. 2010;30(18):4535-47.

3. Dollins DE, Bai W, Fridy PC, Otto JC, Neubauer JL, Gattis SG, et al. Vip1 is a kinase and pyrophosphatase switch that regulates inositol diphosphate signaling. Proceedings of the National Academy of Sciences. 2020;117(17):9356-64.

4. Mulugu S, Bai W, Fridy PC, Bastidas RJ, Otto JC, Dollins DE, et al. A conserved family of enzymes that phosphorylate inositol hexakisphosphate. Science (New York, NY). 2007;316(5821):106-9.

5. Garg A, Shuman S, Schwer B. A genetic screen for suppressors of hyper-repression of the fission yeast PHO regulon by Pol2 CTD mutation T4A implicates inositol 1-pyrophosphates as agonists of precocious lncRNA transcription termination. Nucleic acids research. 2020;48(19):10739-52.

6. Sanchez AM, Garg A, Shuman S, Schwer B. Inositol pyrophosphates impact phosphate homeostasis via modulation of RNA 3′ processing and transcription termination. Nucleic Acids Research. 2019;47(16):8452-69.

7. Shuman S. Transcriptional interference at tandem lncRNA and protein-coding genes: an emerging theme in regulation of cellular nutrient homeostasis. Nucleic Acids Research. 2020;48(15):8243-54.

8. Sanchez AM, Shuman S, Schwer B. RNA polymerase II CTD interactome with 3' processing and termination factors in fission yeast and its impact on phosphate homeostasis. Proceedings of the National Academy of Sciences of the United States of America. 2018.

9. Sanchez AM, Garg A, Shuman S, Schwer B. Inositol pyrophosphates impact phosphate homeostasis via modulation of RNA 3' processing and transcription termination. Nucleic acids research. 2019;47(16):8452-69.

10. Yao MZ, Zhang YH, Lu WL, Hu MQ, Wang W, Liang AH. Phytases: crystal structures, protein engineering and potential biotechnological applications. Journal of Applied Microbiology. 2012;112(1):1-14.

11. Rigden DJ. The histidine phosphatase superfamily: structure and function. Biochemical journal. 2008;409(2):333-48.

12. Jumper J, Evans R, Pritzel A, Green T, Figurnov M, Ronneberger O, et al. Highly accurate protein structure prediction with AlphaFold. Nature. 2021;596(7873):583-9.

13. Varadi M, Anyango S, Deshpande M, Nair S, Natassia C, Yordanova G, et al. AlphaFold Protein Structure Database: massively expanding the structural coverage of protein-sequence space with high-accuracy models. Nucleic Acids Research. 2021;50(D1):D439-D44.

14. Rosenbach H, Walla E, Cutsail GE, Birrell JA, Pascual-Ortiz M, Debeer S, et al. The Asp1 pyrophosphatase from S. pombe hosts a [2Fe-2S]2+ cluster in vivo. JBIC Journal of Biological Inorganic Chemistry. 2021;26(1):93-108.

15. Wang H, Nair VS, Holland AA, Capolicchio S, Jessen HJ, Johnson MK, et al. Asp1 from Schizosaccharomyces pombe Binds a [2Fe-2S]2+ Cluster Which Inhibits Inositol Pyrophosphate 1-Phosphatase Activity. Biochemistry. 2015;54(42):6462-74.

16. Benjamin B, Garg A, Jork N, Jessen HJ, Schwer B, Shuman S. Activities and Structure-Function Analysis of Fission Yeast Inositol Pyrophosphate (IPP) Kinase-Pyrophosphatase Asp1 and Its Impact on Regulation of pho1 Gene Expression. mBio. 2022;13(3):e0103422.

17. Singh H, Felts RL, Schuermann JP, Reilly TJ, Tanner JJ. Crystal Structures of the histidine acid phosphatase from Francisella tularensis provide insight into substrate recognition. J Mol Biol. 2009;394(5):893-904.

18. Capolicchio S, Thakor DT, Linden A, Jessen HJ. Synthesis of unsymmetric diphospho-inositol polyphosphates. Angew Chem Int Ed Engl. 2013;52(27):6912-6.

19. Capolicchio S, Wang H, Thakor DT, Shears SB, Jessen HJ. Synthesis of densely phosphorylated bis-1,5-diphospho-myo-inositol tetrakisphosphate and its enantiomer by bidirectional P-anhydride formation. Angew Chem Int Ed Engl. 2014;53(36):9508-11.

20. Pavlovic I, Thakor DT, Vargas JR, McKinlay CJ, Hauke S, Anstaett P, et al. Cellular delivery and photochemical release of a caged inositol-pyrophosphate induces PH-domain translocation in cellulo. Nature communications. 2016;7:10622.

7.6 Chapter 6

1. Porrua O, Libri D. Transcription termination and the control of the transcriptome: why, where and how to stop. Nature reviews Molecular cell biology. 2015;16(3):190-202.

2. Sanchez AM, Shuman S, Schwer B. RNA polymerase II CTD interactome with 3' processing and termination factors in fission yeast and its impact on phosphate homeostasis. Proceedings of the National Academy of Sciences of the United States of America. 2018.

3. Vanoosthuyse V, Legros P, van der Sar SJ, Yvert G, Toda K, Le Bihan T, et al. CPF-associated phosphatase activity opposes condensin-mediated chromosome condensation. PLoS genetics. 2014;10(6):e1004415.

4. Smith TF, Gaitatzes C, Saxena K, Neer EJ. The WD repeat: a common architecture for diverse functions. Trends Biochem Sci. 1999;24(5):181-5.

5. Harris MA, Rutherford KM, Hayles J, Lock A, Bähler J, Oliver SG, et al. Fission stories: using PomBase to understand Schizosaccharomyces pombe biology. Genetics. 2022;220(4).

6. Henry TC, Power JE, Kerwin CL, Mohammed A, Weissman JS, Cameron DM, et al. Systematic screen of Schizosaccharomyces pombe deletion collection uncovers parallel evolution of the phosphate signal transduction pathway in yeasts. Eukaryot Cell. 2011;10(2):198-206.

7. Sanchez AM, Garg A, Shuman S, Schwer B. Inositol pyrophosphates impact phosphate homeostasis via modulation of RNA 3′ processing and transcription termination. Nucleic Acids Research. 2019;47(16):8452-69.

8. Garg A, Shuman S, Schwer B. A genetic screen for suppressors of hyper-repression of the fission yeast PHO regulon by Pol2 CTD mutation T4A implicates inositol 1-pyrophosphates as agonists of precocious lncRNA transcription termination. Nucleic acids research. 2020;48(19):10739-52.

9. Pascual-Ortiz M, Saiardi A, Walla E, Jakopec V, Künzel NA, Span I, et al. Asp1 Bifunctional Activity Modulates Spindle Function via Controlling Cellular Inositol Pyrophosphate Levels in Schizosaccharomyces pombe. Molecular and cellular biology. 2018;38(9).

8: Appendix

8.1 Validation reports of structures submitted to the Worldwide Protein Data Bank

8.1.1 8E1V: Asp1 kinase in complex with ADPNP Mg IP6

1 Overall quality at a glance

The following experimental techniques were used to determine the structure:
X-RAY DIFFRACTION

The reported resolution of this entry is 1.90 Å.

Percentile scores (ranging between 0-100) for global validation metrics of the entry are shown in the following graphic. The table shows the number of entries on which the scores are based.

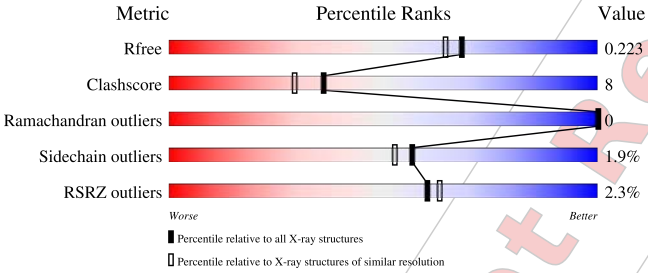

Metric	Whole archive (#Entries)	Similar resolution (#Entries, resolution range(Å))
R_{free}	130704	6207 (1.90-1.90)
Clashscore	141614	6847 (1.90-1.90)
Ramachandran outliers	138981	6760 (1.90-1.90)
Sidechain outliers	138945	6760 (1.90-1.90)
RSRZ outliers	127900	6082 (1.90-1.90)

The table below summarises the geometric issues observed across the polymeric chains and their fit to the electron density. The red, orange, yellow and green segments of the lower bar indicate the fraction of residues that contain outliers for >=3, 2, 1 and 0 types of geometric quality criteria respectively. A grey segment represents the fraction of residues that are not modelled. The numeric value for each fraction is indicated below the corresponding segment, with a dot representing fractions <=5% The upper red bar (where present) indicates the fraction of residues that have poor fit to the electron density. The numeric value is given above the bar.

Mol	Chain	Length	Quality of chain
1	A	335	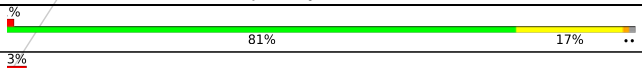
1	B	335	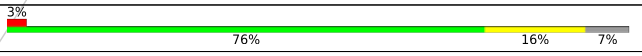

8.1.2 8E1T: Asp1 kinase in complex with ADPNP Mg IP7

1 Overall quality at a glance

The following experimental techniques were used to determine the structure:
X-RAY DIFFRACTION

The reported resolution of this entry is 1.71 Å.

Percentile scores (ranging between 0-100) for global validation metrics of the entry are shown in the following graphic. The table shows the number of entries on which the scores are based.

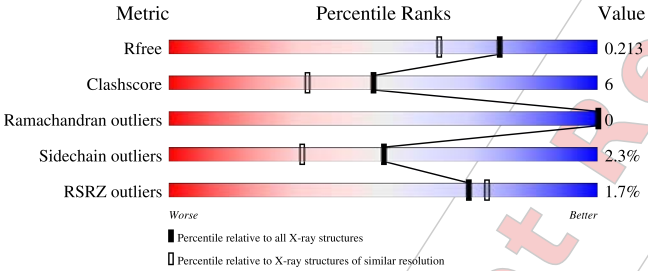

Metric	Whole archive (#Entries)	Similar resolution (#Entries, resolution range(Å))
R_{free}	130704	5722 (1.74-1.70)
Clashscore	141614	6152 (1.74-1.70)
Ramachandran outliers	138981	6051 (1.74-1.70)
Sidechain outliers	138945	6051 (1.74-1.70)
RSRZ outliers	127900	5629 (1.74-1.70)

The table below summarises the geometric issues observed across the polymeric chains and their fit to the electron density. The red, orange, yellow and green segments of the lower bar indicate the fraction of residues that contain outliers for >=3, 2, 1 and 0 types of geometric quality criteria respectively. A grey segment represents the fraction of residues that are not modelled. The numeric value for each fraction is indicated below the corresponding segment, with a dot representing fractions <=5% The upper red bar (where present) indicates the fraction of residues that have poor fit to the electron density. The numeric value is given above the bar.

Mol	Chain	Length	Quality of chain
1	A	335	86% 13%
1	B	335	84% 10% 6%

8.1.3 8E1S: Asp1 kinase in complex with ADPNP Mn IP6

1 Overall quality at a glance

The following experimental techniques were used to determine the structure:
X-RAY DIFFRACTION

The reported resolution of this entry is 1.72 Å.

Percentile scores (ranging between 0-100) for global validation metrics of the entry are shown in the following graphic. The table shows the number of entries on which the scores are based.

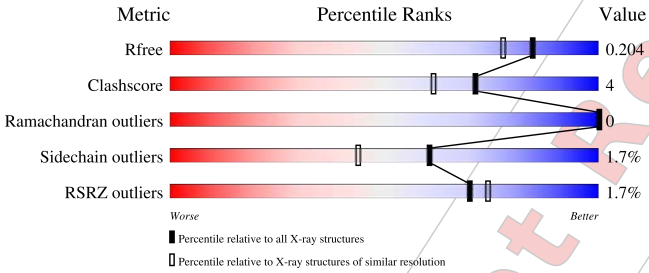

Metric	Whole archive (#Entries)	Similar resolution (#Entries, resolution range(Å))
R_{free}	130704	5722 (1.74-1.70)
Clashscore	141614	6152 (1.74-1.70)
Ramachandran outliers	138981	6051 (1.74-1.70)
Sidechain outliers	138945	6051 (1.74-1.70)
RSRZ outliers	127900	5629 (1.74-1.70)

The table below summarises the geometric issues observed across the polymeric chains and their fit to the electron density. The red, orange, yellow and green segments of the lower bar indicate the fraction of residues that contain outliers for >=3, 2, 1 and 0 types of geometric quality criteria respectively. A grey segment represents the fraction of residues that are not modelled. The numeric value for each fraction is indicated below the corresponding segment, with a dot representing fractions <=5% The upper red bar (where present) indicates the fraction of residues that have poor fit to the electron density. The numeric value is given above the bar.

Mol	Chain	Length	Quality of chain
1	A	335	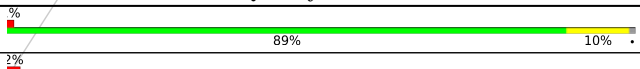
1	B	335	

8.1.4 8E1H: kinase in complex with ADP Mg 5-IP7

1 Overall quality at a glance

The following experimental techniques were used to determine the structure:
X-RAY DIFFRACTION

The reported resolution of this entry is 1.90 Å.

Percentile scores (ranging between 0-100) for global validation metrics of the entry are shown in the following graphic. The table shows the number of entries on which the scores are based.

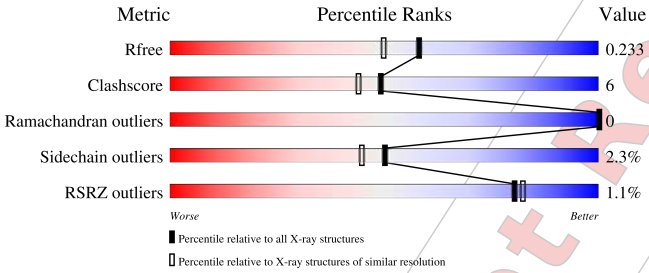

Metric	Whole archive (#Entries)	Similar resolution (#Entries, resolution range(Å))
R_{free}	130704	6207 (1.90-1.90)
Clashscore	141614	6847 (1.90-1.90)
Ramachandran outliers	138981	6760 (1.90-1.90)
Sidechain outliers	138945	6760 (1.90-1.90)
RSRZ outliers	127900	6082 (1.90-1.90)

The table below summarises the geometric issues observed across the polymeric chains and their fit to the electron density. The red, orange, yellow and green segments of the lower bar indicate the fraction of residues that contain outliers for >=3, 2, 1 and 0 types of geometric quality criteria respectively. A grey segment represents the fraction of residues that are not modelled. The numeric value for each fraction is indicated below the corresponding segment, with a dot representing fractions <=5% The upper red bar (where present) indicates the fraction of residues that have poor fit to the electron density. The numeric value is given above the bar.

Mol	Chain	Length	Quality of chain
1	A	335	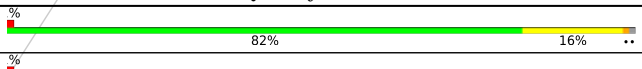
1	B	335	

8.1.5 8E1J: Asp1 kinase in complex with 1,5-IP8

1 Overall quality at a glance (i)

The following experimental techniques were used to determine the structure:
X-RAY DIFFRACTION

The reported resolution of this entry is 1.60 Å.

Percentile scores (ranging between 0-100) for global validation metrics of the entry are shown in the following graphic. The table shows the number of entries on which the scores are based.

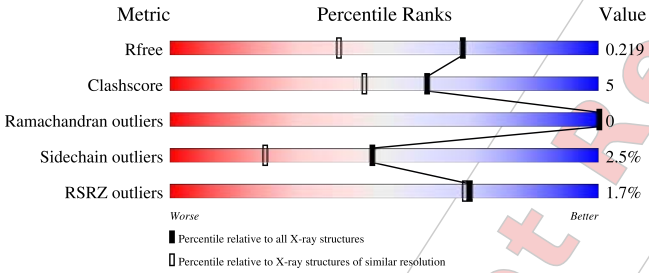

Metric	Whole archive (#Entries)	Similar resolution (#Entries, resolution range(Å))
R_{free}	130704	3398 (1.60-1.60)
Clashscore	141614	3665 (1.60-1.60)
Ramachandran outliers	138981	3564 (1.60-1.60)
Sidechain outliers	138945	3563 (1.60-1.60)
RSRZ outliers	127900	3321 (1.60-1.60)

The table below summarises the geometric issues observed across the polymeric chains and their fit to the electron density. The red, orange, yellow and green segments of the lower bar indicate the fraction of residues that contain outliers for >=3, 2, 1 and 0 types of geometric quality criteria respectively. A grey segment represents the fraction of residues that are not modelled. The numeric value for each fraction is indicated below the corresponding segment, with a dot representing fractions <=5% The upper red bar (where present) indicates the fraction of residues that have poor fit to the electron density. The numeric value is given above the bar.

Mol	Chain	Length	Quality of chain
1	A	335	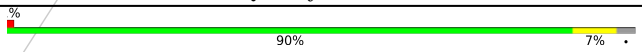
1	B	335	

8.1.6 8E1I: Asp1 kinase in complex with ATP Mg 5-IP7

1 Overall quality at a glance

The following experimental techniques were used to determine the structure:
X-RAY DIFFRACTION

The reported resolution of this entry is 2.00 Å.

Percentile scores (ranging between 0-100) for global validation metrics of the entry are shown in the following graphic. The table shows the number of entries on which the scores are based.

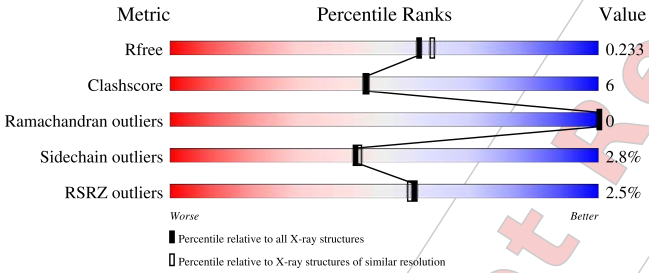

Metric	Whole archive (#Entries)	Similar resolution (#Entries, resolution range(Å))
R_{free}	130704	8085 (2.00-2.00)
Clashscore	141614	9178 (2.00-2.00)
Ramachandran outliers	138981	9054 (2.00-2.00)
Sidechain outliers	138945	9053 (2.00-2.00)
RSRZ outliers	127900	7900 (2.00-2.00)

The table below summarises the geometric issues observed across the polymeric chains and their fit to the electron density. The red, orange, yellow and green segments of the lower bar indicate the fraction of residues that contain outliers for >=3, 2, 1 and 0 types of geometric quality criteria respectively. A grey segment represents the fraction of residues that are not modelled. The numeric value for each fraction is indicated below the corresponding segment, with a dot representing fractions <=5% The upper red bar (where present) indicates the fraction of residues that have poor fit to the electron density. The numeric value is given above the bar.

Mol	Chain	Length	Quality of chain
1	A	335	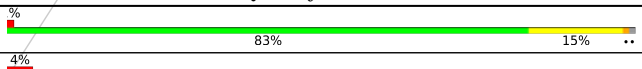
1	B	335